



Delft University of Technology

Document Version

Final published version

Citation (APA)

Brouwer, W. S. (2026). *Radar Interferometry: Parameter estimation and Network design*. [Dissertation (TU Delft), Delft University of Technology]. <https://doi.org/10.4233/uuid:21553aa5-eb0b-4041-9de3-9f53807c3105>

Important note

To cite this publication, please use the final published version (if applicable). Please check the document version above.

Copyright

In case the licence states "Dutch Copyright Act (Article 25fa)", this publication was made available Green Open Access via the TU Delft Institutional Repository pursuant to Dutch Copyright Act (Article 25fa, the Taverne amendment). This provision does not affect copyright ownership. Unless copyright is transferred by contract or statute, it remains with the copyright holder.

Sharing and reuse

Other than for strictly personal use, it is not permitted to download, forward or distribute the text or part of it, without the consent of the author(s) and/or copyright holder(s), unless the work is under an open content license such as Creative Commons.

Takedown policy

Please contact us and provide details if you believe this document breaches copyrights. We will remove access to the work immediately and investigate your claim.

This work is downloaded from Delft University of Technology.

An abstract graphic consisting of several red circular nodes connected by thin red lines. The nodes are positioned at various points: one near the top right, one on the left side, and one near the bottom center. The lines form a network of triangles and other geometric shapes across the page.

Radar Interferometry

Parameter
estimation
and
Network
design

Wietske
Brouwer

RADAR INTERFEROMETRY
PARAMETER ESTIMATION AND NETWORK DESIGN

Dissertation

for the purpose of obtaining the degree of doctor
at Delft University of Technology
by the authority of the Rector Magnificus, prof. dr. ir. H. Bijl,
chair of the Board for Doctorates
to be defended publicly on
Tuesday 7 July 2026 at 15:00

by

Wietske Sara BROUWER

Delft University of Technology, The Netherlands.

This dissertation has been approved by the promotor and the copromotor.

Composition of the doctoral committee:

Rector Magnificus,	chairperson
Prof. dr. ir. R.F. Hanssen,	Delft University of Technology, <i>promotor</i>
Dr. ir. F.J. van Leijen,	Delft University of Technology, <i>copromotor</i>

Independent members:

Em. Prof. Dr.-Ing. habil. R. Klees,	Delft University of Technology
Dr. R.M.A. Govers,	University of Utrecht
Dr. L. Chang,	University of Twente
Dr. ir. S. Samiei Esfahany,	University of Leeds, United Kingdom, University of Tehran, Iran
Dr. ir. V.B.H. Ketelaar,	Nederlandse Aardolie Maatschappij B.V.
Prof. dr. ir. F.C. Vossepoel,	Delft University of Technology, <i>reserve member</i>

This work is part of the project “*Monitoring and Modeling the Groningen Subsurface based on integrated Geodesy and Geophysics: improving the space-time dimension*” in the framework of the DeepNL program, funded by the Dutch Research Council (NWO).



Keywords: InSAR, surface displacements, stochastic model, parameter estimation, network design, decomposition
Printed by: Ridderprint | www.ridderprint.nl
Cover by: Gilles Goosen | www.gillesgoosen.cargo.site
ISBN: 978-94-6384-986-9

Copyright © 2026 by W.S. Brouwer

It is not the mountain we conquer but ourselves

Edmund Hillary

PREFACE

I can recommend everyone to, at a moment of boredom, simply type `bodemdalingska.art.nl` into your browser and start exploring the millions of colored dots that appear. Each dot represents a location in the Netherlands, with colors indicating its displacement velocity. Clicking on a point will show its displacement behavior over time. What becomes striking is how diverse these behaviors are. One point may be slowly subsiding, while a nearby point might be moving upward. Exploring the data, it is easy to forget that all of this is made possible by satellites orbiting the Earth, passing over the same location every six days from 700 km above our heads. When combined with the right models, questions, and data processing, this allows us to monitor deformation processes on Earth from space at the millimeter level. Can you believe it?

This still fascinates me greatly, and about six years ago it led me to choose InSAR as the subject of my MSc thesis, which eventually led to this PhD thesis. But precisely this kind of data exploration raises new questions. How is it possible that two points on the same object show a different displacement behavior? Or how can time series appear very smooth at the beginning of a measurement period, and then suddenly become much noisier? It was exactly this sense of curiosity and wonder that ultimately led to the creation of this thesis. And even now, after finishing it, I still find myself occasionally getting lost in time series, amazed that all of this can be done from behind a laptop, made possible only by a radar satellite taking measurements from 700 km above us. I hope that, as you read this thesis, you will share at least a little of that same sense of wonder.

*Wietske Brouwer
Delft, June 2026*

Statement on the use of generative AI. Generative AI tools were used solely for proofreading, editing, and improving the English language style of this thesis, as well as for programming support, including code review, debugging, and implementation assistance. No AI was used to generate scientific arguments, data, research methods, results, or novel content.

CONTENTS

Preface	v
Summary	xi
Samenvatting	xiii
Nomenclature	xvii
1. Introduction	1
1.1. Motivation	2
1.2. Background	2
1.3. Problem statement	3
1.4. Research objective	5
1.5. Scope limitations	9
1.6. Outline	9
2. An independent stochastic model for InSAR time series	11
2.1. Introduction	12
2.2. The mathematical model	13
2.3. Derivation of the VCM for an arc	14
2.3.1. Computing the single differences (in time)	15
2.3.2. Computing the double differences (in space and time)	20
2.4. Noise component analysis	21
2.4.1. Atmospheric noise	21
2.4.2. Thermal noise	21
2.4.3. Time variant clutter	21
2.5. Results and impact	25
2.5.1. Four example arcs	25
2.5.2. Results over Amsterdam	28
2.5.3. Comparison a priori and posteriori sigma values	28
2.6. Conclusions	29
3. A functional model for InSAR arc time series	33
3.1. Introduction	34
3.2. The mathematical model in the phase domain	35
3.3. Parameters of the functional model	36
3.3.1. Relative cross-range distance	37
3.3.2. Thermal displacement	39
3.3.3. Non-thermal displacement	40

3.4.	The mathematical model in the complex domain	41
3.4.1.	The non-linear model	44
3.4.2.	Smoothness constraints and bounds to solution	44
3.5.	Estimating the phase components	44
3.6.	Results for an arc in Amsterdam	45
3.7.	Discussion	48
3.8.	Conclusions	48
4.	Fundamentals of the spatial network	51
4.1.	Introduction	52
4.2.	Definitions and standing questions	52
4.3.	Adjusting the network in the measurement space	55
4.4.	Adjusting the network in the parameter space	56
4.4.1.	Arc-specific parameterization and arc-specific stochastic models	60
4.5.	Conclusions	62
5.	Network design for InSAR time series analysis of point scatterers	65
5.1.	Introduction	66
5.2.	Overview and principles for the network	68
5.2.1.	Estimation, quality, and testing	68
5.2.2.	A confidence-optimized robust geodetic network	72
5.3.	The control network	76
5.3.1.	Criteria for the control network	76
5.3.2.	Defining arc quality	76
5.3.3.	Design the control network	77
5.3.4.	Adjust the control network	77
5.4.	The local network	79
5.5.	Connection of local networks	80
5.6.	Adjustment parameters and corresponding variance-covariance matrices	83
5.7.	Results and impact	84
5.7.1.	The control network	86
5.7.2.	The local network	89
5.7.3.	Connection of two local networks	93
5.7.4.	Changing the requirements	99
5.8.	Discussion	99
5.9.	Conclusions	100
6.	InSAR geometry and 3D displacement estimation	101
6.1.	Introduction	102
6.2.	Theory	103
6.2.1.	The viewing geometry	103
6.2.2.	Forward model	106
6.3.	Conditions for the inverse model	106
6.3.1.	Spatio-temporally coinciding independent (STCI) LoS observations	107
6.3.2.	Region of uniform motion	108
6.3.3.	Datum connection	108

6.3.4.	Full rank system	108
6.3.5.	Angular diversity	109
6.4.	The null line	110
6.4.1.	Null line orientation evaluation	112
6.4.2.	Impact of the null line orientation	113
6.4.3.	The null line aligned (NLA) frame	114
6.5.	Evaluation of current practice	115
6.5.1.	Attribution	115
6.5.2.	Projection	115
6.5.3.	Decomposition	116
6.6.	Recommendations for InSAR product generation and interpretation	117
6.6.1.	Recommendations for vector decomposition	117
6.6.2.	Recommendations for vector projection	118
6.6.3.	Presenting LoS observations unaltered	119
6.7.	Conclusions	119
7.	Estimating 3D displacements with InSAR: the strapdown approach	121
7.1.	Introduction	122
7.2.	System Geometry	123
7.2.1.	The local strapdown coordinate system	123
7.2.2.	Deformation phenomena	125
7.3.	Estimating displacements using the strapdown approach	127
7.3.1.	The mathematical model	128
7.3.2.	The quality of the estimates	131
7.3.3.	Interpretation of the results	133
7.4.	Results: 2 case studies	133
7.4.1.	Magnesium extraction in Veendam	134
7.4.2.	Hydrological effects in relation to faults	137
7.5.	Merits and limitations	139
7.6.	Conclusions	141
8.	3D surface displacements induced by gas extraction in Groningen	143
8.1.	Introduction	144
8.2.	Scatterer classification: separating deep-only and mixed scatterers	145
8.2.1.	Step I: Quadrant classification	147
8.2.2.	Step II: Point reclassification deep-only to mixed	149
8.2.3.	Step III: Point reclassification mixed to deep-only	151
8.2.4.	Discussion	152
8.3.	Decomposing deep deformation into vertical and directional horizontal components	153
8.3.1.	Approximating the orientation of the TLN frame	154
8.3.2.	Strapdown decomposition	156
8.3.3.	Improvement using contextual premises	160
8.3.4.	From 2D local to 3D global	163
8.3.5.	Comparison with GNSS	163
8.3.6.	Results	164

8.4. Conclusions	166
9. Conclusions and recommendations	169
9.1. Contributions	173
9.2. Recommendations	174
A. Statistics of the SLC, SD, and DD phasors	177
A.1. The single temporal phase differences in the complex domain	177
A.2. The spatio-temporal double differences in the complex domain	178
A.3. NMAD and SCR relation	180
Bibliography	181
Acknowledgements	201
List of publications	204
Curriculum Vitae	207

SUMMARY

OVER the past 35 years, satellite radar interferometry (InSAR) has evolved into a well-established geodetic technique for monitoring displacements. In recent years, many generic wide-area InSAR information products have emerged, suggesting dense spatial coverage and smoothed time series that appear to unambiguously unveil diverse deformation mechanisms. However, such ‘one-size-fits-all’ products are application-agnostic and inherently suboptimal for specific objectives. This stems from the fact that no single, universal InSAR information product exists: the nature of the InSAR phase observables is such that results are inherently non-unique. Consequently, countless InSAR products can be produced over the same area of interest, even while using exactly the same input data. Transforming these phase observations into useful information requires parameter estimation, a procedure that is based on a range of assumptions and processing decisions—both explicit and implicit—that inevitably lead to different results. The usefulness of an InSAR information product is therefore directly dependent on the prior knowledge about the application for which it is produced. In this study, we investigate the potential to improve the usefulness and interpretability of InSAR information products for application-aware and -aligned (triple-A) cases, by re-examining the fundamental parts of the processing chain: i) and ii) the stochastic and functional model, iii) the network configuration, iv) the spatial geometry, and v) quality control. Combined with a method to isolate surface deformation due to hydrocarbon production, part vi), we apply the developed methods to estimate the first uniform product of 3D surface displacement due to gas production in Groningen, the Netherlands, including quality control.

Reliable parameter estimation requires a **stochastic model** (item i) from above) that accurately reflects the quality of the phase observations. Conventionally, this is often determined *a posteriori* from residuals, introducing an undesirable dependence on the functional model. We developed a method to derive a scatterer-specific stochastic model directly from the data, based on partitioned amplitude time series and the Normalized Median Absolute Deviation (NMAD). This enables the estimation of the time-varying variances and covariances of the double-differenced (DD) phase for an arc, i.e., the connection between two points, which was not achievable using existing approaches. This stochastic model can then be used to reliably estimate relative arc parameters (e.g., relative displacements) from the observed DD phase, and describe their quality.

For interpretability, these estimates are preferably expressed relative to a common datum, which requires the design of a network consisting of arcs. We find that different **network configurations** that are currently used produce different estimated parameter values and associated qualities; and therefore some networks are better than others. We develop a Confidence-Optimized Robust Geodetic (CORG) network design strategy tai-

lored to application-specific requirements. Using the stochastic model derived for arcs, the expected quality of each potential arc is quantified and used to prioritize higher-quality arcs. Consequently, the network is optimized to meet the application-dependent quality criteria for precision and reliability. Once designed, the network is adjusted in the parameter space, i.e., on the estimated arc parameters rather than the explicitly unwrapped phases. In a triple-A context, each arc may have its own **functional model**, chosen according to the application and the available contextual information, which leads to a varying parameter space across arcs. Therefore, the adjustment is performed on the shared parameters—specifically the relative cross-range distance (instead of the commonly used relative height) and the thermal displacement factor—as well as on the reduced phase.

While this network adjustment yields relative displacements, these remain expressed in the satellite's Line-of-Sight (LoS) direction. InSAR observations are only sensitive to the projection of the 3D displacement vector onto this LoS direction, and estimating the full 3D displacement vector results typically in an underdetermined inverse problem, as often only two independent observations are available. Therefore, we revisit the fundamentals of **InSAR geometry**, putting key concepts such as decomposition and projection in perspective and introducing the concepts of the null line and the null-line aligned (NLA) coordinate system. These concepts provide a rigorous foundation for unbiased displacement estimation and interpretation, addressing common pitfalls in current practice that lead to biased results. We provide recommendations for the generation and interpretation of InSAR displacement products.

Building on this, we propose a solution to this underdetermined problem: the **strap-down approach**. This new largely generic method enables unbiased 3D displacement estimation from only two LoS observations (i.e. an ascending and descending observation) by incorporating minimal and largely undisputed contextual knowledge about the expected deformation mechanism. It defines a local reference system with transversal, longitudinal, and normal (TLN) axes, where displacement occurs in the transversal-normal plane only. The approach includes full error propagation and produces physically meaningful results that are '3D-global/2D-local'.

Finally, we apply the strapdown method to estimate vertical and directional horizontal displacement components for **Groningen**, the Netherlands, where gas extraction since 1964 has caused surface deformation. We estimate the orientation of the TLN frame directly from the data and incorporate contextual information to apply a bootstrapping method, thereby enhancing the quality of the results. This approach yields reliable 3D displacement estimates for the Groningen gas field, revealing previously unquantified horizontal displacements, including their quality assessment.

In conclusion, by addressing the six fundamental parts of the InSAR processing chain, we have shown that only by incorporating contextual knowledge—about the problem and the intended use of the data—it is possible to produce an InSAR information product that is optimally suited to its specific application. Such an application-aware and -aligned (triple-A) approach yields parameter estimates that are more precise and physically more meaningful. We further developed a method to quantify and present uncertainties with the estimates, providing InSAR results that are more reliable and actionable.

SAMENVATTING

SATELLIET-radarinterferometrie (InSAR) is een van de belangrijkste geodetische technieken voor het monitoren van verplaatsingen van (objecten op) het aardoppervlak. Als gevolg hiervan komen er ook steeds meer InSAR resultaten online beschikbaar: producten die voor miljoenen punten het verplaatsingsgedrag in de tijd weergeven en de indruk wekken dat alle denkbare deformatie-mechanismen overal te meten zijn en zichtbaar zijn in het product. Echter, doordat bij zulke 'one-size-fits-all'-producten de toepassing vooraf niet bekend is, zijn ze juist niet optimaal voor veel specifieke toepassingen. Dit komt doordat we niet kunnen spreken van één universeel InSAR informatieproduct. De eigenschappen van de InSAR-fasewaarnemingen zorgen er namelijk voor dat het resultaat dat wordt berekend uit de waarnemingen (het InSAR informatieproduct) niet uniek is. Als gevolg hiervan zijn er ontelbaar veel resultaten te produceren over een gebied, zelfs wanneer we gebruik maken van exact dezelfde satellietgegevens. Voor het genereren van bruikbare resultaten uit deze InSAR-fasewaarnemingen moeten we een parameterschatting uitvoeren. Deze is gebaseerd op een reeks zowel expliciete als impliciete aannames en keuzes in de dataverwerking, waarbij andere aannames direct zullen leiden tot andere resultaten, en dus ook een ander InSAR-product. De bruikbaarheid van een InSAR-product is daarmee direct afhankelijk van de keuzes en aannames in de dataverwerking. In dit onderzoek onderzoeken we of het mogelijk is om de bruikbaarheid en de interpreteerbaarheid van InSAR-informatieproducten te verbeteren door kennis over de toepassing van het product mee te nemen. Dit noemen we *triple-A: application-aware and aligned*. Hiervoor kijken we met een nieuwe blik naar de fundamentele stappen in de dataverwerking. We bekijken zowel het stochastisch als het functiemodel, de netwerkconfiguratie, de geometrie van de InSAR-waarnemingen, en de kwaliteit van de resultaten. Uiteindelijk passen we de ontwikkelde methoden toe om de 3D-deformaties te schatten als gevolg van de gaswinning in Groningen, in Nederland.

Om te beginnen vereist een betrouwbare parameterschatting een **stochastisch model** dat de kwaliteit van de fasewaarnemingen beschrijft. In de huidige methoden wordt dit stochastisch model vaak a posteriori bepaald op basis van residuen met het functiemodel, waardoor een ongewenste afhankelijkheid van het functiemodel ontstaat. Daarom hebben we een methode ontwikkeld die voor elke reflector (*scatterer*) een uniek stochastisch model afleidt op basis van een gesegmenteerde amplitude-tijdserie en de Normalized Median Absolute Deviation (NMAD). De methode resulteert in tijdsafhankelijke varianties en covarianties voor de interferometrische fase van een arc, waarbij een arc de verbinding is tussen twee punten (of scatterers). Dit stochastisch model gebruiken we vervolgens om betrouwbare relatieve arc-parameters (bijvoorbeeld relatieve verplaatsingen) te schatten en hun kwaliteit te beschrijven.

Om interpreteerbare resultaten te verkrijgen worden relatieve parameters voor de punten bij voorkeur geschat ten opzichte van één gemeenschappelijk referentiepunt. Hiervoor is een **netwerk** nodig, bestaande uit verbinding (*arcs*). We laten zien dat verschillende netwerkconfiguraties leiden tot verschillende geschatte parameterwaarden en kwaliteitswaarden. Sommige netwerken zijn daardoor beter dan andere. Wij stellen daarom de Confidence-Optimized Robust Geodetic (CORG) netwerkontwerpmethode voor, die het netwerk ontwerpt zodanig dat het eindresultaat voldoet aan de toepassingsafhankelijke kwaliteitseisen. Met behulp van het ontwikkelde stochastisch model voor een arc kunnen we de verwachte kwaliteit van alle mogelijke arcs bepalen en de arcs prioriteren. Vervolgens kan het netwerk worden geoptimaliseerd zodat het voldoet aan de vooraf gedefinieerde eisen. Uiteindelijk wordt het netwerk vereffend op de geschatte parameters in plaats van de expliciet berekende faseambigüiteiten. Omdat in een triple-A-context elke arc een eigen **functiemodel** kan hebben (afhankelijk van de toepassing en de beschikbare contextuele informatie), zullen de parameters die we schatten per arc verschillend zijn. De vereffening wordt daarom uitgevoerd op de parameters die wel gemeenschappelijk zijn voor de arcs—zoals de relatieve cross-range afstand (in plaats van de veelgebruikte relatieve hoogte) en de thermische expansiefactor—en de gereduceerde fase.

Het resultaat van de netwerkvereffening zijn geschatte verplaatsingen in de kijkrichting (LoS) van de satelliet. Dit komt doordat de radar alleen gevoelig is voor de projectie van de daadwerkelijke 3D-verplaatsingsvector op de kijkrichting. Voor de interpretatie is het echter vaak gewenst dat de resultaten worden weergegeven in bijvoorbeeld de oostelijke, noordelijke en verticale richting. Dit vraagt om een decompositie van de waarnemingen. Omdat vaak slechts twee onafhankelijke waarnemingen beschikbaar zijn, resulteert dit in veel gevallen in een onderbepaald schattingsprobleem. Veel huidige methoden gaan hier onjuist mee om, hetgeen resulteert in foutieve resultaten. Daarom bekijken we het probleem opnieuw vanuit de **geometrie** van de waarnemingen en formuleren we duidelijke condities die nodig zijn voor een succesvolle decompositie. Ook maken we een onderscheid tussen een projectie en een decompositie en introduceren we de *null line* en het *null-line aligned* (NLA) coördinatenstelsel, die beide een basis bieden voor het schatten van de 3D-verplaatsingen en helpen bij de interpretatie van de schattingen.

Daarop voortbouwend hebben we de **strapdown-methode** ontwikkeld. Deze generieke methode maakt het mogelijk om voor deformatie-mechanismen waarbij het oorzakelijk mechanisme bekend is 3D-verplaatsingen te schatten met slechts twee LoS-waarnemingen. De methode maakt gebruik van een lokaal referentiestelsel met transversale, longitudinale en normale (TLN) assen, waarbij de verplaatsing enkel optreedt in het transversaal-normaal vlak. De methode maakt volledige foutvoortplanting mogelijk en levert resultaten die '3D-globaal/2D-lokaal' zijn.

Ten slotte passen we de strapdown-methode toe om verticale en directioneel horizontale verplaatsingen te schatten voor **Groningen**, waar gaswinning al sinds 1964 leidt tot verplaatsingen van het aardoppervlak. We schatten de oriëntatie van het TLN-stelsel direct uit de data en nemen contextuele informatie mee om de kwaliteit van de resultaten verder te verbeteren. Deze aanpak levert betrouwbare 3D-verplaatsingsschattingen op voor het Groningse gasveld en laat voor het eerst gekwantificeerde horizontale verplaat-

singen zien, inclusief hun kwaliteit.

Samenvattend tonen we aan dat alleen door het meenemen van contextuele kennis (zowel over het probleem als over de toepassing van de data) een InSAR-product kan worden ontwikkeld dat optimaal is voor de specifieke toepassing. Een dergelijke toepassingsbewuste en -gerichte (triple-A) benadering resulteert in geschatte parameters die nauwkeuriger zijn en een fysieke betekenis hebben. Bovendien hebben we een methode ontwikkeld om de onzekerheden bij de schattingen te kwantificeren en te presenteren, waardoor InSAR-resultaten betrouwbaarder en bruikbaarder worden.

NOMENCLATURE

LIST OF ABBREVIATIONS

1D	One-dimensional
2D	Two-dimensional
3D	Three-dimensional
AA	Application-Agnostic
AAA	Application-Aware and -Aligned
asc	ascending
AoI	Area of Interest
APS	Atmospheric Phase Screen
aut	autonomous deformation behavior
BLUE	Best Linear Unbiased Estimation
CORG	Confidence-Optimized Robust Geodetic
CR	Corner Reflector
DD	Double Difference
deep	deep deformation behavior
DEM	Digital Elevation Model
DIA	Detection, Identification, and Adaptation
DRaMA	Delft Radar Modelling and performance Analysis
DS	Distributed Scatterer
dsc	descending
DTM	Digital Terrain Model
EGMS	European Ground Motion Service
ENU	East, North, Up
EU	East-Up
GNSS	Global Navigation Satellite System
GPS	Global Positioning System
IFG	Interferogram
IGRS	Integrated Geodetic Reference Station
ILS	Integer Least Squares
InSAR	SAR Interferometry
PS	Point Scatterer
PSI	Point Scatterer Interferometry
LoS	Line-of-Sight
MAD	Median Absolute Deviation
NAD	Normalized Amplitude Dispersion
NESZ	Noise Equivalent Sigma Zero

NLA	Null Line Aligned
NMAD	Normalized Median Absolute Deviation
OMT	Overall Model Test
PoV	Projected onto the Vertical
RUM	Region of Uniform Motion
SAR	Synthetic Aperture Radar
SD	Single Difference
shlw	shallow deformation behavior
SLC	Single Look Complex
SNR	Signal-to-Noise-Ratio
STCI	Spatio-Temporally Coinciding Independent
TIC	Time Invariant Clutter
TLN	Transversal, Longitudinal, Normal
TN	Transversal-Normal
TVC	Time Variant Clutter
UW	Unweighted
VCE	Variance Component Estimation
VCM	Variance Covariance Matrix
W	Weighted
ZDP	Zero-Doppler Plane

LIST OF SYMBOLS

cm	centimeter
dB	decibel
deg	degrees
K	kelvin
km	kilometer
m	meter
mm	millimeter
rad	radians
y	year
A	design matrix; amplitude
a	phase ambiguity; arc observable
a_p	first geometrical polynomial component for partition p
B	baseline
B_T	temporal baseline
B_{th}	thermal baseline
B_{\perp}	perpendicular baseline
B_{\parallel}	parallel baseline
b_p	second geometrical polynomial component for partition p
C_{atm}	spatial covariance for the atmosphere
Cond(.)	condition number
c_p	third geometrical polynomial component for partition p
$D\{.\}$	dispersion operator
D	nr of daughter acquisitions
d	displacement; daughter acquisition
d_{ENU}	3D displacement vector in east, north, and up direction
d_{LoS}	projection of the 3D displacement vector onto the LoS direction
d_{PoV}	projection of d_{LoS} onto the vertical
d_{PoEU}	projection of d_{LoS} onto the EU plane
d_{nt}	non-thermal displacement
d_{TLN}	3D displacement vector in transversal, longitudinal, and normal direction
diag{.}	diagonal of a matrix
$E\{.\}$	expectation operator
\hat{e}	estimated error
e	east component
exp{.}	exponential operator
fr	far range
H	height
H_0	null hypothesis
H_a	alternative hypothesis
h_{xr}	cross-range distance
I	identity matrix
Im{.}	imaginary part
i	imaginary unit

J	Jacobian matrix
L	Longitudinal direction
l	arc length
M_A	normalized median absolute deviation of the amplitude
m	mother acquisition; number of observations
$\max\{.\}$	maximum operator
$\text{med}\{.\}$	median
N	Normal direction; Normal matrix
n	number of unknowns; null line; north component
nr	near range
P	complex phasor; projector
P_{LoS^\perp}	orthogonal projector onto the LoS
$P_{\text{up,LoS}^\perp}$	oblique projector of the LoS onto the vertical
p	point in a free network; partition
p^c	control point
p^s	secondary point
Q_ψ	VCM of the SLC phase
Q_ϕ	VCM of the SD phase
Q_φ	VCM of the DD phase
Q_{atm}	VCM of the atmospheric noise
Q_{LoS}	VCM of the LoS observations
Q_{thm}	VCM of the thermal noise
Q_{trvc}	VCM of the time variant clutter
$Q_{\hat{x}}$	VCM of the estimates of the unknown parameters
Q_y	VCM of observations
q	point in a base network
R	range distance between satellite and the scatterer; rotation matrix
$\text{Re}\{.\}$	real part
T	Transversal direction
\underline{T}_q	test statistic of dimension q
u	free network parameters; up component
$u_{d/o}$	class of scatterers that solely reflect the deep deformation signal
u_{mix}	class of scatterers that have multiple deformation signals
u_{LoS}	LoS unitvector
v	velocity; base network parameters
x	unknown parameters
y	observations
\hat{y}	adjusted observable
z	offset parameter between free and base network
$\{.\}^{-1}$	inversion
$\{.\}^T$	matrix transpose
$\hat{\cdot}$	estimated value
\cdot	stochastic value

α	level of significance
α_a	slope aspect
α_d	azimuth of the ZDP at the scatterer in the direction towards the satellite
α_h	orbital heading angle of the satellite
β	cross-range to phase factor
δ_{displ}	displacement parameter vector
γ	power of test
ΔT	temperature difference
ζ	elevation angle of the null line
η	relative thermal displacement
$\theta, \theta_{\text{inc}}$	nominal (ellipsoidal) incidence angle
θ_l	look angle
Λ	azimuth of the longitudinal direction (L) relative to the north
λ	radar wavelength; non-centrality parameter
μ	mean value
$\mu\epsilon$	micro-strain
$\mu_{\Delta T}^{L_{\text{LoS}}}$	relative thermal displacement
$\chi^2(q, \lambda)$	χ^2 - distribution with dimension q and non-centrality parameter λ
σ	standard deviation
Φ	elevation angle of the longitudinal direction relative to the horizontal
ψ	SLC Phase
ψ_i^d	SLC Phase for PS i and daughter image d
ϕ	temporal SD phase; azimuth angle of the null line
ϕ_i^{md}	temporal SD phase for PS i of daughter image d relative to the phase of the mother image m
$\phi_{\text{ref.surf}}$	phase of the reference surface
φ	absolute DD phase
φ^w	relative (wrapped) DD phase
φ_{ij}^{md}	DD phase for point scatterer j at epoch d , relative to reference point i at mother epoch m
φ_l	phase reduced for the static components
$\varphi_{d_{\text{nt}}}$	non-thermal displacement phase
$\varphi_{d_{\text{nt}}, \eta}$	total displacement phase
φ_η	thermal displacement phase
$\varphi_{h_{\text{xr}}}$	cross-range distance phase
φ_{S}	atmospheric phase
φ_{n}	phase noise
Ω	elevation angle of the transversal direction
ω	correlation length of atmospheric signal

1

INTRODUCTION

1.1. MOTIVATION

ALTHOUGH InSAR has become a widely used geodetic technique for displacement monitoring, its methods rely heavily on implicit, heuristic, and non-specific assumptions, and do not optimize for a specific application, leading to suboptimal displacement products. This research revisits these fundamental choices and proposes a more robust and application-dependent approach to displacement parameter estimation and InSAR displacement product generation, resulting in more reliable and interpretable outcomes.

1.2. BACKGROUND

Over the past 35 years, InSAR has become a well-established geodetic technique for monitoring displacements of (objects on) the earth's surface. Initially, it was used primarily to monitor natural hazards, such as volcanic activity [4, 63, 123] and earthquakes [22, 57, 122, 203], by analyzing static interferograms. Next came the development of time-series techniques such as Point Scatterer Interferometry¹ (PSI or PS-InSAR), which track a subset of points with constant scattering properties over time, often originating from man-made structures. These techniques allow for the estimation of precise displacement time series for many points. Particularly in the early 2000s, significant research focused on developing PS methods to estimate displacements from the satellite radar observations, i.e., the phase measurements [61, 89, 90, 100, 103, 162, 193]. This was challenging, given the multiple contributors to the observed phase, such as atmospheric delay, deformation, topography, and integer phase cycles, resulting in an underdetermined estimation problem and hence non-unique solutions. Today, PS methods remain widely used. The 'typical' InSAR information product is a map of colored dots, each representing a strong reflection point, with colors indicating the displacement velocity.

In recent years, growing interest in the production of deformation maps at national or continental scales has shifted the research away from fundamental PS methodology toward the development of techniques for efficiently processing data over large areas [39, 119]. Estimating displacements for millions of points introduces significant computational challenges, particularly because InSAR is a relative geodetic technique that relies on solving large, interconnected networks, and because processing vast datasets also involves aligning and merging data from multiple satellite tracks [1, 45, 58, 106, 115]. This has led to the creation of national ground motion maps—such as those for the Netherlands, Norway, Italy, and Germany [11, 38, 46, 99]—and other wide-area products such as the European Ground Motion Service (EGMS) [40]. These products suggest unique and comprehensive results, due to their dense spatial coverage and smooth time series that capture a wide variety of deformation mechanisms [41]. Based on these results, it is tempting to regard InSAR as a fully mature geodetic technique that effectively fulfills its intended purpose. As a consequence, the methodological development of InSAR, particularly in PS techniques, is widely regarded as largely complete, with limited need for further fundamental research into its underlying principles, as evidenced by the growing

¹Throughout this work we use the Delft InSAR taxonomy as proposed by Hu *et al.* [91]

number of articles using these products as (deterministic) input data (e.g., [8, 55, 114, 127, 137, 142]), relative to the studies aimed at methodological improvement.

However, while these wide-area (i.e. products of national or continental scale that capture a variety of deformation phenomena), "one-size-fits-all" solutions may appear appealing for users and can be used for reconnaissance and browsing, they are usually suboptimal for specific applications with a defined objective. Creating InSAR information products that are "fit for purpose" requires input from domain experts beforehand, which leads to explicit assumptions throughout the parameter estimation process, as we will discuss below. The success of companies that offer tailored InSAR products based on user-specific needs illustrates this point. Thus, the mere existence of these companies highlights a contradiction: if default national or wide-area deformation maps were sufficient and fit for purpose, customized services would be unnecessary. Instead, their popularity demonstrates that standard products often fail to meet end users' practical demands.

Moreover, as generic application-agnostic (AA) InSAR information products, i.e., products where the processing choices are made without a specific application in mind, become more widely available, they are increasingly being used by users without a geodetic or InSAR background. This widespread use based on availability poses a risk because the data are often presented and interpreted as "truth" with little consideration for the underlying assumptions, decisions, and uncertainties, i.e., the information products are assumed to be deterministic and undisputed.

1.3. PROBLEM STATEMENT

With so many InSAR information products available and accessible, it is not trivial to assess and compare their quality and evaluate the product's fitness for purpose. Questions such as *Which product should I use?* *Can I trust these results?* and *What is the quality of these results?* may seem straightforward, but are in fact impossible to answer in a generic sense, only in a particular 'application-aware' sense. This can be attributed to four fundamental challenges in InSAR processing and interpretation, which form the basis of this thesis and are addressed in bold below. First, the fundamental nature of InSAR processing leads to **non-uniqueness** in the resulting products, i.e., estimated (displacement) parameters, as "the" InSAR product does not exist. As shown in [31, 163, 205], processing the same data can lead to different results and thus different InSAR products.

What is commonly referred to as an "InSAR displacement measurement" is, in fact, not a measurement but an estimate, i.e., a derived quantity from the radar observation [80]. The fundamental radar observation is a complex signal from which differential wrapped phase values are extracted. Only relative displacements, both in time (between acquisition epochs) and in space (between points), can be estimated from these phases. Furthermore, the observed differential phase is a combination of several components: geometry (including displacement and cross-range position, where the latter is related to topography as we will discuss in Chapter 3), delay (including tropospheric and ionospheric propagation effects), and noise [80]. Transforming these phase observations into a usable InSAR product, also

referred to as *parameter estimation*, requires a range of assumptions and processing decisions. In fact, any InSAR product is the outcome of a processing chain that combines: i) radar data, ii) a processing algorithm, and iii) operator-defined settings. Even small changes in any of these three components—such as the addition of a single observation epoch, the use of a different order in the processing steps, or the adaptation of one parameter setting or assumption (e.g. the point detection threshold)—can lead to a different result and thus a different InSAR product [35, 54, 153, 163].

Because InSAR products depend strongly on the specific data, algorithms, and processing settings used, any generic product is, by definition, suboptimal for a specific application. A product or processing methodology that performs well for one use case (such as monitoring deformation of a bridge) may completely fail in another (identifying motion in landslide-prone areas) [41]. Since each application imposes different requirements, InSAR processing must be tuned accordingly. Without such application-specific tuning, the "high-quality" wide-area products may fail to meet the needs of the intended analysis.

In addition to application-specific tuning, estimating displacements from complex radar observations requires a functional model that parametrizes the expected displacement behavior for the scatterer over time and thus relates the observations to the unknown parameters (e.g., the displacement parameterization—for instance a velocity). However, this **functional model is unknown** [28].² Many InSAR products contain millions of scatterers, each with unique characteristics and unique kinematic behavior. Ideally, each point would require a tailored model, but this is practically infeasible. At the same time, assuming that a single, uniform parameterization (e.g., constant velocity) is suitable for all points is not sustainable and may result in biased or incorrect parameter estimates [193].

Reliable parameter estimation also requires a priori knowledge of observation quality, to guide processing decisions and to assess the quality of the estimated parameters (e.g., the displacement values) [82, 110]. However, this **stochastic model is unknown** (i.e., the model that describes the quality of the observations), as each scatterer has distinct scattering characteristics that may vary over time [92, 93]. The pragmatic solution for this problem—and the most commonly used one in practice—is to assess quality a posteriori, by examining the residuals between the observations and a fitted functional model [90, 197, 210]. However, this solution is problematic, since it creates a direct dependency between the functional model and the stochastic model. Fundamentally, this is not acceptable, since the stochastic model, i.e., the quality of the observables, has no relation or dependency to the particular application of those observables, i.e., the parameters and hence the functional model. Consequently, if the functional model is incorrect or oversimplified, unmodeled motion will be interpreted as noise and absorbed into the stochastic model, which is fundamentally undesirable. It not only leads to biased

²Note that this functional model differs from a physical model, which represents an input–output relationship based on physical processes and can therefore exist independently of observations. While a functional model may be based on or inspired by a physical model, it forms, together with the stochastic model, the mathematical model of the observation equations, describing the relationship between the chosen unknown parameters and the observations.

or misleading estimates of observation quality, but also implicitly assumes that the noise characteristics are homogeneous or stationary, whereas in reality they may vary over time and between scatterers. Moreover, this issue is further complicated by the fact that, at the level of individual epochs, only a single observation is available. As a result, it is not possible to distinguish whether a deviation from the model originates from noise, unmodeled motion, or other effects. Importantly, it is well established that the stochastic model should be independent of the functional model, as it is typically used to weight the observations accordingly and for testing the functional model. However, in current InSAR practice, such an independent characterization of observation quality is generally lacking, particularly for PS-InSAR. Moreover, most wide-area products present displacement time series without any indication of uncertainty. In many cases, uncertainties are neither quantified nor reported. As a result, the observations are effectively treated as deterministic and undisputed, presented without error bars, which severely limits the user's ability to interpret the data.

Finally, **data interpretation** is further complicated by the satellite's line-of-sight (LoS) geometry. Displacements are observed along the LoS direction, making them difficult to interpret in terms of physical three-dimensional (3D) deformation [80]. While it is often desirable to express motion in east, north, and up components, the lack of multiple viewing geometries restricts the ability to perform a 3D decomposition. Nevertheless, many InSAR products present displacements in vertical and eastward components (under the assumption that a northward component cannot be retrieved), which result in biased and potentially misleading results.

1.4. RESEARCH OBJECTIVE

Given the four fundamental challenges outlined in bold Sec. 1.3, it becomes clear that although PS-InSAR is a powerful technique, generating interpretable and meaningful results (i.e., estimating displacement parameters) requires an application-dependent mathematical model. In current practice, however, such tailored modeling is uncommon. Many existing approaches rely on standard modeling choices, such as applying the same functional model to all scatterers, and on heuristic approaches that are not necessarily suitable for all use cases [10, 61, 87, 193]. While these methods are, in principle, flexible enough to accommodate specific tuning, this potential is rarely exploited in practice. As a result, the mismatch between the chosen model and the chosen parameterization limits both the interpretability and the reliability of the (displacement) estimates.

Therefore, the objective of this study is to define an optimal, application-specific mathematical model. We systematically revisit the fundamental aspects of InSAR parameter estimation. Rather than taking established practices for granted, this work aims to evaluate whether alternative approaches—grounded in fundamental principles and informed by contextual information, rather than heuristic approaches—may lead to more reliable and physically meaningful results. This leads to the main research question of this study:

Can the PS-InSAR parameter estimation problem be reformulated and improved to provide more precise, reliable, and physically meaningful parameter estimates, aiming for better interpretable and actionable information?

To answer this question, we defined four more specific research questions:

1. Is it possible to define an a priori, independent, and unique stochastic model for each arc?

Precise and reliable PS-InSAR parameter estimation requires a realistic stochastic model that properly represents the quality of phase observations along an arc (i.e., the connection between two points), while accounting for the individual characteristics of each scatterer [82]. Current approaches often use the Normalized Amplitude Dispersion (NAD), which is related to the quality of the phase measurements, during point selection [61]. However, this information is not systematically incorporated into the stochastic model. Alternatively, the quality is often derived a posteriori from residuals with respect to the model [90, 197, 210], which introduces an undesirable dependence on the (validity of the) functional model. Consequently, unmodeled displacements at points with complex dynamic displacement behavior will be misinterpreted as noise. Ideally, the stochastic model should be defined a priori and should be scatterer-specific (i.e., each scatterer will have its own unique stochastic behavior), epoch-specific (i.e., the quality or noise of a scatterer may change over time)[92, 93], and independent of its actual deformation behavior. This also facilitates informed selection of points or arcs in further analysis the identification of scatterers with low uncertainties.

Therefore, the objective is to define a stochastic model independently of the phase observations and the functional model. For longer InSAR time series, the quality of a scatterer may vary over time, and the stochastic model must thus account for a potential non-stationarity of the quality of the scatterer. In Chapter 2, we propose a method for deriving such a model, which can be created from the amplitude time series of the points.

2. Is it possible to design an optimal network of arcs that is quality-driven and application-specific?

InSAR is a relative technique in which relative displacements can only be estimated for an arc. In contrast, InSAR results usually show results for points relative to a single reference point, which requires a network consisting of arcs [36, 193]. The simplest implementation is a star network, in which all points connect directly to the reference point. Here, each point (vertex)—except the reference point—has degree 1, i.e., it is connected to one other point. Although it is easy to construct, the star

network is prone to errors when the arc length (i.e., the connection between two points) increases, e.g., due to atmospheric phase delays, and it has no redundancy, which makes statistical testing impossible [102].

Creating a network of interconnected arcs increases the degree of each vertex, which enables testing and detection of potential errors and adjustment of the estimates [6]. By default, due to its straightforward implementation, many InSAR algorithms use a Delaunay network with degree 2 or higher [37, 102, 144]. Yet, this network is aimed to maximize the smallest angle of each triangle in the network, which is an irrelevant metric for InSAR. Furthermore, it does not account for the physical, kinematic, or quality characteristics of scatterers. Consequently, low-quality points may be connected, resulting in poor-quality arcs and propagating errors throughout the network. This would be avoidable by using alternative network design approaches.

Having prior knowledge of the quality of the scatterers and the quality of the arcs (see the previous sub-question) helps identify which arcs are most likely to result in precise and reliable parameter estimates. This suggests the possibility of a more effective network design since it would enable avoiding low-quality arcs as much as possible. Moreover, the a priori arc quality discussed above allows for computing the quality with which the parameters for the points can be estimated, even before the network adjustment [156]. Since quality requirements are application-dependent, the network configuration should be tailored accordingly.

An additional complication concerns the choice of the variate on which the network is adjusted. Kampes [101] suggests adjusting the network directly on the estimated arc parameters. While appealing, this strategy requires an identical functional model, i.e., the same set of parameters, for every arc. In practice, however, this assumption cannot be sustained over wide areas with lot of different deformation mechanisms. Therefore, a more flexible approach is required that i) allows for arc-specific functional models (addressed in Chapter 3), and ii) enables network adjustment in the presence of unique functional and stochastic models across arcs.

Therefore, the objective is to develop a methodology for designing a network that is quality-driven, application-specific, and can work with unique functional models for different arcs. This approach is further explored in Chapters 4 and 5, using the stochastic and functional models defined in Chapters 2 and 3 respectively.

3. Can a reevaluation of the InSAR acquisition geometry lead to more accurate, precise, reliable, and interpretable displacement estimates?

Although deformation phenomena occur in three dimensions, InSAR phase observations are only sensitive to the projection of the three-dimensional (3D) displacement vector onto the radar line-of-sight (LoS). Estimating 3D displacements from LoS observations requires a decomposition. However, there are usually insufficient viewing geometries available for full 3D reconstruction, which leads to

non-unique solutions [164].

In practice, this limitation is often addressed in ways that introduce biases. Our literature study [15] confirms that the ‘projection of the LoS observations onto the vertical direction’ is frequently mislabeled as ‘the vertical’ displacement. Alternatively, when two LoS observations are at hand, it has become standard practice to disregard the north component under the assumption that it is not observable given the orbital geometry, thereby asserting a decomposition into east and up components. Both methods lead to incorrect and biased estimates. The underlying assumptions and their consequences are rarely made explicit.

This highlights the need for standardization as well as mathematical and semantic rigor. Concepts such as decomposition and projection should not be mixed and any underlying assumptions must be explicitly stated. The objective of answering this research question is to provide a comprehensive and fundamental overview of the InSAR acquisition geometry, proposing the necessary terminology and estimation conditions for decomposition. This is discussed in Chapter 6.

4. Is it possible to estimate 3D displacement vectors combining ascending and descending InSAR observations with minimal contextual knowledge on the expected driving mechanism, and can we assess the quality of such 3D estimates?

Since LoS observations are the projection of the 3D displacement vector onto the LoS, a 3D decomposition is often performed to enhance physical understanding. In several studies, prior knowledge of the deformation driving mechanism has been used to define a local reference system used for the decomposition. For instance, for landslides [130, 196], ice-sheets [98, 126], and line-infrastructure [30, 141], assumptions can be made on the expected deformation direction.

However, no standardized method exists to incorporate such prior knowledge in a consistent way. Moreover, uncertainties in the orientation or accuracy of the assumed deformation direction are typically not accounted for, limiting the reliability of the resulting decomposition.

Our objective is to develop a generic method for the decomposition that takes into account minimal prior knowledge of the physics of the problem at hand. Moreover, the a-priori uncertainty approximation on the orientation of the local frame must be taken into account to assess the precision of the final estimates. In Chapter 7 we will introduce the solution in the form of the strapdown approach.

Subsequently, we will apply an approach that uses a location-dependent coordinate system (strapdown) on a case study of the Groningen gas field where gas production has led to substantial pressure depletion in the reservoir, resulting in induced seismicity and surface displacements [103, 187]. Although vertical displacements have been extensively monitored, the horizontal components, which are particularly present at the edges of the gas field and pointing inward, remain largely unexplored [104, 148]. However, since the Groningen field is irregularly shaped, the direction of

the inward motion, i.e., the orientation of the decomposition frame, varies spatially and remains unknown. Additionally, after estimating the 3D displacements, the horizontal estimates have a low confidence when these vectors are pointing in the north or south direction because of the satellite orbit geometry [80].

Therefore, our objective is to derive a method to define the orientation of the location-dependent decomposition frame that can be used for the entire gas field. Furthermore, we aim to produce a deformation product of equal quality throughout the entire gas field. This will be discussed in Chapter 8.

1.5. SCOPE LIMITATIONS

To limit the scope of this research, the focus is primarily on point scatterers and PS algorithms, rather than on distributed scatterers (DS). This choice particularly applies to the stochastic model developed in Chapter 2. While the functional model in Chapter 3 and the proposed network design in Chapter 5 are applied and evaluated using PS, their formulation does not exclude potential application to DS.

Another important consideration is that Chapters 2, 3, and 5 focus on short arcs, for which atmospheric phase delays are negligible, and therefore not estimated. As such, the findings in these chapters may not directly apply to longer arcs. If they would be used for longer arcs, an additional atmospheric delay estimation would be required.

Finally, this work does not address the challenges associated with wide-area InSAR processing. While recent developments in the field have focused on increasing computational efficiency and scalability, those aspects fall outside the scope of this research. The emphasis here lies on methodological rigor and physical interpretability, even if this comes at the expense of processing speed or algorithmic optimization.

1.6. OUTLINE

In Chapter 2, we derive a method to obtain the stochastic model for phase observations at individual points and demonstrate how to derive the stochastic model for an arc (the connection between two points) from there. Chapter 3 explores how to construct a functional model for an arc. We describe the components that contribute to phase observations and demonstrate how this model can be arc-specific. To estimate point parameters relative to a single reference point for the estimated arc parameters, a network is required. In Chapter 4, we discuss the fundamentals of an InSAR network, including its purpose and the conditions that can be defined within the network. Building on insights from Chapters 2, 3, and 4, Chapter 5 presents a method for constructing a quality-driven network tailored to the requirements of a given application. This approach allows us to include arcs selectively based on their expected contribution to the reliability and interpretability of the final estimates.

Chapter 6 shifts the focus to interpreting the line-of-sight (LoS) estimates. We provide an overview of InSAR geometry and propose the necessary terminology

and estimation conditions for decomposition. Chapter 7 introduces the strapdown decomposition method that estimates 3D displacements from LoS observations. This method incorporates knowledge of the physical mechanism and deformation drivers.

Chapter 8 applies the strapdown method to estimate 3D deformations due to gas extraction in the Groningen gas field.

Finally, Chapter 9 presents the main conclusions of this study and reflects on the broader implications of the findings.

2

AN INDEPENDENT STOCHASTIC MODEL FOR InSAR TIME SERIES

Reliable estimation of arc parameters requires a stochastic model that accurately reflects the quality of phase observations. Conventional approaches often determine the stochastic model a posteriori from residuals, which introduces an undesirable dependence on the functional model. Although the relationship between phase quality and Normalized Amplitude Dispersion (NAD) is well known, NAD is typically used only for point selection rather than for constructing a stochastic model. In this chapter, we present a method for deriving a scatterer-specific stochastic model using partitioned amplitude time series and its Normalized Median Absolute Deviation (NMAD). This method enables estimation of the time-varying variance-covariance matrix (VCM) of temporal phase differences for points. Consequently, we can propagate this to a VCM for the double-differenced phase for an arc.

This chapter is published as: W. S. Brouwer and R. F. Hanssen. “On the definition of an independent stochastic model for InSAR time series”. In: *IEEE Transactions on Geoscience and Remote Sensing* 63 (2025), pp. 1–11. DOI: 10.1109/TGRS.2025.3600893. <https://doi.org/10.1109/TGRS.2025.3600893>

2.1. INTRODUCTION

INSAR (SAR Interferometry) is a geodetic technique that enables the estimation of displacement of (objects on) the Earth's surface. Although results are often visualized as displacements of a set of (point or distributed) scatterers, they should in fact be interpreted as the motion of an arc formed by two scatterers. The original observation corresponding to such an arc is the double-differenced (DD) phase, i.e., the phase difference between a scatterer and a reference scatterer, relative to a reference epoch [80]. To estimate displacement parameters from this DD phase observation, both a proper functional and stochastic model are required [82], where the functional model describes the relation between the observables and the unknown parameters, and the stochastic model describes the uncertainty or stochasticity of the data [110].

The fundamental problem of InSAR is that both models are unknown and different for each scatterer and even each epoch. For instance, when using Point Scatterers (PS) [61, 93], it is generally not known from which (part of an) object the dominant signal originates, resulting in an unknown kinematic behavior that should be captured in the functional model. This problem is particularly significant in the built environment [190]. Regarding the stochastic model, the quality of a phase observation at a single epoch is inherently unknown, and each scatterer has unique scattering properties that may change over time [92, 93]. In conventional PSI methodologies, the quality of the observations is typically assessed a posteriori, based on the residuals between the observations and the model evaluated from the estimated parameters [28, 193]. This introduces a strong and undesirable dependence on the correctness of the functional model [90, 197, 210]. Consequently, for arcs with a complex displacement behavior, the unmodeled displacements are typically interpreted as noise, and a posteriori assigned to the stochastic model, leading to an underestimation of quality or even the rejection of the scatterer. The same applies for conventional methods such as variance-component estimation (VCE) [179], which are always directly linked with the formulation of the functional model, and are therefore not independent. Finally, all these methods are applied at the level of arcs instead of points, resulting in an estimate of phase quality for an arc, i.e., of the double-differenced phase. Ideally, we are interested in information on the quality of individual points.

Thus, the stochastic model should be known *prior to*, and independently of, the parameter estimation. An independent first-order approximation of the stochastic model enables the weighting of points relative to one another and supports a more informed selection of which points (or arcs) to evaluate. Moreover, it is indispensable for testing the validity of the entire mathematical model [28]. A stochastic model that is chosen too conservatively may lead to sustaining the null hypothesis (e.g., of steady-state motion) while it should be rejected.

However, independently approximating the variance-covariance matrix (VCM) of the double-differenced (DD) phase observations for each arc is non-trivial. We address this problem in a stepwise manner. First, we demonstrate that the VCM of the DD phases can be derived from the VCM of the single-look complex (SLC) phases. While deriving temporal phase differences may seem straightforward at

first glance, different methodological choices—especially in the treatment of the reference acquisition—can lead to distinct results. This is discussed in Sec. 2.3. Second, the VCM of the DD phase observations is composed of several noise contributions: atmospheric noise, time-variant clutter (TVC), and thermal noise. In Sec. 2.4, we elaborate on each of these components and how their respective VCMs can be derived. Building on the approach proposed by Ferretti et al. [61], we exploit amplitude data to estimate phase dispersion. To account for time-varying phase quality, we partition the amplitude time series and estimate the phase quality separately for each partition. We propose the use of the Normalized Median Absolute Deviation (NMAD) of the amplitude, rather than the commonly used Normalized Amplitude Dispersion (NAD), as it is more robust to outliers.

2.2. THE MATHEMATICAL MODEL

After the selection of potentially coherent point scatterers¹, the temporal single difference phase ϕ_j^{md} for point scatterer j is the SLC phase, denoted by $\{\psi \mid -\pi \leq \psi < \pi, \psi \in \mathbb{R}\}$, of daughter² image d relative to the phase of the mother image m , i.e., $\phi_j^{md} = \underline{\psi}_j^d - \psi_j^m$, with $\{\phi \mid -\pi \leq \phi < \pi, \phi \in \mathbb{R}\}$, which is computed using complex multiplication [80]. The underline expresses the stochastic nature of the observables, where the mother image is considered to be deterministic as we use for the mother its numerical values and not the stochastic observable, see Sec. 2.3.1. Since a temporal difference of one point is meaningless, the spatial difference between this point j and a reference point i needs to be considered. Via complex multiplication this yields a spatio-temporal double difference (DD) phase ϕ_{ij}^{md} , with $\{\varphi \mid -\pi \leq \varphi < \pi, \varphi \in \mathbb{R}\}$, which represents the phase for point scatterer j at epoch d , relative to reference point i at mother epoch m . The DD phase is generally considered as

$$\underline{\varphi}_{ij}^{md} = \underline{\phi}_j^{md} - \underline{\phi}_i^{md}, \quad (2.1)$$

which would result in $\{\varphi \mid -2\pi \leq \varphi < 2\pi, \varphi \in \mathbb{R}\}$. But note that Eq. 2.1 is strictly not correct as the double difference phase is in fact the exponent of the complex multiplication. The DD phase is the sum of different components:

$$\underline{\varphi}_{ij}^{md} = -2\pi a_{ij}^{md} + \varphi_{ij,d_{nt}}^{md} + \varphi_{ij,\eta}^{md} + \varphi_{ij,h_{xr}}^{md} + \varphi_{ij,S}^{md} + \varphi_{ij,n}^{md}, \quad (2.2)$$

where $a \in \mathbb{Z}$ is the integer ambiguity, $\varphi_{d_{nt}}$ the non-thermal displacement phase, φ_{η} the thermal displacement phase, and $\varphi_{h_{xr}}$, φ_S , and φ_n the phases due to the residual cross-range distance h_{xr} , the superposed atmospheric phase screens from epoch m and d , and noise, respectively. The main signals of interest are the residual cross-range distance and the displacement phase. The mathematical model for the

¹In this study, we use the term "point" to refer to either a Point Scatterer or a Distributed Scatterer.

²We refer to 'mother and daughters,' where the mother image is defined as the reference image.

absolute phase (which is not wrapped) therefore becomes

$$E\left\{\begin{bmatrix} \underline{\varphi}_{ij}^{md_1} \\ \vdots \\ \underline{\varphi}_{ij}^{mD} \end{bmatrix}\right\} = \underbrace{(\delta_{\text{displ}}|B_T)}_{\varphi_{ij,dnt}^{md}} + \underbrace{(\eta|B_{\text{th}})}_{\varphi_{ij,\eta}^{md}} + \underbrace{(h_{\text{xr}}|B_{\perp})}_{\varphi_{ij,hxr}^{md}}; \quad (2.3)$$

$$D\left\{\begin{bmatrix} \underline{\varphi}_{ij}^{md_1} \\ \vdots \\ \underline{\varphi}_{ij}^{mD} \end{bmatrix}\right\} = Q_{\varphi_{ij}} = \underbrace{Q_{\varphi_{ij,\text{atm}}}}_{\varphi_{ij,S}^{md}} + \underbrace{Q_{\varphi_{ij,\text{tvc}}} + Q_{\varphi_{ij,\text{thm}}}}_{\varphi_{ij,n}^{md}}, \quad (2.4)$$

where $E\{\cdot\}$ is the expectation operator, and the vector of unknown parameters contains δ_{displ} : the relative non-thermal displacement parameter vector (as a function of the temporal baseline B_T); η : the relative thermal displacement (as a function of thermal baseline B_{th}), and residual cross-range distance h_{xr} (as a function of perpendicular baseline B_{\perp}). $D\{\cdot\}$ describes the dispersion of the observations described by the Variance Covariance Matrix (VCM), $Q_{\varphi_{ij}}$, which is the sum of (i) the atmospheric noise, $Q_{\varphi_{ij,\text{atm}}}$, (ii) the Time Variant Clutter (TVC) $Q_{\varphi_{ij,\text{tvc}}}$, and (iii) the thermal noise, $Q_{\varphi_{ij,\text{thm}}}$. In the following, we will show that by using error propagation, the VCM of the DD phases can be derived once the VCM of the SLC phases, Q_{ψ} , is known.

2.3. DERIVATION OF THE VCM FOR AN ARC

The vector of SLC phase observations for point scatterer i is defined as

$$\underline{\psi}_i = [\underline{\psi}_i^m, \underline{\psi}_i^{d_1}, \underline{\psi}_i^{d_2}, \dots, \underline{\psi}_i^{d_D}]^T. \quad (2.5)$$

For convenience, the first image is defined as the mother image, but this is arbitrary. The VCM of the observations is

$$Q_{\psi_i} = \begin{bmatrix} \sigma_{\psi_i^m}^2 & 0 & \dots & 0 \\ 0 & \sigma_{\psi_i^{d_1}}^2 & & \vdots \\ \vdots & & \ddots & \\ 0 & \dots & & \sigma_{\psi_i^{d_D}}^2 \end{bmatrix}, \quad (2.6)$$

where the different SLC observations are considered to be uncorrelated [21].³ Since this SLC phase is meaningless, double differences, both in time and in space, need to be formed [80]. In the following we first discuss how the temporal single phase differences should be computed, followed by the computation of the spatial differences.

³This assumption holds for point scatterers, as each measurement reflects a single pixel. Note that the scattering properties of pixels are independent of other pixels.

2.3.1. COMPUTING THE SINGLE DIFFERENCES (IN TIME)

The temporal phase differences, here referred to as Single Differences (SD), ϕ_i , and the corresponding VCM, Q_{ϕ_i} , can be computed following three possible approaches that differ primarily in whether the mother image is treated as a deterministic quantity or a stochastic variable. We simulated SLC values⁴ for one mother and five daughters⁵ to demonstrate the effect of the three different approaches, see Fig. 2.1. The representation of the SLC phase observations in Fig. 2.1a is defined as a ‘position graph’, i.e., the phases are measured at a particular epoch, and the vertical axis shows the ‘position’ (in this case the observed phase) at a particular epoch. The horizontal axis therefore expresses time as a date. Below, we discuss the three subsequent possibilities to treat the mother acquisition.

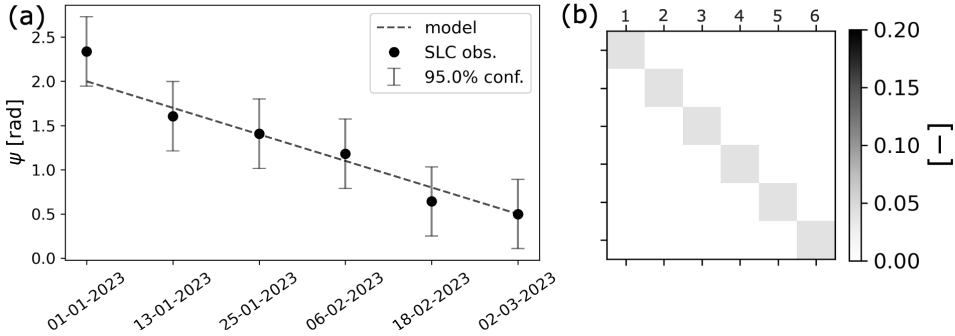


Figure 2.1.: (a): simulated SLC phase observations for point i with a particular trend shown by the dashed line. (b) variance-covariance matrix of the SLC phase observations: all observations have the same quality and the observations are uncorrelated.

APPROACH 1: DISREGARDING THE TEMPORAL PHASE DIFFERENCE OF THE MOTHER WITH ITSELF, A.K.A. ‘ELIMINATING MOTHER’

Perhaps the most conventional approach for computing the SD values is by using the differencing matrix,

$$\underbrace{\begin{bmatrix} \phi_i^{md_1} \\ \phi_i^{md_2} \\ \phi_i^{md_3} \\ \vdots \\ \phi_i^{md_D} \end{bmatrix}}_{\underline{\phi}_i} = \underbrace{\begin{bmatrix} -1 & 1 & 0 & \cdots & 0 \\ -1 & 0 & 1 & \cdots & 0 \\ \vdots & \vdots & \vdots & \ddots & \vdots \\ -1 & 0 & 0 & \cdots & 1 \end{bmatrix}}_A \underbrace{\begin{bmatrix} \psi_i^m \\ \psi_i^{d_1} \\ \psi_i^{d_2} \\ \vdots \\ \psi_i^{d_D} \end{bmatrix}}_{\underline{\psi}_i}, \quad (2.7)$$

⁴Note that in reality there cannot be a trend in the SLC observations, since the phase distribution is a uniform distribution between $-\pi$ and π based on the scattering mechanism only. Yet, we simulate SLC observations with a trend to highlight the consequences of the different approaches.

⁵Obviously current InSAR time series may contain hundreds of epochs, the small number of acquisitions helps in highlighting this differences between the three methods.

where D is the number of daughter acquisitions, as in [60, 61, 193]. Using error propagation the stochastic model for the SD phase values is computed with

$$Q_{\phi_i} = A Q_{\psi_i} A^T, \quad (2.8)$$

which will be a full matrix. Fig. 2.2a shows the consequence of this approach, plotting the SD together with an error bar which represents the 95% confidence interval obtained from the diagonal of Q_{ϕ_i} . The most obvious consequence of this approach is that only D SD phase values are derived from $D + 1$ SLC phase values, since the mother epoch is eliminated in the differencing operation. Consequently, plotting the obtained SD phases against absolute (calendar) dates on the horizontal axis, similar to Fig. 2.1, is no longer possible, indicated by the crossed-out dates. Each phase difference corresponds to a specific time *difference* rather than a time. In contrast to the *position graph* of Fig. 2.1, this type of graph is referred to as a '*displacement graph*.'

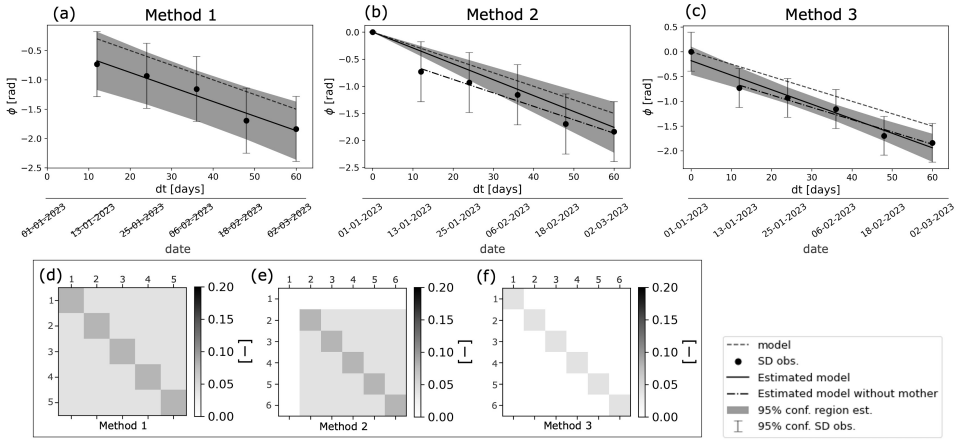


Figure 2.2.: In (a), (b), and (c) we show the single difference phase values resulting from the three different approaches to compute the SD phase values. The gray zones indicate the 95% confidence region of the estimated model. In (d), (e), and (f) the obtained variance-covariance matrices (VCM) are shown. In (a) we obtain five SD phase values, i.e., the temporal phase difference at the mother epoch is missing. Therefore the SD phases should be plotted with the delta time at the horizontal axis. In (b) the temporal phase difference at the mother epoch is added as a deterministic value, resulting in the fact that the estimated displacement model passes through this value, resulting in an erroneous estimated model (the solid black line's slope differs from the simulated velocity shown by the dashed line). In (c) six SD stochastic phase values are obtained and resulting in the correct estimated velocity.

The modeled (simulated) trend, used as ground truth for comparison, is shown by the black dashed line. Subsequently, we estimate a trend and an offset through the obtained single differences, shown by the black solid line. The estimated trend is very similar to the simulated trend. However, comparing the 95% confidence bars of

the SD phases (Fig. 2.2a) with the confidence bars of the SLC phases (Fig. 2.1), we observe that the confidence bars of the SD phases are larger, i.e., lower precision. This can also be observed comparing the VCM of the SD phases (Fig. 2.2d) with the VCM of the SLC phases (Fig. 2.1b). This is a direct result of the definition of the differencing approach, where the stochastic SLC phase vector, $\underline{\psi}_i$, has a particular precision for each single observation. The precision of the derived SD phase is straightforwardly $\sigma_{\phi_i^{md}}^2 = \sigma_{\psi_i^m}^2 + \sigma_{\psi_i^d}^2$, i.e., the variance of ϕ_i^{md} is the sum of the SLC phase variances of the mother and the daughter acquisition. Since the VCM shown in Fig. 2.2d becomes a full matrix, the complete VCM is required when estimating displacement parameters. Using only the diagonal elements of the VCM to describe the quality of the SD phases results in a too conservative quality estimation for the displacement parameters, and the error bars in Fig. 2.2a are not sufficient to visualize the quality of the result. The gray zones in Figs. 2.2a–c are positioned around the adjusted observations and indicate the 95% confidence region of these adjusted observations.

Finally, acknowledging that Fig. 2.2a is a displacement graph rather than a position graph implies that the interpretation of a point in the graph at time $dt = t - t_m$ is ‘the displacement estimated between t and t_m ,’ where t_m is the absolute date of the mother acquisition. Note that due to the differencing operation the obtained result becomes irreversible.

APPROACH 2: A DETERMINISTIC TEMPORAL PHASE DIFFERENCE WITH THE MOTHER, A.K.A. ‘FIXING MOTHER’

One possibility to use a position plot with absolute dates, rather than a displacement plot, is to include the SD phase value of the mother with itself in the SD phase vector, i.e., $\phi_i^{mm} = \psi_i^m - \psi_i^m = 0$ resulting in:

$$\underline{\phi}_i = [\phi_i^{mm}, \underline{\phi}_i^{md_1}, \underline{\phi}_i^{md_2}, \underline{\phi}_i^{md_3}, \dots, \underline{\phi}_i^{md_D}]^T, \quad (2.9)$$

where $\phi_i^{mm} = 0$ by definition. Note that ϕ_i^{mm} is deterministic, i.e., in Fig. 2.2b it does not have an error bar. Therefore, we introduce a row and column of zeros in the stochastic model, as depicted in the VCM in Fig. 2.2e. Utilizing this VCM we can again estimate a model through the SD phases, represented by the solid black line in Fig. 2.2b. As ϕ_i^{mm} is deterministic, the estimated model is constrained to pass through that value. Upon comparing the estimated model with the true simulated model (the dashed line) and the model estimated with the first approach (the dash-dotted line), it is evident that the estimated average velocity differs substantially from the simulated value. In fact, the trend is significantly biased by adding the deterministic SD of the mother with itself. While this bias may effectively decrease when the time series includes more epochs, this example proves that the ‘fixing mother’ approach is incorrect. The gray zone in Fig. 2.2b is positioned around the adjusted observations and indicates their 95% confidence region. This also erroneously suggests that the quality of the adjusted observations temporally closer to the mother are better.

As both approach 1 is suboptimal (as the full VCM need to be considered and the result is irreversible) and approach 2 prove to be flawed, the mother acquisition has to be treated differently, as discussed below. For both approach 1 and approach 2, the error bars of the SD phases are greater than those of the SLC phases, which is not expected. Upon consideration, this becomes clear: subtracting one SLC value from a set of SLC values should not affect the distribution; it merely introduces a shift. In Appendix A, we demonstrate this through a simple simulation.

APPROACH 3: SUBTRACTING MOTHER REALIZATION FROM VARIATES, A.K.A. 'EMBRACING MOTHER'

The third and preferred approach to compute the SD phase values is by differencing the stochastic variates of all epochs with the deterministic realization of the mother epoch, i.e.,

$$\underbrace{\begin{bmatrix} \phi_i^{mm} \\ \phi_i^{md_1} \\ \phi_i^{md_2} \\ \vdots \\ \phi_i^{md_D} \end{bmatrix}}_{\underline{\phi}_i} = \underbrace{\begin{bmatrix} \psi_i^m \\ \psi_i^{d_1} \\ \psi_i^{d_2} \\ \vdots \\ \psi_i^{d_D} \end{bmatrix}}_{\underline{\psi}_i} - \psi_i^m. \quad (2.10)$$

This way, with $D+1$ SLC phases, we retain $D+1$ single difference phase values since the SD phase for the mother variate, $\underline{\psi}_i$, relative to its realization ψ_i is computed as well.

Fig. 2.2c is the corresponding graphical representation, i.e., a position graph. In comparison with Figs. 2.2a and b, it is clear that adding the mother image appreciates and visualizes all epochs including the reference one. However, even though the single-difference phase value of the mother epoch is equal to zero, it is now stochastic, similar to all other epochs. The estimated average velocity (the solid line) is parallel to the simulated (true) average velocity, and it is not forced to pass precisely through the temporal phase at the mother epoch. The gray zone in Fig. 2.2c is a correct representation of the quality of the adjusted observations, and indicates the 95% confidence region of these adjusted observations.

The most important consequence of this approach is that the distribution of the single-difference phase differences, represented by $\underline{\phi}_i$, is equivalent to that of the original SLC phases $\underline{\psi}_i$, i.e., $Q_{\phi_i} = Q_{\psi_i}$. This equivalence is trivial, as subtracting a deterministic value from a vector of stochastic variates should not alter the distribution of the resulting variate. This is further supported through the simulations discussed in Appendix A and shown in Fig. A.1. As a practical consequence, the equivalence implies that the VCM of the single-difference vector remains a diagonal matrix, which is advantageous from a computational and visualization perspective.

Fig. 2.3 presents the subsequent building blocks to establish the stochastic model for a vector of derived double-difference observations for an arc between point i and j with 11 epochs, i.e., $Q_{\phi_{ij}}$. The first column, "SLC", describes the Q_{ψ} matrices of the SLC phases for both points, regarding the clutter and the atmospheric contributions.

The second column, "IFG", represents the single (temporal) differences Q_ϕ for both points, relative to the mother epoch. This demonstrates the identity between Q_{ϕ_i} and Q_{ψ_i} , and the absence of correlation.

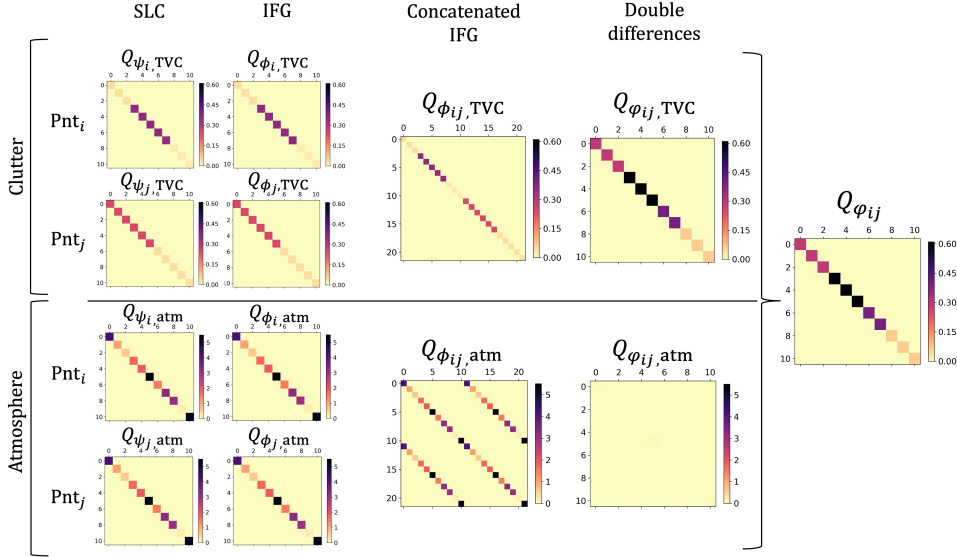


Figure 2.3.: An example of $Q_{\phi_{ij}}$ as the sum of $Q_{\phi_{ij}, TVC}$ (above) and $Q_{\phi_{ij}, atm}$ below, for a *short* arc, i.e., $l \leq 200$ m. Column 1: VCM of the SLC phases of point i and j separately, with 11 epochs. For point i the time series was subdivided into three partitions, with one value $\sigma_{\psi, TVC}$ per partition, $\sigma_{\psi, atm}$ has a different value for every epoch. Column 2 shows that Q_{ϕ_i} and Q_{ϕ_j} are equal to Q_{ψ_i} and Q_{ψ_j} because of the deterministic nature of the mother SLC phase value that is subtracted to obtain the interferometric phases. Note that columns 3, 4, and, 5 will be explained from Sec. 2.3.2 onward in the thesis. Column 3 shows the VCM of the stacked interferometric phases of point i and j where the off diagonal part represents the correlation between the two points. Correlation in $Q_{\phi_{ij}, atm}$ is observed because the simulated *short* arc, i.e., short enough that the atmospheric phase delay of both points is correlated. Consequently, column 4 represents $Q_{\phi_{ij}}$ for the clutter and atmosphere separately, where it can be seen that it is still a diagonal matrix. Note that $Q_{\phi_{ij}, atm}$ is almost zero because of the high correlation between the two points. Which will be the case for short arcs, e.g., $l \leq 1000$ m. Finally, column 5 shows $Q_{\phi_{ij}}$ that is the sum of $Q_{\phi_{ij}, TVC}$ and $Q_{\phi_{ij}, atm}$.

2.3.2. COMPUTING THE DOUBLE DIFFERENCES (IN SPACE AND TIME)

Given the temporal SD phase values for point i and j , the spatio-temporal DD phases for the arc are computed with

$$\underbrace{\begin{bmatrix} \varphi_{ij}^{mm} \\ \varphi_{ij}^{md_1} \\ \varphi_{ij}^{md_2} \\ \vdots \\ \varphi_{ij}^{md_D} \end{bmatrix}}_{\underline{\varphi}_{ij}} = \Omega \underbrace{\begin{bmatrix} (\phi_i^{mm}, \dots, \phi_i^{md_D})^T \\ (\phi_j^{mm}, \dots, \phi_j^{md_D})^T \end{bmatrix}}_{\underline{\phi}}, \text{ where} \quad (2.11)$$

$$\Omega = \begin{bmatrix} -1 & 1 \end{bmatrix} \otimes I_{D+1}. \quad (2.12)$$

The concatenated vector $\underline{\phi}$ of dimension $2(D+1) \times 1$ results in a dispersion as

$$D\left\{ \underbrace{\begin{bmatrix} (\phi_i^{mm}, \dots, \phi_i^{md_D})^T \\ (\phi_j^{mm}, \dots, \phi_j^{md_D})^T \end{bmatrix}}_{\underline{\phi}} \right\} = \underbrace{\begin{bmatrix} Q_{\phi_i} & Q_{\phi_i, \phi_j} \\ Q_{\phi_i, \phi_j} & Q_{\phi_j} \end{bmatrix}}_{Q_{\phi_{ij}}}, \quad (2.13)$$

where Q_{ϕ_i, ϕ_j} describes the covariance between the SD phases of point i and j . In Fig. 2.3 the third column illustrates $Q_{\phi_{ij}}$, of the concatenated vector $\underline{\phi}$. The difference between the clutter and the atmosphere component is discussed below in Sec. 2.4.

Subsequently, the VCM of the DD phases, $\underline{\varphi}_{ij}$, is computed with

$$Q_{\varphi_{ij}} = \Omega Q_{\phi_{ij}} \Omega, \quad (2.14)$$

shown in the fourth, "Double differences", column of Fig. 2.3, with dimension $(D+1) \times (D+1)$. Thus, the dispersion of φ_{ij} depends on the dispersion of the SD values of both point i and point j , and the standard deviation of the DD phase $\sigma_{\varphi_{ij}^{md}}$ is

$$\sigma_{\varphi_{ij}^{md}} = \sqrt{\sigma_{\phi_i^{md}}^2 + \sigma_{\phi_j^{md}}^2}, \quad (2.15)$$

in the case that there is no correlation between the two points. Below, in Sec. 2.4, we show that for the TVC and the thermal noise this is a valid assumption. We also show the validity of this model with simulations that are shown in the Appendix A.

In conclusion, we have shown that if the VCMs of the SLC phase observations are given, as well as the covariance between the two PS, the VCM of the DD interferometric phases can easily be derived. Below we address the method to obtain quantitative estimates of the relevant noise components.

2.4. NOISE COMPONENT ANALYSIS

It follows from Eq. (2.4) that the VCM of the DD phase observations is defined as the sum of three components: i) the atmospheric noise, ii) the thermal noise, and iii) the time variant clutter. These will be discussed subsequently below.

2.4.1. ATMOSPHERIC NOISE

The troposphere causes a phase delay on the observed SLC phases, known as the Atmospheric Phase Screen (APS), depending on turbulent mixing and vertical stratification [80]. Since the turbulent atmospheric delay is completely uncorrelated between different acquisitions, all off-diagonal terms in $Q_{\psi_{i,\text{atm}}}$ are zero [80], and each individual epoch has a unique value. This is illustrated in the first column of Fig. 2.3 where we simulated $Q_{\psi_{i,\text{atm}}}$ for 11 epochs for two points.

While the APS is uncorrelated in time, it is spatially correlated, i.e., $Q_{\phi_i,\phi_j} \neq 0$, and depends on the distance between the two PS, typically following a power-law [80]. The single-epoch spatial covariance values can be approximated with

$$C_{\text{atm}}(l) = \sigma_{\text{atm}}^2 \exp(-l^2 \omega^2), \quad (2.16)$$

where l is the arc length (the distance between the two scatterers) and ω relates to the correlation length of the atmospheric signal l_c , and is defined as $\omega^2 = \ln(2)/l_c^2$. The lower block, "Atmosphere", of Fig. 2.3 shows the approximation of $Q_{\phi_{ij,\text{atm}}}$ for a *short* arc, i.e., $l \leq 2000$ m. While the atmospheric phase delay for the SLC observations can be quite significant, the variance of the atmospheric phase delay is close to zero for the DD phases for short arcs. This is because Q_{ϕ_i,ϕ_j} , which defines the correlation between the two scatterers, is almost equal to the variances of the SLC phase delays.⁶

2.4.2. THERMAL NOISE

The thermal noise is caused by the radar instrument itself and is represented by the Noise Equivalent Sigma Zero (NESZ). For Sentinel-1 the NESZ has a value around -25 dB [183]. In Fig. 2.4 we show different realizations of the complex phasor for two PS. The observed phasor is always the sum of i) the signal, in this example constant over time and shown by the black phasor, ii) the clutter, shown in purple and green, and iii) the thermal noise, shown in red. Since the thermal noise differs per epoch, the phasor will be different for every epoch.

2.4.3. TIME VARIANT CLUTTER

The observed SLC phase for one PS is the sum of all reflections within the same resolution cell. For ideal point scatterers there is often one dominant scatterer in the resolution cell. Thus, signals from other reflective objects within the same resolution

⁶For long arc lengths, the influence of ionospheric delay needs to be included in Eq. (2.16), see [51]. For arcs between points with a significant height difference, the influence of stratification needs to be taken into account, see [80].

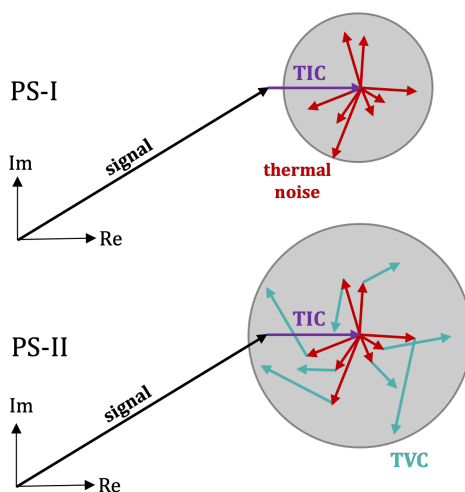


Figure 2.4.: Different realizations of the SLC phasor observations for two PS over time. The observed complex SLC phasor is the sum of four components. The signal, shown by the black phasor, and the Time Invariant Clutter, shown in purple, are both time invariant, i.e., the observations do not change over time. The thermal noise, shown by the red phasors, and the Time Variant Clutter, shown in green, result in a different realization for each epoch. Therefore, also the summative combined phasor will have a different realization over time. PS-I only has Time Invariant Clutter and thermal noise. The thermal noise expresses the noise on the final observation, as shown by the gray confidence circle behind it. PS-II also has some additional time variant clutter, resulting in a larger confidence circle.

cell can be regarded as noise, or clutter, as they are not necessarily related to the behavior of the main scatterer.

The clutter can be divided in two parts: the Time Invariant Clutter (TIC) and Time Variant Clutter (TVC). The TIC is the clutter that remains constant between different acquisitions. An extreme example would be a Corner Reflector (CR) on top of a rough concrete plate. The signal of interest is strong and relates to the CR, but the rough concrete surface also generates reflections that are considered clutter. When there is no displacement signal, the clutter caused by the concrete plate does not change over time, i.e., it is time *invariant*, see the purple TIC phasor in Fig. 2.4. Obviously, it is impossible to distinguish between the *signal* of interest and the TIC from the observations since both are time invariant. Consequently, both terms are combined into the signal phasor, and considered in the functional rather than the stochastic model.

On the contrary, the Time Variant Clutter (TVC) does change over time. An example would be a CR in a vegetated area. As long as the CR is not moving, the signal is constant, whereas the reflections caused by the vegetation differ per acquisition, see the green phasors in Fig. 2.4. In the following we will first show how $Q_{\psi_i, \text{TVC}}$ can be derived and consequently how the values change over time.

THE DERIVATION OF $Q_{\psi_i, \text{TVC}}$

The TVC and thermal noise both contribute to the noise in the SLC phase observations. However, from the complex SLC phase observations only it is not possible to distinguish between the two components. Therefore, the TVC and thermal noise will be lumped together in $Q_{\psi_i, \text{TVC}}$. Since both have a random distribution and vary with time by definition, there is no correlation in time, and $Q_{\psi_i, \text{TVC}}$ reduces to a diagonal matrix with variances values for the SLC phases on the diagonal, cf. Fig. 2.3, first column. From this point onward, we will discuss how $Q_{\psi_i, \text{TVC}}$ can be derived for PS. Note that for DS, $Q_{\psi_i, \text{TVC}}$ can be derived in a different way, i.e., with the coherence matrix, as presented in [52].

To estimate the phase contribution $\sigma_{\psi, \text{TVC}}$, also the magnitude of the signal itself is important. The effect of both noise components will be larger on low-magnitude PS compared to high-magnitude PS, i.e., the TVC concerns the ratio between the dominant point scatterer representing the signal and the rest of the reflecting objects in the resolution cell, and it is thus related to the SCR [158].

The Normalized Amplitude Dispersion (NAD) is a good proxy to estimate $\sigma_{\psi, \text{TVC}}$, with [61]

$$\sigma_{\psi, \text{TVC}} \approx \frac{\sigma_A}{\mu_A} = \text{NAD}, \quad (2.17)$$

where A is the vector of the amplitude time series, μ_A is its mean, and σ_A its standard deviation. However, the disadvantage of the NAD is that it is relatively sensitive to outliers, which are more likely in busy urban areas. This results in a rather pessimistic estimate of the phase quality, i.e., greater values for σ_A , the NAD, and consequently σ_{ψ} . As a result, the outlier negatively affects the estimated quality of all observations.

To mitigate this effect, we introduce the Normalized Median Absolute Deviation (NMAD) of the amplitude, defined by M_A , which is less affected by outliers, and is defined as

$$M_A = \frac{\text{MAD}}{\text{med}(A)}, \quad (2.18)$$

where A is the vector representing the amplitude time series and $\text{med}(A)$ the corresponding median. MAD is the Median Absolute Deviation that is defined as [117]

$$\text{MAD} = \text{med}(|A - \text{med}(A)|). \quad (2.19)$$

Note that for normally distributed data the MAD is related to the standard deviation with

$$\sigma_A = k \cdot \text{MAD}, \quad (2.20)$$

where $k \approx 1.4826$ [151]. Based on simulations as [61, 101, 193] we derive an empirical relation between M_A and $\sigma_{\psi, \text{TVC}}$, see Fig. 2.5. We simulate phasors at various noise levels, using 50 SAR scenes. For each phasor, both M_A and σ_{ψ} are computed and visualized as gray dots. For each noise level, the mean σ_{ψ} and its standard deviation are calculated and represented by 2σ black error bars. We then derive the relationship between M_A and σ_{ψ} using the 97.7 percentile, i.e., $\mu + 2\sigma$, shown by the red line. Using this percentile, instead of fitting through the mean of the cloud, we conservatively avoid overestimating the PS quality, acknowledging that

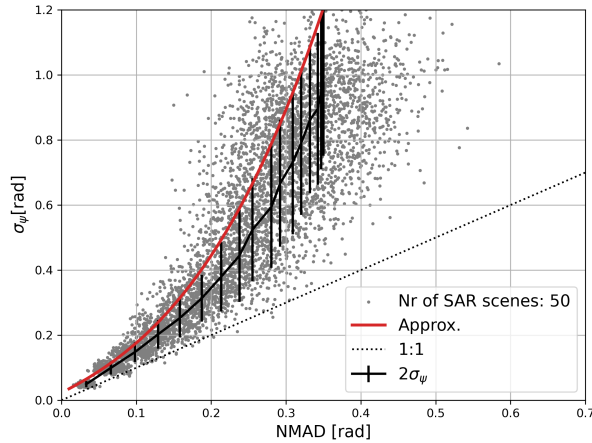


Figure 2.5.: We simulated scatterers for different noise levels consisting of 50 SAR scenes. For every scatterer (represented with a gray dot), we estimated the NMAD of the amplitude and σ_{ψ} . The black error bars represent the $2\sigma_{\psi}$ values that we computed per simulated noise level. The red line represents the derived empirical relation, see Eq.(2.21), between the NMAD and σ_{ϕ} based on the 2σ error bars. The dotted line represents the 1:1 relation between the NMAD and σ_{ϕ} . Figure based on [61].

real-world scenarios differ from simulations. In Sec. 2.5.3 we show the validity of this assumption with a test case on real data. The derived empirical relation is

$$\sigma_{\psi, \text{TVC}} = 1.3 M_A + 1.9 M_A^2 + 11.6 M_A^3. \quad (2.21)$$

Hence, once we estimate M_A based on a given amplitude time series, we find an a priori estimate for the SLC phase quality.

PARTITIONS

In reality, the amplitude of a scatterer may vary over time, and consequently so does $\sigma_{\psi, \text{TVC}}$ [93]. Therefore, the time series can be subdivided into multiple partitions, where each partition has its own behavior. Four examples of this are shown in the upper row of Fig. 2.7. As long as there are enough observations within a partition, the M_A and consequently $\sigma_{\psi, \text{TVC}}$ can be estimated. Since the amplitude behavior of scatterers may exhibit seasonal patterns, we chose the partitions to be not shorter than half a year. Remark that this derivation is based on the assumption of ergodicity. Ideally, σ_{ψ} would be estimated per epoch, but since this is not feasible, we assume that the magnitude of the amplitude and its variability within a partition reflect the noise level of the individual epochs in that partition.

As a result, for each partition of the time series the M_A and accordingly $\sigma_{\psi, \text{TVC}}$ can be conservatively approximated with Eq. (2.21). All SLC phase observations within a partition have the same precision value of $\sigma_{\psi, \text{TVC}}$, and these values are used to fill the diagonal of $Q_{\psi, \text{TVC}}$, see Eq. (2.6). In Fig. 2.3 we show an example of the derivation of the VCM containing the sum of $Q_{\varphi_{ij, \text{TVC}}}$ (upper block) and $Q_{\varphi_{ij, \text{atm}}}$ (lower block). The first column of Fig. 2.3 shows this for two points (i and j) defining one arc with different partitions.

2.5. RESULTS AND IMPACT

The availability of a stochastic model of an arc that is independent on the actual displacement behavior is beneficial for the subsequent parameter estimation, the quality assessment of those parameters, and for testing the validity of the functional model. We test this for a descending Sentinel-1 time series over Amsterdam, detecting 1852 points across an area of approximately 700×800 m, see Fig. 2.6a. With this limited size we assume that the relative atmospheric delay is negligible, i.e., $Q_{\varphi, \text{atm}} = 0$. For four example arcs, we show the derivation of $Q_{\varphi, \text{TVC}}$, demonstrate the effect of incorporating $Q_{\varphi, \text{TVC}}$ on the estimated parameters, and compare this to the case without a stochastic model. Then we show the effect of using a proper stochastic model on all the detected points.

2.5.1. FOUR EXAMPLE ARCS

Fig. 2.7 shows the results of our method for the four different arcs shown in Fig. 2.6a.

All four arcs share the same reference point, i , whose amplitude time series is shown in Fig. 2.6b, identifying four different partitions with NMAD values of 0.073, 0.060, 0.070, and 0.059 respectively, using a breakpoint detection method proposed

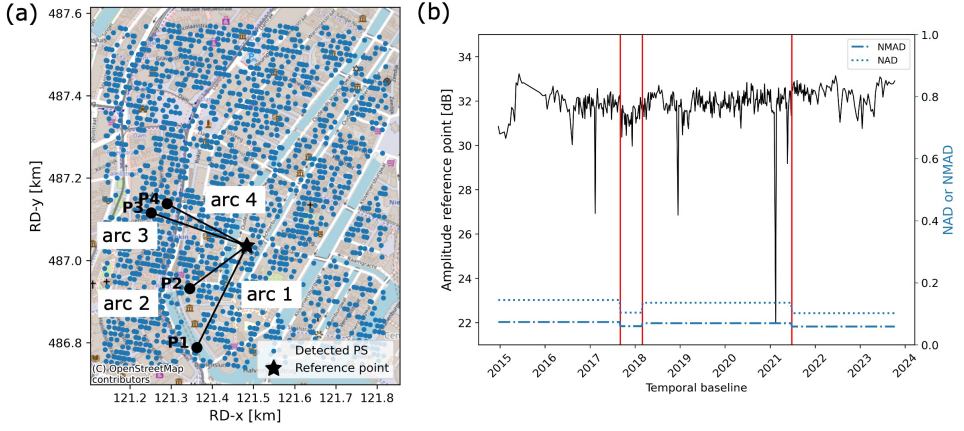


Figure 2.6.: **a)** Detected PS over Amsterdam and the four example arcs that are highlighted in Fig. 2.7. RD coordinates are the Dutch national coordinates. **b)** Amplitude time series for the reference point. Four different partitions are detected using a breakpoint detection algorithm. For each partition, the NAD and NMAD of the amplitude are calculated. Using the NMAD values and Eq. (2.21) we estimate the standard deviation of the SLC phase values that fall within that partitions.

Table 2.1.: Properties and estimated parameters for the four arcs shown in Fig. 7. The W and UW between brackets indicate a weighted or unweighted estimation respectively. The \pm margins indicate 2σ values. All parameters estimated using the proposed stochastic model exhibit less uncertainty.

		Arc 1	Arc 2	Arc 3	Arc 4
Arc length	[m]	274.96	172.76	245.60	219.15
Average sigma	[rad]	0.83	0.42	0.67	0.94
Cross range (W)	[m]	13.69 ± 1.54	-8.09 ± 1.25	12.73 ± 1.81	-7.66 ± 1.80
Cross range (UW)	[m]	19.77 ± 3.03	-5.47 ± 1.64	15.53 ± 2.92	-6.37 ± 3.02
Thermal (W)	[mm/K]	0.11 ± 0.02	-0.11 ± 0.01	0.08 ± 0.02	-0.02 ± 0.02
Thermal (UW)	[mm/K]	-0.08 ± 0.03	-0.12 ± 0.02	0.09 ± 0.03	-0.02 ± 0.03
Velocity (W)	[mm/yr]	-0.69 ± 0.06	-0.02 ± 0.04	0.78 ± 0.05	-0.97 ± 0.08
Velocity (UW)	[mm/yr]	-1.38 ± 0.09	-0.15 ± 0.05	0.34 ± 0.08	-0.77 ± 0.09

by Truong et al. [184]. Using Eq. (2.21) this leads to the corresponding values for σ_{ψ_i} , i.e., 0.128, 0.105, 0.122 and 0.104 radians, respectively. The top row of Fig. 2.7 shows the amplitude time series for the four points P1–P4, each with distinct partitions. For example, in arc 1 (left column) three partitions were identified with NMAD values of 0.317, 0.398, and 0.156, corresponding to σ_{ψ_j} values of 0.985, 1.561, and 0.31 radians. Consequently, arc 1 of P1 with reference point i , which had four partitions, has a total of six partitions, and thus six distinct values for $\sigma_{\phi_{ij}}$.

The second row of Fig. 2.7 shows the resulting $Q_{\phi, \text{TVC}}$, which is a diagonal matrix, cf. Fig. 2.3. The horizontal blue lines are an alternative representation of the diagonal values of $Q_{\phi_{ij}}$ (refer to the right axis). The six values of $\sigma_{\phi_{ij}}$ are 0.944, 1.566, 1.564, 1.565, 0.333, and 0.326 radians, indicating that the quality of the last two partitions is significantly better than that of the first four. This interpretation is supported by the double-difference phase observations for the arc, shown in the third row of Fig. 2.7. The black and gray dots represent the observed double-difference phases and the corresponding 2π -ambiguity levels, respectively. As expected, the dispersion of the DD phases within the first four partitions (up to March 2019) is greater than in the later observations.

The proposed stochastic model is now used to estimate the unknown parameters, i.e., a constant velocity δ_{displ} , thermal expansion factor η (where $\mu_{\Delta T}$ is the linear expansion coefficient and L_{LoS} is the dimension of the object in the LoS direction), and relative residual cross range distance h_{XR} , as shown in Eq. (2.3). We estimate these three unknown parameters using

$$\hat{\underline{x}} = Q_{\hat{x}} A^T Q_y^{-1} \underline{y}, \text{ with} \quad (2.22)$$

$$Q_{\hat{x}} = (A^T Q_y^{-1} A)^{-1}, \quad (2.23)$$

where $Q_{\hat{x}}$ is the variance-covariance matrix of the estimates of the unknown parameters $\hat{\underline{x}}$. Here, \underline{y} are the double difference phase observations of the arc. To evaluate the performance of the parameter estimation, we compare the newly developed stochastic model, $Q_{\phi_{ij}}$, with a unit weight matrix Q_{UW} , which would be equivalent to a conventional result. The estimated parameters are shown in Table 2.1.

Additionally, we compute the double-difference absolute phase using the estimated parameters, i.e., $\hat{\phi}_{ij} = A\hat{\underline{x}}$, with results for both $Q_{\phi_{ij}}$ (weighted) and Q_{UW} (unweighted) represented by the blue and red lines, respectively, in the third row of Fig. 2.7⁷. For arc 1, we estimate a constant velocity of 0.7 mm/y using the weighted matrix, where the first noisier observations were assigned lower weights. In contrast, the estimated constant velocity using the unweighted matrix was 1.4 mm/y, a significant difference. While the differences between the red and blue lines in the third row of Fig. 2.7 may appear negligible, the effect of a proper weight matrix will be more influential with a shorter time series.

We also compute the residuals between the observations and the evaluated model, i.e., $\hat{\underline{e}} = \underline{\varphi}_{ij} - \hat{\underline{\phi}}_{ij}$, shown in the bottom row of Fig. 2.7. We visualize the 95% confidence interval based on the computed $Q_{\phi_{ij}}$ with the blue horizontal lines,

⁷The unit weight matrix was calculated using the mean value of the diagonal of $Q_{\phi_{ij}}$

which shows that the confidence interval for the first partitions is indeed bigger than for the observations in the other three partitions. Clearly, when both the functional and stochastic model are correct, 95% of the residues (black dots) should lie within the 95% confidence bounds based on the diagonal of $Q_{\varphi_{ij}}$. The same behavior can be observed for the other three arcs, suggesting that using partitions for $Q_{\varphi_{ij}}$ is valuable for quality assessment and parameter estimation. The proposed stochastic model is defined *prior* to parameter estimation—a key difference from conventional methods, where quality of scatterers is only determined retrospectively by analyzing the residuals between the model and observations. This distinction is illustrated by the red line in the bottom row of Fig. 2.7. The advantage of the proposed stochastic model is obvious: assessing observation quality only in hindsight fails to account for variations over time. For instance, in arc 1, the red line shows that quality is overestimated in the first half of the time series and underestimated in the second half. Furthermore, conventional methods rely heavily on accurate parameterization (i.e., a correct functional model), and consequently unmodeled displacements are attributed to the stochastic model. This can be particularly problematic in the built environment, where many different displacement signals may be present.

2.5.2. RESULTS OVER AMSTERDAM

To demonstrate that the stochastic model indeed results in different estimated parameters, and that the examples shown in Fig. 2.7 are not anecdotal, we estimate the constant velocity, relative residual cross range distance, and thermal expansion factor for all points. In Fig. 2.8 we show the histograms of the differences between the estimates using the two weight matrices. Differences in constant velocity can be up to 1 mm/y, and relative cross range distance up to ± 7 m. While the differences cannot be used to uniquely identify the 'correct' solution, it is clear that the stochastic model contributes more (independent) information to the inverse problem, making it at least more likely that including $Q_{\varphi_{ij}}$ leads to more reasonable parameter estimates.

2.5.3. COMPARISON A PRIORI AND POSTERIORI SIGMA VALUES

If the a priori stochastic model $Q_{\varphi_{ij}}$ indeed represents the noise of that particular arc, and the functional model used to estimate the unknown parameters represents its behavior, then the priori sigma ($Q_{\varphi_{ij}}$) should approximate the posterior sigma, i.e., it would match the standard deviation of the residuals between the observed DD and the estimated DD values. Here we validate the proposed stochastic model, assess whether indeed the NMAD of the amplitude is preferred over the NAD, and confirm whether the derived relation between the NMAD and σ_{ψ} as in Eq. (2.21) is valid.

To this end, we estimate the unknown parameters for all points shown in Fig. 2.6a using three different stochastic models. The first stochastic model is the proposed one, using the NMAD per partition, and Eq. (2.21) for the relation between the NMAD and σ_{ψ} using the 97.7 percentile. The second model also relies on NMAD values per partition but uses the 50th percentile, as represented by the black line

in Fig. 2.5. The third model uses the NAD per partition instead of NMAD, with a similar relationship between NAD and σ_ψ derived from the 97.7 percentile.

We estimate the unknown parameters per point using the three different stochastic models. Consequently, the posterior sigma values were estimated, and we computed the correlation between the assumed a priori sigma and the calculated posterior sigmas. If our stochastic model would be perfect, we expect a correlation of 1. The results are 0.48, 0.46, and 0.15 for model 1, model 2, and model 3, respectively.⁸ These results show that the NMAD of the amplitude is preferred over the NAD since both models 1 and 2 result in a correlation that is ~ 3 times greater than model 3. Moreover, the relation that is based on using the 97.7 percentile values from the simulation results in a slightly higher correlation compared to the 50th percentile. The reason why the correlation values are not closer to 1 is to be explained by the partitions. The partitions as detected for a single point consist of at least 30 observations. However, the stochastic model for an arc is based on the partitions of both point i and point j . Thus it is feasible that we evaluate arc partitions that contain less than 30 observations, for which it is difficult to compute statistics as the posterior sigma.

2.6. CONCLUSIONS

The fundamental problem of parameter estimation from InSAR time series is that both the functional models and the stochastic model are unknown and different for each scatterer and epoch. Conventionally, the same functional model is chosen for all points in the area of interest, and the quality of an arc is assessed retrospectively by analyzing residuals between the observations and the model, creating a strong and undesired dependency on the accuracy of the functional model. A stochastic model for double-difference phase observations of an arc is proposed, independent of the functional model, defined *prior* to parameter estimation. It is shown how the reference (mother) acquisition needs to be handled in the estimation procedure to obtain a diagonal VCM for the temporal single-differences, which is numerically beneficial. Using the amplitude vector per point, subdivided in temporal partitions, and its Normalized Median Absolute Deviation (NMAD), which is less sensitive to outliers than the conventional NAD, the variance-covariance matrix of the double differences of the arc is derived.

The result is an independent a priori stochastic model for each individual point (and arc) in the area of interest, describing time variable quality values of the observations.

This allows us to discriminate between points based on expected quality, between relevant epochs, and assign different weights to observations from different time periods. Incorporating these weights improves the estimation of unknown parameters, making it a critical component of the parameter estimation process.

⁸Note that we compared the prior and posterior sigmas per partition, since sigma values do not vary within one partition.

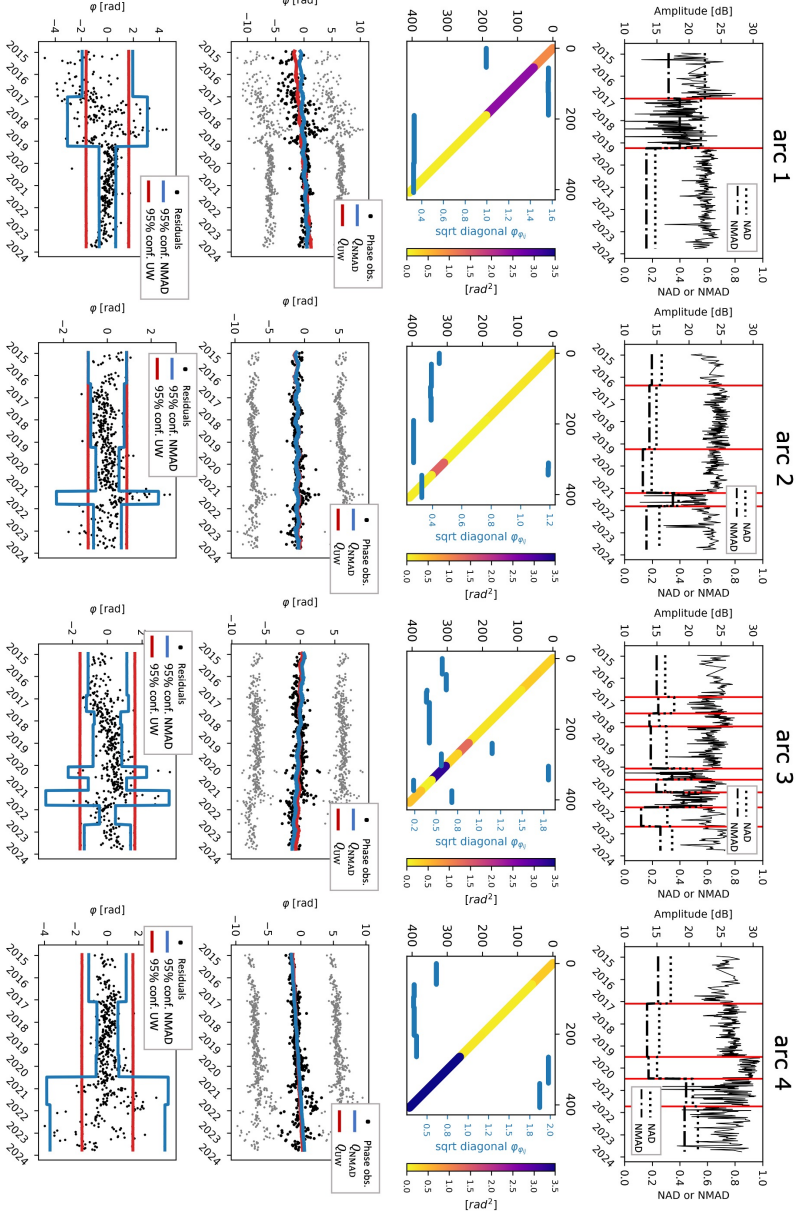


Figure 2.7: Four example arcs. The top row shows the amplitude time series, together with the detected partitions indicated by the red vertical lines, for points 1 to 4 of Fig. 2.6a. The horizontal dotted and dash-dotted lines represent the NAD and NMAD values per partitions, respectively, indicated on the vertical axis on the right side. The second row shows the VCM, $Q\phi_{ij}$, for the arc with the colorbar corresponding to the values in the matrix. The observations are uncorrelated, i.e., the off-diagonal elements are zero. The horizontal blue lines correspond to the square root of the diagonal of $Q\phi_{ij}$, and the values are shown on the vertical axis on the right side (in blue). These values clearly differ per partition. The third row shows the double-difference phase observations for the arc and the proposed stochastic model using $Q\phi_{ij}$, corresponding to the blue line, and using a unit-weight matrix, corresponding to the red line. Especially for arc 1, using a different variance-covariance matrix results in different estimated model parameters. The last row shows the residuals between the estimated model and the observations shown by the black dots, and confidence intervals using the $Q\phi_{ij}$ and the unit weight matrix (UW, unweighted). Using the proposed method for the variance-covariance matrix makes sense, since we indeed find larger residues for the partitions that are assigned a lower quality.

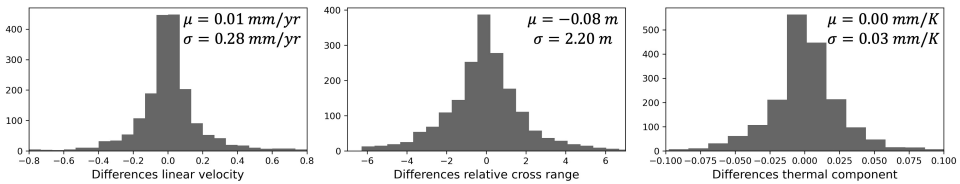


Figure 2.8.: For all points shown in Fig. 2.6a we estimated the constant velocity, relative residual cross range distance, and thermal component using two weight matrices: i) with our method and ii) the unit weight matrix. The differences between the estimated parameters are shown in the histograms.

3

A FUNCTIONAL MODEL FOR INSAR ARC TIME SERIES

Reliable estimation of arc parameters, such as relative displacements or cross-range distance, requires a functional model that accurately reflects the kinematic behavior of each arc. To achieve an overdetermined system of equations, usually a simplified parameterization of the displacements is chosen, e.g., using a constant velocity, sinusoids, polynomials, or splines, which is uniform for all scatterers or arcs in the area of interest. Yet, as InSAR products easily contain millions of scatterers that each exhibit unique behavior, each arc would ideally require a unique and tailored parameterization, hence unique and tailored functional model. While contextual information could support informed model selection, such information may be incomplete for applications containing many different scatterers. In this chapter, we propose a method to construct an arc-specific functional model, using the temporal amplitude partitions introduced in Chapter 2. Instead of estimating the unknown parameters in the conventional phase domain, we formulate the model in the complex domain, which eliminates the need for explicit estimation of phase ambiguities.

3.1. INTRODUCTION

INSAR has an advantage over traditional geodetic techniques in its ability to estimate and monitor displacements for a large number of points as demonstrated by many case studies, including nationwide monitoring services and wide-area products such as the European Ground Motion Service (EGMS) [40].

However, with InSAR we cannot observe displacements directly, as the fundamental radar observable is a complex signal from which modulo- 2π differential phase values are derived [80]. These measurements are inherently relative, both temporally (between acquisitions) and spatially (between points), and are associated with a specific arc, i.e., the connection between two points. As a result, only relative displacements along an arc can be estimated from these phases. The observed differential phase itself is a combination of several components, including geometry (displacement and cross-range position, where the latter is related to topography), delay (tropospheric and ionospheric propagation effects), and noise. Additionally, as the observed relative phase is wrapped—i.e., observed modulo- 2π —we also need to *estimate* the unknown integer ambiguities needed to compute the *absolute* phase, also termed phase ambiguity resolution, or phase unwrapping. Transforming the phase observations into an usable InSAR product, referred to as *parameter estimation*, requires an adequate and realistic functional model [80, 101, 193].

However, selecting an appropriate functional model is challenging, particularly in InSAR applications in the built environment, where arc behavior may vary significantly in both space and time due to the non-homogeneity of the scatterers and the varying dynamics of the structures they represent. While prior knowledge, such as on the expected smoothness or on the physical drivers of the deformation, should be used when available, such information will inevitably be incomplete or unknown for all scatterers. By the same token, the assumption that a single, uniform parameterization (e.g., a constant velocity) is suitable for each single scatterer is an overstretch and cannot be sustained. Thus, a universally optimal functional model for InSAR parameter estimation does not exist, nor is it realistic to assume that the correct model is known for all points [28, 35, 113].

What is needed, therefore, is a flexible modeling approach that can adapt to the behavior of individual arcs, even in the absence of detailed prior knowledge. The model proposed in this chapter does not aim to be universally optimal, but provides a pragmatic way to parameterize arc behavior. Should advanced physical knowledge or application-specific smoothness criteria be available, they should be used instead, as choosing the right model at the right moment remains essential for obtaining optimal results leading to meaningful interpretation.

Moreover, the focus of this chapter is on describing the temporal behavior of scatterers based on the observations available up to the present epoch. We refer to such an approach as *batch* processing, where we use a given and fixed set of SAR data to estimate a predefined set of time-invariant parameters. The objective is therefore not to sequentially estimate the instantaneous state of a scatterer through time, which we refer to as a *sequential* estimation problem. Dynamic state-space approaches, such as dynamic linear models or the instantaneous-state InSAR method, see e.g., Wang *et al.* [202], may be more suitable for adaptive

or real-time estimation problems, and may be more flexible, but they address a fundamentally different problem formulation than the one considered here.

In this chapter, we therefore propose to use the amplitude behavior of the two points forming the arc to define an arc-specific functional model. Variations in the amplitude signal are used to construct a time-varying displacement model, following an approach similar to fitting a B-spline [201]. The model is evaluated in the complex domain, allowing to estimate the parameters of interest. The ambiguity parameters then follow implicitly as a result of the parameter estimation.

This chapter is organized as follows. Sec. 3.2 introduces the functional model in the phase domain. In Sec. 3.3, we discuss the unknown parameters of this model in more detail and propose to use the relative cross-range distance as a better alternative to the commonly used relative height. Sec. 3.4 presents the mathematical model in the complex domain and outlines how the parameters can be estimated. The estimated parameters can then be used to implicitly unwrap the phases, which is further explained in Sec. 3.5. A practical example is shown in Sec. 3.6, followed by a discussion in Sec. 3.7.

3.2. THE MATHEMATICAL MODEL IN THE PHASE DOMAIN

We first briefly recall the definition of the double-differenced phase and the resulting mathematical model for an arc, as introduced in Sec. 2.2.

The *relative* double-differenced (DD) phase for an arc is defined as the spatio-temporal double-difference phase φ_{ij}^{md} , which represents the temporal phase difference for point scatterer j at epoch d relative to the mother epoch m , denoted ϕ_j^{md} , relative to reference point i , denoted ϕ_i^{md} . The DD phase consists of different components [101, 193]:

$$\begin{aligned}\varphi_{ij}^{w,md} &= \phi_j^{md} - \phi_i^{md} \\ &= -2\pi a_{ij}^{md} + \varphi_{ij,d_{nt}}^{md} + \varphi_{ij,\eta}^{md} + \varphi_{ij,h_{xr}}^{md} + \varphi_{ij,S}^{md} + \varphi_{ij,n}^{md},\end{aligned}\quad (3.1)$$

where $a \in \mathbb{Z}$ is the integer ambiguity that ensures $\varphi_{ij}^{w,md}$ is wrapped, i.e., within the interval $[-\pi, \pi)$, denoted by the ^w in the superscript. $\varphi_{d_{nt}}$ is the non-thermal displacement phase, φ_{η} the thermal displacement phase, and $\varphi_{h_{xr}}$, φ_S , and φ_n the phases due to the residual cross-range distance, atmospheric delay, and noise, respectively. The signals of interest to be estimated are the residual cross-range distance and displacement phase, where the latter is the sum of the non-thermal and thermal displacement phase. The atmospheric delay and the integer ambiguities can be regarded as nuisance parameters; required in the equations but with no direct physical for the signal of interest.¹ The mathematical model (for the wrapped

¹In atmospheric or meteorological applications, atmospheric delay can be regarded as the main signal of interest, see e.g., [83, 84, 125, 132]. Note also that it is possible to estimate the atmospheric phase screen of the mother acquisition as in van Leijen [193]. However, in this work we choose not to do so and add it in the stochastic model.

phase) therefore results in

$$E\left\{\begin{bmatrix} \varphi_{ij}^{w,m1} \\ \vdots \\ \varphi_{ij}^{w,mD} \end{bmatrix}\right\} = -2\pi a + \underbrace{(\delta_{\text{displ}}|B_{\Gamma})}_{\varphi_{ij,dnt}^{md}} + \underbrace{(\eta|B_{\text{th}})}_{\varphi_{ij,\eta}^{md}} + \underbrace{(h_{\text{xr}}|B_{\perp})}_{\varphi_{ij,h_{\text{xr}}}^{md}}; \quad (3.2)$$

$$D\left\{\underbrace{\begin{bmatrix} \varphi_{ij}^{w,m1} \\ \vdots \\ \varphi_{ij}^{w,mD} \end{bmatrix}}_{\underline{y}}\right\} = Q\varphi_{ij} = \underbrace{Q\varphi_{ij,\text{atm}}}_{\varphi_{ij,S}^{md}} + \underbrace{Q\varphi_{ij,\text{TVC}} + Q\varphi_{ij,\text{thm}}}_{\varphi_{ij,n}^{md}}, \quad (3.3)$$

where $E\{\cdot\}$ denotes the expectation of the model, which consists of $D+3$ unknown parameters. These are: (i) D integer ambiguity values a , (ii) δ_{displ} , representing the parameter vector of the non-thermal displacement phase², (iii) the relative thermal displacement η , and (iv) the residual cross-range distance h_{xr} .³ Note that the forward models of $\varphi_{ij,dnt}^{md}$, $\varphi_{ij,\eta}^{md}$, and $\varphi_{ij,h_{\text{xr}}}^{md}$ are forced to produce the relative (wrapped) phase by adding the integer ambiguity term a , as they originally result in the absolute phase.

The *total* (relative) displacement phase for the arc, $\varphi_{ij,dnt,\eta}^{md}$ is the sum of two components: δ_{displ} as a function of the temporal baseline B_{Γ} , and the thermal displacement as a function of the thermal baseline B_{th} . The residual cross-range distance, h_{xr} , is a function of the perpendicular baseline B_{\perp} .

$D\{\cdot\}$ is the dispersion operator, described by the Variance Covariance Matrix (VCM) $Q\varphi_{ij}$, which is the sum of (i) the atmospheric noise $Q\varphi_{ij,\text{atm}}$, (ii) the thermal noise $Q\varphi_{ij,\text{thm}}$, and (iii) the Time Variant Clutter (TVC) $Q\varphi_{ij,\text{TVC}}$. For the definition of these matrices, we refer to Chapter 2 of this thesis.

With D double difference-phase observations, Eq. (3.2) results in an underdetermined problem as there are at least $3+D$ unknown model parameters: δ_{displ} , η , h_{xr} , and D ambiguity values. This immediately implies that the system cannot be solved without introducing additional assumptions, such as an appropriate parameterization of the displacement phase.

3.3. PARAMETERS OF THE FUNCTIONAL MODEL

In the following we describe the unknown parameters of the functional model, i.e., the relative cross-range distance h_{xr} , thermal displacement factor η , and non-thermal displacement parameter vector δ_{displ} , in further detail.

²It is important to stress that the parameter vector δ_{displ} is the parameterization of the displacement phase, e.g., a velocity. It therefore differs from the displacement time series. The latter can be evaluated from δ_{displ} with a forward model.

³Note that in fact the unknowns are relative parameters as well but for shorter notation we omitted the subscript ij .

3.3.1. RELATIVE CROSS-RANGE DISTANCE

The residual cross-range distance $h_{\text{xr},i}$ for scatterer i is defined as the cross-range distance between the reference surface (for instance the local ellipsoid or a DEM) and the effective scattering center of the scatterer, see Fig. 3.1.⁴ Because of the different perpendicular baselines for each acquisition, the reference surface itself induces a phase signal, ϕ_{ref} [212], which can be computed and subtracted from the phase observations. The values for ϕ_{ref} are computed from the orbit position at the mother acquisition, for the range and azimuth positions of the mother image, relative for each mother-daughter interferometric combination. The look angle, θ_1 , determines how the satellite observes the pixels on the reference surface.

However, scatterers are not located exactly on the reference surface, due to local topography or the presence of buildings or structures. Fig. 3.1 illustrates this by showing the difference between $P_{h_{\text{xr}}}$, i.e., the actual scatterer location, and P_0 , the location on the reference surface for which the phase is corrected. Because of this difference, scatterers are observed with look angle $\theta_1 + \delta\theta_1$, cf. the blue look vectors in Fig. 3.1. This additional look angle introduces the cross-range (xr) phase signal, i.e., $\phi_{h_{\text{xr}}}$, which remains in the observations after correcting the DD for ϕ_{ref} . Note that this holds for every scatterer.

Consequently, the relation between cross-range distance $h_{\text{xr},i}$ for a single scatterer i and the corresponding phase $\phi_{i,h_{\text{xr}}}$ is defined as [80, 212]

$$\begin{aligned}\phi_{i,h_{\text{xr}}}^{md} &= \frac{-4\pi}{\lambda} \frac{B_i^{md} \cos(\theta_{1,i}^m - \alpha_i^{md})}{R_i^m} h_{\text{xr},i}, \\ &= \frac{-4\pi}{\lambda} \frac{B_{\perp,i}^{md}}{R_i^m} h_{\text{xr},i}, \\ &= \beta_i^{md} h_{\text{xr},i},\end{aligned}\tag{3.4}$$

where β_i^{md} is the so-called ‘cross-range-to-phase factor’. B_i^{md} is the baseline between the satellite orbit positions at the mother and daughter acquisitions, α_i^{md} the baseline orientation angle, $B_{\perp,i}^{md}$ the perpendicular baseline, R_i^m the range distance between the scatterer and mother satellite position, and θ_{inc} the local incidence angle which is defined as the angle between the normal vector on the local ellipsoid, and the line of sight toward the satellite.⁵

⁴A scatterer represents the sum of all reflections within a resolution cell. If this sum is dominated by a single strong scatterer, the signal can be attributed to a single physical object. However, often the signal of one PS is the sum of multiple reflecting elements within a resolution cell, and can therefore not be related to a single object [206].

⁵Note that the look angle θ_1 cannot be replaced by θ_{inc} in Eq. (3.4) (due to the curved earth), since the cross-range phase is caused by the scatterer being not located at the reference surface. As a result, the scatterer is observed with a look angle $\theta_1 + \delta\theta_1$. From the satellites perspective, the orientation of the local normal (that defines the incidence angle θ) at the scatterer center is irrelevant. This is also illustrated by comparing the left and right situation in Fig. 3.1. Both have the same acquisition geometry and look angle, but the orientation of the local normal with respect to the ellipsoid differs, resulting in different incidence angles. Despite this, the cross-range component is the same—demonstrating that the cross-range is independent of incidence angle.

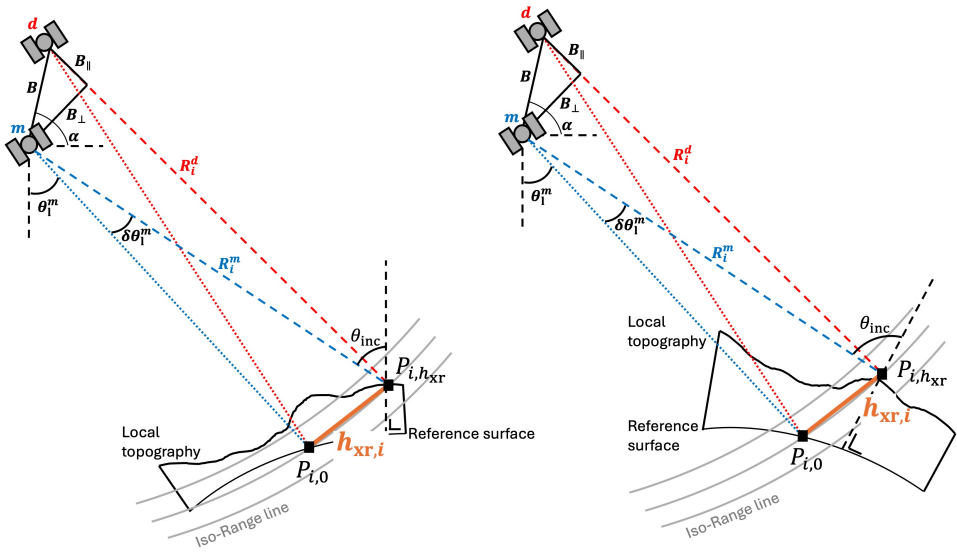


Figure 3.1.: Geometry of repeat-pass interferometry between mother acquisition m and daughter acquisition d . B is the baseline, B_{\perp} the perpendicular baseline, and B_{\parallel} the parallel baseline. R is the range between the satellite and scatterer i , which is expected to be observed with look angle θ_1 (dotted blue line) if situated on the reference surface (location $P_{i,0}$). Local topography is causing a slightly different viewing geometry (dashed blue line), with an additional look angle $\delta\theta_1$, resulting in a cross-range component $h_{xr,i}$ (orange vector). Note that computing the reference phase requires the look angle, θ_1 , instead of the local incidence angle θ_{inc} (which is defined as the angle between the normal vector on the ellipsoid and the satellite's LoS). This is shown by the difference between the left and right figure: both pixels are observed with equal look angle θ_1 , but θ_{inc} differs significantly. Figure adapted from [80] and [33].

We choose to work with ‘relative cross-range’ rather than ‘relative height.’ As a result, we can work with the look angles and the local incidence angles do not need to be known. Subsequently, the relative height of the point can be estimated from the estimated cross-range distance with

$$H_i = \sin \theta_i \cdot h_{xr,i}, \quad (3.5)$$

where H_i is the height difference between the local topography and reference surface (at the same range distance) for scatterer i .

So far, we discussed the phase contribution for a temporal difference for a single scatterer. However, we need to consider the spatial phase difference as well, resulting in

$$\varphi_{ij,h_{xr}}^{md} = \beta_j^{md} h_{xr,j} - \beta_i^{md} h_{xr,i}. \quad (3.6)$$

Since scatterer i is considered to be the reference scatterer, the cross-range distance $h_{xr,i}$ is set to zero, and we estimate relative cross-range distances between scatterers i and j . In other words, an unknown offset remains between the reference point and the reference surface, since the cross-range distance of scatterer i itself cannot be estimated. Effectively, the reference surface is ‘lifted’ to coincide with the reference point i . Therefore, the final functional relation reduces to

$$\varphi_{ij,h_{xr}}^{md} = \beta_j^{md} h_{xr,ij}. \quad (3.7)$$

3.3.2. THERMAL DISPLACEMENT

The relative thermal expansion factor η is an unknown constant parameter per arc, driven by material properties and object dimensions. When it is multiplied with a temperature change, the thermal expansion on either side of an arc can be obtained [28, 59, 67, 131, 147]. Following the notation of [28, 29], this is

$$\eta = \mu_{\Delta K_t} \cdot L_{LoS}, \quad (3.8)$$

where $\mu_{\Delta K_t}$ is the linear expansion coefficient, i.e., a material property, and L_{LoS} is the dimension of the object (hosting the scatterer) in the LoS direction. The functional relation between temperature variation and the observed thermal displacement phase is then defined as

$$\varphi_{ij,\eta}^{md} = \eta B_{ij,th}^{md}, \quad (3.9)$$

where $B_{ij,th}^{md}$ is the ‘thermal baseline’, i.e., the relative temperature difference between epochs m and d and PS i and j . Since the difference in thermal expansion may lead to vertical and horizontal displacement alike, e.g., consider an arc at a bridge, in which case the arc may shorten or lengthen horizontally, the difference in thermal expansion needs to be considered in the line of sight (LoS) direction. Note that the observed thermal displacement phase $\varphi_{ij,\eta}^{md}$ may also absorb other temperature-related effects, such as the movement of soft soil layers. Although these effects are mainly driven by changes in the phreatic water level, this may be significantly correlated with temperature [34].

3.3.3. NON-THERMAL DISPLACEMENT

The model for the non-thermal displacement phase describes the difference in displacement behavior between point i and j . This is challenging, as point behavior may vary significantly in space and time, especially in the built environment [28]. It is therefore not realistic to assume that there exists one optimal model that is always valid to all arcs in all cases. For example, it is unlikely that all arcs can be parameterized by a constant velocity model or that a constant velocity model with an additional precipitation term would be appropriate in every case. Rather, the choice of the model depends on the specific case, which we refer to as a triple-A approach (Application-Aware and -Aligned). Consequently, rather than identifying a universally optimal model, the goal should be to understand when a particular model can be used. Here, we distinguish three types of models:

- Geometric models, which rely on mathematical formulations (e.g., lines, sinusoids, polynomials) without any physical interpretation, see Wang *et al.* [201];
- Kinematic models, using e.g., position, instantaneous or mean velocity, and instantaneous or mean acceleration, see Wang *et al.* [202]; and
- Physical models, which explicitly use physically interpretable parameters describing the displacements (e.g., precipitation or volume changes in a reservoir), see e.g., Conroy [33].

Note that both geometric and kinematic models are descriptive models: they fit the data without necessarily explaining the underlying physical processes. Knowledge of the underlying physics is not required, and without observations these models have no value. In contrast, physical models are mechanistic models in which the parameters represent real-world processes that generate the data. Such models retain value even in the absence of observations and can, for example, be used for simulations. If prior knowledge on the expected displacement behavior is available, in the form of physical information or expected smoothness, physical or kinematic models should be used. However, this information is not likely to be available for all points in InSAR studies involving millions of points. Nevertheless, in many triple-A projects, the assumption that all arcs follow the same model, e.g., a constant velocity model⁶, is unrealistic and cannot be sustained.

Geometrical models can then be a solution, even though the parameterization may not be physically interpretable. In this chapter, we will primarily consider geometrical models, but the discussed theory is also valid for other types of models. Furthermore, our focus is primarily on point scatterers (PS) in the built environment.

PARAMETERIZATION

With the increased data availability and the associated longer time series, the displacement behavior along an arc is more likely to change over time. To

⁶Applying a steady-state (i.e., constant velocity) model is equivalent to imposing an infinitely strict smoothness criterion, as any displacement behavior that differs from the steady-state model is attributed to noise or other components.

accommodate this, we evaluate whether the time series need to be divided into several partitions. This approach is based on the methodology from Brouwer and Hanssen [20] discussed in Chapter 2, where changes in the amplitude time series are used to detect potential changes in the stochastic behavior. However, since these changes may also be an indication for (abrupt) changes in kinematic behavior, we estimate different displacement parameters for each partition, comparable to fitting a B-spline [43]. Consequently, as these partitions are unique for each arc, the displacement parameterization becomes arc specific. We parameterize the displacements with a second order polynomial per partition, resulting in

$$\varphi_{ij,d_{n},p}^{md} = a_p + b_p B_T^{md} + c_p (B_T^{md})^2, \quad (3.10)$$

where the subscript p refers to the partition, and a_p , b_p , and c_p represent the unknown geometric displacement parameters of δ_{displ} , which differ for each partition. The decision to use a second-order polynomial is made because (i) it imposes a less restrictive smoothness constraint than the steady-state model, (ii) the steady-state model remains valid when $c = 0$, and (iii) it allows for meaningful physical assumptions about maximum velocity and acceleration, which would be less straightforward with a third-order model. Note that this forward model results in absolute phase values.

CONTINUITY CONDITION

To ensure a continuous displacement signal, the polynomials on both sides of the breakpoint t_p , i.e., the epoch at which a new partition starts, must yield the same value. This implies the following condition

$$(a_{p_i} + b_{p_i} t_p + c_{p_i} (t_p)^2) - (a_{p_{i+1}} + b_{p_{i+1}} t_p + c_{p_{i+1}} (t_p)^2) = 0, \quad \forall i. \quad (3.11)$$

For PS that remain coherent throughout the entire observation period the continuity condition is reasonable. However, there may be situations in which the continuity condition should not be applied. Consider, for instance, a road under construction. Once exposed to roadwork, the signal changes resulting in an ‘unknown’ phase shift and a potentially discontinuous displacement signal.

DIFFERENTIABILITY CONDITION

Additionally, one could also impose the condition of differentiability between different partitions, meaning that the first derivatives of the two functions at the two partitions must be equal at t_p . Yet, imposing this condition is a choice that is application-dependent.

3.4. THE MATHEMATICAL MODEL IN THE COMPLEX DOMAIN

The relations between the unknown parameters and the baselines (temporal, geometric, and thermal), as described in the previous section, can be used in the mathematical model of Eq. (3.2). However, a significant disadvantage of this model is the need to explicitly estimate ambiguity values a , as it renders the model to

be underdetermined—there are at least $3 + D$ unknown model parameters $\delta_{\text{displ}}, \eta$, h_{xr} , and D ambiguity values. To circumvent this inconvenience, we evaluate the functional model in the complex domain where the DD phasor $\underline{P}_{\varphi_{ij}}$ of the arc is defined as

$$\begin{aligned}\underline{P}_{\varphi_{ij}} &= \underline{P}_{\phi_j} \cdot \underline{P}_{\phi_i}^* \\ &= \underline{A}_{\phi_j} \underline{A}_{\phi_i} \exp(i(\underline{\phi}_j - \underline{\phi}_i)),\end{aligned}\tag{3.12}$$

where \underline{P}_{ϕ} is the phasor representative to the temporal differences. The asterisk * implies the complex conjugate, and A is the amplitude. The real and imaginary part of the phasor are defined as

$$\text{Re}(P) = A \cos(\varphi) = A \cos\left(\frac{4\pi}{\lambda}((\delta_{\text{displ}}|B_{\text{T}}) + (\eta|B_{\text{th}}) + (h_{\text{xr},ij}|B_{\perp}))\right) \text{ and}\tag{3.13}$$

$$\text{Im}(P) = A \sin(\varphi) = A \sin\left(\frac{4\pi}{\lambda}((\delta_{\text{displ}}|B_{\text{T}}) + (\eta|B_{\text{th}}) + (h_{\text{xr},ij}|B_{\perp}))\right).\tag{3.14}$$

It can be seen that the ambiguities a are no longer explicitly part of the model. They are not eliminated, but the reparameterization into the complex domain, i.e., by expressing the phase in terms of sine and cosine, transforms the problem into a continuous function. In the complex domain, the model consists of only three unknowns: δ_{displ} , η , and h_{xr} . By incorporating the parameterizations of these components as derived in Sec. 3.3, the final functional model can be defined.⁷ For an observation time series of length D , partitioned into P segments, the complex-valued

⁷From this point onward, we denote the real and imaginary parts of the phasor P as Re and Im, respectively. Additionally, the subscript 'ij' is omitted, though the model still describes spatial differences.

model becomes:

$$E\left\{ \underbrace{\begin{bmatrix} \underline{\text{Re}}_{p_1}^{md_1} \\ \underline{\text{Re}}_{p_1}^{md_2} \\ \vdots \\ \underline{\text{Re}}_P^{md_{D-1}} \\ \underline{\text{Re}}_P^{md_D} \\ \underline{\text{Im}}_{p_1}^{md_1} \\ \underline{\text{Im}}_{p_1}^{md_2} \\ \vdots \\ \underline{\text{Im}}_P^{md_{D-1}} \\ \underline{\text{Im}}_P^{md_D} \end{bmatrix}}_y \right\} = \underbrace{\begin{bmatrix} A_{p_1} \cos\left(\frac{4\pi}{\lambda}\left((h_{\text{xr}}|B_{\perp}^{md_1}) + (\eta|B_{\text{th}}^{md_1}) + (a_{p_1}, b_{p_1}, c_{p_1}|B_{\text{T}}^{md_1})\right)\right) \\ A_{p_1} \cos\left(\frac{4\pi}{\lambda}\left((h_{\text{xr}}|B_{\perp}^{md_2}) + (\eta|B_{\text{th}}^{md_2}) + (a_{p_1}, b_{p_1}, c_{p_1}|B_{\text{T}}^{md_2})\right)\right) \\ \vdots \\ A_P \cos\left(\frac{4\pi}{\lambda}\left((h_{\text{xr}}|B_{\perp}^{md_{D-1}}) + (\eta|B_{\text{th}}^{md_{D-1}}) + (a_P, b_P, c_P|B_{\text{T}}^{md_{D-1}})\right)\right) \\ A_P \cos\left(\frac{4\pi}{\lambda}\left((h_{\text{xr}}|B_{\perp}^{md_D}) + (\eta|B_{\text{th}}^{md_D}) + (a_P, b_P, c_P|B_{\text{T}}^{md_D})\right)\right) \\ A_{p_1} \sin\left(\frac{4\pi}{\lambda}\left((h_{\text{xr}}|B_{\perp}^{md_1}) + (\eta|B_{\text{th}}^{md_1}) + (a_{p_1}, b_{p_1}, c_{p_1}|B_{\text{T}}^{md_1})\right)\right) \\ A_{p_1} \sin\left(\frac{4\pi}{\lambda}\left((h_{\text{xr}}|B_{\perp}^{md_2}) + (\eta|B_{\text{th}}^{md_2}) + (a_{p_1}, b_{p_1}, c_{p_1}|B_{\text{T}}^{md_2})\right)\right) \\ \vdots \\ A_P \sin\left(\frac{4\pi}{\lambda}\left((h_{\text{xr}}|B_{\perp}^{md_{D-1}}) + (\eta|B_{\text{th}}^{md_{D-1}}) + (a_P, b_P, c_P|B_{\text{T}}^{md_{D-1}})\right)\right) \\ A_P \sin\left(\frac{4\pi}{\lambda}\left((h_{\text{xr}}|B_{\perp}^{md_D}) + (\eta|B_{\text{th}}^{md_D}) + (a_P, b_P, c_P|B_{\text{T}}^{md_D})\right)\right) \end{bmatrix}}_{A(x)} ; \quad (3.15)$$

$$D\left\{ \underbrace{\begin{bmatrix} \underline{\text{Re}}_{p_1}^{md_1} \\ \underline{\text{Re}}_{p_1}^{md_2} \\ \vdots \\ \underline{\text{Re}}_P^{md_{D-1}} \\ \underline{\text{Re}}_P^{md_D} \\ \underline{\text{Im}}_{p_1}^{md_1} \\ \underline{\text{Im}}_{p_1}^{md_2} \\ \vdots \\ \underline{\text{Im}}_P^{md_{D-1}} \\ \underline{\text{Im}}_P^{md_D} \end{bmatrix}}_y \right\} = \underbrace{\text{diag}(v)}_{Q_{\text{Re,Im}}}, \text{ with} \quad (3.16)$$

$$v = \left[\sigma_{\text{Re}_{p_1}^{md_1}}^2 \quad \cdots \quad \sigma_{\text{Re}_P^{md_D}}^2 \quad \sigma_{\text{Im}_{p_1}^{md_1}}^2 \quad \cdots \quad \sigma_{\text{Im}_P^{md_D}}^2 \right]^T,$$

where the subscript p_1 until P refers the partition to which the observation and unknown parameter belong. The model consists of $P \times 3$ unknown displacement parameters represented by a_p , b_p , and c_p , P unknown values for the mean amplitude A per partition, and unknown relative cross-range distance h_{xr} and thermal expansion factor η . The model can be solved when there are at least $3 + 3P$ observations. $Q_{\text{Re,Im}}$ is the variance-covariance matrix (VCM) representing the quality of the observations in the complex domain. The observations are uncorrelated, as discussed in Sec. 2.4.3, and therefore $Q_{\text{Re,Im}}$ is a diagonal matrix. While we discussed in Chapter 2 how the VCM for the *phase observations* could be derived, the *complex variance values* can be obtained with Eq. (A.10) from Appendix A.

3.4.1. THE NON-LINEAR MODEL

The model of Eqs. (3.15) and (3.16) is non-linear and must therefore be solved using iterative techniques, such as Gauss-Newton or using other non-linear least squares solvers. Such approaches require initial estimates of the parameters (i.e., the geometrical displacement parameters a_p , b_p , and c_p , as well as η and h_{xr}) to find a solution. To ensure convergence to the correct solution, these initial estimates should be close enough to the true parameter values. We use prior information on the problem at hand or use 0 as an initial estimate as the arc can be defined in two directions, where the sign of the estimated parameters would be flipped. Moreover, for the initial estimate of h_{xr} and η , prior knowledge on the local topography and the type of area that is monitored can help to obtain initial estimates.

3.4.2. SMOOTHNESS CONSTRAINTS AND BOUNDS TO SOLUTION

The trigonometric nature of the model can result in multiple local minima, increasing the risk of convergence to an incorrect solution. To mitigate such issues and ensure physically plausible results, constraints can be introduced to limit the solution space. In particular, the geometric polynomial parameters (a_p , b_p , and c_p) can be bounded using prior knowledge about expected maximum velocity and acceleration, as they relate to:

$$b_p = v_{\max} - c_p B_T, \quad (3.17)$$

$$c_p = a_{\max}. \quad (3.18)$$

Knowledge on the local topography can help to define minimum and maximum values for the relative cross-range distance as the two values are related, see Eq. 3.5.

3.5. ESTIMATING THE PHASE COMPONENTS

Solving the system of equations in Eqs. (3.15) and (3.16) yields the estimated parameters which can be used to evaluate the forward model in the phase domain with

$$\hat{\varphi}_{ij,p}^{md} = (\hat{h}_{xr}|B_{\perp}^{md}) + (\hat{\eta}|B_{th}^{md}) + \underbrace{(\hat{a}_p, \hat{b}_p, \hat{c}_p|B_T^{md})}_{\delta_{\text{displ}}}, \quad (3.19)$$

where $\hat{\varphi}_{ij,p}^{md}$ denotes the adjusted *absolute* DD phase at epoch d in partition p for the arc between points i and j . It can be seen that it follows directly from the estimated parameters.

For some applications it may be necessary to also estimate the observed phase reduced for the static components, denoted $\hat{\varphi}_{ij}^{\prime md}$, i.e., the phase corrected for cross-range distance and thermal displacements. Since the geometric parameterization with polynomials per partition is a model itself, not the full displacement behavior of the arc may be fully captured in the parameter vector, δ_{displ} . Reducing the observed phase for the static components yields a time series that, in principle, should contain the full displacement behavior.

This requires the estimation of the two static phase components that are computed with

$$\hat{\varphi}_{ij,h_{xr}}^{md} = \hat{h}_{xr}\beta_j^{md} \text{ and} \quad (3.20)$$

$$\hat{\varphi}_{ij,\eta}^{md} = \hat{\eta}B_{ij,th}^{md}, \quad (3.21)$$

where $\hat{\varphi}_{ij,h_{xr}}^{md}$ is the cross-range phase, and $\hat{\varphi}_{ij,\eta}^{md}$, the thermal displacement phase. The reduced observed phase is then estimated with

$$\hat{\varphi}_{ij}^{md} = \varphi_{ij}^{w,md} - \hat{\varphi}_{ij,h_{xr}}^{md} - \hat{\varphi}_{ij,\eta}^{md} + 2\pi\hat{a}, \quad (3.22)$$

where \hat{a} are the estimated ambiguities, that follow from the parameter estimation. The ambiguities a can be estimated when the observed *wrapped* phase, $\varphi_{ij,p}^{w,md}$, is compared to the adjusted *absolute* phase of Eq. (3.19). I.e., when $|\varphi_{ij,p}^{w,md} - \hat{\varphi}_{ij,p}^{md}| > \pi$ this might indicate that an ambiguity needs to be added or removed to the observed phase at epoch d .⁸

Note that the reduced observed phase of Eq. (3.22) in fact represents the absolute non-thermal displacement phase time series plus noise. The estimated non-thermal displacement phase per partition is computed with

$$\hat{\varphi}_{ij,d_{nt}}^{md} = \hat{a} + \hat{b}B_T^{md} + \hat{c}(B_T^{md})^2. \quad (3.23)$$

However, this representation is not physically interpretable, and the chosen parameterization may not fully capture the non-thermal displacement behavior of the arc. Therefore, if a parametric representation of the non-thermal displacement is still desired, the multiple hypothesis testing (MHT) approach proposed by Chang and Hanssen [28] can be applied to the phase time series reduced for the static components in Eq. (3.22). The total procedure of the parameter estimation as proposed in this section, is also summarized in a flowchart as shown in Fig. 3.2.

3.6. RESULTS FOR AN ARC IN AMSTERDAM

We illustrate the proposed functional model with an example arc from a descending Sentinel-1 dataset covering Amsterdam. The arc is depicted in Fig. 3.3a. The amplitude time series for points i and j are shown in Figs. 3.3b and c, respectively. The observed real and imaginary parts of the double-difference arc phasors, P_{ij}^{md} , are represented by blue dots in Figs. 3.4a and b, respectively, while the double-difference phase is shown in Fig. 3.4c. To estimate the unknown parameters, we follow the steps as shown in Fig. 3.2.

To construct the stochastic and functional models, we first identify partitions in the amplitude time series, using a breakpoint detection method as proposed by

⁸Such an approach may be regarded as a form of implicit phase unwrapping, since the estimated ambiguities follow directly from the estimated parameters. However, this would also require accounting for the uncertainty of the estimated ambiguities. For a more detailed explanation on implicit unwrapping we refer to Chapter 4.

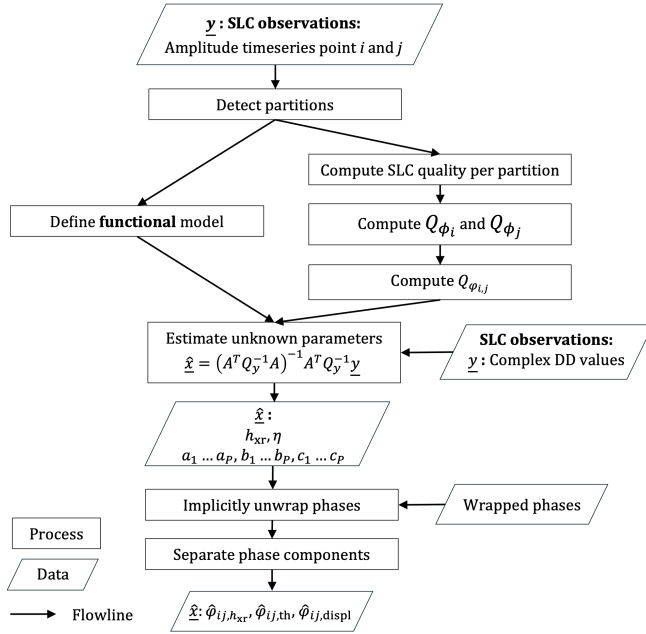


Figure 3.2.: Flowchart of parameter estimation using the mathematical model from Eqs. (3.15) and (3.16). The rectangles represent a (mathematical) operation while a parallelogram represents ‘data’ in the form of input or output.

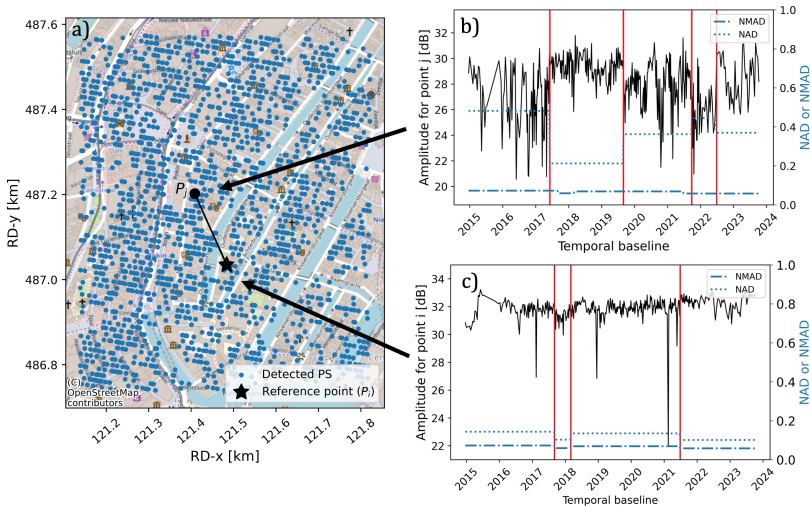


Figure 3.3.: a) Detected coherent point scatterers over Amsterdam in blue and the example arc (black line) that is evaluated in Fig. 3.4. b) and c) show amplitude time series for point *j* and for the reference point *i*, respectively. Different partitions are detected using a breakpoint detection algorithm [184]. Per partition, the NMAD of the amplitude is computed.

Truong *et al.* [184], indicated by the vertical red lines in Figs. 3.3b) and c).⁹ Since the amplitude behavior of scatterers may exhibit seasonal patterns, we chose the partitions to be not shorter than half a year. This results in four partitions for point i (the reference) and five for point j . Since the mathematical model is evaluated in the complex domain and not in the phase domain, quality estimates per partition are required for the real and imaginary components of the complex phasor P_{ij}^{md} . These values are first estimated for the single-difference phasors P_i^{md} and P_j^{md} , using Eq. (A.5) at p. 178, based on the median and MAD of the amplitude time series per partition. Consequently, the corresponding double-difference values are obtained via error propagation using Eq. (A.9) at p. 179. In Appendix A we elaborate on how the stochastic model in the complex domain should be constructed.

Merging the partitions of both points yields a total of eight partitions. For each partition, we estimate the mean amplitude and three geometric displacement parameters: a_p , b_p , and c_p . We account for a coherent displacement signal by imposing continuity conditions between consecutive partitions as defined by Eq. (3.10).

We estimate the unknown parameters by solving the model defined by Eqs. (3.15) and (3.16). Consequently, the adjusted observables, i.e., \hat{R}_{ij} and \hat{I}_{ij} , are computed, shown by the purple line in Figs. 3.4a and 3.4b. We also evaluated the model in the phase domain, resulting in the adjusted absolute phase $\hat{\varphi}_{ij}^{md}$, and the ambiguities, as shown by the purple line in Fig. 3.4c. The blue dots represent the wrapped phase observations $\varphi_{ij}^{w,md}$ and the red dots the implicitly unwrapped phase observations φ_{ij}^{md} .

The estimation resulted in a relative thermal expansion factor of 0.43 ± 0.02 mm/K and relative cross-range distance of 25.1 ± 1.6 m, where the second number indicates the standard deviation. We also visualized these two phase components in Figs. 3.4d and 3.4e, respectively, plotting the observed wrapped phase $\varphi_{ij}^{w,md}$ shown in blue versus the thermal and perpendicular baselines, respectively. The estimates for the thermal phase $\hat{\varphi}_{ij,\eta}^{md}$ and cross-range phase $\hat{\varphi}_{ij,h_{xr}}^{md}$ are shown by the purple lines.

Since the estimated parametric non-thermal displacement phase, $\hat{\varphi}_{ij,d_{nt}}^{md}$, is often not physically interpretable, and might not contain the full displacement behavior of the arc, we correct the absolute DD phase values for the thermal and cross-range phases, i.e., $\hat{\varphi}_{ij,\eta}^{md}$ and $\hat{\varphi}_{ij,h_{xr}}^{md}$ respectively, as shown in Fig. 3.4f, using Eq. 3.22. The red dots represent the absolute reduced phase observation and the purple line shows the evaluated displacement model $\hat{\varphi}_{ij,d_{nt}}^{md}$, which includes the effects of partitioning. It can be seen that the seasonal behavior for the arc is reduced when the phases are corrected for the two components. This becomes especially clear when we compare the red dots of c) and f), where the seasonal pattern became less, as the thermal displacement phase (that has a seasonal behavior) has been removed.

⁹Note that the detection of partitions typically requires the definition of specific criteria. In our case, we applied a method that identifies partitions based on changes in the behavior of the mean and standard deviation values. The choice of thresholds, however, will be application-dependent.

3.7. DISCUSSION

At first glance, the displacement model using partition-wise polynomials in Fig. 3.4 may appear to overfit the data. However, the method is i) less restrictive than imposing a single linear velocity model across all arcs, which in itself represents a very strong smoothness constraint, but is still commonly applied, and ii) inherently arc-specific, as the partitioning is driven by the amplitude behavior of the scatterers.

It is difficult, if not impossible, to claim whether the proposed model performs better or worse than alternative models because the ground truth is unknown. Ideally, if the physical or kinematic behavior for the arc is known, models based on known external physical parameters should be used. However, in the built environment, such information is often incomplete or unavailable.

Indeed, if the goal is to fully capture differences in dynamic behavior between arcs in a flexible manner, dynamic linear models, such as the instantaneous-state InSAR approach [202], may provide a more suitable framework than the method proposed here. However, as already discussed in the introduction, the focus of this chapter is on a batch-processing approach, in which a fixed and given set of SAR data is used to estimate a predefined set of time-invariant parameters. Consequently, the objective is not to perform sequential estimation over time, even though such approaches may yield improved performance. For such methods, we refer to Wang *et al.* [202].

As previously mentioned, the parametric polynomial model per partition is not necessarily physical interpretable. However this is also not the intention. Once the estimated thermal and cross-range phase components are removed from the unwrapped phase time series, the remaining signal primarily contains displacement and noise. These corrected time series can then be used for further analysis and used for a displacement interpretation.

3.8. CONCLUSIONS

The fundamental problem of parameter estimation from InSAR time series is that both the functional models and the stochastic model are unknown and different for each scatterer. Conventionally, the same functional model is chosen for all points in the area of interest, often relying on a simple linear velocity model to parameterize the displacements. In this chapter, an arc-specific functional model for double-difference phase observations is proposed, in which the parameterization is driven by the temporal amplitude behavior of the two scatterers. Therefore, even when no prior knowledge about the underlying physical or kinematic behavior is available, the approach still allows for an arc-specific functional model.

In addition to the displacement signal, we propose to estimate the relative cross-range, rather than the conventionally estimated relative height, together with the thermal phase. After estimating these components, their corresponding phase signals can be removed from the double-difference phase observations, resulting in reduced phase observations that primarily contain the displacement signal. These reduced phase time series may later be used by end users for further interpretation and analysis of the physical behavior of individual scatterers.

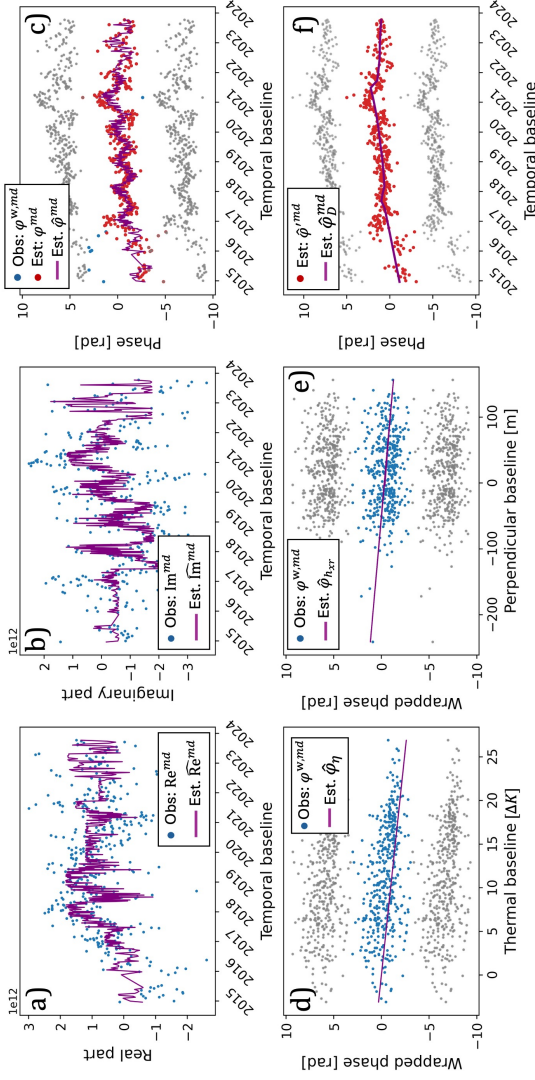


Figure 3.4: Observations (in blue) and estimates (in purple) for the arc represented in Fig. 3.3. a) and b) show the observed and estimated real and imaginary parts of the DD phasor. In c) the wrapped DD phase is shown in blue, the implicitly unwrapped DD phase values, φ_{ij}^{md} , are shown in red and the evaluated model in the phase domain in purple. It can be seen that for some epochs in 2015, one ambiguity level was estimated. In d) and e) we show the phase observations versus the thermal and perpendicular baselines respectively, together with the estimated phase components, φ_{ij}^{md} and $\varphi_{ij,h,xt}^{md}$ respectively. Consequently, we reduce the phase for the static components to obtain $\hat{\varphi}'_{ij, D}^{md}$, see Eq. (3.22), and we visualized the values in f) together with the values $\hat{\varphi}_{ij, D}^{md}$.

4

FUNDAMENTALS OF THE SPATIAL NETWORK

InSAR parameter estimation problems involve connecting a spatially distributed set of points using a spatial network of arcs. In this Chapter we investigate whether the way this network is constructed matters and whether applying ‘closed loops’ introduce redundancy or lead to additional constraints. We show that adjustment in the observation space is neither possible nor meaningful, as phase observations close by definition. Instead, the network adjustment should be performed in the parameter space, where arcs can have different functional and stochastic models. As a result, the precision of the estimated point parameters can be improved through an optimal network design. Finally, we distinguish between implicit and explicit phase unwrapping, stressing that explicit unwrapping should be avoided as it assumes that the ambiguities can be resolved independent of the parameter estimation. In reality the absolute, i.e., unwrapped, phase follows implicitly during the estimation of the unknown parameters and, consequently, is a stochastic variate.

4.1. INTRODUCTION

CONVENTIONAL InSAR parameter estimation problems involve connecting a spatially distributed set of points—whether these are scatterers, pixels, or clustered groups of pixels—using a spatial network of arcs. As there are many ways to connect the points, also known as the *network topology*, there are several standing questions related to this problem in the context of InSAR. **Does the way the network is constructed matter, and if so, is it a problem that admits an optimum configuration?** Moreover, **does applying ‘closed loops’ introduce redundancy, or is this redundancy artificial—and can it lead to additional constraints in the parameter estimation problem?** Finally, **what role do the integer phase ambiguities play in this context?** Below, we provide a fundamental discussion and evaluation on these questions, starting with defining the basic concepts and formulating the relevant questions. Subsequently, we discuss the possibilities of adjustment either in the observation space or in the parameter space. We end with conclusions that serve as a point of reference for future studies.

4

4.2. DEFINITIONS AND STANDING QUESTIONS

The fundamental observable in the context of InSAR is a complex signal of a single SAR scatterer from which single differences, i.e., temporal phase differences denoted $\{\phi \mid -\pi \leq \phi < \pi, \phi \in \mathbb{R}\}$, between two epochs can be extracted. However, the first physically interpretable variable is the *relative* double-differenced (DD) phase [82], denoted by $\{\varphi^w \mid -\pi \leq \varphi^w < \pi, \varphi^w \in \mathbb{R}\}$, which we define for an arc and is the phase difference between two points. Note that this *relative* phase is modulo- 2π (wrapped) hence the superscript ^w.

ARC PARAMETER ESTIMATION

As multiple components of the parameter vector x (i.e., the cross-range position, the thermal expansion factor, displacement parameters, atmospheric delay) contribute to the observed DD phase, we estimate *relative arc parameters*, \hat{x} from the DD phase observation, we refer to this process as **arc parameter estimation**. This requires a (linearized) mathematical model for an arc, consisting of

$$E\{\underline{\varphi}^w\} = Ax \quad ; \quad D\{\underline{\varphi}^w\} = Q_{\varphi^w}, \quad (4.1)$$

where A is the design matrix describing the relation between the observed DD phases and the unknown parameters x , and Q_{φ} the variance-covariance matrix (VCM) describing the quality of DD phases.¹ There are many options to define the functional model, depending on the application at hand, which results in different parameterizations; see also Chapter 3. Moreover, it is important to note that if no integer phase ambiguities would be included in the model of Eq. (4.1), evaluating the forward model would result in an *absolute* phase, instead of a wrapped phase.

¹Note that as long as we consider high-amplitude scatterers, we assume that the distribution of the phases is ‘peaked’ and can be assumed to be Gaussian, even though the wrapped nature of the observables prohibits values smaller than $-\pi$ and greater than $+\pi$.

Thus, for Eq. (4.1) to hold, corrective integer ambiguities would need to be added to the equation to convert the absolute phase back to the principal $[-\pi, +\pi]$ interval, see Eq. 3.2.

IMPLICIT AND EXPLICIT UNWRAPPING

As the observed relative phase $\varphi^w \in [-\pi, +\pi] \in \mathbb{R}$ is ‘wrapped’, we need to *estimate* integer phase ambiguities to arrive at the *absolute* phase, $\varphi \in \mathbb{R}$, a procedure termed ‘phase ambiguity resolution’ [175–177], or ‘phase unwrapping’ [72, 73], which can be implicit or explicit.

Traditionally, InSAR has approached phase unwrapping (integer ambiguity resolution) as an independent step—a problem to be resolved *prior* to carrying out the actual parameter estimation on the real-valued (unwrapped) estimates [72, 73]. We refer to this traditional approach as **explicit unwrapping**. The consequence of this philosophy is that phase-unwrapping errors and blunders propagate undetected, are not included in the stochastic model, and are used as input for the parameter estimation. Consequently, they directly affect the quality of the estimated parameters, in a (non-linear) way that cannot be captured in the stochastic model of the estimated parameters.

With **implicit unwrapping**, we try to avoid this dependency on a phase unwrapping algorithm and its underlying assumptions, as we don’t consider the phase unwrapping as a separate process, independent of and preceding the actual parameter estimation. Instead, we consider the parameter estimation problem as a process applied on the parameters of interest as well as the (nuisance) ambiguity parameters, directly applied on the original complex (hence wrapped) observables [100, 178]. Thus, the integer ambiguities follow implicitly as a consequence of the parameter estimation, but are not a goal in itself. The consequence is that irrespective of the fact that the ambiguities are integer in nature, they are unknowns, similar to all other parameters. As the other unknown parameters are only defined for an arc, this also holds for the integer ambiguities (hence, the absolute phase): we only have them for arcs, not for points.

THE NETWORK

To enhance interpretability and enable standard map visualizations, relative parameters per point are typically expressed relative to one common datum. This can be regarded as a ‘star-network’, where every point is connected by an arc to the common reference point, i.e., the datum. This transformation from individual single-arcs to datum-connected parameters is achieved by **designing and adjusting a connected network** that consists of arc variates. This network suggests also the possibility to impose conditions such as the requirement that variates over a triangle in a network, see e.g., Fig. 4.1a, should ‘close’, i.e., the sum of the variate over three arcs should be equal to zero. Yet, we will argue that this condition does not necessarily apply for all variates. In fact, we distinguish closure ‘by-definition’ and ‘conditional’ closure, where the latter involves external contextual information, which can be used as a constraint, while the former is a tautology and trivial.

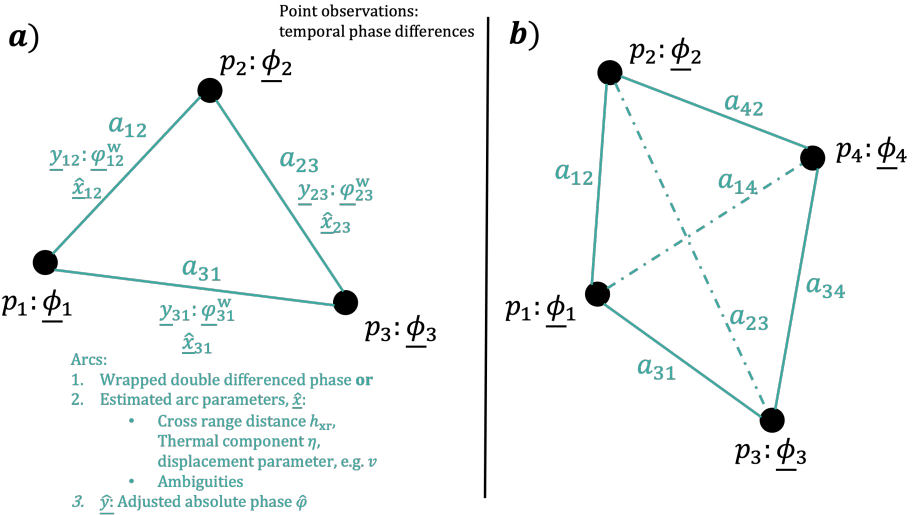


Figure 4.1.: a) shows the most simple network consisting of three points (in black) and three arcs (in green). With InSAR we *observe* temporal phase differences for points, ϕ , and we can *derive* DD (wrapped) phases for the arcs, φ . From these DD phases we estimate relative unknown parameters \hat{x} along these arcs. In b) we show a more complicated network consisting of more points and more arcs.

For a network consisting of three arcs and three points, see Fig. 4.1a, the DD relative phase values are *derived* from the observables per point, i.e.,

$$\begin{aligned}\underline{\varphi}_{12}^{2w} &= \underline{\varphi}_2^w - \underline{\varphi}_1^w \\ \underline{\varphi}_{23}^{2w} &= \underline{\varphi}_3^w - \underline{\varphi}_2^w \\ \underline{\varphi}_{31}^{2w} &= \underline{\varphi}_1^w - \underline{\varphi}_3^w,\end{aligned}\tag{4.2}$$

where we use the superscript 2w to indicate that the value of the parameter resides in the interval $[-2\pi, +2\pi)$. However, as illustrated in Fig. 4.1a, each arc is not only associated with the relative DD phase (a derived observable), but also with estimated arc parameters, including the integer phase ambiguities. Consequently, there are two potential ‘flavors’ of network adjustment: in the measurement space (\underline{y}) or in the parameter space (\hat{x}), each potentially with its own set of conditions. More generically, we may also define larger networks, as schematized in Fig. 4.1b, consisting of more points and more arcs.

STANDING QUESTIONS

Based on the definitions provided above, we identify six standing questions that need further consideration.

1. Does the network topology, i.e., the choice of the arcs that connect points, affect the estimated point parameters and/or their quality?

2. Does it matter which variates we use for the network adjustment, i.e., whether we adjust in the measurement space (the relative DD phase) or in the parameter space (the estimated parameters)? If so, which is preferred, and why?
3. Is there a difference between *implicit* and *explicit* unwrapping, and what are the implications of this distinction for the network adjustment and estimation process?
4. Can (and should) constraints be imposed on the network? For example, should the arc variates necessarily sum to zero over closed² loops? And does this requirement depend on the variate being adjusted?
5. Should all arc parameters within an InSAR network be estimated using identical functional and stochastic models, as commonly assumed in conventional InSAR approaches, or should each arc be assigned its own arc-specific model? If the latter, how would such an approach affect the network adjustment process and the precision of the estimated point parameters?
6. Is there added value in including additional arcs once all points are already connected? In other words, does adding more arcs contribute new information, or is it redundant once the network is fully connected?
7. Can the precision of the estimated point parameters be improved by increasing the number of arcs in the network?

Below, we evaluate these questions by discussing the options we have for the network adjustment, focusing on the situation of ‘single scatterers’.

4.3. ADJUSTING THE NETWORK IN THE MEASUREMENT SPACE

The first option would be to adjust the network in the measurement space, i.e., on the derived DD phase. From Eq. (4.2) it follows that

$$\varphi_{12}^{2w} + \varphi_{23}^{2w} + \varphi_{31}^{2w} = (\phi_2^w - \phi_1^w) + (\phi_3^w - \phi_2^w) + (\phi_1^w - \phi_3^w) = 0 \quad (4.3)$$

by definition, since the realization of the stochastic observables—which are deterministic ‘numbers’—appear twice with opposite signs in the loop. Adding more arcs see Fig. 4.1b, when all points are already connected—e.g., adding the dashed arcs a_{14} and a_{23} —adds no more information, since all points are already connected: all ‘information’ is already used in the network. Consequently, it would just be sufficient to create a star network where points are directly connected to one point. From this we conclude that

- i. the relative phase observations close *by definition* in a triangle, and

²Note that in this discussion, the ‘closure’ (whether it is by definition or as an imposed condition) is primarily considered on point scatterers, and not on distributed scatterers. Therefore, it does not consider the well-documented problem of ‘phase-closure’ and ‘phase-triangulation’ that occurs in distributed scatterers, which can be related to a physical process [5, 44].

- ii. adding more arcs to the network does **not** add redundancy, hence it serves no purpose: a_{31} can be inferred directly from a_{12} and a_{23} . Thus, once all points are connected, adding additional arcs does not contribute additional information. Therefore,
- iii. adjusting the network in the observation space is neither possible nor meaningful.

4.4. ADJUSTING THE NETWORK IN THE PARAMETER SPACE

As adjusting the network in the measurement space is neither possible nor meaningful, as loop closure occurs by definition, the alternative is an adjustment in the parameter space. Arc parameter estimation must first be performed to obtain \hat{x} , i.e., the physical parameters such as cross-range distance h_{xr} , thermal expansion factor η , displacement parameters δ_{displ} (such as, e.g., the constant velocity v) and the vector of integer ambiguities a . Subsequently, the adjusted phase $\hat{\phi}$ can be computed by evaluating the forward model on the estimated parameters. If the estimated integer ambiguities would be left out of this evaluation of the forward model, this would result in the adjusted *absolute* phase. The network adjustment can then be applied to these estimates. The question is whether the closure condition applies to the estimated parameters, and whether this is *by definition* or as an *imposed constraint*. In the latter case, it can be considered as new information to be added to the problem.

As estimating arc parameters requires both a functional and stochastic model **per arc**, see Eq. (4.1), the choice of these models directly affects both the estimated parameters—i.e., the number of parameters, their nature, and their numerical value—as well as their precision, see also Eq. (5.2), p. 70. This raises the question whether—and if so, how—variations in the functional or stochastic model across arcs affect the conditions that can be imposed in the network.

To investigate this question, we consider two options for the **functional model** across arcs. The first option considers a **uniform parameterization** across all arcs, i.e., all arcs share the same parameter space (e.g., linear velocity, cross-range, thermal expansion factor), ensuring consistent parameterization across the network. While this option is often used in InSAR parameter estimation algorithms, as it provides a pragmatic and uniform approach for all points in the area of interest, it is physically unrealistic to assume that the motion of all points within the AoI can be described with the same model. This is especially unrealistic in the built environment. Instead, this uniform parameterization option can be considered as a special case of the more generic second option, the **arc-specific parameterization**. In a generic setting, each arc should have its own unique functional model, leading to arc-specific parameters and varying parameter spaces across the network.

Likewise, we distinguish three options for the **stochastic model**. The first option considers an **identical stochastic model for all arcs**, i.e., each arc is assigned the same stochastic model, i.e., $Q_{a_{12}} = Q_{a_{23}} = Q_{a_{31}}$. This is a common (though simplistic) assumption, especially when the stochastic model is unknown or not incorporated in the parameter estimation—i.e., when quality is only estimated a posteriori. However,

for the lack of other options, this is what is usually done. The second option is more generic and considers **linearly dependent stochastic models**. In this case, the stochastic models differ per arc, but are linearly dependent on each other, i.e., they span the same linear subspace: i.e.,

$$Q_{a_{12}} = \lambda_1 Q_{a_{23}} = \lambda_2 Q_{a_{31}}, \text{ i.e., } Q_{a_{12}} \propto Q_{a_{23}} \propto Q_{a_{31}}. \quad (4.4)$$

The third and most generic—hence most realistic—option considers **arc-specific stochastic models**, where each scatterer exhibits its own unique scattering behavior, which may also vary over time (as discussed in Chapter 2). Since the stochastic model is defined per arc, capturing the behavior of both scatterers, the resulting Q_{yy} matrices are not linearly dependent, i.e.,

$$Q_{a_{12}} \neq \lambda_1 Q_{a_{23}} \neq \lambda_2 Q_{a_{31}}, \text{ i.e., } Q_{a_{12}} \not\propto Q_{a_{23}} \not\propto Q_{a_{31}}. \quad (4.5)$$

Given these different options for the functional and stochastic model per arc, we can now examine their effect on whether the realizations \hat{x} of the estimated parameters ‘close’ (conditionally or by-definition) within a loop. This leads to six possible combinations, as summarized in Table 4.1. This shows that the “closure condition” for the parameters is only valid for the special case where the functional model has (i) a uniform parameterization, *and* (ii) the stochastic model for each

Table 4.1: Combinations between different functional and stochastic models and the implications on whether \hat{x} and \hat{y} close conditional or by-definition in a triangle. $A_{a_{i,j}}$ refers to the design matrix, i.e., the functional model. $Q_{a_{i,j}}$ refers to the variance-covariance matrix, i.e., the stochastic model. $\varphi_{a_{i,j}}^{2w}$ represents the observations, i.e., the realizations of the wrapped interferometric DD phase observables for the arc between points i and j , \hat{x} represents the vector of estimated parameters, and \hat{y} represents the adjusted observables, with $\hat{y} = A\hat{x}$. Loops indicated in black close ‘by-definition’, while loops indicated in red close ‘conditional’.

		Functional model	
		$A_{a_{12}} = A_{a_{23}} = A_{a_{31}}$	$A_{a_{12}} = A_{a_{23}} \neq A_{a_{31}}$
Stochastic model	$Q_{a_{12}} = Q_{a_{23}} = Q_{a_{31}}$ $\sigma_{a_{12}} I = \sigma_{a_{23}} I = \sigma_{a_{31}} I$	$\varphi_{a_{12}}^{2w} + \varphi_{a_{23}}^{2w} + \varphi_{a_{31}}^{2w} = 0$ $\hat{x}_{a_{12}} + \hat{x}_{a_{23}} + \hat{x}_{a_{31}} = 0$ $\hat{y}_{a_{12}} + \hat{y}_{a_{23}} + \hat{y}_{a_{31}} = 0$	$\varphi_{a_{12}}^{2w} + \varphi_{a_{23}}^{2w} + \varphi_{a_{31}}^{2w} = 0$ $\hat{x}_{a_{12}} + \hat{x}_{a_{23}} + \hat{x}_{a_{31}} \neq 0$ $\hat{y}_{a_{12}} + \hat{y}_{a_{23}} + \hat{y}_{a_{31}} \neq 0$
	$Q_{a_{12}} \propto Q_{a_{23}} \propto Q_{a_{31}}$ $Q_{a_{12}} = \lambda_1 Q_{a_{23}} = \lambda_2 Q_{a_{31}}$	Simulation 1: $\varphi_{a_{12}}^{2w} + \varphi_{a_{23}}^{2w} + \varphi_{a_{31}}^{2w} = 0$ $\hat{x}_{a_{12}} + \hat{x}_{a_{23}} + \hat{x}_{a_{31}} = 0$ $\hat{y}_{a_{12}} + \hat{y}_{a_{23}} + \hat{y}_{a_{31}} = 0$	$\varphi_{a_{12}}^{2w} + \varphi_{a_{23}}^{2w} + \varphi_{a_{31}}^{2w} = 0$ $\hat{x}_{a_{12}} + \hat{x}_{a_{23}} + \hat{x}_{a_{31}} \neq 0$ $\hat{y}_{a_{12}} + \hat{y}_{a_{23}} + \hat{y}_{a_{31}} \neq 0$
	$Q_{a_{12}} \propto Q_{a_{23}} \not\propto Q_{a_{31}}$ $Q_{a_{12}} = \lambda_1 Q_{a_{23}} \neq \lambda_2 Q_{a_{31}}$	Simulation 2: $\varphi_{a_{12}}^{2w} + \varphi_{a_{23}}^{2w} + \varphi_{a_{31}}^{2w} = 0$ $\hat{x}_{a_{12}} + \hat{x}_{a_{23}} + \hat{x}_{a_{31}} \neq 0$ $\hat{y}_{a_{12}} + \hat{y}_{a_{23}} + \hat{y}_{a_{31}} \neq 0$	Generic situation: $\varphi_{a_{12}}^{2w} + \varphi_{a_{23}}^{2w} + \varphi_{a_{31}}^{2w} = 0$ $\hat{x}_{a_{12}} + \hat{x}_{a_{23}} + \hat{x}_{a_{31}} \neq 0$ $\hat{y}_{a_{12}} + \hat{y}_{a_{23}} + \hat{y}_{a_{31}} \neq 0$

point spans the same linear subspace, evaluated in simulation 1 below. The case in which every stochastic model is identical is a specific case of the latter.

In the following section we use simulations to examine the effect on whether \hat{x} closes for two of these six combinations of the stochastic and functional models.

SIMULATION 1: UNIFORM PARAMETERIZATION AND LINEAR DEPENDENT STOCHASTIC MODELS

We simulate phase time series of 200 epochs for three points, where the total phase is composed of four components: a cross-range distance phase, a thermal displacement phase, a constant velocity displacement phase, and noise. The true simulated values for the points are listed in Tab. 4.2, and the resulting time series are shown in Figs. 4.2a–c. Each of the three points is assigned a unique noise level, which is constant over time. Therefore, the corresponding Q_y matrices can be written as $\sigma^2 \mathbf{I}_{200}$, and are linearly dependent. From the simulated point values, we derive arc phases using Eq. (4.2), which are shown in Figs. 4.2d–f. Additionally, we simulate a quadratic displacement component for point 1. As a result, this term appears in both a_{12} and a_{31} , but with opposite sign.

For the arc parameter estimation, we use the same functional model for each arc, consisting of a cross-range distance h_{xr} , thermal expansion factor η , and constant velocity v . Therefore, for arcs a_{12} and a_{31} , the model estimates are in fact biased, as the underlying signal includes an additional quadratic term. However, since this term appears with opposite sign in each of these two arcs, it cancels out when combined. Each of the three arcs is assigned a different stochastic model, whose diagonals are plotted in Fig. 4.2g. Although the models differ, they are linearly dependent as they are all a scaling of the identity matrix.

In Fig. 4.2h, we show the estimated arc parameters \hat{x} . It can be seen that the sum of the estimated parameters over the three arcs is zero for each component, i.e., $\hat{x}_{12} + \hat{x}_{23} + \hat{x}_{31} = 0$, by definition. Consequently, we can estimate \hat{y} for each arc shown by the black lines in Figs. 4.2d–f. When summing the estimated phases over the three arcs, we again find that they sum to zero, as shown in Fig. 4.2h.

We can thus conclude that, if the parameter space for all arcs in the network is the same, and if the stochastic models are linearly dependent, then, the sum of the estimated parameters \hat{x} will indeed be zero for a loop in a network. This holds for both the physical parameters and for the absolute phase. It does not matter whether the chosen functional model is the most suitable functional model, as non-modeled

Table 4.2.: Simulated parameter values for each point p_i in the network, which results in relative arc values, a_{ij} .

Parameter	p_1	p_2	p_3	a_{12}	a_{23}	a_{31}
h_{xr}	−10	15	20	25	5	−30
v	0.5	0.7	0.2	−0.2	0.5	−0.3
η	0.03	−0.03	0.05	0.00	−0.08	0.02

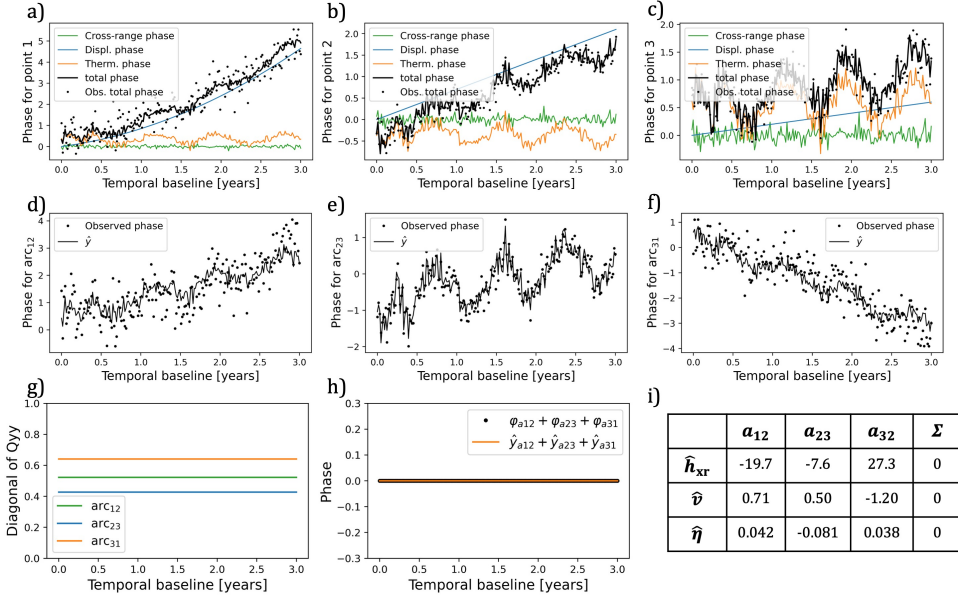


Figure 4.2.: Simulated phase behavior for three points shown in a), b), and c), based on a linear velocity (blue), thermal displacement (orange) and cross-range distance (green), leading to the combined ‘total phase’. All three points have their own noise level, shown as the scatter around the observed total phase. d), e), and f) show the derived absolute phase timeseries for the three arcs, leading to the estimated relative arc parameters $\hat{\mathbf{x}}$ are shown in i). The black lines in d)–f) are the adjusted arc observations $\hat{\mathbf{y}}$, derived from the estimated parameters via $\hat{\mathbf{y}} = \mathbf{A}\hat{\mathbf{x}}$. g) shows the diagonals of the three Q_{φ^w} matrices, for each arc, and h) shows the sum of the simulated arc observables and the adjusted observations. It can be seen that, since we used the same parameterization for the three arcs, and since the three Q_{φ^w} matrices are linearly dependent, the sum of the estimated parameters $\hat{\mathbf{x}}$ is zero, and consequently, the sum of $\hat{\mathbf{y}}$ over the three arcs is also zero, cf. Table 4.1, under ‘Simulation-1’. Thus, both the estimated parameters $\hat{\mathbf{x}}$ and the adjusted observations $\hat{\mathbf{y}}$ ‘close’ over a loop.

terms have different signs in the two affected arcs.

If all arcs share the same functional model and have linearly dependent stochastic models, such that the estimated parameters close, then adding more arcs, once all points in the network are already connected, does not provide any additional information. This would, for instance, be the case for the dashed arcs in Fig. 4.1b. In other words, when parameters are estimated based on identical models, it is sufficient for each point to be connected only once in order to capture all the available information correctly.

SIMULATION 2: UNIFORM PARAMETERIZATION AND ARC-SPECIFIC STOCHASTIC MODELS

4

The situation simulated above can be considered as a specific subset of cases of a more generic set of cases where each scatterer, and thus each point in the network, has its own time-varying stochastic model, see also Chapter 2 of this thesis. Given the physical nature of scatterers in the real world, with a plethora of various situations—in particular in the built environment—we introduce a time-partitioned noise model for point 2. This case is simulated in Fig. 4.3. Consequently, also the stochastic models of arcs a_{12} and a_{23} become partitioned, and the three stochastic models are no longer linearly dependent, i.e., $Q_{a_{12}} \propto Q_{a_{23}} \not\propto Q_{a_{31}}$, see Fig. 4.3g. When estimating the unknown parameters for the three arcs, their sum is no longer equal to zero, see Fig. 4.3i. For example, the velocity estimates are $\hat{v}_{12} = 0.669$, $\hat{v}_{23} = 0.486$, and $\hat{v}_{31} = -1.204$, resulting in a sum of -0.05 . Consequently, also the sum of \hat{y} over the three arcs deviates from zero (see Fig. 4.3h). This deviation arises from both measurement noise and unmodeled signal components leaking into the estimated parameters. Since the stochastic models are no longer linearly dependent—as is typical in real-world scenarios—this leakage is distributed unevenly across the three arcs.

Nevertheless, a network adjustment can still be performed on the estimated parameters, since we also obtain the corresponding $Q_{\hat{x}}$ matrices, which differ per arc. The use of distinct stochastic models per arc implies that each arc contributes new and unique information and is no longer maximally correlated with the other arcs in the network, as was the case in scenario 1. Therefore, as illustrated in Fig. 4.1b, adding arcs—even when all points are already connected—does indeed provide additional information, leading to more precise estimates of the point parameters within the network. Moreover, since the $Q_{\hat{x}}$ matrices differ across arcs, this implies that, in terms of precision, there exists an optimal network configuration.

4.4.1. ARC-SPECIFIC PARAMETERIZATION AND ARC-SPECIFIC STOCHASTIC MODELS

In reality, not only the stochastic models will be different for each point, and consequently differ between arcs, but the functional models may vary as well, as each scatterer may exhibit its own unique kinematic behavior, i.e., the situation in the lower right corner of Table 4.1. For example, a house, a road, a railway, and a park will behave according to different driving mechanisms, even though they may

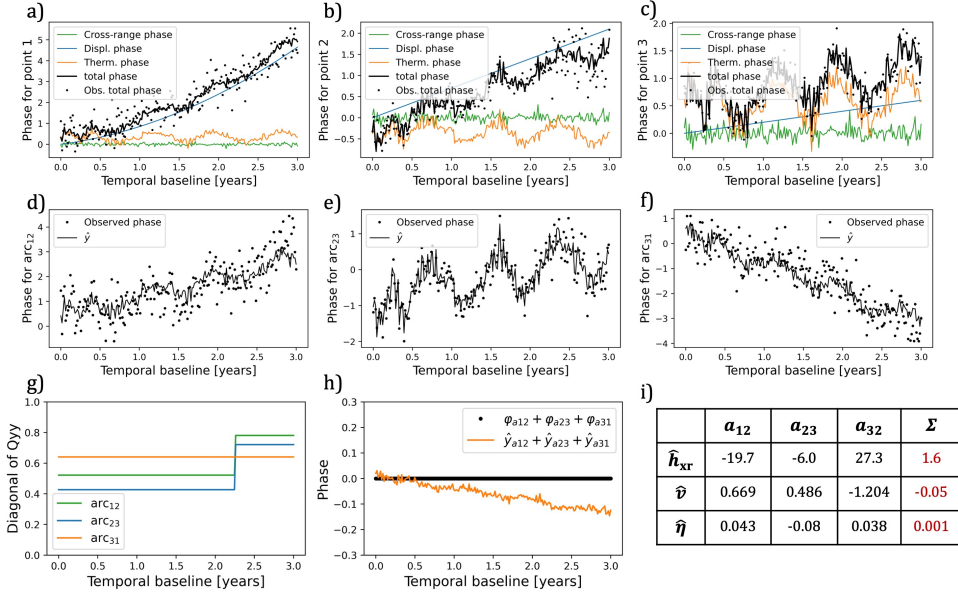


Figure 4.3.: Simulated phase behavior for three points shown in a), b), and c), based on a linear velocity (blue), thermal expansion factor (orange) and cross-range distance (green), leading to the combined ‘total phase’. All three points have their own noise level, shown as the scatter around the observed total phase, where the noise level of point 2 (b) is larger during the last part of the time series. d), e), and f) show the derived absolute phase timeseries for the three arcs, leading to the estimated relative arc parameters \hat{x} are shown in i). The black lines in d)–f) are the adjusted arc observations \hat{y} , derived from the estimated parameters via $\hat{y} = A\hat{x}$. g) shows the diagonals of the three Q_{φ^w} matrices, for each arc, and h) shows the sum of the simulated arc observables and the adjusted observations. It can be seen that the three VCM matrices are no longer linearly dependent on each other. Therefore, the sum of the estimated parameters \hat{x} is not equal to zero, and consequently, the sum of \hat{y} over the three arcs is also not zero anymore, cf. Table 4.1, under ‘Simulation-2’. Thus, both the estimated parameters \hat{x} and the adjusted observations \hat{y} do not ‘close’ over a loop.

be situated directly adjacent to each other in the neighborhood. In such cases, with different parameterizations, the parameter space differs across arcs. Nonetheless, it is still possible to adjust the network based on the shared unknown parameters and the reduced phase, as defined in Eq. (3.22), p. 45, where the reduced absolute phase is also an estimate. In this case, adding new arcs to the network adds new information to the network, and the estimated parameters become more precise once more arcs are added to the network.

4.5. CONCLUSIONS

Based on the analysis and simulations above we draw conclusions and referring back to the open questions posed in Sec. 4.2.

1. Does the network topology, i.e., the choice of the arcs that connect points, affect the estimated point parameters and/or their quality?
2. Does it matter which variates we use for the network adjustment, i.e., whether we adjust in the measurement space (the relative DD phase) or in the parameter space (the estimated parameters)? If so, which is preferred, and why?

Whether the network topology affects the estimated point parameters and/or their quality depends on the variates used. Adjusting the network in the observation space is neither possible nor meaningful as the phase observations close by definition, and therefore the network topology is irrelevant. Adjustment in the parameter space can be advantageous—i.e., leading to different values for the estimates and better quality—in a generic sense, but not always. In a generic sense, assuming that the functional model of each arc can be different, the parameters estimated for each arc will be different as well. Moreover, also the stochastic model can (and often will) be significantly different³ for each arc. In those cases, the network topology matters, i.e., not every network topology will produce the same results, and therefore optimization will be possible, as we will discuss in Chapter 5. Only in the special case when (i) the parameter space spanned by vector x is identical across all arcs and (ii) their stochastic models Q_φ span the same linear subspace, the estimated parameters will "close-by-definition" within a loop in the network. Thus, no new information is introduced into the system by evaluating the loop, and the network topology is irrelevant. Adjusting the network under the strict assumption of identical functional and stochastic models does not make optimal use of all available information. In such a scenario, adding new arcs no longer improves the solution, as no new information is gained. This makes it a suboptimal adjustment strategy.

3. Is there a difference between *implicit* and *explicit* unwrapping, and what are the implications of this distinction for the network adjustment and estimation process?

³In this context, 'significantly different' implies that the stochastic models for the arcs do not span the same linear subspace, see Eq. (4.4) in Sec. 4.4. In other words, the variance-covariance matrices of the arcs are not scaled versions of each other.

There is a clear difference between implicit and explicit unwrapping. Explicit unwrapping refers to the approach where phase ambiguities are resolved in an ‘independent’ separate step prior to the actual parameter estimation, and in implicit unwrapping the ambiguities are estimated (resolved) together with the other unknown parameters. Explicit phase unwrapping should be avoided, as it assumes that the integer phase ambiguities can be resolved with a 100% success rate, i.e., the ambiguity values are considered to be deterministic variates. In reality, the absolute, i.e., ‘unwrapped’, phase follows implicitly during the estimation of the unknown parameters and, consequently, it is a stochastic variate.

4. Should all arc parameters within an InSAR network be estimated using identical functional and stochastic models, as commonly assumed in conventional InSAR approaches, or should each arc be assigned its own arc-specific model? If the latter, how would such an approach affect the network adjustment process and the precision of the estimated point parameters?

We have shown that only in the case if the same functional models and stochastic models for different arcs are used, the estimated parameters will ‘close-by-definition’ within a loop in the network. Potentially unmodeled components in the functional model affect the estimated parameters for the corresponding arc. But as this unmodeled behavior will appear with alternating sign across the network, it will not affect the closure of the estimated parameters \hat{x} .

In a generic case, it is unrealistic to assume identical functional or stochastic models across arcs; each pair of points may require a unique parameterization and has its own stochastic characteristics. As a result, both \hat{x} and \hat{y} will *not* close over a loop. We can only use the ‘closure’ of \hat{x} and \hat{y} as a constraint in the adjustment. This also holds for the estimated ambiguities. As a result, adding arcs to the network may improve the estimated parameters for the points (even if no new point is added), since that way new independent information is introduced, leading to additional constraints. Note that, in the network adjustment, it is essential to account for the arc-specific covariance matrices $Q_{\hat{x}}$, as these differ between arcs.

Since each arc results in the estimation of a parameter vector with its own associated covariance matrix $Q_{\hat{x}}$, some network configurations are inherently better than others in terms of estimation precision if the goal is to estimate point parameters with the highest precision, as we will show in Chapter 5.

5. Can (and should) constraints be imposed on the network? For example, should the arc variates necessarily sum to zero over closed loops? And does this requirement depend on the variate being adjusted?
6. Is there added value in including additional arcs once all points are already connected? In other words, does adding more arcs contribute new information, or is it redundant once the network is fully connected?

Arc variates do not always necessarily sum to zero over closed loops. As discussed above, the answer to this question depends on which variates are used. When designing and adjusting the network based on the relative phase, i.e., in the

observation space, it will sum to zero ‘by-definition’, which implies that it cannot be used as a condition. For these variates, if all points are already connected by at least one arc, adding a new arc—without introducing a new point—does not contribute additional information, as no new information is added in the network. Yet, in the parameter space, in the case when functional models and stochastic models are different between arcs, adding arcs will influence the results, since they impose new loop closure conditions that can be used in the adjustment.

7. Can the precision of the estimated point parameters be improved by increasing the number of arcs in the network?

The precision of the estimated point parameters—i.e., relative to a common reference point—can be improved by optimizing the network design, as we will discuss in Chapter 5. Yet, this is not necessarily a matter of simply increasing the number of arcs. We will show that the improvement in precision can be reached by selecting arcs based on quality considerations.

5

NETWORK DESIGN FOR INSAR TIME SERIES ANALYSIS OF POINT SCATTERERS

To estimate data-connected parameters for points from arc observations, a connected spatial network of arcs must first be designed and adjusted. Since different network configurations appear to produce different outcomes, some networks are closer to optimal than others. This chapter introduces a Confidence-Optimized Geodetic Network design strategy tailored to application-specific requirements. Using the stochastic model introduced in Chapter 2, the expected quality of each potential arc is quantified and used to prioritize higher-quality arcs. This increases confidence in obtaining reliable parameter estimates. Based on these quality measures, we design a network that meets application-dependent criteria for precision and reliability without relying on purely geometric networks such as a Delaunay network. Rather than adjusting the network based on explicitly unwrapped phases, we perform the adjustment in parameter space, improving precision.

5.1. INTRODUCTION

INSAR observations are inherently relative: only displacement differences between two points, referred to as an arc, can be estimated [80]. However, to enhance interpretability, displacement estimates are preferably expressed relative to a common datum, often a reference point or the combination of a set of points. This datum connection requires the design of a network in which arcs connect points to the common reference. Adjusting the parameters in this network results in relative displacement estimates per point [36].

The simplest approach to establish a network is a star network, in which all points connect directly to the reference point. Yet, this method often produces errors for long arc connections, due to atmospheric phase delays [80, 102, 193]. Moreover, the star network lacks redundancy, which makes it impossible to test for model imperfections between arcs. This is particularly problematic as arc parameters, such as relative displacements or cross-range distances, must be estimated from wrapped *relative* double-difference (DD) phases, i.e., the spatial phase difference between two scatterers and the temporal phase difference relative to a reference epoch. Due to the presence of 2π phase ambiguities and the unknown functional model that relates these arc parameters to the DD phase, an infinite number of solutions exist.

To address this, a network with a higher connectivity,¹ i.e., more arcs compared to the number of points, is required [6], as this suggests that testing between estimated parameters is possible. In that case, point parameters are estimated within a specific network topology, which directly influences both their numerical values and associated precisions [102, 180, 194]. As different network configurations (i.e., the network topology) appear to have different outcomes, some networks are closer to optimal than others, and the challenge is to find the most "optimal" network. This would require optimality criteria [120].

In other geodetic techniques, such as triangulation and leveling, network design is typically performed prior to data acquisition, using predefined optimality criteria [156]. These are based both on e.g., the geometric strength of the network (for triangulation) and on the requirements of the quality of the results [112]. In the context of deformation monitoring, two key optimality criteria are commonly used: precision (how well the parameters of interest can be estimated) and reliability (whether outliers in the observations can be detected and eliminated) [6, 25, 74, 112, 165]. Ideally, similar criteria should be applied when designing and solving InSAR networks.

Many current point scatterer (PSI) processing algorithms rely on Delaunay or 'redundant' networks [37, 60, 61, 102, 144, 193]. Both are examples of geometrically optimized networks: they connect points (that are typically detected based on amplitude information) based on their spatial distribution—an irrelevant aspect for InSAR parameter estimation—without considering the quality of the arcs themselves. As such, they are inherently sub-optimal for displacement estimation, as they do not necessarily lead to the most precise and reliable estimates.

Ideally, we seek a network that yields point parameter estimates with the desired

¹In graph theory, *connectivity* refers to how well the vertices (nodes) of a graph are connected to each other. It's a measure of the graph's robustness or the minimum effort needed to disconnect it [48].

level of precision. Moreover, every InSAR case study is unique and comes with its own application-dependent quality criteria. For example, displacement estimates used for monitoring critical infrastructure might be subject to stricter quality constraints than estimates used for regional deformation mapping. This highlights the need for a quality-optimized and application-dependent network design strategy. We refer to this as a 'triple-A', or 'AAA' approach, which represents an approach that is 'application-aware and application-aligned'.

Such an InSAR-specific network design approach does not yet exist [120]. To design such a network, the quality of every potential arc must be known prior to the network design. Here we demonstrate that, by applying the stochastic-model proposed by Brouwer and Hanssen [20], see also Chapter 2, the expected quality of all arcs within the area of interest can be quantified before the network adjustment. These values enable the prioritization and selection of arcs that meet the application-specific requirements for precision and reliability.

An additional complication concerns the choice of the variate on which the network is adjusted. For each arc, the derived observable is the wrapped relative DD phase from which unknown parameters \hat{x} , including the cross-range distance and displacement parameters, can be estimated. As the absolute (unwrapped) phase follows implicitly as a consequence of the parameter estimation, it is also considered as an unknown parameter. Kampes [102] suggests adjusting the network directly on the physical arc parameters. While appealing, this strategy requires an identical functional model, i.e., the same parameters, for every arc. In practice, this is an assumption that cannot be sustained over wide-areas of complex environments. On the other hand, van Leijen [193] proposes to adjust and test the network on the integer ambiguity values, and estimate the physical parameters afterwards. However, as the integer ambiguities are also unknown parameters, and follow from the parameter estimation, this approach should be avoided. Adjusting and testing the network on the integer ambiguities cannot be treated as an independent and stand alone process.

Here we propose to use unique functional models for all arcs, and adjust the network on the shared parameters among arcs, e.g., the cross-range distance and thermal expansion factors. Consequently, we can estimate the phase that is reduced for the static components, i.e., the cross-range phase and thermal displacement phase, which we call the displacement phase (or reduced phase). This phase is estimated per epoch for each arc, see also Sec. 3.5 of this thesis, and we can thus adjust per epoch.

This chapter is organized as follows. First, we discuss the mathematical framework of the network adjustment in Sec. 5.2.1. From this, we can then deduce what an optimal InSAR network looks like and show that it ideally consists of three steps, see Sec. 5.2.2. These steps are discussed in detail in Secs. 5.3, 5.4, and 5.5. Then, we apply the proposed method to a test case in Amsterdam, with the results presented in Sec. 5.7. Finally, the conclusions are discussed in Sec. 5.9.

5.2. OVERVIEW AND PRINCIPLES FOR THE NETWORK

In this section, we first outline the mathematical concepts of a network and the procedure to estimate the parameters. In Sec. 5.2.2, we discuss how the network affects the estimated parameters and how it should be tuned to optimize the InSAR parameter estimation. Note that the remainder of this chapter builds upon the conclusions drawn in Chapter 4, where we discuss what conditions can be applied in the network adjustment, on what variates the network should be adjusted, and whether the design of the network affects the estimation of unknown parameters.

5.2.1. ESTIMATION, QUALITY, AND TESTING

A geodetic InSAR network consists of point scatterers (PS) or distributed scatterers (DS) connected by arcs, acting as vertices and edges in graph theory [85]. Since InSAR is a relative technique, only relative parameters, such as displacement, cross-range distance, and the thermal expansion factor, can be estimated from the Double-Differenced (DD) wrapped phase observations along individual arcs, preferably between points that are not too far apart. However, to enhance interpretability and enable standard map visualizations, these relative parameters are typically expressed per point, with long arcs relative to one common datum, or reference point. This transformation from individual short arcs to datum-connected parameters is achieved by adjusting a network that consists of arc parameters.

We can distinguish three main steps, also illustrated in the flowchart in Fig. 5.1. In **Step 1: Network design**, the configuration of the network is defined by selecting which points should be connected. **Step 2: Arc parameter estimation** focuses on estimating the relative parameters of the arcs in the network. This includes both the unknown parameters (e.g., the cross-range distance h_{xr} , thermal expansion factor η , and displacement parameters δ_{displ} ; see also Sec. 3.3) and the integer phase ambiguities a , we term this *implicit* phase unwrapping, see Chapter 4 for a detailed description. Various stochastic and functional models and estimation methods exist for this arc parameter estimation, see e.g. [60, 193, 200]. Here, the arc parameters are estimated using the models described in Chapters 2 and 3. Importantly, this step yields not only the parameter estimates, but also their associated uncertainties, represented by variance-covariance matrices. Subsequently, in **Step 3: Network adjustment**, the estimated arc parameters and their variance-covariance matrices serve as the arc variates, i.e., the ‘observations’. In this final step, the network is adjusted to estimate the relative parameters for the points relative to a chosen datum. Mathematically this is formulated as follows

$$E\{\underline{y}\} = Ax \quad ; \quad D\{\underline{y}\} = Q_y, \quad (5.1)$$

where \underline{y} is the vector of relative parameters for m arcs, x the vector of unknowns for n points and A the design matrix describing the relation between arcs and points. $E\{\cdot\}$ and $D\{\cdot\}$ denote the expectation and dispersion operators, respectively. The vector of arc parameters \underline{y} is a stochastic variable, assumed to follow a normal distribution.² Its precision is characterized by the stochastic model Q_y , which

²More exactly, the wrapped phase observation cannot have a normal distribution due to its limited

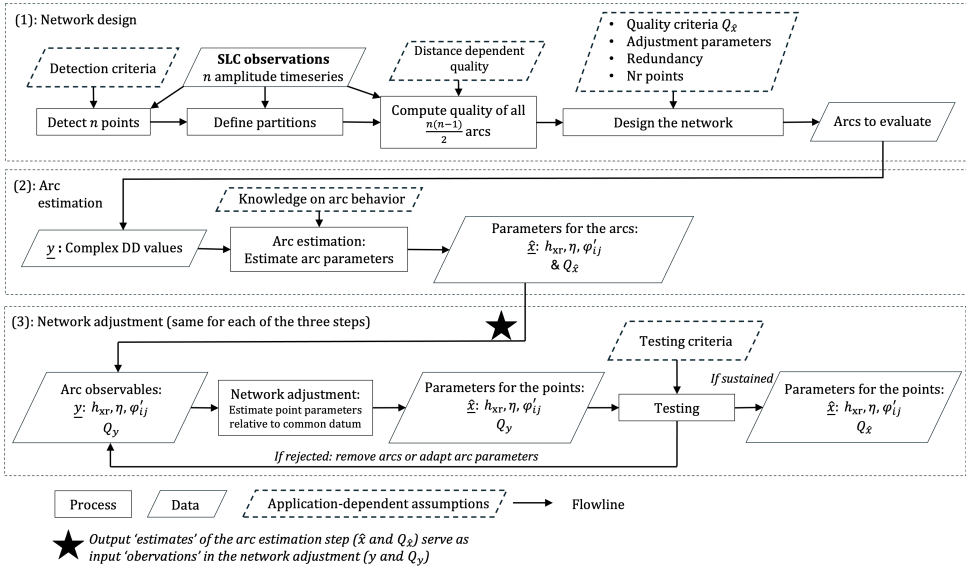


Figure 5.1.: A general overview of the network design and adjustment procedure. The initial network design is application-dependent, as the criteria for selecting arcs and points, as well as the required precision for point estimates, differ between applications. Once the network is constructed, the arc parameters are estimated in the arc estimation step, which are then used in the network adjustment. In this step, the estimated arc parameters form the y vector, and the relative point parameters are estimated. Afterwards we apply testing on the estimated parameters. Note that the network adjustment step applies to all three steps as will be discussed later in Secs. 5.3, 5.4, and 5.5.

contains the variances and covariances of the relative parameters derived in the preceding arc estimation step. The unknown parameters for the points, x , can be estimated using direct inversion or Best Linear Unbiased Estimation [180], i.e.,

$$\hat{x} = \begin{cases} A^{-1}\underline{y}, & \text{for } m = n, \text{ and} \\ Q_{\hat{x}}A^TQ_y^{-1}\underline{y} & \text{for } m > n, \text{ with} \end{cases} \quad (5.2)$$

$$Q_{\hat{x}} = \begin{cases} A^{-1}Q_y(A^{-1})^T, & \text{for } m = n, \text{ and} \\ N^{-1} & \text{for } m > n, \text{ with} \end{cases} \quad (5.3)$$

$$N = A^TQ_y^{-1}A, \quad (5.4)$$

where N is the normal matrix. If there are more arcs than points, i.e., $m > n$, the network needs to be *adjusted* [180].

It follows that the network configuration, defined by matrix A , has a direct influence on the estimation of the point parameters. Thus, modifying A by considering different arcs directly affects which points are included in the network and how well their relative parameters can be estimated. Furthermore, the quality of the estimated parameters, $Q_{\hat{x}}$, depends solely on the design matrix A , and the stochastic model Q_y , which together form the normal matrix N , and is independent on the actual arc parameters \underline{y} . As a result, the quality of the estimated parameters for the *points* can be assessed *a priori*, i.e., before any arc estimation or network adjustment is performed. Moreover, the condition number of the matrix N will give insight in how well the point parameters for the points in the network can be estimated [195]. In other words, once the functional and stochastic models for the network have been defined, the expected precision with which the point parameters can be estimated is already known. In Sec. 5.2.2 we will elaborate on how this prior quality assessment can be used to guide the design of the network.

While Eq. (5.3) provides insight into the expected estimation precision, it does not guarantee the correctness of the estimated point parameters. A network adjustment alone is therefore insufficient, as it relies heavily on the correctness of both the functional and stochastic models. In addition, the estimation of the relative arc parameters themselves (step 2 in Fig. 5.1) is prone to errors, as these parameters—including the integer phase ambiguities—are estimated from wrapped *relative* DD phase observations. This requires an appropriate functional and stochastic model for each arc. Different parameterizations may not only affect the estimated physical parameters (such as the relative cross-range distance), but may also lead to a different adjusted absolute phase time series. Consequently, this would propagate through the network, resulting in biased estimates for the point parameters.

To ensure reliably estimated parameters for the points, statistical *testing* is required. As there may be several potential model errors (e.g., the estimated parameters for the arcs might be incorrect due to errors in the ambiguity resolution) we apply a three-step testing procedure: detection, identification, and adaptation (DIA) [181]. In

domain. Instead, it has a Von Mises probability density function [198], which is similar to a normal distribution for high-quality observations [121].

the detection step the overall model test (OMT) is applied to test the validity of the assumed models for the network adjustment. The corresponding test statistic is defined as

$$T_{m-n} = \underline{\hat{e}}^T Q_y^{-1} \underline{\hat{e}}, \quad (5.5)$$

where $\underline{\hat{e}}$ are the residues, defined as $\underline{\hat{e}} = \underline{y} - \underline{\hat{y}}$, with $\underline{\hat{y}}$ the adjusted arc parameters computed as $\underline{\hat{y}} = A\underline{\hat{x}}$. The model is rejected when $T_{m-n} > \chi_{\alpha_{m-n}}^2(m-n, 0)$, where α is the level of significance.

If the model is rejected, the next step is to identify the most likely error. Since the parameters may be incorrectly estimated for one or more arcs, data snooping can be used to test which arc has the incorrectly estimated parameter. The alternative hypothesis is defined as

$$H_{a_i} = E\{\underline{y}\} = A\underline{x} + c_i \nabla \quad \text{for } i = 1, \dots, m, \quad (5.6)$$

with

$$c_i = [0, \dots, 0, 1, 0, \dots, 0]^T, \quad (5.7)$$

with the i at index i . The term $c_i \nabla$ models the presence of an erroneous arc parameter in the i th arc. The corresponding test statistic becomes

$$\underline{w}_i = \frac{c_i^T Q_y^{-1} \underline{\hat{e}}}{\sqrt{c_i^T Q_y^{-1} Q_{\hat{e}} Q_y^{-1} c_i}}, \quad (5.8)$$

also known as the w -test, where $Q_{\hat{e}}$ is the variance-covariance matrix of the residues which is computed with $Q_{\hat{e}} = Q_y - Q_{\hat{y}}$. If the arc parameters are uncorrelated, i.e., Q_y is diagonal, the w -test simplifies to

$$\underline{w}_i = \frac{\hat{e}_i}{\sigma_{\hat{e}_i}}. \quad (5.9)$$

When we apply the w -test m times, by changing the c -vector, the test statistic \underline{w}_i with the largest absolute value corresponds to the arc most likely to have an erroneous estimated parameter. After identifying the erroneous arc, the model in Eq. (5.1) can be adapted in different ways. One option is to exclude the arc with the highest w -test statistic from the network and again estimate the unknown parameters for the points. Alternatively, when performing the adjustment epoch-wise on the displacement phase time series—that is, on the reduced phase observation, which corresponds to the observed phase after removing the static components (the cross-range phase, thermal displacement phase, and estimated ambiguities; see also Eq. (3.22) on p. 45)—an integer ambiguity may have been incorrectly estimated at a specific epoch t for arc i . In such cases, that phase observation can be adapted (i.e., an integer ambiguity can be added or removed), and the adjustment repeated using the adapted phase. The OMT is then reapplied, and if the test is passed, the corrected displacement phase is retained.

5.2.2. A CONFIDENCE-OPTIMIZED ROBUST GEODETIC NETWORK

From Eqs. (5.2) and (5.3) and the evaluation in Chapter 4 it has become evident that the network configuration does not only affect which points are included but also the numerical value and precision of their estimated parameters. This depends on both the selected arcs, encoded in the design matrix A , and associated quality of the arc parameters, captured in Q_y . In the generic case, even for the same set of points, alternative network configurations yield different estimated parameters with different precision, when the stochastic and functional models used in the arc parameter estimation are not in the same linear subspace, see Chapter 4. Therefore, some networks are closer to optimal than others, and the challenge is to find the "most optimal" network. This requires optimality criteria [120].

In other geodetic techniques, such as leveling and triangulation, network design is typically performed *before* data acquisition, using such optimality criteria [156]. Often, two key optimality criteria are used: precision (how well the parameters of interest can be estimated) and reliability (whether outliers in the observations can be detected and eliminated) [25, 74, 112, 165]. These same criteria should ideally also be applied when designing an InSAR network.

In practice, however, InSAR network design is rarely treated as an actual design problem. It is typically imposed as a fixed input, based on geometric heuristics [37, 102, 144, 193]. A commonly used configuration is the Delaunay triangulation, which connects points to maximize the minimum angle within each triangle. This optimization criterion—purely based on the geometric position of the points rather than their information content—is entirely unrelated to the InSAR estimation problem, where the relative position of points is near-irrelevant. As such, Delaunay-based networks are not likely to yield optimal estimation results.

This raises a fundamental question: what defines an optimal InSAR network, i.e., what outcomes should we consider optimal? If we can answer that question, we can formulate criteria and evaluate whether a given network satisfies them.

AN APPLICATION-DEPENDENT NETWORK

The question on optimality is inherently application-dependent. Each InSAR application comes with distinct objectives and requirements, which can be met by adapting the network accordingly. Below, we highlight a few key aspects:

- **Number, density, and type of points**

The selection of points (PS or DS) depends on the characteristics of the study area and the intended application. While complex regional deformation monitoring may require tens of thousands of points, monitoring a single structure, such as a building or a bridge, may only demand a handful of high-quality points. These choices determine the dimension and content of the unknown vector x .

- **Parameters of interest**

The choice of physical parameters to be estimated (e.g., displacements, thermal effects, or atmospheric phase screens) influences both the relative arc parameters as well as the parameters estimated per point after network

connection, as it determines the appropriate functional model for arc parameter estimation. For instance, the physical mechanism driving the displacements defines which displacement parameterization should ideally be used. As a result, different arcs may require different functional models, leading to a varying parameter space across the network. This complicates the network adjustment, as it prevents a straightforward adjustment on the unknown parameters.

- **Required quality**

The required quality of the estimated parameters, $Q_{\hat{x}}$, is perhaps the most application-dependent factor, as it depends on the intended application and how the data will be used. This requirement should be determined by the end user. For example, a municipality using the InSAR product to monitor critical infrastructure may require a much higher quality than a user interested only in general deformation trends.

As the examples above demonstrate, network design must be tailored to the specific goals and requirements of each InSAR application. **Ultimately, one must know (i) which parameters to estimate, (ii) for which points, and (iii) what level of precision is required for these parameters.** Therefore, every InSAR study requires an application-dependent network.

5

CRITERIA FOR THE CONFIDENCE-OPTIMIZED ROBUST GEODETIC (CORG) NETWORK

Since an optimal InSAR network is inherently application-dependent, clear design criteria must be defined. Given the parameters of interest, such as displacement, cross-range distance, and thermal expansion, we define an optimal network as one in which these parameters can be estimated with a predefined level of precision. We refer to such a network as a Confidence-Optimized Robust Geodetic (CORG) network for InSAR, emphasizing that its geometry and connectivity are explicitly designed such that the network meets application-specific accuracy requirements. In addition, the network is considered robust because its performance is not only optimized, but also evaluated through statistical testing. To achieve this, the required precision with which the relative point parameters need to be estimated must be specified for each application. With this in mind, the CORG network can be constructed or adapted accordingly. The design of the CORG network should be guided by the following four criteria:

1. **Optimization of the normal matrix N** (primary criterion)

Optimizing the network involves improving the properties of the normal matrix N (see Eq. (5.4)), which directly determines the precision of the estimated parameters $Q_{\hat{x}}$, thereby increasing confidence in the estimated parameters. This can be achieved by modifying the topology of the CORG network (i.e., selecting which and how many arcs are included, as defined by A) and by prioritizing arcs based on their quality, defined by Q_y . The main idea of the CORG network is to construct it incrementally: starting from the highest-quality arcs, and adding arcs in order of descending quality, until all

desired points are included and the parameters can be estimated with the required precision (i.e., until $Q_{\hat{x}}$ meets the application-dependent threshold). Since N is independent of the arc parameters y , the only requirement for this approach is prior knowledge of the quality of all potential arcs within the area of interest (AoI). This quality-driven approach optimizes the likelihood of a higher quality of the final estimates.

The remaining criteria serve as additional constraints to ensure the robustness and usability of the resulting CORG network.³

2. Redundancy through minimum degree of connectivity

To enable testing to validate the estimates, each point in the CORG network must be connected to at least two other points. In network theory terms, this means that the *degree* of every node (point) should be at least two.

3. A connected (contiguous) network

For the estimated parameters to be meaningfully compared across the entire network, the CORG network must be fully connected. A single connected, or contiguous, network ensures that all points connect to the same datum, avoiding isolated clusters which cannot be referenced to one another.

4. Distance constraints

Depending on the size of the AoI it may be necessary to assign different weights to arcs based on their length. In some cases, shorter arcs may be preferred due to their higher quality and lower susceptibility to atmospheric effects, whereas in other cases, including longer arcs may provide essential spatial coverage or connections.

THREE STEP APPROACH

While the above design criteria are instrumental to the CORG network, strictly applying them may lead to two practical problems. First, the selection process tends to favor a small subset of very high-quality points, as the best arcs often connect the same few points, resulting in disconnected points in the AoI. Second, when aiming to include a large number of points the resulting CORG network can become excessively large and adjusting it becomes computationally demanding. Therefore, we propose a multi-step approach for the CORG network consisting of the following three steps, as schematically shown in Fig. 5.2:

1. The control network

First, a control network⁴ is constructed using the highest-quality arcs within

³Here, robustness refers to the ability to statistically validate the estimated parameters and detect potential inconsistencies through redundancy in the network. Usability refers to the ability to interpret and compare all estimated parameters within a common reference frame across the area of interest.

⁴Dutch: *grondslag*, or *grondslagennetwerk*. The purpose of the control network is to establish a network of reference points, i.e., a *reference frame* which can then be considered as 'fixed' (deterministic) for the purpose of the survey goals. It forms the basis of the subsequent detail survey (*detailmeting*) in the *local network* that links secondary points to the control network.

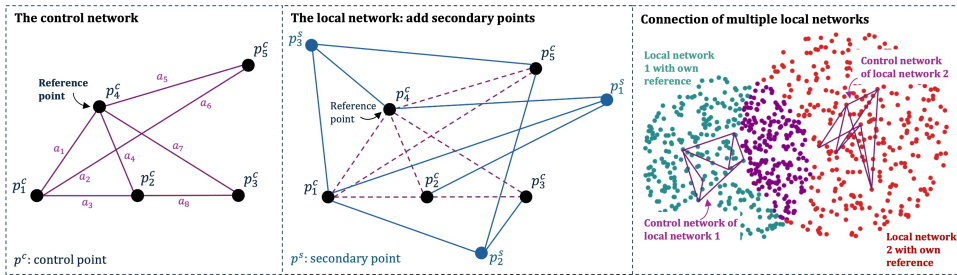


Figure 5.2.: The three steps within the spatial estimation of point parameters. The control networks consists of high quality arcs and points and is constructed under strict quality criteria. Once the control network is adjusted, secondary points can be connected to the control points, via de best arcs available, resulting in a local network. When larger areas are processed, it might be needed that multiple local networks are connected. This requires another adjustment as both local networks have different reference points.

the AoI. In Sec. 5.3.2 we will elaborate on how this arc quality can be derived, were arcs are iteratively added until the parameters for the control points can be estimated with the predefined precision. The control network is relatively small, typically comprising 8 to 15 control points, and it covers a limited area of interest where atmospheric phase delays are negligible. The control network is highly redundant; there are significantly more arcs than control points to ensure high-quality estimated parameters. This is discussed in Sec. 5.3.

2. The local network: adding secondary points

After establishing the control network, the parameters for the control points can be fixed and treated as deterministic. They will serve as a basis for the nearby secondary points. These secondary points will be connected again using the highest-quality arcs available. The control points and secondary points together form a local network. This is discussed further in Sec. 5.4.

3. Connecting local networks

For larger areas of interest, multiple local networks can be connected, each including their own secondary points and reference points. A connection of these networks can be done through connection points that occur in multiple local networks. This is discussed in Sec. 5.5.

The implementation of these steps for the CORG network varies depending on the application. In some cases, when only a few high-quality points are required, a single control network is sufficient. In other cases, one local network is sufficient, whereas processing larger areas requires the connection of multiple local networks via connection points. In the following three sections, we will discuss the design and adjustment of these three networks in more detail. Note that, from this point onward we only consider small areas where atmospheric effects are negligible.

5.3. THE CONTROL NETWORK

The design and adjustment of the control network follows three main steps. First, the control network's criteria must be defined, see Sec. 5.3.1. Next, the prior quality of all possible arcs must be assessed, which is discussed in Sec. 5.3.2 and finally, the network is constructed and adjusted accordingly, see Secs. 5.3.3 and 5.3.4.

5.3.1. CRITERIA FOR THE CONTROL NETWORK

For the design of the control network, we follow the principles outlined in Sec. 5.2.2, supplemented by specific design criteria. At a minimum, this includes:

1. The spatial extent of the control network. This refers to the maximum arc length allowed, under the assumption that atmospheric phase delays are negligible. This criterion determines how large the control network might be and which points may be included.
2. The required precision of the parameters of interest for the control points, providing target values for the main diagonal elements of the covariance matrix $Q_{\hat{x}}$.
3. The number of control points that need to be included.
4. Optionally, redundancy criteria can be defined, such as the desired number of arcs relative to the number of points, to further enhance the reliability and precision of the network.

5.3.2. DEFINING ARC QUALITY

The criteria above result in target values for the covariance matrix $Q_{\hat{x}}$ for a required number of points within the AoI, which allows to design the control network using the criteria highlighted in Sec. 5.2.2. However, it requires knowledge of the quality of each potential arc within the area to be able to rank the arcs. In Chapter 2, we introduced a method for estimating the quality of the double differenced (DD) phase observations per epoch per arc, based on amplitude time series. This enables us to compute the prior quality of all potential arcs before performing any arc parameter estimation or network adjustment.

For n detected points, the quality of $1/2n(n-1)$ possible arcs can be evaluated per epoch, resulting in $1/2Dn(n-1)$ quality estimates for a time series of length D . To allow meaningful comparison between arcs despite temporal variability, we assign each arc a single representative value: the maximum standard deviation (σ) of the DD phase observed over the entire time series. This ensures that the arc maintains an acceptable quality level throughout the entire observation period.⁵

Note that the stochastic model developed in Chapter 2 does not account for atmospheric effects. To compensate, we introduce a distance-dependent term by

⁵Although alternative methods, such as using the mean or median quality, could be used, we have found that relying on the worst-case value is more robust. Arcs that are generally reliable but degrade over a short period can still cause unwrapping errors, which negatively affect the network adjustment when performed per epoch.

adding an additional standard deviation of 1.2 radians per kilometer arc length [133]. This value can be adjusted, where increasing it favors shorter arcs, while decreasing it reduces the influence of distance.

5.3.3. DESIGN THE CONTROL NETWORK

With the ordered list of arcs established, the control network can be designed. Starting with the highest-quality arc in the AoI, arcs are iteratively added under the condition that each new arc connects to the current network, ensuring a single connected graph. Arcs are added until the defined criteria are met.

Once the network is constructed, the relative arc parameters can be estimated from the DD phase observations, defined as the *arc estimation* step. However, since the functional model that we use in the arc estimation step might be highly non-linear, sometimes no feasible solution can be found for an arc. Moreover, the prior arc quality estimate (based on the amplitude time series) may not correspond to the actual quality of the DD phase timeseries. In both cases, the arc must be removed from the network, and it must be verified whether the remaining network still meets the defined criteria. If not, additional arcs must be selected and added. The full procedure is illustrated in Fig. 5.3.

5.3.4. ADJUST THE CONTROL NETWORK

The selected arcs form a network from which a system of observation equations can be constructed. However, to obtain a solution, a datum must be defined—typically by selecting a reference point where all parameters are set to zero. As a result, the estimated parameters for all other points are expressed relative to this reference point. It is important to note that this constraint is not unique; infinitely many valid constraints exist, each yielding a different solution. Consequently, with m arcs in the network, the observation vector \underline{y} , consisting of the relative arc parameters⁶ is defined as:

$$\underline{y} = [\underline{a}_{12}, \underline{a}_{23}, \underline{a}_{24}, \underline{a}_{13}, \dots, \underline{a}_{1n}], \quad (5.10)$$

where a_{ij} denotes an arc parameter, defined as the value at point j relative to the value at point i . If the network contains n control points, denoted by p^c , and applying the constraint that p^c serves as a datum, i.e., $p_1^c = 0$, the mathematical

⁶We propose to adjust the network based on the parameters estimated from the DD phase observations, i.e., h_{xr} and η . Since different arcs may have different displacement parameterizations, i.e., different displacement parameter vectors δ_{displ} , the network cannot be adjusted directly on the displacement parameters. Therefore, in addition to adjusting the network on h_{xr} and η , we propose to adjust the network epoch-wise on the reduced phase observation, ϕ'_{ij} (see also Eq. (3.22) on p. 45). This reduced phase in fact corresponds to the displacement phase time series plus noise. We will elaborate on this in Sec. 5.6.

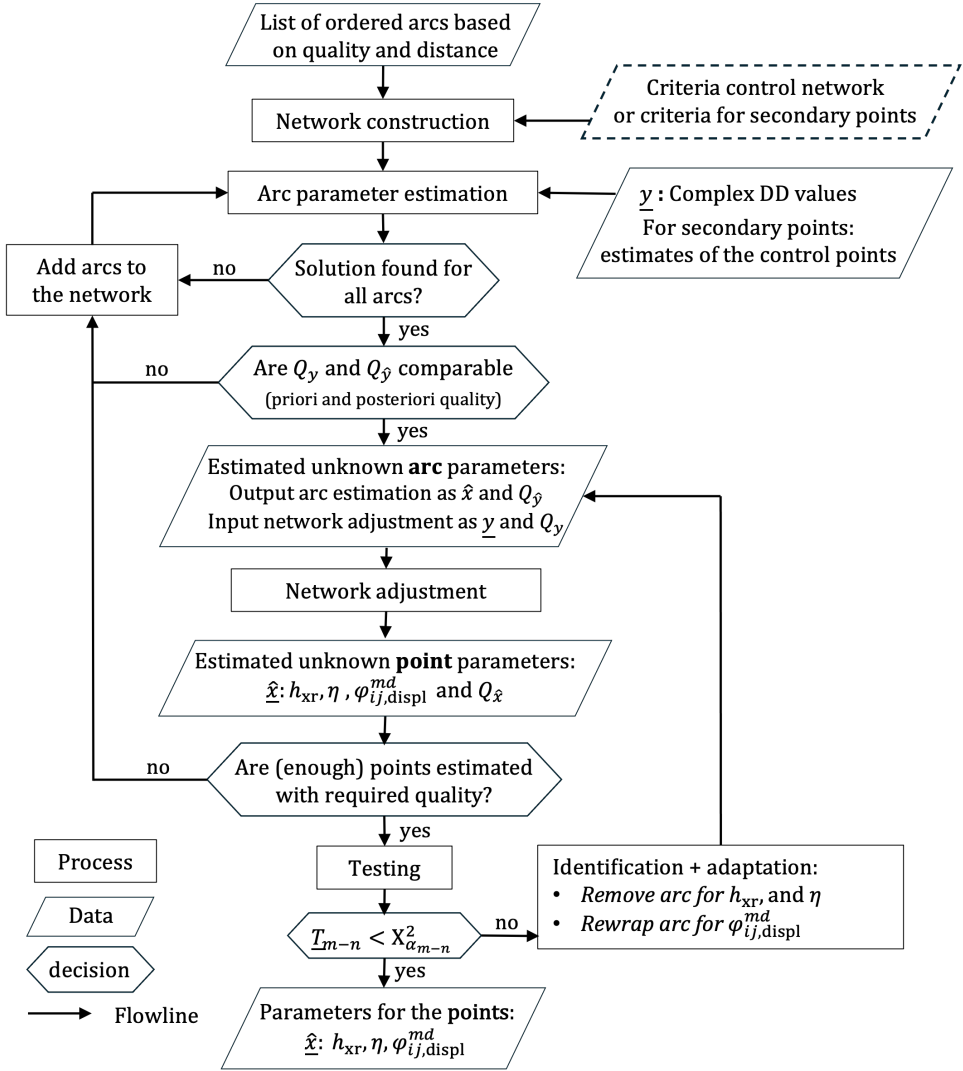


Figure 5.3.: Flowchart of the procedure followed in the design and estimation of the control network and when secondary points are added. Note that the way the network is designed differs for both cases. In the control network, the network is designed starting with the best arcs in the AoI. Whereas adding secondary points is done via de best arcs between the secondary points and the fixed control points.

specific arcs are selected, and the mathematical model is defined as

$$E\left\{\underbrace{\begin{bmatrix} \underline{a}_{p_1^c, p^s} + p_1^c \\ \underline{a}_{p_2^c, p^s} + p_2^c \\ \vdots \\ \underline{a}_{p_m^c, p^s} + p_m^c \end{bmatrix}}_y\right\} = \underbrace{\begin{bmatrix} 1 \\ 1 \\ \vdots \\ 1 \end{bmatrix}}_A \underbrace{p^s}_x \quad (5.13)$$

$$D\left\{\underbrace{\begin{bmatrix} \underline{a}_{p_1^c, p^s} + p_1^c \\ \underline{a}_{p_2^c, p^s} + p_2^c \\ \vdots \\ \underline{a}_{p_m^c, p^s} + p_m^c \end{bmatrix}}_y\right\} = \underbrace{\begin{bmatrix} \sigma_{a_{p_1^c, p^s}}^2 & \sigma_{a_{p_1^c, p^s}, a_{p_2^c, p^s}} & \sigma_{a_{p_1^c, p^s}, a_{p_m^c, p^s}} \\ \sigma_{a_{p_1^c, p^s}, a_{p_2^c, p^s}} & \sigma_{a_{p_2^c, p^s}}^2 & \vdots \\ \vdots & \vdots & \vdots \\ \sigma_{a_{p_1^c, p^s}, a_{p_m^c, p^s}} & \sigma_{a_{p_{m-1}^c, p^s}, a_{p_m^c, p^s}} & \sigma_{a_{p_m^c, p^s}}^2 \end{bmatrix}}_{Q_y}, \quad (5.14)$$

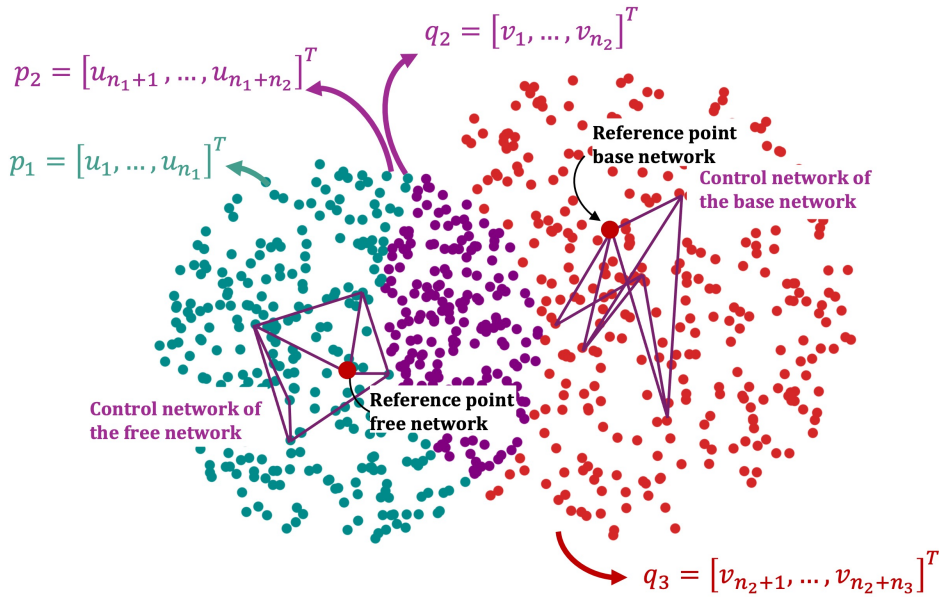
where secondary point p^s is added with m arcs to the control network. The y vector consists of two components: the sum of the estimated relative arc parameters (a stochastic quantity, hence the underline), and the estimated values of the control points, which are treated as deterministic since they serve as the fixed datum. As with the control network, we follow the same steps as presented in Fig. 5.3. Once all secondary points are connected to the control network, the combined set of points forms a *local network*. This way of connecting secondary points has two key advantages. First, it is computationally efficient, as each secondary point can be added independently of the others. Second, each secondary point remains relatively 'close' to the chosen datum, limiting the propagation of errors throughout the network.

5.5. CONNECTION OF LOCAL NETWORKS

Generating InSAR products over larger areas may require multiple local networks, each with its own datum, i.e., reference point. Since parameters are estimated relative to the specific datum, parameters from different networks are not directly comparable. However, the networks can be connected through *connection points*, i.e., identical scatterers included in both networks. To do so, one network is defined as the *base network*, which will serve as the datum to the other network defined as the *free network*. A datum transformation is applied on the parameters in the free network. Three sets of points can be distinguished: (1) points exclusively in the free network, (2) connection points in both the base and free networks, and (3) points exclusively in the base network, see also Fig. 5.4.

Within the free network, point parameters relative to its datum are denoted as u . For example, $u_1 = [\hat{h}_{x_1}, \hat{\eta}_1, \hat{\phi}'_{ij}]^T$ is the vector of estimated parameters for point 1.⁷

⁷In Sec. 5.6 we will elaborate on the parameters used in the adjustment.

Free network with $n_1 + n_2$ pointsBase network with $n_2 + n_3$ points

5

Figure 5.4.: Connection of two local networks (in green and red) via connection points (shown by the purple dots). The points $p = [p_1^T, p_2^T]^T$ belong to the free network, and the points $q = [q_2^T, q_3^T]^T$ belong to the base network. There are n_2 points shared by both networks, with parameters estimated relative to both reference points in the two networks. Connecting the two networks relies on these connection points, with the goal of relating all p points to the local datum in the base network.

The two sets of points in the free network are defined as vectors p_1 and p_2 , with

$$\begin{aligned} p_1 &= [u_1, \dots, u_{n_1}]^T, \\ p_2 &= [u_{n_1+1}, \dots, u_{n_1+n_2}]^T, \end{aligned}$$

where p_1 contains the n_1 points that are only part of the free network, and p_2 the n_2 connection points. The total number of points in the free network is $n_1 + n_2$. Similarly, the two sets of points in the base network are defined as vectors q_1 and q_2 , with

$$\begin{aligned} q_2 &= [v_1, \dots, v_{n_2}]^T, \\ q_3 &= [v_{n_2+1}, \dots, v_{n_2+n_3}]^T, \end{aligned}$$

where the relative parameters are denoted by v . Here, vector q_2 contains the n_2 connection points, and q_3 the n_3 points exclusively in the base network. The parameters u and v are the estimation results of the network adjustments of the control network and local network, see Secs. 5.3 and 5.4.

To connect the free network to the base network, the parameters of the points in the free network are transformed by applying a constant offset parameter z to all points, i.e., $z = [\Delta h_{xr}, \Delta \eta, \Delta \hat{\varphi}'_{ij}]^T$. This offset parameter needs to be estimated for each adjusted variable. Since points in p_1 and q_3 are not involved in the connection, the observation model simplifies to

$$E\left\{\underbrace{\begin{bmatrix} p_2 \\ q_2 \end{bmatrix}}_y\right\} = E\left\{\underbrace{\begin{bmatrix} u_{n_1+1} \\ \vdots \\ u_{n_1+n_2} \\ v_1 \\ \vdots \\ v_{n_2} \end{bmatrix}}_y\right\} = \underbrace{\begin{bmatrix} 1 & & & & & & & & 1 \\ & \ddots & & & & & & & \vdots \\ & & & & & & & & 1 \\ & & & & & & & & 1 \\ 1 & & & & & & & & 0 \\ & & & & & & & & \vdots \\ & & & & & & & & 1 \\ & & & & & & & & 0 \end{bmatrix}}_A \underbrace{\begin{bmatrix} v_1 \\ \vdots \\ v_{n_2} \\ z \end{bmatrix}}_x \quad (5.15)$$

$$D\left\{\underbrace{\begin{bmatrix} p_2 \\ q_2 \end{bmatrix}}_y\right\} = \underbrace{\begin{bmatrix} Q_{p_2} & 0 \\ 0 & Q_{q_2} \end{bmatrix}}_{Q_{pq}}, \quad (5.16)$$

where we have no reason to consider any correlation between the estimated parameters of the free and base networks, i.e., the off-diagonal elements in Q_{pq} are zero.

While Eqs. (5.15) and (5.16) describe an unconstrained model, it is impractical if the estimated point parameters of the base network would change every time a free network is connected to it. Therefore, we constrain the model such that the parameters in the base network cannot change, i.e., we treat them as deterministic

quantities, resulting in

$$E\left\{ \underbrace{\begin{bmatrix} \underline{u}_{n_1+1} - v_1 \\ \vdots \\ \underline{u}_{n_1+n_2} - v_{n_2} \end{bmatrix}}_{\underline{y}} \right\} = \underbrace{\begin{bmatrix} 1 \\ \vdots \\ 1 \end{bmatrix}}_A \underbrace{\begin{matrix} z \\ x \end{matrix}}_x \quad (5.17)$$

$$D\left\{ \underbrace{\begin{bmatrix} \underline{u}_{n_1+1} - v_1 \\ \vdots \\ \underline{u}_{n_1+n_2} - v_{n_2} \end{bmatrix}}_{\underline{y}} \right\} = Q_{p_2}, \quad (5.18)$$

where Q_{p_2} is the variance-covariance matrix of the estimated parameters for the connection points in the free network. Therefore, the quality of the estimated offset parameter \hat{z} depends only on these points. Note that after the estimation of z we also need to apply statistical testing as described in Sec. 5.2.1. After testing, detecting, and excluding potential erroneous points, we can apply the estimated offset to all points in the free network using the following forward model:

$$\underline{q}_1 = \underline{p}_1 - \hat{z}. \quad (5.19)$$

Note that we have to do this independently for each parameter, e.g., the cross-range distance, thermal expansion factor, and reduced phase observation per epoch, see for the latter also Eq. (3.22) at p. 45. As a result, all points have parameters relative to the base network's reference point. The procedure can be repeated independently for multiple free networks.

5.6. ADJUSTMENT PARAMETERS AND CORRESPONDING VARIANCE-COVARIANCE MATRICES

As elaborated in Chapter 4, the network is adjusted in the parameter space, using the results from the arc parameter estimation. In the most general—and therefore most realistic—case, each arc is characterized by its own stochastic model, and the functional model may also differ across arcs. As a consequence, the estimated parameters \hat{x} do not necessarily "close" within a triangle of the network, while they *should* close based on trivial logic. For example, a loop between points on the estimated cross-track distances per arc should 'close', i.e., sum up to zero. This contextual information results in a constraint that can be used to improve (adjust) the final estimates.

Obviously, network adjustment is only possible for the *shared* estimated parameters, i.e., those parameters that are estimated consistently across all arcs, such as the relative cross-range distance h_{xr} , the thermal expansion factor η , as well as the integer phase ambiguities. Displacement parameters, by contrast, cannot be adjusted directly, as their parameterization may vary from arc to arc.

We use the estimated static and shared parameters in the forward model per arc to compute their contributions to the observed phase, and subtract them subsequently from this observed (wrapped) phase, see Eq. (3.22) at p. 45. This yields the *reduced phase observation*, denoted $\hat{\phi}'_{ij}$, which is an absolute phase value, with contributions from (i) the non-static phase components (such as the non-thermal displacement phase per epoch) and (ii) the original measurement noise. We subsequently use these reduced phase observations per arc in the adjustment of the network per epoch. For a time series of length D , this implies that a total of $D+2$ independent network adjustments are possible, where the +2 addition represent the adjustment for the cross-range distance h_{xr} and thermal expansion factor η . This is also illustrated by the right side of Fig. 5.5.

At this stage, we start—in parallel—the independent network adjustments per parameter. For the static parameters (h_{xr} and η), this comprises two separate independent adjustments. For the non-static phase component per epoch (i.e., the sum of the non-thermal displacement phase and the original measurement noise), these are independent network adjustments per epoch.

If one of these independent adjustments results in the rejection of (parts of) the network, this may lead to different follow-up actions. Currently, the rejection of the adjustment in one parameter group is not considered to result in actions for other parameter groups, but other decisions can be taken in particular application-specific circumstances.

After estimating these arc-based parameters including their associated variance-covariance matrices (VCM) $Q_{\hat{x}}$ per arc, see also the left side of Fig. 5.5, these are considered as the new ‘observables’ y' and their VCM $Q_{y'}$ in the network adjustment, respectively. As sketched in Fig. 5.5, this implies that also the covariances between the arcs need to be considered, indicated with the light-gray matrices. Considering the elements of the new observation vector per arc, there are different considerations. For the static components h_{xr} as well as η , there is no correlation between different arcs, as the estimation of the parameters was done using unique models for the arcs, even if they are sharing a common point. Likewise, they are not cross-correlated. Yet, the non-static component, i.e., the reduced phase observation, may exhibit a non-zero covariance term. This is due to the fact that this term is the sum of the non-thermal displacement and the original observation noise. While the non-thermal displacement term is not correlated between arcs, the original observation noise is point-dependent instead of arc-dependent, and is therefore correlated between arcs. In the remainder of this chapter, we adopt the variance–covariance matrix of the observed DD phase per arc, while assuming no correlation between different arcs.

5.7. RESULTS AND IMPACT

We demonstrate the proposed method for the Confidence-Optimized Robust Geodetic (CORG) network using a Sentinel-1 dataset over Amsterdam, the Netherlands. As the CORG network design is application-dependent, it is impractical to present all potential configurations. Instead, we illustrate the approach outlined in Secs. 5.3, 5.4, and 5.5 through a case study in the city center of Amsterdam. In this example,

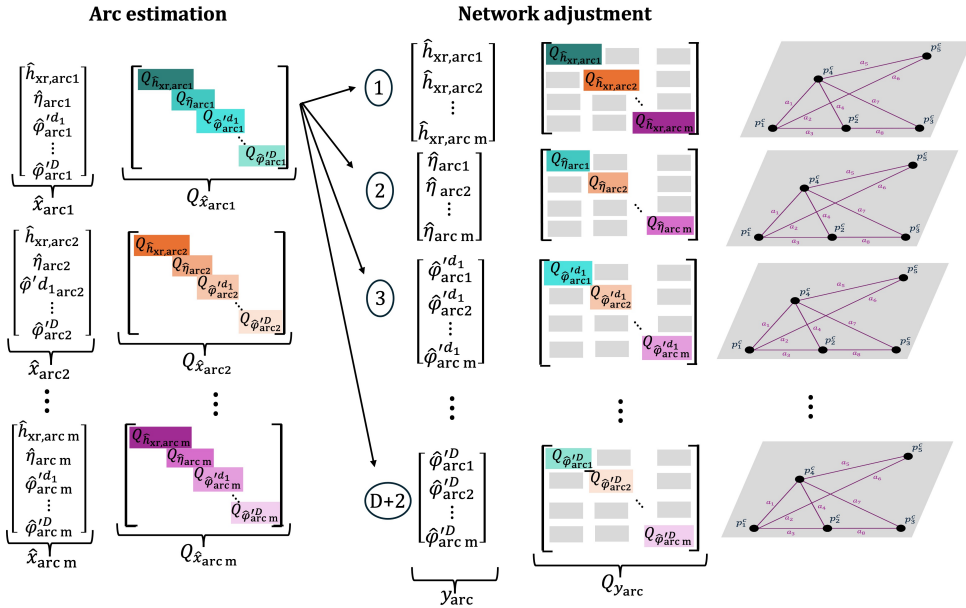


Figure 5.5.: Sketch of the transition between the estimated parameters *per arc* (left), which are subsequently used as vector of observables for the network adjustment (right). The parameters per arc are estimated independently, with their respective variance covariance matrices. When combined in vector, this implies that potential covariances between the observables, indicated with the light-gray matrices, need to be considered.

the area of interest spans 2×2 km, an area that is too large for a single local network due to arc length limitations.

5.7.1. THE CONTROL NETWORK

To design the CORG control network, we define the maximum spatial extent by a circular area with a radius of 700 meter. Within this area we detected about 2000 points, as shown in Fig. 5.6a. Although the size of this area is somewhat arbitrary, it must be small enough to neglect atmospheric effects, as no atmospheric phase estimation is applied yet. Next, we evaluate the temporal quality of the ~ 2 million potential arcs using the stochastic model described in Chapter 2.⁸ In addition to this arc quality, which is based on the amplitude time series of the points, we include a distance-dependent term: an additional standard deviation of 0.1 radians per kilometer of arc length, to account for atmospheric effects [133]. Consequently, all arcs are ranked from highest to lowest quality, and the control network is designed by iteratively adding arcs while making sure we fulfill the requirements discussed in Sec. 5.2.2. See also the flowchart as presented in Fig. 5.3.

In this specific case study the criteria were chosen as: (i) at least ten points are included; (ii) the relative cross-range precision is better than 0.7 meters; and (iii) the reduced phase observation per epoch is estimated with a precision of at least 0.4 radians. The reduced phase observation contains contributions from non-static phase components (e.g., the non-thermal displacements) and noise. These requirements are application-dependent and ideally defined in consultation with the end user, as the required quality depends on the intended application. In our case, the criteria are met after 20 iterations, i.e., 20 arcs are part of the network, resulting in control network shown in Fig. 5.6b), where the color of the arcs indicates the iteration in which it is added to the network.⁹ The reference point, shown in red, is chosen as the point with the highest degree, i.e., the most connections.

In every iteration, an arc is added and a new network adjustment is performed. Therefore, the estimated point parameters change for each iteration, i.e., when an arc is added. Fig. 5.7 and 5.8 illustrate the estimated parameters, and their quality, for control points 5 and 6, respectively, per iteration. As shown in Fig. 5.7, point 5 becomes part of the control network in iteration 7. The parameters estimated at each iteration are the relative cross-range distance and thermal expansion factor, shown in Fig. 5.7a, and the reduced phase per epoch shown in Fig. 5.7c. As each iteration includes a new arc, the network differs between iterations, and the estimated parameters evolve over time. Moreover, it can be seen that precision for the estimated parameters steadily improves: the $1\text{-}\sigma$ uncertainty of the cross-range distance decreases from 0.37 m to 0.22 m, see Fig. 5.7b.

Figs. 5.7c and d show the reduced phase time series (which can be regarded as the non-thermal displacement phase plus noise) and the corresponding quality for the different iterations. The estimated time series from the last iteration is shown in black, while the colored lines represent results from earlier iterations. Although

⁸With 2094 points this resulted in $\frac{2094 \cdot 2093}{2} \approx 2.2 \cdot 10^6$ arcs

⁹Note that this resulting network is very different from the conventional Delaunay network.

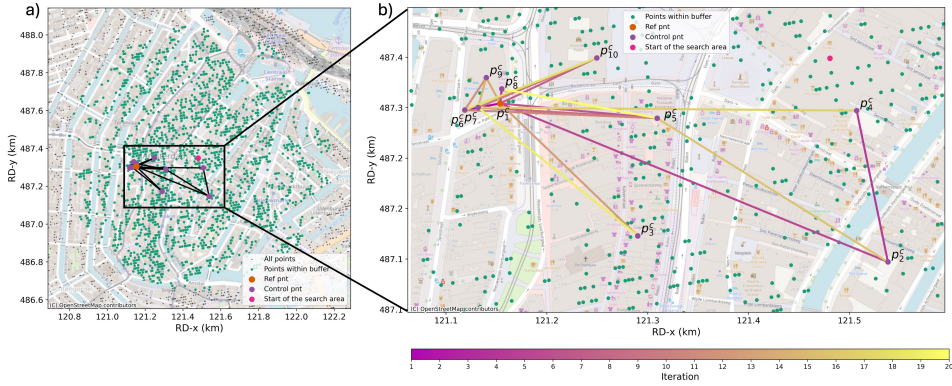


Figure 5.6: a) shows the 2000 points detected within the area where the control network is allowed to grow, defined by a 700-meter buffer around a starting point. b) shows the resulting control network, constructed by evaluating the quality of 2 million potential arcs and iteratively adding the highest-quality ones. The arc color indicates the iteration in which the arc was added. After 20 iterations, the network meets the specified requirements and includes 10 control points. The reference point is shown in red, and as was chosen as the point with the most connections.

the reduced phase time series estimates themselves change by less than 0.01 radians between iterations, their precision improves significantly, from around 0.16 radians to 0.08 radians. We also observe multiple partitions in the estimated quality, which arise because the reduced phase time series for each point depends on multiple arcs in the network, each associated with its own partitioned stochastic model.

COMPARISON WITH THE DELAUNAY NETWORK

We compare the resulting CORG control network to a Delaunay network constructed from the same set of points, see Fig. 5.9, with arc colors indicating mean arc quality for the DD phases. The Delaunay network contains 21 arcs with a mean arc quality of 0.135 radians, while the CORG control network has 19 arcs and a slightly better mean quality of 0.127 radians. Moreover, the Delaunay network contains fewer high-quality arcs. We also computed the condition numbers of the Normal matrix N corresponding to both networks where we find $\text{Cond}(N_{\text{Del}}) \approx 13 \cdot \text{Cond}(N_{\text{CORG}})$, with $\text{Cond}(N_{\text{Del}})$ and $\text{Cond}(N_{\text{CORG}})$ the condition numbers of the Delaunay and CORG control network respectively. The condition number of the matrix provides an indication of the stability of the system. A small condition number implies that the solution is stable, whereas a large condition number indicates an unstable solution, meaning that small errors in the measurements can lead to large errors in the estimated parameters. Therefore, we conclude that Delaunay network is less optimized for estimating the unknown parameters compared to the CORG control network.

Subsequently, both networks are used to estimate the relative cross-range distance and reduced phase time series, with results summarized in Tab. 5.1. The Delaunay

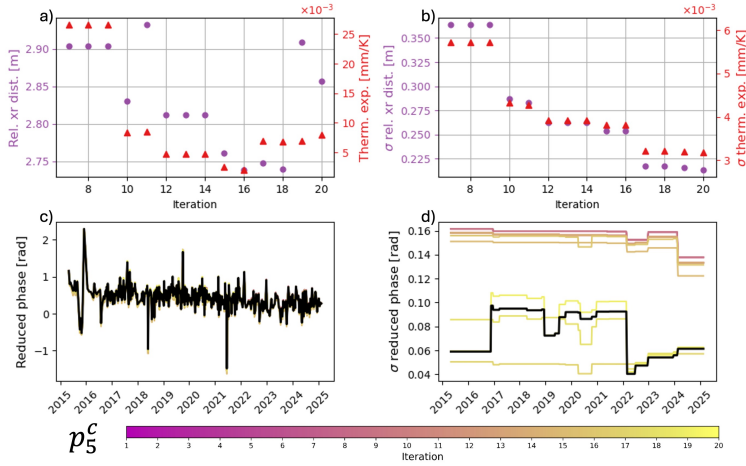


Figure 5.7.: Estimated parameters for control point 5 across different iterations, where the point becomes part of the control network from iteration 7 onward. a) shows the estimated relative cross-range distance (purple) and thermal expansion factor (red). As more arcs are added to the control network, the parameter estimates evolve. b) shows the corresponding quality values, 1σ , which decrease as more arcs are added to the network. c) and d) show the estimated non-thermal displacement time series and the corresponding quality values per-epoch, respectively. The colored lines indicate the estimates at each iteration, with the final estimate shown in black. While the non-thermal displacement values change only slightly between iterations, the quality improves substantially: the average uncertainty decreases from 0.16 radians in the first iteration to between 0.06 and 0.10 radians in the final one.

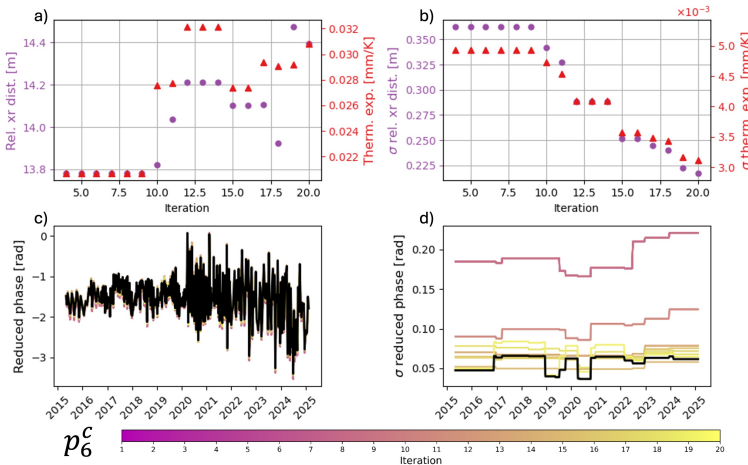


Figure 5.8.: Estimated parameters for control point 6 across different iterations, where the point becomes part of the control network from iteration 4 onward. See for a description of the subfigures the caption in Fig. 5.7.

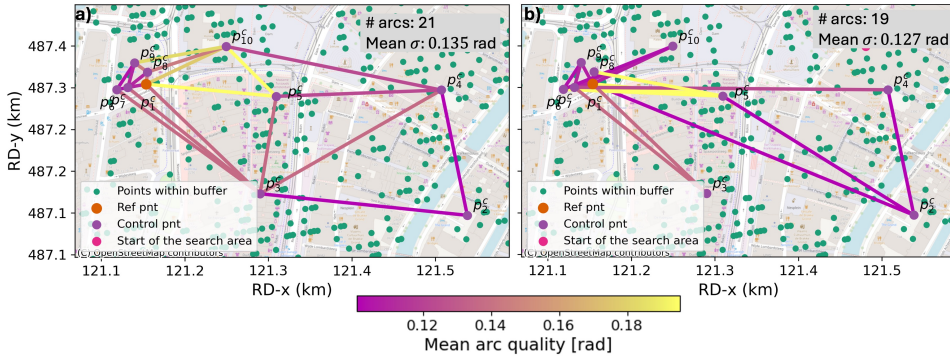


Figure 5.9.: Comparison between the Delaunay network in a) and the CORG control network in b), both based on the same set of points. Arc colors indicate the mean arc quality of the DD phases. The Delaunay network shows overall lower arc quality, with a mean of 0.135 radians compared to 0.127 radians for the control network. The arc configuration also differs significantly: for example, control point 10 is connected to points 6 and 7 in the control network, but to five entirely different points: 9, 8, 1, 5, and 4 in the Delaunay network.

5

network is clearly suboptimal. For example, control point 10, one of the lower-quality points, is connected to five points in the Delaunay network but to only two in the control network (see also Fig. 5.9). Tab. 5.1 further shows significant differences in the estimated parameters for the control points: cross-range estimates differ by up to 5 meters and the mean time series values by up to 5 mm. While the true solution is unknown, the quality with which we can estimate the unknown parameters are better for the CORG control network compared to the Delaunay network. Moreover, note that we compare the very best points within the AoI, where even larger differences are expected for lower quality points.

5.7.2. THE LOCAL NETWORK

Once the CORG control network is adjusted and the estimates meet the requirements, the solutions can be fixed, and they will serve as a datum for the connection of secondary points. The way secondary points are connected is again application-dependent. Here, we require each secondary point to be connected via three arcs, but another option would be to use as many arcs until specific quality criteria are met.¹⁰

In this case, we focus on the Rokin area, indicated by the green points in Fig. 5.10. All points are connected to the control network using the highest-quality arcs.¹¹ Two example points are highlighted, with their estimated parameters and arc parameters shown in Figs. 5.11 and 5.12. It can be seen that the highest-quality arcs are not

¹⁰The number and location of points connected to the control network strongly depend on the application. If the goal is to monitor a particular object, only points located on that object need to be connected to the control network. In contrast, if the aim is to study an entire city, all points within a certain distance from the control network can be included.

¹¹With 10 control points, only 10 arcs need to be evaluated.

Table 5.1.: Comparison of point statistics using the CORG control and Delaunay networks. Each row corresponds to a different point. For each point, we show the number of connections and the quality in both networks. We then present the difference in the estimated relative cross-range distance between the two methods, along with the associated standard deviation (σ). Additionally, we compute the mean reduced phase time series for both methods (and convert them to meters) and show their difference and corresponding σ values.

Point	Point quality [rad]	# conn. CORG network	# conn. Delaunay network.	Difference in h_{XR} [m]	σh_{XR} CORG [m]	σh_{XR} del. [m]	Difference in φ^r [mm]	$\sigma \varphi^r$ CORG [m]	$\sigma \varphi^r$ del. [m]
p_2^c	0.07	3	2	4.92	0.19	2.51	0.55	0.42	0.50
p_3^c	0.10	2	6	-0.28	0.23	0.21	-0.16	0.48	0.52
p_4^c	0.09	2	4	4.35	0.24	2.50	1.14	0.56	0.51
p_5^c	0.14	5	4	-0.05	0.20	0.28	-0.44	0.31	0.27
p_6^c	0.07	4	3	-0.87	0.21	0.25	-0.81	0.23	0.43
p_7^c	0.08	7	5	-0.37	0.16	0.20	-0.59	0.16	0.26
p_8^c	0.10	2	4	0.59	0.24	0.29	-5.24	0.50	0.25
p_9^c	0.13	3	4	-0.47	0.24	0.29	-0.80	0.60	0.44
p_{10}^c	0.13	3	5	1.50	0.24	0.30	-0.27	0.58	0.47

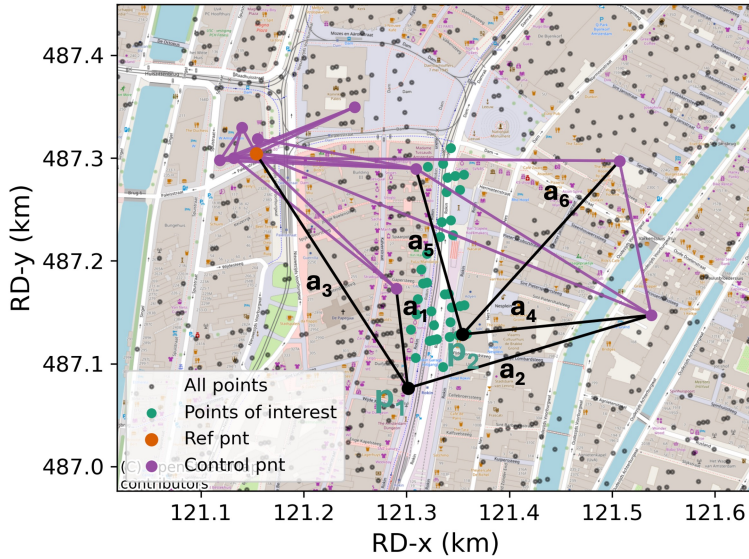


Figure 5.10.: Secondary points (shown in green) are connected to the CORG control network using the highest-quality arcs, resulting in a CORG local network. Two of these secondary points, p_1 and p_2 , are highlighted. It can be seen that they are connected to the control network through different arcs, and not necessarily to the geographically closest control points.

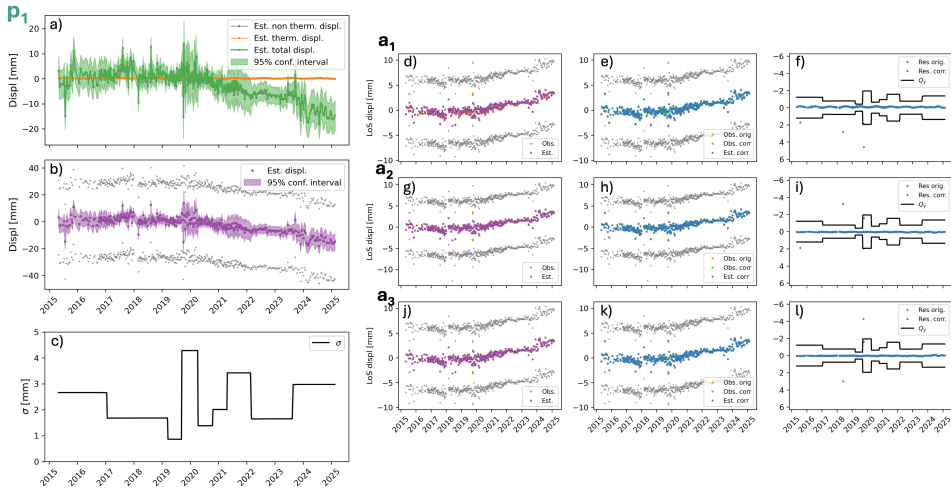


Figure 5.11.: Estimated parameters of secondary point 1 relative to the reference point in the control network. a) shows the final estimated displacement time series, which is the sum of the thermal displacements and the reduced phase (that is also shown in b). Note that the latter is in fact the non-thermal displacement phase plus noise. c) shows the corresponding σ values, where it can be observed that the quality varies over time. d) until l) present the variables corresponding to the arcs used to connect the point to the control network; these arcs are also shown spatially in Fig. 5.10. In d), g), and j), the reduced phase time series for the arc are shown in orange, while the adjusted values are shown in purple. If the OMT is rejected for a particular epoch, a w-test is applied to identify the erroneous arc, and if necessary, the reduced phase is adapted by an integer ambiguity. The adapted observations are shown in green in e), h), and k), with the corresponding adjusted values shown in blue. The final column (f, i, l) shows the residuals of the arc parameters. Note that we transformed the phase time series to meters, and thus, the values are defined in the line-of-sight (LoS) of the satellite.

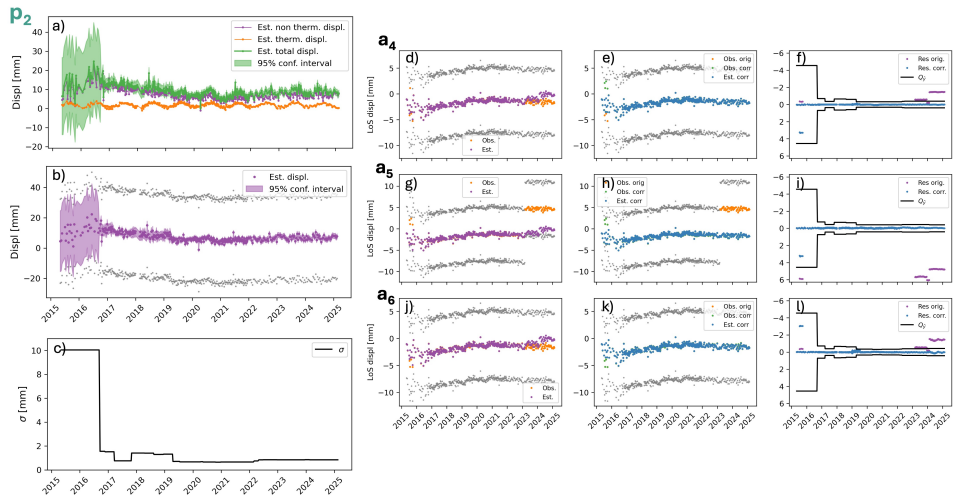


Figure 5.12.: Estimated parameters of secondary point 2 relative to the reference point in the control network. For an explanation of the subfigures we refer to Fig. 5.11. In d), g), and j), it can be observed that during the last two years of the time series, the residuals between the observed arc displacements and the adjusted observations are substantial (i.e., the difference between the orange and purple dots). This discrepancy is caused by arc 5 (a5), which exhibits behavior that deviates from the other arcs. As a result, the OMT is rejected and a w-test is applied, and the ambiguities of arc 5 are adapted for these epochs. Subsequently, the displacement time series of the point is re-estimated using the corrected observations.

necessarily the arcs to the points closest by.

In Fig. 5.12, the estimated parameters for secondary point 2 are shown, where a) shows the total estimated displacement time series, including noise, (in green), which is the sum of the reduced phase (in purple, in b) and the thermal displacement (in orange). In c) we show the corresponding σ values per epoch. These results clearly demonstrate the strength and importance of incorporating a time-varying stochastic model. The σ values per epoch are derived from the network adjustment performed on the reduced phase timeseries, φ'_{ij} , which is in fact the non-thermal displacement plus noise, where the estimated quality depends directly on the quality of the DD arc phases, Q_y , which is inferred from the amplitude time series of the two points forming the arc. Notably, the first two years of the time series are characterized by lower quality values and also show a noisier displacement behavior. This illustrates that applying a single (time-invariant) stochastic value would misrepresent the underlying variability and lead to misleading interpretations or unreliable statistical testing. The strength of the time-varying stochastic model therefore lies not only in the improved reliability of the estimation process, but also in enabling correct interpretation and hypothesis testing.

Figs. 5.12d–l show variables related to the arcs that connect secondary point 2 to the control network. These arcs are also visualized spatially in Fig. 5.10. In Figs. 5.12d, g, and j the reduced phase time series for the three arcs can be seen in orange (i.e., \underline{y} in Eq. (5.13)), while the adjusted observations, \hat{y} , are shown in purple. In the last two years of the time series, a discrepancy between the observed and adjusted values can be observed, see also the residuals shown in Figs. 5.12f, i, and l. This discrepancy leads to the rejection of the OMT and a w-test, see Eq. (5.8), is applied to identify the problematic arc, revealing that arc 5 is the source of the inconsistency. After adapting the reduced phase by 2π for arc 5, the adjustment is recomputed, where results are shown in green and blue in Figs. 5.12e, h, and k, respectively. This example illustrates how a quality-optimized network, i.e., a CORG network, in which each arc observation is weighted according to the stochastic model introduced in Chapter 2, can aid in identifying and correcting erroneous arcs, while simultaneously ensuring that the highest-quality arcs are retained for parameter estimation.

5.7.3. CONNECTION OF TWO LOCAL NETWORKS

When the AoI becomes too large, e.g., covering the entire city of Amsterdam, a single local CORG network is no longer sufficient, as points could only be connected to the control network via long arcs. In such cases, multiple local networks can be connected via connection points, as described in Sec. 5.5.

The base network is defined as all points within an 700-meter radius of the control network, shown in red in Fig. 5.13. All parameters in this network are estimated relative to the datum, i.e., the reference point, (black star) and serve as the datum when the free network (in green) is connected to it. The two networks are connected through 149 connection points, shown in purple.

For all estimated point parameters, i.e., the relative cross-range distance, thermal expansion factor, and reduced phase per epoch, we estimate the offset parameter z

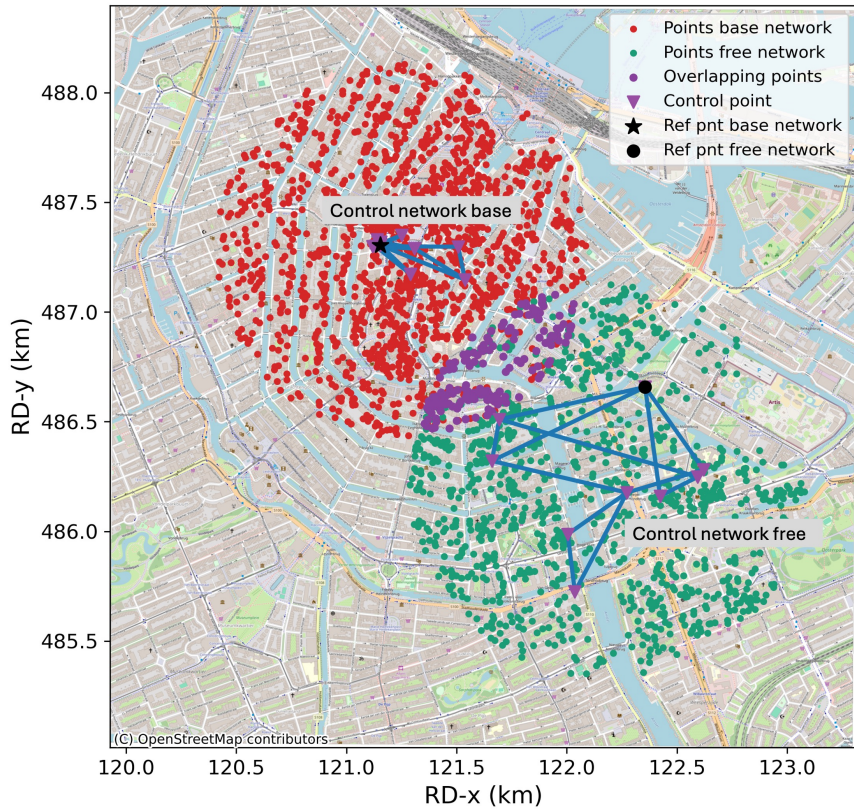


Figure 5.13: The connection of a free network (shown in green) to a base network (shown in red) is done via the connection points that are shown in purple. The parameters of the connection points are estimated both relative to the datum in the free network and to the datum in the base network. Immediately estimating the parameters of the points in the free network relative to the control network in the base network would result in too long arcs.

using the mathematical model defined by Eqs. (5.17) and (5.18). With 426 epochs this results in 428 estimated offset parameters z .

We show two examples of z in Figs. 5.14a and b, which show z for the reduced phase at epoch 9 and the relative cross-range distance, respectively. Each point on the vertical axis represents the difference between \underline{u} and v , i.e., the difference between the estimated parameter relative to the free network datum, and the datum in the base network. The error bars reflect only the quality of \underline{u} , as the parameters relative to the datum in the base network act as the datum, i.e., they are fixed. After the estimation of z , the OMT is applied, and if rejected, a w-test is performed to detect and remove potential outliers. In Fig. 5.14 it can be seen that for $z^{\phi'}$, H_0 was rejected and several outliers were identified and removed, shown in red.

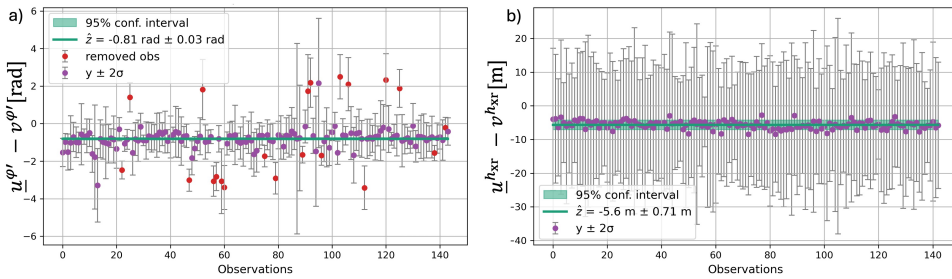


Figure 5.14.: For the connection points shown in purple in Fig. 5.13, we compute the difference between the estimated reduced phase at epoch 9 relative to the local datum in the base network, and the same parameter estimated relative to the local datum in the free network, see a). b) shows the differences in relative cross-range distance. The error bars denote 2σ confidence intervals based on the uncertainty in the estimates relative to the datum of the free network. The green horizontal line indicates the estimated value of the offset parameter z , i.e., the reduced phase (or cross-range distance) of the datum in the free network relative to the datum in the base network.

As $z^{\phi'}$ is estimated for all epochs, this results in a offset time series (see Fig. 5.15a).¹² Since the offset parameter z reflects the behavior of the reference point in the free network relative to that in the base network, we also estimated this reduced phase directly from the DD phase observations of the arc between the two reference points (shown in orange in Fig. 5.15a) for validation. We observe only minor differences between the two time-series, see Fig. 5.15b, with a mean absolute deviation of 0.3 mm.

We also compared the quality of the estimates (σ values) using both methods, see Fig. 5.15d. It can be seen that the estimates obtained via the adjustment (based on all connection points) have a significantly higher quality than those based on the DD phase observations of the arc. The mean standard deviation for the adjustment-based time series is 0.15 radians, compared to 0.48 radians for

¹²Note that we interpret the reduced phase as the non-thermal displacement phase, as the static components (the thermal displacements and cross-range phase) are removed from the observed phase.

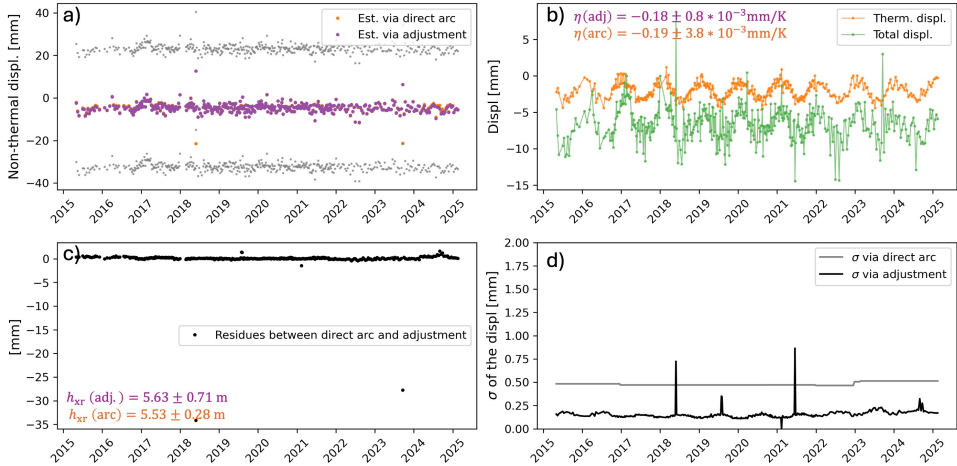


Figure 5.15.: Estimated offset parameters of the free network relative to the base network. a) shows $z^{\varphi'}$ for all epochs. Note that this is in fact the reduced phase that we transformed to meters. We interpret it as the non-thermal displacements since the static phase components are removed. The purple time series are the estimated values resulting from the adjustment and all connection points. The time series in orange results from the parameter estimation from the DD phase values between the two reference points directly. In c) we show the differences between the two timeseries. d) shows the corresponding σ values of the estimated time series, it can be seen that the result based on the adjustment is much more precise compared to the results obtained from the DD phase observations. The thermal expansion factor was also estimated, which is shown in b).

the DD-based series. This difference is expected, as the adjustment incorporates information from 149 connection points rather than relying on a single arc. The σ values from the adjustment do show a seasonal pattern, likely due to some leakage between the estimated thermal expansion factor and reduced phase relative to one of the reference points of the connection points. Finally, we observe that the independently estimated thermal expansion factor and relative cross-range distance also show a close match between both methods. The close agreement between the reduced phase (or non-thermal displacement), thermal expansion factor, and relative cross-range distance estimated via the direct arc (based on DD observations) and the adjustment using connection points supports the validity of our proposed method using the three step approach of the optimized network.

With the estimated offset parameters \hat{z} , all points in the free network can now be expressed relative to the datum in the base network using Eq. (5.19). Since we also have the associated covariance matrix Q_z , uncertainty can be properly accounted for by applying covariance propagation.

As a result, for all points in both the free and base network, we now obtain an estimated reduced phase time series, expressed relative to the local datum in the base network, together with a corresponding time-varying quality value. From this point on, these σ values are referred to as the **prior** quality values. They result from the full covariance propagation throughout all processing steps: starting from the stochastic model used for the DD phase observations per arc, we derive the corresponding reduced phase uncertainties per arc. By systematically applying covariance propagation at every subsequent network adjustment step, including the control network adjustment, the extension of the network with secondary points, and finally the connection between the free and base networks, we obtain a time-varying quality of the reduced phase for the *points* in the network.

Additionally, we also compute **posterior** quality values, which are obtained by fitting a second-degree polynomial to each time series and calculating the variance of the residuals. Note that this approach is actually something we ideally should not do, but we apply it here to compare and verify whether our sigma values are meaningful. In Figs. 5.16a and b we show the average posterior and prior σ values, respectively, for all time series relative to the local datum in the free network. We observe that the prior σ values are slightly lower than the posterior values, as also illustrated in Fig. 5.16e. While the prior values appear somewhat optimistic, there is a correlation between the two sets of values. Moreover, the posterior sigma values are estimated by fitting a second-degree polynomial, which means that more complex displacement behavior is effectively attributed to noise. Note that the values shown here are mean values, while in reality each epoch has its own σ value.

Moreover, it might be expected that, after the transformation of the points in the free network, the quality of these time series becomes worse since the offset parameter z has an uncertainty as well, defined by Q_z . To assess this, we compared σ values before and after the transformation, shown in Figs. 5.16c and d. We found that the posterior σ values were on average increased by 0.14 radian, whereas the priori σ values are increased by 0.03 radians.

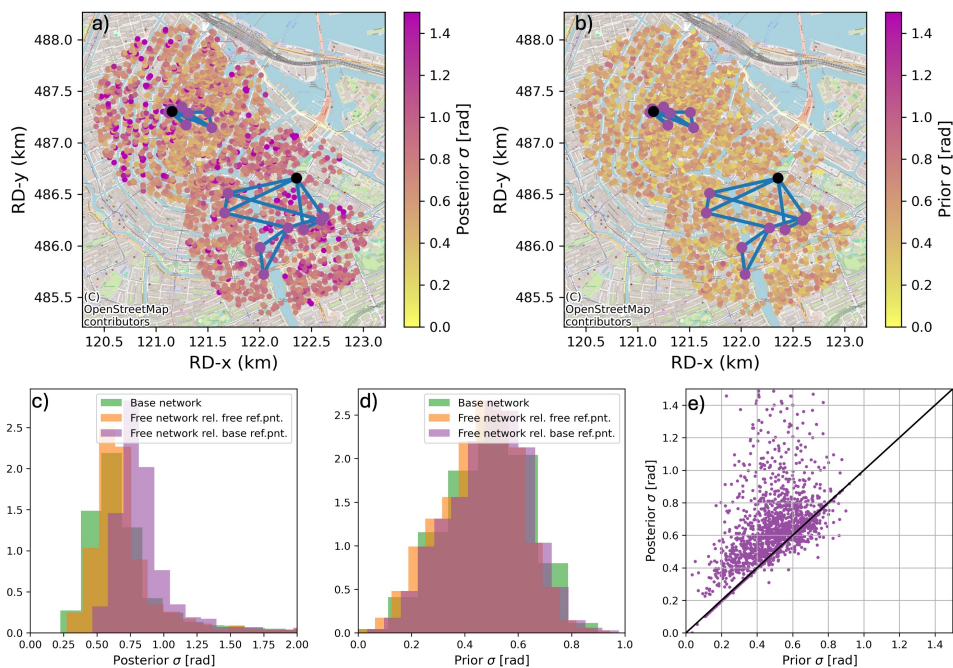


Figure 5.16.: After the adjustment, reduced phase time series and corresponding σ values are obtained for all points. For each point, we compute the mean prior σ value, shown in b), which results from covariance propagation in the adjustment steps. Additionally, a polynomial is fitted to each reduced phase time series, and the standard deviation of the residuals is calculated — this defines the posterior σ , shown in a). e) shows the correlation between both estimates, indicating that the posterior σ values are slightly higher. c) and d) show the change in posterior and prior σ values, respectively, after transforming the free network points into the reference frame of the base network.

5.7.4. CHANGING THE REQUIREMENTS

As discussed, the design of the CORG network is inherently application-dependent (Sec. 5.2.2). While the results section focused on a single example, different application requirements may lead to different InSAR products.

In this study, an additional uncertainty of 1.2 radians per kilometer of arc length was assumed when defining arc quality (Sec. 5.3.2). A lower value would allow longer arcs and could result in a more uniformly distributed control network. The criteria imposed on the control network also affect its design: some applications require many control points, whereas others can tolerate fewer points with higher precision. Likewise, application-specific knowledge can inform the arc parameter estimation by helping define the functional model and parameterization of the unknown parameters.

The necessity of all three network design steps likewise depends on the application. For monitoring critical infrastructure, we recommend building the control network near the asset of interest. Scatterers on the infrastructure should then be connected to this network, which serves as a local datum, via multiple arcs, ensuring redundancy and improving the reliability of detecting anomalous behavior. On the other hand, if the objective is to map wider deformation patterns over large areas, more points, in multiple local networks must be connected.

Ultimately, only the end user can define the quality requirements of the InSAR product, as these are determined by the intended application and use of the results.

5.8. DISCUSSION

In Sec. 5.6, we discussed the covariance between the estimated reduced phase from different arcs affect the precision with which we can estimate the reduced phase for points. In this chapter, we adopt the variance–covariance matrix of the observed DD phase per arc, while assuming no correlation between different arcs for the VCM of the reduced phase. However, this assumption might not be entirely correct as there might be a non-zero covariance term. Therefore, this should be investigated in further studies. Another option is to perform the arc parameter estimation and the network adjustment at the same time. This would allow to properly incorporate the covariance between different arcs as we do know the covariance term between arcs for the DD phase observations.

The results shown in Fig. 5.16e suggest that the stochastic model as proposed in Chapter 2 for the phase observations may be too optimistic, as the propagated quality based on this stochastic model appears to be better than the posterior quality derived from residuals. Two hypotheses can be considered. As discussed earlier, unmodeled deformation may still be present in the posterior residuals. A second hypothesis is that the effect is caused by unmodeled atmospheric delays. To mitigate this effect, increasing the distance-dependent phase term per kilometer of arc length (which accounts for unmodeled atmospheric signals) will reduce the predicted arc quality.

5.9. CONCLUSIONS

Since the network design directly affects both the quality and the values of the estimated relative parameters, it forms a crucial step in any InSAR processing. This implies that, for each application, an optimal network configuration exists. We define a Confidence-Optimized Robust Geodetic (CORG) network as one that optimizes the estimation quality for the points of interest. However, such a network can only be determined once the quality requirements, which are user- and application-specific, are defined. As a result, each application demands its own tailored network. The commonly adopted Delaunay triangulation is therefore inherently sub-optimal, as it does not account for quality requirements and always yields the same static configuration.

To identify the CORG network, a stochastic model for the double-differenced phases is required. It enables to (i) prioritize arcs based on their expected quality prior to the parameter estimation, (ii) estimate physical arc parameters together with their full variance-covariance matrices, and (iii) rigorously propagate these uncertainties to the estimated point parameters. This last step is critical: without reliable uncertainty information, interpretation of the estimated parameters becomes meaningless. In addition, (iv) the stochastic model allows for proper statistical testing of the network adjustment. Since the stochastic model used here is time-dependent, this testing can be performed per epoch, allowing arcs to be individually weighted or rejected at each time step.

Rather than adjusting the CORG network on explicitly unwrapped phases, it should be adjusted in the parameter space as this allows each arc to have its own specific mathematical model to estimate these parameters from the DD phases.

Finally, the three-step strategy by (i) designing a small, high-quality control network, (ii) connecting secondary points directly to it, and (iii) connecting local networks through connection points, keeps every point as close as possible to the reference datum. This limits the propagation of errors and enhances the reliability of the estimates. Unlike commonly used approaches, where points might be connected to the reference datum via long chains of arcs, our method ensures a more direct and robust link to the reference datum. Moreover, this multi-step approach offers the flexibility to adapt the CORG network design to the needs of specific applications. Some applications require a network that spans a wide area, and therefore all steps are needed, while others only require a small network consisting only of high quality points. This makes the method more flexible than the commonly adopted Delaunay network.

6

INSAR GEOMETRY AND 3D DISPLACEMENT ESTIMATION

InSAR observations are only sensitive to the projection of the 3-dimensional (3D) displacement vector onto the satellite's line-of-sight (LoS) direction. Estimating the full 3D displacement vector from these observations yields an underdetermined inverse problem because the near-polar orbit geometry of SAR satellites typically results in only two independent viewing geometries. This chapter revisits the fundamentals of InSAR geometry, clarifies key concepts such as decomposition and projection, and introduces the null line and null-line-aligned (NLA) coordinate system. These concepts provide a rigorous foundation for unbiased displacement estimation and interpretation, addressing common pitfalls in current practice. Based on this framework, we provide specific recommendations for for generating and interpreting InSAR displacement products.

This chapter is published as: W. S. Brouwer and R. F. Hanssen. "A treatise on InSAR geometry and 3-D displacement estimation". In: *IEEE Transactions on Geoscience and Remote Sensing* 61 (2023), pp. 1–11. DOI: 10.1109/TGRS.2023.3322595. <https://doi.org/10.1109/TGRS.2023.3322595>

6.1. INTRODUCTION

IT is well known that InSAR phase observations are only sensitive to the projection of the 3D displacement vector onto the radar line-of-sight (LoS) direction, along a plane orthogonal to the LoS [80]. This projection, d_{LoS} , in a Cartesian east, north, up (ENU) coordinate system is described by

$$d_{\text{LoS}} = P_{\text{LoS}^\perp} d_{\text{ENU}}, \quad (6.1)$$

where $P_{\text{LoS}^\perp} = [\sin\theta \sin\alpha_d, \sin\theta \cos\alpha_d, \cos\theta]$ is the orthogonal projector onto the line of sight, $d_{\text{ENU}} = [d_e, d_n, d_u]^T$ is the 3D displacement vector in east, north, and up direction, respectively, θ is the incidence angle towards the radar, and α_d is the azimuth of the zero-Doppler plane at the position of the target, in the direction towards the satellite, see Fig. 6.1. In the early years of InSAR, one viewing geometry was used for estimating displacements [122, 123, 211]. However, the possibility to combine ascending and descending orbits imaging the same area of interest triggered attempts to estimate the 3D displacement vectors [63, 69, 94, 204]. Evidently, to estimate the full 3D displacement vector, one would need three independent viewing geometries, using three different P_{LoS^\perp} projectors forming a full rank matrix with a low condition number [164]. Yet, while the near-polar orbits of contemporary SAR missions cause an imaging geometry that differs significantly between ascending and descending orbits, it does not for adjacent tracks [150, 204]. As a result, the sensitivity is rather unbalanced for the three Cartesian directions [80]. Moreover,

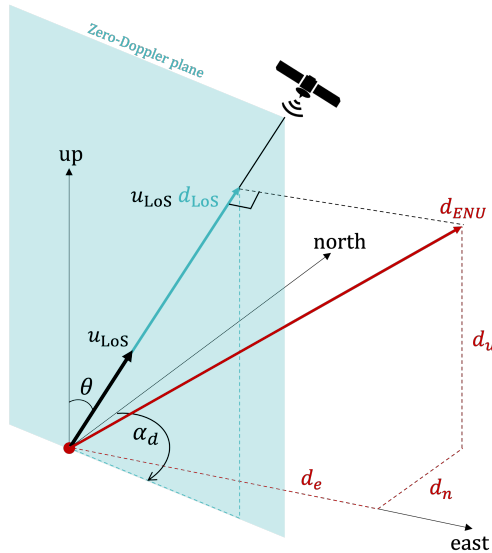


Figure 6.1.: Schematic overview of the projection of the displacement vector d_{ENU} onto the LoS direction of a satellite in a descending orbit. The LoS direction of the satellite can be described with two angles: the incidence angle θ and the azimuth of the zero-Doppler plane α_d . Those angles are described at the position of the target.

in many practical situations only two LoS observation geometries are available, i.e., ascending and descending, resulting in an underdetermined system with an infinite amount of possible solutions.

The way in which this problem is typically handled in InSAR literature and operational practice often leads to biased estimation, and requires more standardization and mathematical and semantic rigor. Concepts such as *decomposition* and *projection* need to be distinguished, substantiated assumptions that can serve as boundary conditions, need to be explicitly stated. In this study, we provide a comprehensive overview of the topic, proposing necessary terminology and estimation techniques for the inverse problem. We discuss the limitations of the decomposition and propose a standardized approach. In Sec. 6.2 we give an overarching mathematical framework rooted in linear algebra, building on previous work by [80, 94, 204] and [69]. In Sec. 6.3 we explicitly state the conditions for a successful inversion, and in Sec. 6.4 we introduce the concept of the *null line*, which can be used to propose a coordinate system that is intrinsically unbiased. Using these concepts, we evaluate current practice and identify three types of typical geometric flaws encountered in literature in Sec. 6.5 and provide recommendations for InSAR product generation and interpretation in Sec. 6.6.

6.2. THEORY

To solve for the full 3D displacement vector, several conditions (all necessary but individually not sufficient) need to be satisfied. Therefore, we first review the relevant InSAR geometry and the forward model in Sec. 6.2.1 and 6.2.2, respectively.

6.2.1. THE VIEWING GEOMETRY

The estimated relative displacements resulting from InSAR parameter estimation are projections of the 3D displacement vector onto the line-of-sight (LoS) direction defined at the position of the target, see Eq. (6.1). The LoS direction depends on the viewing geometry towards the satellite. Therefore, the LoS direction is described using two angles:¹ the azimuth of the zero-Doppler plane at the Earth's surface, α_d , and the incidence angle, θ , see Fig. 6.1.

AZIMUTH OF THE ZERO-DOPPLER PLANE

Most SAR satellites operate from retrograde sun-synchronous near-polar orbits. While the orbital plane of the satellite has a fixed inclination, the satellite has a time-varying orbital heading α_h , which is the angle between the velocity vector of the satellite and the geometrical north. Most contemporary SAR observations are taken at zero-Doppler [80], which defines the zero-Doppler plane (ZDP): the plane perpendicular to the heading of the satellite. Thus, the LoS vector lies in the ZDP.

The heading, α_h and the orientation of the ZDP—in a satellite-centered coordinate frame—are different from the direction of the velocity vector and the azimuth of the

¹These angles are not to be confused with the heading angle and look angle of the satellite, respectively, as we will discuss below.

ZDP, α_d , in a target-centered coordinate frame on the Earth's surface, see Fig. 6.2. This effect is caused by the side-looking geometry of the SAR and the non-parallel nature (convergence) of the Earth's meridians. Additionally, the azimuth of the zero-Doppler plane is range dependent. These effects are relevant when computing the viewing geometry. Thus, the projector P_{LoS^\perp} should be defined using α_d rather than using α_h .

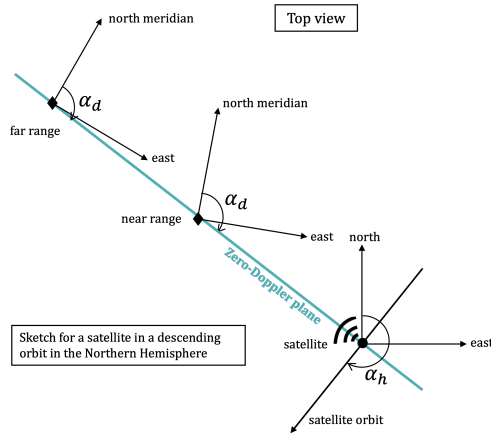


Figure 6.2.: Two targets on Earth (black diamonds) observed from a satellite (black dot) in a descending orbit in the Northern Hemisphere. The velocity vector of the satellite has azimuth angle α_h with respect to the geographical north. Due to the meridian convergence, the north direction at the Earth's surface at near range (nr) differs from the north direction at far range (fr). Thus, the orientation of the zero-Doppler plane (in green) depends on the target position in range, i.e., $\alpha_{d,nr} \neq \alpha_{d,fr}$.

INCIDENCE ANGLE

The incidence angle, θ , refers to the nominal (ellipsoidal) incidence angle, i.e., the angle between the normal vector on the local ellipsoid, at the position of the target, and the line of sight towards the satellite in the ZDP. The incidence angle differs from the satellite look angle θ_l , which is the angle between the LoS direction and the nadir of the satellite sensor, due to the curvature of the Earth, see Fig. 6.3. Moreover, the nominal incidence angle varies with the range direction resulting in different incidence angles for different targets (pixels) within the same image [53].²

As both the incidence angle and azimuth of the ZDP are range dependent, they are correlated. Due to the meridian convergence, the orientation of the target-centered coordinate system with respect to the satellite-centered coordinate system differs from near to far range, see Fig. 6.2. Therefore, α_d is range dependent, i.e., $\alpha_{d,nr} \neq \alpha_{d,fr}$ where nr and fr represent near and far range, respectively. The interdependence between θ and α_d is visualized in Fig. 6.4 for Sentinel-1 acquisitions

²For example, the incidence angle for the Sentinel-1 Interferometric Wide swath varies between 29° and 46°.

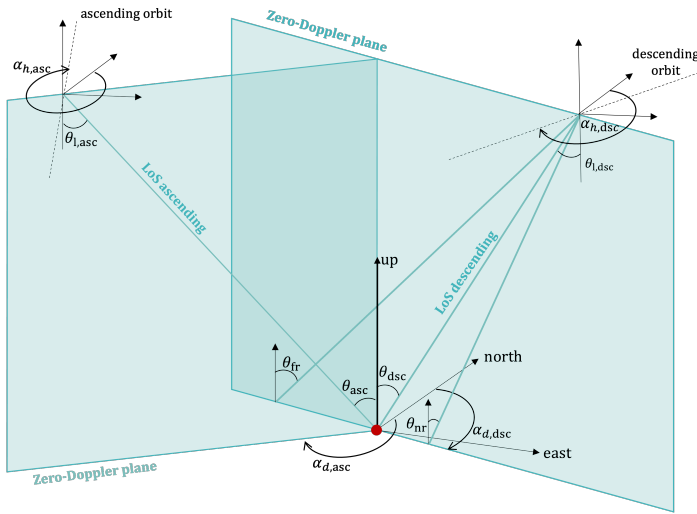


Figure 6.3.: Schematic overview of the viewing geometry. The heading angles $\alpha_{h,asc}$ and $\alpha_{h,dsc}$ are the azimuth angles of the velocity vectors of the satellites with respect to the geometrical north. α_d is the azimuth of the zero-Doppler plane, at the position of the target (red dot), in the direction towards the satellite. The incidence angle is the angle between the LoS vector and the local zenith and varies from near to far range, i.e., $\theta_{fr} > \theta_{nr}$.

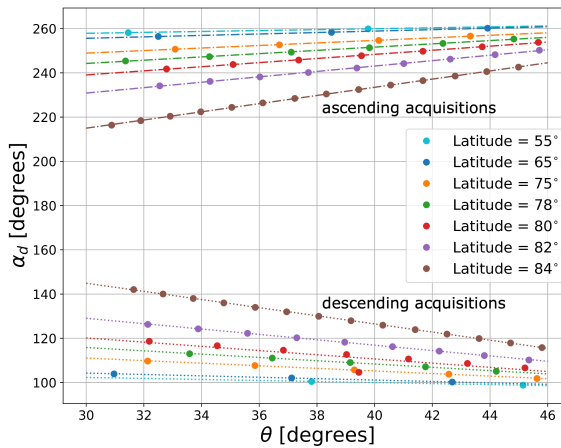


Figure 6.4.: Viewing geometries towards all visible Sentinel-1 swaths (circular marks), for different latitudes on the Northern Hemisphere, at an arbitrary longitude 40°E . For ascending acquisitions (top), the correlation is positive, for descending acquisitions (bottom), it is negative. For the Southern Hemisphere this is reversed.

at sea level with a varying latitude and an arbitrary longitude, here 40°E, for all available ascending (top) and descending (bottom) acquisitions [118].

6.2.2. FORWARD MODEL

The displacement d_{LoS} of a target observed from a satellite is the orthogonal projection of d_{ENU} onto the LoS direction, see Eq. (6.1). We refer to this as a *forced* projection, as it is an implicit autonomous operation. As Eq. (6.1) represents the displacement as a scalar, it requires a directional unit vector to specify its direction, i.e.,

$$d_{\text{LoS}} \mathbf{u}_{\text{LoS}} = \text{diag}(P_{\text{LoS}^\perp}) d_{\text{ENU}}, \quad (6.2)$$

where \mathbf{u}_{LoS} is the LoS unit vector, defined as

$$\mathbf{u}_{\text{LoS}} = \begin{bmatrix} \mathbf{u}_1 \\ \mathbf{u}_2 \\ \mathbf{u}_3 \end{bmatrix} = \begin{bmatrix} \sin\theta \sin\alpha_d \\ \sin\theta \cos\alpha_d \\ \cos\theta \end{bmatrix}, \quad (6.3)$$

and P_{LoS^\perp} refers to a projector *onto* the LoS, *along* a plane orthogonal to the LoS unit vector, see Eq. (6.1). The LoS unit vector has its origin at the target, i.e., motion towards the satellite yields a decrease in slant range.

Given this forward model, we evaluate the inverse model to estimate the displacement parameters and discuss the necessary and sufficient conditions for this estimation.

6.3. CONDITIONS FOR THE INVERSE MODEL

Estimated LoS displacements are one-dimensional and may be difficult to interpret by end-users, who are mostly interested in the ‘real’ (3D) displacements. This requires a *decomposition* of the LoS displacements, i.e., the inverse problem [172]. The functional relation of Eq. (6.1) is therefore extended to a full mathematical model, including

$$E\left\{ \underbrace{\begin{bmatrix} d_{\text{LoS}}^{(1)} \\ d_{\text{LoS}}^{(2)} \\ \vdots \\ d_{\text{LoS}}^{(m)} \end{bmatrix}}_y \right\} = \underbrace{\begin{bmatrix} P_{\text{LoS}^\perp}^{(1)} \\ P_{\text{LoS}^\perp}^{(2)} \\ \vdots \\ P_{\text{LoS}^\perp}^{(m)} \end{bmatrix}}_A \underbrace{\begin{bmatrix} d_e \\ d_n \\ d_u \end{bmatrix}}_x, \text{ and} \quad (6.4)$$

$$D\left\{ \underbrace{\begin{bmatrix} d_{\text{LoS}}^{(1)} \\ d_{\text{LoS}}^{(2)} \\ \vdots \\ d_{\text{LoS}}^{(m)} \end{bmatrix}}_y \right\} = \underbrace{\begin{bmatrix} Q_{\text{LoS},1} & 0 & \dots & 0 \\ 0 & Q_{\text{LoS},2} & \dots & 0 \\ \vdots & \vdots & \ddots & \vdots \\ 0 & 0 & \dots & Q_{\text{LoS},m} \end{bmatrix}}_{Q_y}, \quad (6.5)$$

where \underline{y} is the observation vector, containing vectors $\underline{d}_{\text{LoS}}^{(1)}$ until $\underline{d}_{\text{LoS}}^{(m)}$, which are m sets of LoS displacement observations. The underline indicates the stochastic nature of the vector. Each vector $\underline{d}_{\text{LoS}}^{(i)}$ represents an independent viewing geometry (orbital position), and contains the observations from all scatterers within the same region of uniform motion (RUM, discussed in Sec. 6.3.2), which we henceforth term a *set*. The size of each set can be different since the number of available coherent scatterers within a RUM can differ. $E\{\cdot\}$ and $D\{\cdot\}$ are the expectation and dispersion operator, respectively, and $Q_{\text{LoS},i}$ is the variance-covariance matrix of an independent observation set. When $\underline{d}_{\text{LoS}}^{(i)}$ has size $p \times 1$ there are p scatterers within the RUM for that particular viewing geometry. $Q_{\text{LoS},i}$ is a $p \times p$ diagonal matrix with the variances of the LoS observations on the diagonal. For small RUMs (< 100 m) the off-diagonal elements are equal to zero, since all observations represent different uncorrelated physical scatterers acquired at different times and the atmospheric delay can be considered as constant for all scatterers [80]. For larger RUMs this assumption may no longer be valid and the off-diagonal terms will depend on the distance between the scatterers.

The system of observation equations can be solved with at least three sets of LoS observations, under the condition that they are spatio-temporally coinciding and independent (STCI, discussed in Sec. 6.3.1). The row for the first set in the design matrix A is the projection of the 3D displacements onto the LoS vectors towards the first satellite position, cf. Eq. (6.1). We assume that for observations within one set, the angles θ and α_d are constant within the RUM.

When $m \geq 3$, the unknown displacement parameters in vector x can be estimated using direct inversion or Best Linear Unbiased Estimation [180], i.e.,

$$\hat{x} = \begin{cases} A^{-1}y, & \text{for } m = 3, \text{ and} \\ Q_{\hat{x}}A^TQ_y^{-1}y & \text{for } m > 3, \text{ with} \end{cases} \quad (6.6)$$

$$Q_{\hat{x}} = \begin{cases} A^{-1}Q_y(A^{-1})^T, & \text{for } m = 3, \text{ and} \\ (A^TQ_y^{-1}A)^{-1} & \text{for } m > 3. \end{cases} \quad (6.7)$$

For a successful estimation of the unknown displacement parameters this approach needs to satisfy several conditions, which are discussed below.³

6.3.1. SPATIO-TEMPORALLY COINCIDING INDEPENDENT (STCI) LOS OBSERVATIONS

The mathematical expression of Eq. (6.6) is only valid if all LoS observation sets from different viewing geometries are unambiguously linked to the same physical displacement signal, x . In this context, we introduce the condition of *spatio-temporally coinciding* and *independent* (STCI) LoS observations, i.e., (i) the same scatterers, from (ii) an object that is not subject to internal deformation, are observed (iii) simultaneously and (iv) from sufficiently different viewing geometries.

³Within this work we focus on the decomposition of interferometric LoS observations, i.e., we do not consider adding pixel offset tracking or GNSS observations.

Obviously, the STCI condition is never fulfilled for a single target, since point scatterers (PS) observed from one orbital viewing geometry typically do not coincide with PS from another viewing geometry, apart from, e.g., lamp posts [215] or integrated geodetic reference stations (IGRS) [81]. Moreover, scatterers close to each other are not necessarily stemming from the same object, considering, e.g., a scatterer on the roof of a house and a scatterer nearby on the street, which may represent different deformation phenomena [107]. Added to this, different (parts of) objects can show different deformation phenomena [47, 206]. Finally, SAR acquisitions from different viewing geometries are never taken at the same moment, and since deformation phenomena, by definition, change over time this will result in incomparable displacement parameters. Especially for rapidly changing deformation phenomena such as landslides [196] or highly dynamic soils [35], it may be impossible to assume that observations from different epochs are comparable.

Consequently, as the strict STCI condition can never be met, the success of a decomposition is highly dependent on relaxing this conditions using additional assumptions.

6.3.2. REGION OF UNIFORM MOTION

A plausible assumption that can relax the STCI condition follows from identifying *Regions of Uniform Motion* (RUMs), defined such that points that fall within a single RUM behave uniformly, driven by the same deformation phenomenon. Thus, only after defining a RUM (and aligning the different data sets in time) it will be possible to decompose the LoS observations into the unknown displacements parameters. In many cases, defining a RUM can be difficult, since it can easily contain scatterers that represent different deformation phenomena [107].

6.3.3. DATUM CONNECTION

LoS observations from different observational sets should be referenced to the same spatio-temporal datum, i.e., the same spatial reference point and the same temporal reference epoch. Commonly, different viewing geometries will result in different spatial reference points. Therefore, it is at least required that the reference points of different viewing geometries represent the same deformation phenomenon i.e., the same RUM. Temporally, the selected reference SAR acquisitions, per stack, need to be aligned to refer to the same displacement parameters, x , in Eq. (6.6). Spatial or temporal interpolation may be required for this purpose. For displacement signals which are rapidly changing between epochs this interpolation will be more influential.

6.3.4. FULL RANK SYSTEM

To unambiguously solve for the three unknown displacement components we require at least three sets of (STCI) observations from different viewing geometries to assure a full rank system, and consequently a unique solution. We define the *solution space* as the space that contains all possible solutions of the linear system. With only one LoS observation set, the solution space is a *solution plane* orthogonal to the LoS

displacement vector that contains the end-point of the LoS displacement vector. All points located in this plane are a possible solution to the inverse problem. The orientation of the solution plane is thus completely defined by the LoS unit vector, \mathbf{u}_{LoS} , see Eq. (6.3), as it is normal to the solution plane. The plane contains the end point of the LoS vector, see Eq. (6.2).

The equation of the solution plane with unit vector \mathbf{u}_{LoS} through the point $d_{\text{LoS}}\mathbf{u}_{\text{LoS}}$ is

$$\mathbf{u}_{\text{LoS}} \cdot (d_{\text{ENU}} - d_{\text{LoS}}\mathbf{u}_{\text{LoS}}) = 0, \quad (6.8)$$

with $d_{\text{ENU}} = [d_e, d_n, d_u]^T$, $\mathbf{u}_{\text{LoS}} = [u_1, u_2, u_3]^T$, cf. Eq. (6.3).

When two LoS observation sets are available, the solution space reduces to a line, i.e., the intersection of the two solution planes. All points on the *solution line* are a potential solution to the inverse problem, since the line contains the endpoint of the unknown displacement vector.

To solve unambiguously for the 3D displacement vector, albeit with various degrees of precision, three or more sets of LoS observations are required. Only then, there is one unique point where the three solution planes intersect. The quality of the displacement estimator $\hat{\mathbf{x}}$, see Eqs. (6.6) and (6.7), follows from error propagation as

$$Q_{\hat{\mathbf{x}}} = (A^T Q_y^{-1} A)^{-1} = \begin{bmatrix} \sigma_e^2 & \sigma_{en} & \sigma_{eu} \\ \sigma_{en} & \sigma_n^2 & \sigma_{nu} \\ \sigma_{eu} & \sigma_{nu} & \sigma_u^2 \end{bmatrix}. \quad (6.9)$$

The diagonal elements of $Q_{\hat{\mathbf{x}}}$ give the variances for \hat{d}_e , \hat{d}_n , and \hat{d}_u respectively. The requirement of working with three STCI LoS observation sets, stemming from the same RUM is a *necessary but insufficient* requirement. The three STCI LoS observation sets also need to have sufficiently different angular diversity to ensure full rank.

6.3.5. ANGULAR DIVERSITY

As almost all SAR satellites operate right-looking, orbiting the Earth in near-polar retrograde orbits, they all have very similar viewing geometries, resulting in limited angular diversity. Thus, the solution lines for each combination of any ascending and descending viewing geometry will have very similar orientations. Consequently, even with LoS observations from three viewing geometries, the inverse problem is often ill-posed [172], A is close to rank deficient, and the solution is unstable: a small difference in the LoS observations may lead to a large change in the estimated displacement components [150, 204]. This follows from the variance-covariance matrix, $Q_{\hat{\mathbf{x}}}$, of the estimated displacement components, see Fig. 6.5.

Simulating three different viewing geometries, e.g., one descending and two ascending acquisitions, we compute the precision for the estimated displacement parameters using Eq. (6.9). Simulating one scatterer per viewing geometry (Tab. 6.1) and using $\sigma_{\text{LoS}}^2 = 1 \text{ mm}^2$ for all three observations, we estimate $Q_{\hat{\mathbf{x}}}$, see Fig. 6.5a. The diagonal of $Q_{\hat{\mathbf{x}}}$ shows the variances of \hat{d}_e , \hat{d}_n , and \hat{d}_u . The precision (σ) with which we can estimate the north component is ~ 40 times larger than the simulated σ_{LoS}

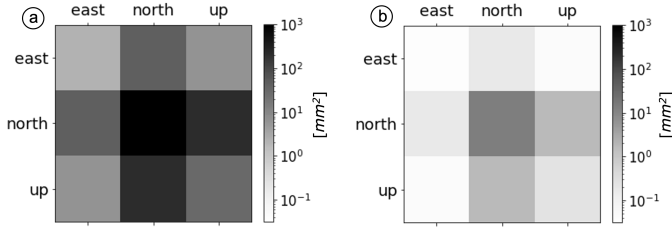


Figure 6.5.: Full variance-covariance matrix, $Q_{\hat{x}}$, see Eq. (6.9), of the estimates of the three displacement components, on a logarithmic scale. a) All observations from right-looking satellites, see Tab. 6.1. b) Two right-looking and one left-looking satellite. This yields a significant improvement in the estimate of d_n , but also the other displacement components benefit from the addition of a left-looking radar acquisition.

Table 6.1.: Characteristics of the simulated viewing geometries

	Geometry type	Incidence angle θ	Azimuth ZDP α_d
A1	ascending-1	30°	260°
A2	ascending-2	41°	261°
D1	descending-1	44°	100°

6

values. The precisions for the east and up components are much better, i.e., 1.5 mm and 5.5 mm, respectively.

One solution to improve d_n is to add a left-looking observation as suggested by [204] and [150].⁴ Fig. 6.5b shows $Q_{\hat{x}}$ for a situation where the second ascending acquisition is left looking. The precisions of the unknown parameters are now 0.3, 4.5, and 0.7 mm for d_e , d_n , and d_u respectively, which is about one order of magnitude improvement for all components. Nevertheless, σ_n is still the largest, especially considering that σ_{LoS} was 1 mm. Other options to retrieve d_n include using non-interferometric observables, such as along-track offset measurements [63], which are only feasible for smooth wide-area phenomena and large displacements, not for PS in the built environment with millimeter displacements. Finally, future multistatic squinted systems may also enable more variety in viewing geometry, see [88].

6.4. THE NULL LINE

In many practical situations, the maximum number of STCI LoS sets is two (ascending and descending). This results in an underdetermined problem with an infinite number of possible solutions. However, when the viewing geometry of the two available acquisitions is known (i.e., before we need to have actual observations) we can define the *null line*, n , which is the null space of the projection matrix A i.e. the solution to $Ad_{ENU} = 0$. The null line is visualized in Fig. 6.6, where the

⁴Left-looking geometries will be feasible with the NISAR mission [160].

blue and green arrows are the LoS unit vectors corresponding to an ascending and a descending acquisition, the blue and green planes are the null planes, and the orange line is the null line.

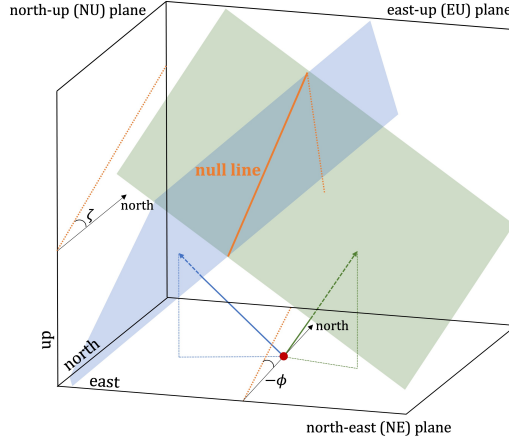


Figure 6.6.: When two LoS viewing geometries are available, the null line can be defined (i.e., the null space of the corresponding projection matrix). The orientation of the null line is defined as the intersection of the two null planes of the two available LoS vectors. Here we visualized one ascending (blue) and one descending (green) unit vector, and corresponding null planes. The null line is fully described by azimuth angle ϕ and elevation angle ζ since the position is irrelevant.

The orientation of the null line is an important metric for InSAR interpretation since we cannot, interferometrically, observe any displacement component in its direction i.e., both of the two viewing geometries have zero sensitivity in the direction of the null line. This direction is therefore valuable to know, before starting an InSAR survey as well as accompanying InSAR results. The null line is described by azimuth angle ϕ and elevation angle ζ . When the viewing geometry for each acquisition is known, the orientation of the null line can be computed from the cross product of the two normal vectors of the null planes (the LoS unit vectors):

$$\begin{aligned} n &= \mathbf{u}_{\text{LoS}}^{(1)} \times \mathbf{u}_{\text{LoS}}^{(2)} \\ &= \begin{bmatrix} \sin\theta_1 \sin\theta_2 \cos\alpha_{d,1} - \sin\theta_2 \cos\theta_1 \cos\alpha_{d,2} \\ -\sin\theta_1 \cos\theta_2 \sin\alpha_{d,1} + \sin\theta_2 \cos\theta_1 \sin\alpha_{d,2} \\ \sin\theta_1 \sin\theta_2 \sin(\alpha_{d,1} - \alpha_{d,2}) \end{bmatrix} \end{aligned} \quad (6.10)$$

where $(\theta_1, \alpha_{d,1})$ and $(\theta_2, \alpha_{d,2})$ correspond to the first and the second viewing geometry, respectively. With n it is possible to compute ϕ and ζ :

$$\phi = \tan^{-1}\left(\frac{n_1}{n_2}\right), \text{ and } \zeta = \tan^{-1}\left(\frac{n_3}{\sqrt{n_1^2 + n_2^2}}\right), \quad (6.11)$$

where n_1, n_2 , and n_3 are the east, north, and up component of n respectively.

6.4.1. NULL LINE ORIENTATION EVALUATION

To evaluate the orientation of the null line for an actual mission at an arbitrary position on Earth, we apply Eq. (6.11) to the Sentinel-1 viewing geometry, see Figs. 6.7a and b.⁵ This shows the values for ϕ and ζ , respectively the azimuth and elevation of the null line. We find that $\phi \approx 0^\circ$ for the Northern Hemisphere, but that this is not always the case for the Southern Hemisphere. Moreover, everywhere on Earth the elevation angle $\zeta > 0^\circ$.

At higher latitudes, different tracks overlap, enabling multiple ascending and descending viewing geometries per location. Therefore, Figs. 6.7a and b use the largest possible α_d per location, i.e., favorably the largest asymmetry between the two viewing geometries.

To investigate whether $\phi = 0^\circ$ can really be considered a ‘rule of thumb’ for the Northern Hemisphere for Sentinel-1, we compute ϕ and ζ for all possible combinations between ascending and descending acquisitions for latitudes varying between -75° and $+85^\circ$, at arbitrary longitude 30° , see Figs. 6.7c and d. Typically for the Northern Hemisphere, all combinations result in $\phi \approx 0^\circ$. Yet, for the higher southern latitudes, different combinations result in $\phi \neq 0^\circ$, e.g., for applications in Antarctica. Elevation angles ζ increase significantly at higher latitudes, affecting the Arctic, South America, South Africa, New Zealand, and the Antarctic.

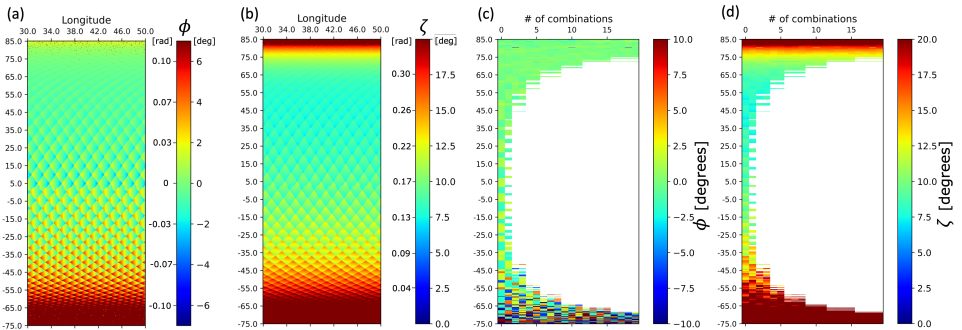


Figure 6.7.: Orientation of the null line for Sentinel-1, defined by ϕ and ζ , see Fig. 6.6. The checkered pattern is due to the S1 orbit pattern. (a): azimuth ϕ , (b): elevation ζ . Values are calculated by combining the ascending and descending observations that have a maximum azimuth of the ZDP, for each location on Earth, considering the maximum asymmetry between the two ZDP’s. This demonstrates that $\phi \approx 0^\circ$ for the Northern Hemisphere. The values for ϕ and ζ in radians are near-identical to the $\tan\phi$ and $\tan\zeta$ factors in Eq. (6.13), for the east- and up-bias, respectively. (c) and (d), ϕ and ζ values for all possible combinations between overlapping ascending and descending acquisitions. Results computed using [16].

⁵The software that computes the orientation of the null line for different satellite missions at different locations on Earth, is made available via [16].

6.4.2. IMPACT OF THE NULL LINE ORIENTATION

Frequently⁶ it is postulated that with the current orbits and viewing geometries of SAR missions, there is no sensitivity for displacement components in the north direction, and that it is therefore possible to simply ‘remove’ or ‘disregard’ d_n from the inverse problem, cf. Eq. (6.4), resulting in

$$E\left\{\underbrace{\begin{bmatrix} d_{\text{LoS}}^{(1)} \\ d_{\text{LoS}}^{(2)} \\ \vdots \\ d_{\text{LoS}}^{(m)} \end{bmatrix}}_y\right\} = \underbrace{\begin{bmatrix} \sin\theta_1 \sin\alpha_{d,1} & \cos\theta_1 \\ \sin\theta_2 \sin\alpha_{d,2} & \cos\theta_2 \\ \vdots & \vdots \\ \sin\theta_m \sin\alpha_{d,m} & \cos\theta_m \end{bmatrix}}_A \underbrace{\begin{bmatrix} d_e \\ d_u \end{bmatrix}}_x. \quad (6.12)$$

This would only be a valid approach when the orientation of the null line is $\phi = 0^\circ \wedge \zeta = 0^\circ$. However, even while ϕ may be close to zero, ζ never is. Fig. 6.5 reveals that the estimators for d_e, d_n and d_u are correlated. Therefore, removing d_n from the inverse problem will result in biased estimates for d_e and d_u , i.e.,

$$\begin{aligned} \hat{d}_e &= d_e + B_e, \text{ with } B_e = \tan\phi d_n \\ \hat{d}_u &= d_u + B_u, \text{ with } B_u = \tan\zeta d_n, \end{aligned} \quad (6.13)$$

where B_e and B_u are the biases on the estimated east and up component, respectively. The bias terms are thus the product of (i) the the orientation of the null line n , and (ii) the magnitude of the actual (but unknown) north displacement. In Tab. 6.2 we show the values for $\tan\phi$ and $\tan\zeta$ for different cities in the world. E.g., for Melbourne a 1 unit north displacement leads to a bias in the east and up component of 0.01 and 0.13 units, respectively. These values are near-identical to the azimuth ϕ and elevation ζ angles, when expressed in radians, see Fig. 6.7

Geometrically, removing d_n from the decomposition equation is equivalent to projecting both LoS observations onto the east-up (EU) plane.⁷ Thus, also the 3D

⁶e.g., [3, 96, 97, 109, 128, 143, 152, 170, 173, 207, 209]

⁷Note that this is a *discretionary* projection, and not a *forced* projection, as introduced in Sec. 6.2.2.

Table 6.2.: Scaling factors for the bias in the east and up direction for different cities in the world, indicating that a non-zero north component multiplied by the given number will yield the bias in the east and up component, respectively, see Eq. (6.13).

City	East ($\tan\phi$)	Up ($\tan\zeta$)
London	0.01	0.09
New York	0.01	0.08
Los Angeles	0.01	0.08
Melbourne	0.01	0.13
Svalbard	0	0.16
Antarctic Peninsula	0.05	0.22
Singapore	0.01	0.10

null line will be projected onto the EU plane, which yields a line that we refer to as k , see Fig. 6.8. Line k has elevation angle ξ , and as long as $\xi \neq 90^\circ$ and $\xi \neq 0^\circ$, k has both a component in the up and east direction, i.e., k contains infinitely many combinations of d_e and d_u . Consequently, it is not possible to give unbiased estimates for both d_e and d_n . If and only if $\phi = 0^\circ$, line k has no component in the east direction and $\xi = 90^\circ$, yielding an unbiased d_e and a biased d_u component.

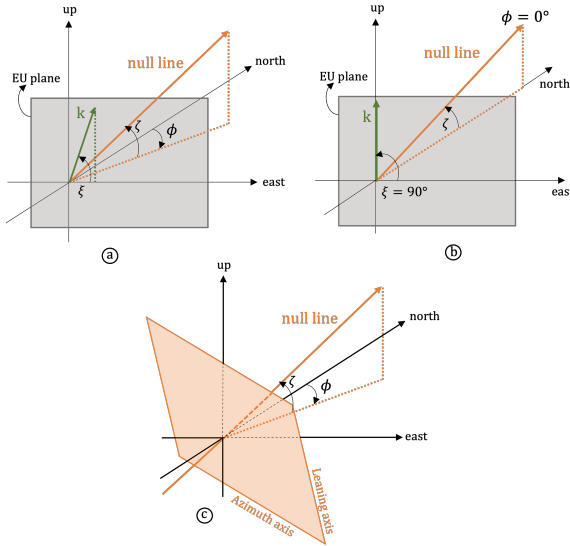


Figure 6.8.: The orientation of the null line n in the ENU reference frame is given by azimuth angle ϕ and elevation angle ζ . The projection of n onto the east-up (EU) plane is line k which has elevation angle ξ . In (a), $\phi \neq 0^\circ$ and $\zeta \neq 0^\circ$ and therefore k has a component in the east and up direction, i.e., $\xi \neq 90^\circ$. In (b), $\phi = 0^\circ$ and therefore $\xi = 90^\circ$, k only has a component in the up direction. In (c) we show the orientation of the NLA frame with the plane spanned by the Leaning axis (with elevation angle $\zeta + 90^\circ$) and Azimuth axis (with azimuth $\phi + 90^\circ$) in orange. The null line is orthogonal to this plane.

6.4.3. THE NULL LINE ALIGNED (NLA) FRAME

Using the concept of the null line with its unique orientation in 3D space, we propose a *null line aligned* (NLA) coordinate system with the first axis in the local horizontal plane, the second axis aligned along the null line, and the third one complementing the right-handed 3D Cartesian system, see Fig. 6.8c.

The plane orthogonal to the null line (i.e., spanned by the first and third axes) is termed the NLA-plane and has the unique characteristic that an orthogonal projection of any displacement vector onto that plane will not influence (bias) the two in-plane components. This characteristic of unbiasedness makes the NLA system optimally suited for direct usage in mathematical or geophysical models, as opposed

to the frequently-used⁸ east-up (EU) plane, which is biased by definition. Obviously, intuitive interpretability of NLA results and visualizations may require some training.

Using the NLA acronym as mnemonic, the axes can be referred to as the Null-line (axis), the Leaning axis, which is tilted backward with an elevation angle of $\zeta + 90^\circ$, and the Azimuth axis, which is horizontal with azimuth $\phi + 90^\circ$, see also Fig. 6.8c.

Projecting the two LoS observation vectors independently onto the NLA-plane allows for the simple (and unbiased) retrieval of the resultant vector.

6.5. EVALUATION OF CURRENT PRACTICE

While the geometry of InSAR follows from conventional linear algebra, its application in practice is conditional to assumptions and requires strict adherence to the conditions formulated in Sec. 6.3. Evaluating contemporary literature on InSAR geometry shows that this is not always the case. We identify three types of typical geometric flaws in InSAR, related to attribution, projection, and decomposition.

6.5.1. ATTRIBUTION

Attribution errors occur when the line-of-sight observation is literally attributed to one displacement direction (usually the vertical), given only a single viewing geometry, without projection and without further justification. Obviously, this is erroneous, and results in a severe underestimation (bias) of vertical displacements proportional to $(\cos\theta)^{-1}$, i.e., up to 40%, see Eq. (6.1). While explicit attribution errors were more common in the early days of InSAR, ambiguous statements or colorbar labels can still be found in recent literature and products.⁹ Moreover, describing LoS motion with words such as 'subsidence' adds another layer of semantic confusion.¹⁰ Attribution errors can be easily avoided by explicitly stating prior assumptions and using unambiguous axes and colorbar labels.

6.5.2. PROJECTION

Projection errors occur, e.g., when LoS displacement estimates are actually '*projected onto the vertical*,' (PoV) but are subsequently presented as '*vertical displacements*'. Obviously, these two estimates would only be identical under the assumption that any non-vertical displacement component of the 3D displacement vector is zero. Since this assumption is in many cases incorrect, e.g., for landslides, but even for subsidence bowls, it leads to a biased estimate. Such a bias can have a significant impact combined with a small likelihood of being detected.¹¹ Often, explicit assumptions on the non-existence of the horizontal component are lacking.¹² Typically, projection errors go hand in hand with indistinct verbs, such as 'converted', 'transformed', 'computed', 'calculated', or 'determined'. These all suggest that there

⁸e.g., [40, 97, 109, 128, 209]

⁹e.g., [161, 166, 174, 213, 214]

¹⁰e.g., [161, 169]

¹¹e.g., [12, 78, 138, 139, 171]

¹²e.g., [2, 149, 159, 168]

is a unique relation between the LoS displacements and the vertical displacements, which is in general incorrect.

6.5.3. DECOMPOSITION

The most frequently occurring geometric InSAR fallacy is a *decomposition error*, which occurs when the existence of a null space is ignored, see Sec. 6.4. A typical example of a decomposition error is the suggestion that *by combining an ascending and a descending time-series, it is possible to disentangle east-west horizontal deformation from vertical deformation*.¹³ Statements such as these have in common that they suggest that it is possible to unambiguously and unbiasedly ‘disentangle’, ‘estimate’, ‘determine’, ‘compute’, or ‘reconstruct’ two displacements components, usually the vertical and east component, with two LoS observations. As discussed in Sec. 6.4.2, with these viewing geometries this will always result in biased estimates, except for the NLA coordinate system proposed in Sec. 6.4.3. Consequently, also a decomposition into the plane spanned by the up direction and the azimuth look direction of one of the satellites is incorrect (i.e., biased) since this plane is not orthogonal to the null line.

Two variations on decomposition errors can be distinguished.

6

ASSUMING SIGNAL-SENSITIVITY DEPENDENCY

The first variant of a decomposition error occurs when it is assumed that due to the *lack of sensitivity* for the north-component, d_n , it can be removed from the inverse problem altogether.¹⁴ This assumption would only be valid if the orientation of the null line n is $(\phi, \zeta) = (0, 0)$, hence in the north and horizontal direction respectively, which is never the case, see Fig. 6.7. Thus, removing d_n from Eq. (6.4) cannot be justified by the low sensitivity for that component unless we have prior knowledge of the expected magnitude of the north-component. When d_n is larger than the noise level of the projected LoS observations, it can still be discriminated from the observations.

ASSUMING DISPLACEMENT COMPONENTS TO BE KNOWN

The second variant of a decomposition error occurs when it is argued that $d_n = 0$ as a consequence of the insensitivity to displacements into the north direction.^{15,16} Obviously, this assumption refers to the actual size of the physical signal, i.e., the unknown parameter, which is evidently not correlated to the sensitivity of a particular radar instrument. The flawed argument is made in order to reduce the number of unknowns from three to two, and subsequently arrive at a square linear system.

¹³e.g., [97, 109, 128, 209]

¹⁴e.g., [3, 96, 97, 109, 128, 143, 145, 152, 170, 173, 207, 209].

¹⁵e.g., [3, 128, 143]. Note that the $d_n = 0$ assumption is a specific case of the more generic assumption that d_n is known.

¹⁶Note the subtle difference between variant 1, which simply removes the d_n component, and variant 2, which assumes it is equal to a known value, i.e., zero.

In conclusion, the implicit assumption that with two observation geometries we can estimate any arbitrary two directions in 3D space (including the fashionable EU decomposition), by deliberately ignoring d_n , or by assuming that d_n is known, leads to an erroneous (i.e., biased) decomposition.

6.6. RECOMMENDATIONS FOR INSAR PRODUCT GENERATION AND INTERPRETATION

While the underdetermined nature of the problem cannot be formally solved, we propose to pursue standardization for InSAR product generation and interpretation. First, we discuss two options for performing a displacement vector *decomposition* given two viewing geometries. Then, we evaluate the options for displacement vector *projection* onto a 1D direction and a 2D plane.

6.6.1. RECOMMENDATIONS FOR VECTOR DECOMPOSITION

A decomposition of two LoS observations is feasible when the two LoS observations are STCI. Yet, as this is practically impossible (Section 6.3.1), it is necessary to define a RUM, and perform a datum connection, see Section 6.3. Given the model of observation equations of Eqs. (6.4) and (6.5) with only two observation geometries, the only way to reduce the rank deficiency is to reduce the parameter space from three to two unknown parameters. This goal can be achieved in two ways.

The first ‘physical’ option is to change the orientation of the Cartesian reference frame in combination with a priori physical information: the *strapdown system*, which we discuss in detail in [14]. For example, for many physical phenomena gravity is the driving force for displacements, which allows us to define a two-dimensional vertical plane in which the displacement vector is expected to be situated. Examples include landslides and glaciers, where this plane is spanned by the vector normal to the slope and the gravity vector [24, 76, 130, 196], or for line infrastructure where it may be assumed that no displacements occur in its longitudinal direction [30, 141]. Both require a known rotation of the Cartesian frame such that one direction can be plausibly assumed to be displacement-free. Consequently, any frame misalignment will result in biased estimates, see Section 6.4.

A second ‘geometric’ option is to take advantage of the orientation of the null space, by choosing a *null line aligned* (NLA) Cartesian coordinate system, see Section 6.4.3. This yields a plane orthogonal to the null line, and the (forced) orthogonal projection of a displacement vector onto that plane will not influence (bias) the two in-plane components. Thus, these in-plane components can be uniquely and unbiasedly estimated. This option is particularly recommended when the InSAR results are used as input in a physical or mathematical model, since their unbiased nature will not compromise the output of that model.

For both the ‘physical’ as well as the ‘geometrical’ option, we recommend to explicitly mention the orientation of the null line with the InSAR product since it comprises information on the direction in which displacements cannot be observed.

Frequently-used alternative options are not recommended. Theoretically, when

it would be known from physics that a displacement component is zero in a cardinal compass direction, i.e., a northbound component equal to zero ($d_n = 0$), the parameter space has dimension two, and the remaining parameters may be uniquely estimated. However, while this physics-based rank-reduction may not be impossible, e.g. considering perfectly east-west oriented tectonic faults [204], it is a solution that is in a generic sense physically unrealistic and often unsubstantiated, since dynamic processes on earth typically do not have a preference for a cardinal compass direction. Likewise, it is not recommended to use the widely advocated and applied decomposition in the EU-plane, as this introduces biases, is prone to misinterpretation, and suggests an estimation possibility that is non-existent, see Section 6.4.2.

6.6.2. RECOMMENDATIONS FOR VECTOR PROJECTION

When there is no deformation direction in which displacements are known to be zero, or when it is inconvenient to decompose the two LoS observations in the plane orthogonal to the null line, it will not be possible to *decompose* the LoS observations. Yet, a *projection* is an operation that that is admissible and can always be performed without exceptions or assumptions. Clearly, a projection product is different from *estimating* the unknown parameter in the corresponding direction. Moreover, ‘projection-onto’ products are *discretionary* projections, and it is up to the user to decide on whether such a projection contains intelligible information. We distinguish *projection* onto a 1D direction from a single viewing geometry, and onto a 2D plane from dual viewing geometries.

PROJECTING ONE LOS OBSERVATION ONTO ONE DIRECTION

With only one LoS observation available, it is possible to project that observation onto any particular direction. For example, often d_{LoS} is projected onto the vertical (PoV) direction using

$$d_{\text{PoV}} = P_{\text{up,LoS}^\perp} d_{\text{LoS}} = (\cos\theta)^{-1} d_{\text{LoS}}, \quad (6.14)$$

where $P_{\text{up,LoS}^\perp}$ is the projector, and d_{PoV} is the projection of d_{LoS} onto the vertical direction. Note that in general $d_{\text{PoV}} \neq d_{\text{up}}$. The operation is an *oblique* projection of the LoS observations onto the vertical axis, along a plane orthogonal to the LoS unit vector. In contrast, when the LoS observations would be projected *orthogonally* onto the vertical, i.e., along a plane orthogonal to the ‘up’ unit vector, that would result in

$$d_{\text{PoV}^\perp} = P_{\text{up,up}^\perp} d_{\text{LoS}} = \underbrace{\begin{bmatrix} 0 & 0 & 0 \\ 0 & 0 & 0 \\ 0 & 0 & 1 \end{bmatrix}}_P u_{\text{LoS}} d_{\text{LoS}} = \cos\theta d_{\text{LoS}}, \quad (6.15)$$

Thus, both $P_{\text{up,LoS}^\perp}$ and $P_{\text{up,up}^\perp}$ are allowable discretionary projectors, but with a different result.

The main recommendation is therefore to (i) explicitly mention the use of a *projection-onto* product, e.g. using the PoV as subscript similar to the LoS subscript,

and (ii) explicitly distinguish an oblique from an orthogonal projection, using the \perp indicator. This is necessary both in text as well as in cartographic symbols and, e.g., colorbar annotations. Furthermore, we recommend to report the orientation of the null plane, since it is the plane where no displacements can be observed.

PROJECTING TWO LOS OBSERVATIONS ONTO A PLANE

When two LoS observations are available, the observations can be projected onto any arbitrary plane. When a LoS displacement vector is projected onto the plane spanned by the east and up axis, i.e., the EU plane, we have

$$d_{\text{poEU}} = \underbrace{\begin{bmatrix} 1 & 0 & 0 \\ 0 & 0 & 0 \\ 0 & 0 & 1 \end{bmatrix}}_P u_{\text{LoS}} d_{\text{LoS}}, \quad (6.16)$$

where d_{poEU} is the projection of d_{LoS} onto the EU plane. When this projection is performed for the two LoS observations it is possible to transform the projections into east and up components with Eq. (6.12) resulting in $d_{e,\text{poEU}}$ and $d_{u,\text{poEU}}$. However, it should be stressed that the results ($d_{e,\text{poEU}}, d_{u,\text{poEU}}$), are not the same as the unknown displacement components (d_e, d_u).

6.6.3. PRESENTING LOS OBSERVATIONS UNALTERED

The last option for handling the underdeterminedness problem is presenting the LoS observations unaltered as the final product. This is obviously correct, as it does not attempt to do any projection, attribution, or decomposition, as in [56, 77, 199, 207]. The drawback of the LoS product is that it is typically more difficult to interpret, especially for non-experts. As the actual vertical and horizontal displacement components are projected onto the LoS and superposed, what happens in the real world remains obscured. Yet, this is the preferred option when the InSAR results are used as input in a physical or mathematical model, since their unbiased nature will not compromise the output of that model.

6.7. CONCLUSIONS

Based on a general review of InSAR geometry, including the geometry-defining parameters from the satellite orbits in combination with the curved earth, the relationship between the LoS observables and the 3D displacement components is described. Whether decomposition—i.e., estimation of (some of the) 3D displacement parameters—is permitted is dependent on the **STCI** condition: spatio-temporally coinciding independent observations. As this condition is typically never fulfilled, it can be relaxed using the explicit assumption of **RUMs**: regions of uniform motion. Together with explicit spatio-temporal datum connection between the SAR datasets and ≤ 3 (full rank) viewing geometries with sufficient angular diversity, the quality of the estimates can be derived. In many practical situations, at most two viewing geometries are available, defining the **null line**, whose orientation

defines the estimability of displacement components. It depends on the orbital and viewing geometry as well as on the location on earth. The null line orientation should be stated explicitly in any standard InSAR product, as it is one of the fundamental metrics required for a proper interpretation. The null line also allows for the definition of the only unbiased reference system for displacement component estimation without without necessarily adding assumptions, termed **NLA**: the null-line aligned coordinate system.

Evaluating current practice yields three types of errors that are frequently encountered: which are termed attribution, projection, and decomposition errors. These lead to recommendations for InSAR product generation and interpretation. For vector decomposition, it is recommended to use the strapdown or the null-line aligned coordinate system, to prevent biased estimation, and refrain from using the biased decomposition on the East-Up plane. For vector projections, it is recommended to use descriptive subscripts, d_{LOS} , d_{PoV} , d_{PoV^\perp} , or d_{PoEU} to unambiguously define projected InSAR products, both textual as well as in maps and graphs.

The code to compute the null line orientation for any arbitrary location on Earth is available for download via <https://gitlab.tudelft.nl/drama/drama> [16].

7

ESTIMATING 3D DISPLACEMENTS WITH INSAR: THE STRAPDOWN APPROACH

Estimating three-dimensional (3D) surface displacements from InSAR Line-of-Sight (LoS) observations is challenging due to the limited number of independent viewing geometries. This chapter introduces the strapdown method, which is a practical and largely generic approach that enables unbiased estimation of 3D displacements using only two LoS observations. This method incorporates minimal contextual knowledge about the expected deformation mechanism. Under the assumption that displacement occurs only in the transversal-normal plane, the method establishes a local reference system with transversal, longitudinal, and normal (TLN) axes. The strapdown method provides full error propagation and yields physically meaningful "3D global/2D local" results.

This chapter is published as: W. S. Brouwer and R. F. Hanssen. "Estimating three-dimensional displacements with InSAR: the strapdown approach". In: *Journal of Geodesy* 98.110 (2024), pp. 1–15. DOI: 10.1007/s00190-024-01918-2. <https://doi.org/10.1007/s00190-024-01918-2>

7.1. INTRODUCTION

INSAR scatterers obtained from SAR interferometry are typically not situated at ideal locations, and the observations have an imaging geometry that is not optimal for retrieving full three-dimensional (3D) displacements. Moreover, they are only sensitive to the projection of the 3D displacement vector onto the radar line-of-sight (LoS) direction, d_{LoS} , along a plane orthogonal to the LoS [17, 62, 80, 124, 204], i.e.,

$$\begin{aligned} d_{\text{LoS}} &= P_{\text{LoS}^\perp} d_{\text{ENU}}, \\ &= [\sin\theta \sin\alpha_d, \sin\theta \cos\alpha_d, \cos\theta] d_{\text{ENU}}, \end{aligned} \quad (7.1)$$

where $d_{\text{ENU}} = [d_e, d_n, d_u]^T$ is the 3D displacement vector in east, north, and up direction, respectively.¹ P_{LoS^\perp} is the orthogonal projector onto the LoS, where θ is the incidence angle towards the radar, and α_d is the azimuth of its zero-Doppler plane (ZDP) at the position of the target, in the direction towards the satellite, see Brouwer and Hanssen [17, Fig. 1].

A decomposition of the LoS displacement vector into three orthogonal directions would be ideal. Yet, this requires at least three independent LoS observations from significantly different viewing geometries, but since almost all the SAR satellites operate right-looking,² orbiting the Earth in near-polar retrograde orbit, they have very similar viewing geometries and the maximum number of available and effective observations often reduces to two, i.e., ascending and descending, resulting in an underdetermined problem with an infinite number of solutions along a solution line [17].

Contemporary InSAR information products come in two classes: the geodetic products, which use mainly geometric information and minimal or no information on the physics, and the geophysical products, which aim at producing best-fit models describing the physical mechanisms at hand. Many geodetic InSAR information products, including most publicly available ones, circumvent the problem of underdetermination by disregarding the north component of the deformation, and asserting a decomposition into the east and up components only [42]. Yet, it is well known that this approach produces inherently biased estimates, particularly for the up component [17]. An alternative geodetic option is using the the null-line aligned (NLA) coordinate system as proposed by Brouwer and Hanssen [17], which ensures unbiased estimates, but produces results that can be more challenging to interpret for non-experts. For geophysical products there is a wide range of more optimal models, including the possibility to use the LoS observations directly in for instance modeling of fault slip or magma reservoir pressure change. Since these type of inversions can work directly with LoS data no decomposition is required.³

Here we demonstrate a practical, effective, and largely generic solution to the problem of underdetermination, introducing the ‘strapdown’ method, which uses

¹Note that a displacement vector d , with unit [mm], may also be interpreted as, e.g., an (average or instantaneous) displacement velocity, unit [mm/y], since this is geometry-invariant.

²Adding an observation from a left-looking radar will improve the accuracy for the estimated parameters [150, 204], but the precision for the estimated north component is still rather poor.

³In this study we focus on interferometric estimates of displacements. In case of large displacements SAR offset tracking may provide an additional displacement observable [9, 75, 155, 167].

a location-dependent local reference system that is tuned to the deformation phenomenon.

Special cases of this approach have been applied in particular applications, such as landslides [24, 32, 76, 130, 140, 196], ice sheets [66, 98, 126, 129], and line-infrastructure [30, 141]. Yet, apart from being a wider generalization and a mathematical framework, the strapdown approach offers complete error propagation and therefore a proper quality description of the final estimated displacements. Moreover, effectively it leads to an optimal unbiased solution which is locally two-dimensional, but globally three-dimensional, requiring only a limited degree of rather undisputed contextual information on the expected deformation phenomena.

We first discuss the geometry of the strapdown approach and the deformation phenomena for which it can be used in Sec. 7.2. In Sec. 7.3 we discuss how the displacements can be estimated and we elaborate on the quality of the estimated displacements. Finally, we demonstrate the strapdown approach in two examples in Sec. 7.4 and reflect on the method in Sec. 7.6.

7.2. SYSTEM GEOMETRY

In the following, we define the geometry of the strapdown system and elaborate on different classes of deformation phenomena.

7.2.1. THE LOCAL STRAPDOWN COORDINATE SYSTEM

Instead of choosing one coordinate system for the entire area of interest, we define a local, right-handed Cartesian coordinate system that is fixed to the local deformation phenomenon with transversal, longitudinal, and normal (TLN) components, $d_{\text{TLN}} = [d_T, d_L, d_N]^T$, see Fig. 7.1. The term *local* implies that the orientation of the TLN frame will differ for each location, hence the term ‘*strapdown*’, adapted from inertial navigation technology [182]. Thus, a displacement vector d_{TLN} is projected onto the LoS with Eq. (7.1) as [30]:

$$d_{\text{LoS}} = P_{\text{LoS}^\perp} R_1 R_2 R_3 d_{\text{TLN}} = P_{\text{LoS}^\perp}^R d_{\text{TLN}}, \quad (7.2)$$

where R_1, R_2 , and R_3 are rotation matrices:

$$\begin{aligned} R_1 &= \begin{bmatrix} \cos \Lambda & \sin \Lambda & 0 \\ -\sin \Lambda & \cos \Lambda & 0 \\ 0 & 0 & 1 \end{bmatrix}, \\ R_2 &= \begin{bmatrix} 1 & 0 & 0 \\ 0 & \cos \Phi & -\sin \Phi \\ 0 & \sin \Phi & \cos \Phi \end{bmatrix}, \\ R_3 &= \begin{bmatrix} \cos \Omega & 0 & \sin \Omega \\ 0 & 1 & 0 \\ -\sin \Omega & 0 & \cos \Omega \end{bmatrix}, \end{aligned} \quad (7.3)$$

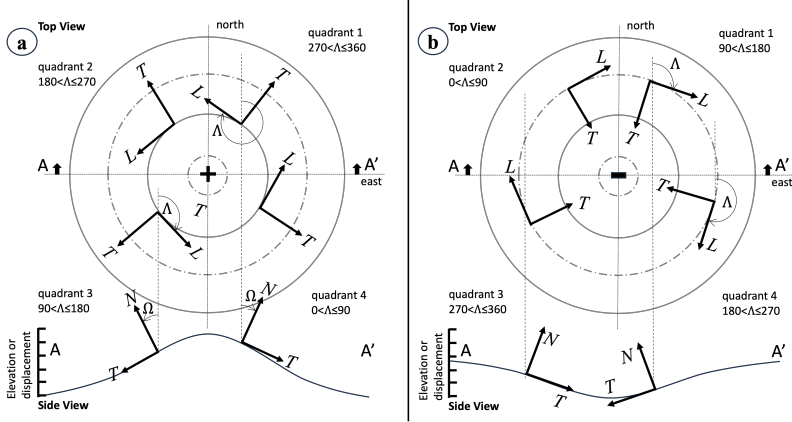


Figure 7.1.: Orientation of the TLN reference system for gravity-induced downslope deformation phenomena and/or subsidence and uplift. (a) shows the orientation for a schematized mountain (with iso-elevation lines) or equivalently an uplift dome (with iso-displacement lines). Note that the transversal direction is always downslope or centrifugal. Therefore, the slope aspect determines the boundaries within which Λ should lie. (b) Similar situation sketch for a valley or equivalently a subsidence bowl. Note that the transversal axis is always downslope, and thus centripetal for subsidence.

where $\Lambda \in [0^\circ, 360^\circ)$ is the azimuth of the longitudinal direction (L) relative to the north.⁴ The elevation angle of the longitudinal direction is $\Phi \in (-90^\circ, +90^\circ]$, relative to the horizontal (where up-hill is positive) and the elevation angle of the transversal direction (T) is $\Omega \in (0^\circ, +90^\circ]$. The normal direction (N) completes the orthogonal right-handed TLN system. $P_{\text{LoS}^\perp}^R$ is the projector that projects the displacement vector d_{TLN} onto the LoS along a plane orthogonal to the LoS. Thus, $P_{\text{LoS}^\perp}^R$ is a function of Λ , Ω , and Φ with size 1×3 , i.e., $P_{\text{LoS}^\perp}^R = [P_T, P_L, P_N]$, with

$$\begin{aligned}
 P_T &= (\sin\theta \sin\alpha_d \cos\Lambda - \sin\theta \cos\alpha_d \sin\Lambda) \cos\Omega - \\
 &\quad (-(\sin\theta \sin\alpha_d \sin\Lambda + \sin\theta \cos\alpha_d \cos\Lambda) \sin\Phi + \cos\theta \cos\Phi) \sin\Omega \\
 P_L &= (\sin\theta \sin\alpha_d \sin\Lambda + \sin\theta \cos\alpha_d \cos\Lambda) \cos\Phi + \cos\theta \sin\Phi \\
 P_N &= (\sin\theta_m \sin\alpha_d \cos\Lambda - \sin\theta \cos\alpha_d \sin\Lambda) \sin\Omega + \\
 &\quad (-(\sin\theta_m \sin\alpha_d \sin\Lambda + \sin\theta \cos\alpha_d \cos\Lambda) \sin\Phi + \cos\theta \cos\Phi) \cos\Omega.
 \end{aligned} \tag{7.4}$$

Geometrically, any displacement vector can be regarded as being situated in a 2D plane, with zero-displacement in the complementary direction, by definition. In the TLN frame, the displacement vector is always situated in the plane spanned by the transversal and normal unit vectors, and is therefore by definition zero in the

⁴Due to the 180° ambiguity in longitudinal direction, in case of a topographic slope or a subsidence slope, the longitudinal axis is defined tangential to the local iso-elevation or iso-deformation lines, such that the positive transversal direction is always directed down-slope. In the absence of a clear slope, we use the smallest angle w.r.t. the north, i.e. $\Lambda \in (-90^\circ, +90^\circ]$, following Chang *et al.* [30].

longitudinal direction. Note that this is not an assumption or an approximation, as it follows deductively from the definition of the coordinate system. Of all 2D planes that contain the displacement vector as subset, there is typically only one plane orientation that is physically genuinely relevant, i.e., uniquely interpretable. This is due to the fact that all observable displacements are caused by forces, or stresses, that are acting upon the object. In many cases, displacement mechanisms of interest have a physical context that can be regarded as ‘known’ to some extent. Obviously, the force of gravity is omnipresent in every case, and is in many cases also the root cause of the observed motion. In other cases, forces are due to kinetic causes, such as deforming roads and railways imposed by traffic load or due to, e.g., volumetric (e.g., a subsidence bowl caused by a subsurface volume change) or tectonic mechanisms [26, 208]. Consequently, we can orient the TLN system, viz. the longitudinal direction, to the direction in which there is physically no displacement to be expected, as we will elaborate below. From orthogonality, the longitudinal direction defines the local *displacement plane*, in which the two orthogonal displacement components (T and N) are situated. With this definition, Eq. (7.2) can be locally solved with LoS observations from two sufficiently different viewing geometries. Consequently, the main challenge is (i) to find the orientation of the local displacement plane in 3D space, given by (Λ, Φ, Ω) and (ii) to approximate the precision of these orientation parameters in order to perform an error propagation to assess the final quality of the local solution.

7.2.2. DEFORMATION PHENOMENA

The generic description of the methodology can be elaborated for typical classes of deformation phenomena. Here we discuss downslope displacements, subsidence and uplift, (line)-infrastructure, and motion associated with idealized faults. Note that when the displacement direction can be considered as ‘known’ (e.g. vertical), the LoS observations can be projected directly on the unit vector of the displacement direction, and the strapdown system is not necessary.

GRAVITY-DRIVEN DOWNSLOPE DEFORMATION

Landslides, moving glaciers, or slope instabilities of a dike are examples of phenomena where the main deformation occurs in a vertical plane that contains the downslope direction and the local gravity vector. The plane is perpendicular to the local gradient and gravity is the main driving force, see Fig. 7.1.

When the longitudinal axis is parallel to the iso-elevation lines of the slope of the occurring landslide, it can, in first approximation, be assumed that the forces in the longitudinal direction will be negligible, i.e., $d_L = 0$. Hence, all displacements are expected to occur in the (vertical) plane spanned by the transversal and normal axis, shown in the side views of Fig. 7.1, and $\Phi = 0^\circ$ by definition, see Eq. (7.3). The slope *aspect*, α_a , i.e., the compass direction that a terrain surface faces, determines the value for the angle Λ since the (angle of the) slope, Ω , is always referred to as a positive number, see Fig. 7.1, i.e., $\alpha_a = \Lambda + 90^\circ$. The positive transversal direction is always directed down-slope.

Note that these approximations are a strong simplification of reality. In certain cases, displacements along the longitudinal axis can occur, e.g., in a glacier where the gravitational force may induce internal stresses, which may result in displacements along the longitudinal direction.

SUBSIDENCE AND UPLIFT

Subsidence bowls and uplift domes are caused by a subsurface volume change, in combination with gravity, see Fig. 7.1, e.g., as a result of fluid pressure decrease or increase [49, 70] or due to surface loading or unloading. These types of phenomena exhibit vertical and horizontal displacement components [111]. The horizontal displacement directions are in first approximation centripetal for subsidence, and centrifugal for uplift [134]. The longitudinal direction, indicated by azimuth Λ , is oriented parallel to the isodeformation lines, and the transversal direction is downslope (centripetal) for subsidence, and centrifugal for uplift. Similar to the downslope case, there is—by definition—no displacement component in the longitudinal direction. The normal displacements are maximum in the center of the field, decreasing asymptotically to the edge of the field. The example in section 7.4.1 elaborates this further.

LINE-INFRASTRUCTURE

Line infrastructure assets are characterized by an extended spatial dimension in one direction (by definition the longitudinal direction), where the spatial extent in the other two directions is limited, such as roads, railways, dikes, and pipelines. The slope of the asset is given by Φ , while Ω represents the cant of the asset or the slope in the transversal direction [27, 30]. The latter is usually small, see Fig. 7.2. Often, it is possible to assume that no significant continuous (stationary) displacements occur in the longitudinal direction [27, 30, 141], apart from perhaps thermal expansion and contraction which can be independently modeled and has a non-secular character.

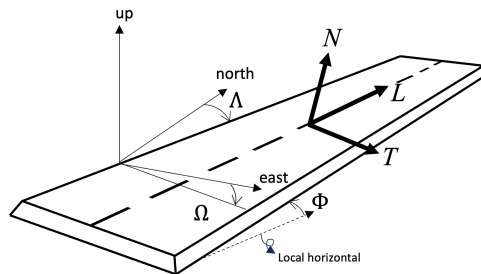


Figure 7.2.: The orientation of the TLN reference system for line-infrastructure: Λ and Φ represent the azimuth and slope of the longitudinal direction, respectively, and Ω the cant. Figure adapted from Chang *et al.* [27].

MOTION ASSOCIATED WITH FAULTS

Although deformations resulting from tectonics (post, co-, and inter-seismic) may often be too complex to uniquely identify the 2D plane in which the displacements occur, we can still utilize the strapdown method for first-order approximations and deformations associated with faults as hydrological boundaries. Considering, e.g., rising mine water after mine closure associated with normal or reverse faults [23], see Fig. 7.3. In such cases the driver of the deformation is sufficiently well defined and determines its directionality. As a result, no displacements are expected along the fault and the longitudinal direction can thus be directed parallel to the fault. In section 7.4.2 this example is further elaborated. For ideal strike-slip faults, the sides move along each other and the longitudinal direction is directed perpendicular to the fault. To prevent directional ambiguity, the smallest azimuth angle is chosen, i.e., $\Lambda \in (-90^\circ, 90^\circ]$. For all three fundamental fault types, d_T has a different sign at both sides of the fault.

Obviously, there will be many cases in which slip on a fault will not enable a simple unambiguous directionality assumption for the displacement, in which cases more advanced (geophysical) models are required.

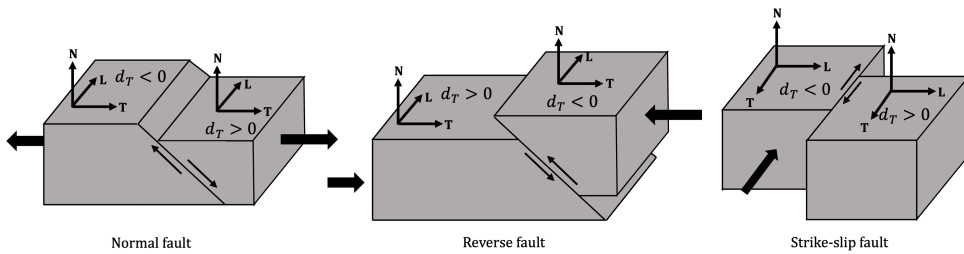


Figure 7.3.: Orientation of the TLN reference frame for the fundamental types of fault motion [68]. For normal and reverse faults, displacement is expected to occur dominantly in a vertical plane perpendicular to the strike of the fault, which aligns with the longitudinal direction. For vertical strike-slip faults, horizontal displacement happens dominantly parallel to the strike direction, and the longitudinal direction is thus aligned perpendicular to the strike of the fault.

7.3. ESTIMATING DISPLACEMENTS USING THE STRAPDOWN APPROACH

As longitudinal displacements are null by definition, any displacement vector can be unambiguously represented in a 2D (d_T, d_N) system, and thus d_T and d_N can be estimated with two LoS observations. There are several options for estimating d_T and d_N . Chang *et al.* [27] and Chang *et al.* [30] add a pseudo observation, $d_L = 0$, to the mathematical model. However, this approach requires the orientation of the TLN frame to be perfectly known, since a misalignment will result in biased estimates for d_T and d_N . Adding pseudo observation $d_L = 0$ to the system of equations,

while in fact $d_L \neq 0$, results in a 'decomposition error' similar to 'neglecting' the north component in a conventional ENU decomposition, see Brouwer and Hanssen [17]. In reality, the orientation of the TN plane will always have some alignment uncertainty, expressed by σ_Λ^2 , σ_Ω^2 , and σ_Φ^2 . A better alignment precision results in a better estimation of the unknown displacements d_T and d_N . Below, we consider the impact of the alignment uncertainty in the mathematical model.

7.3.1. THE MATHEMATICAL MODEL

Since the longitudinal displacements are null by definition, d_L can be removed from Eq. (7.2) and $P_{\text{LoS}^\perp}^R$ reduces to a 1×2 matrix with only P_T and P_N , see Eq. (7.4), and the 2×1 displacement vector contains only d_T and d_N . The TLN frame orientation is introduced using pseudo observations $\underline{\Lambda}$, $\underline{\Omega}$, and $\underline{\Phi}$ (the underline indicates the stochastic nature of the observable) in the mathematical model:

$$E\left\{ \underbrace{\begin{bmatrix} \underline{d}_{\text{LoS}}^{(1)} \\ \vdots \\ \underline{d}_{\text{LoS}}^{(m)} \\ \underline{\Lambda} \\ \underline{\Omega} \\ \underline{\Phi} \end{bmatrix}}_y \right\} = \underbrace{\begin{bmatrix} a_1(x) \\ \vdots \\ a_m(x) \\ a_{m+1}(x) \\ a_{m+2}(x) \\ a_{m+3}(x) \end{bmatrix}}_{A(x)}, \text{ and} \quad (7.5)$$

$$D\left\{ \underbrace{\begin{bmatrix} \underline{d}_{\text{LoS}}^{(1)} \\ \vdots \\ \underline{d}_{\text{LoS}}^{(m)} \\ \underline{\Lambda} \\ \underline{\Omega} \\ \underline{\Phi} \end{bmatrix}}_y \right\} = \underbrace{\begin{bmatrix} Q_{\text{LoS},1} & \dots & 0 & 0 & 0 & 0 \\ \vdots & \ddots & \vdots & 0 & 0 & 0 \\ 0 & \dots & Q_{\text{LoS},m} & 0 & 0 & 0 \\ 0 & 0 & 0 & \sigma_\Lambda^2 & 0 & 0 \\ 0 & 0 & 0 & 0 & \sigma_\Omega^2 & 0 \\ 0 & 0 & 0 & 0 & 0 & \sigma_\Phi^2 \end{bmatrix}}_{Q_{yy}}, \quad (7.6)$$

where for $i \in [1, m]$

$$\begin{aligned} a_i(x) &= P_T^{(i)}(\Lambda, \Omega, \Phi)d_T + P_N^{(i)}(\Lambda, \Omega, \Phi)d_N \\ a_{m+1}(x) &= \Lambda \\ a_{m+2}(x) &= \Omega \\ a_{m+3}(x) &= \Phi, \end{aligned}$$

and $x = [d_T, d_N, \Lambda, \Omega, \Phi]^T$ is the vector of unknown displacements and orientation angles. $E\{\cdot\}$ expresses the expectation of the model, which can be solved with at least two sets, i.e., $m = 2$, of LoS observations: $\underline{d}_{\text{LoS}}^{(1)}$ and $\underline{d}_{\text{LoS}}^{(2)}$, each having a different viewing geometry. Here, a 'set' refers to all observations from one particular viewing geometry, either ascending or descending, over a Region of Uniform Motion

(RUM).⁵ Note that the size of each set can be different due to a different number of LoS observations, which can be either Point Scatterers (PS) or Distributed Scatterers (DS). Rows $i \in [1, m]$ in matrix A are non-linear equations of x , where each row is unique due to the difference in viewing geometry. To overcome the rank deficiency, pseudo observations for $\underline{\Lambda}$, $\underline{\Omega}$, and $\underline{\Phi}$ are added representing our best-effort approximation for the frame orientation. These values can be purely data-driven based on iso-displacement lines retrieved from the original line-of-sight results, or on contextual information, as long as conservative precision estimates are used. $D\{\cdot\}$ is the dispersion of the model, where $Q_{\text{LoS},i}$ is the covariance matrix of the LoS observations for set i . This covariance matrix is a diagonal matrix containing the variances of displacements for each PS or DS within the set. The off-diagonal elements are null, since all PS or DS within a set represent different physical scatterers. The uncertainty in our best-effort attempt to orient the TLN frame, or equivalently the level of trust that we have in our knowledge in the orientation of the frame, is represented in σ_{Λ}^2 , σ_{Ω}^2 , and σ_{Φ}^2 . Choosing these values realistically (we recommend conservatively) is important, as this uncertainty propagates into the (co)variances of the final displacement parameters, which is a key feature of the strapdown methodology.

PARAMETER ESTIMATION

To estimate the five unknown parameters and provide a proper quality description the linearized system of equations needs to be solved,

$$\Delta \underline{y}_{[0]} \approx J_{[0]} \Delta x_{[0]}, \quad (7.7)$$

where

$$J_{[0]} = \begin{bmatrix} \frac{\partial}{\partial d_T} a_1(x_{[0]}) & \dots & \frac{\partial}{\partial \Phi} a_1(x_{[0]}) \\ \vdots & \ddots & \vdots \\ \frac{\partial}{\partial d_T} a_{m+3}(x_{[0]}) & \dots & \frac{\partial}{\partial \Phi} a_{m+3}(x_{[0]}) \end{bmatrix} \quad (7.8)$$

is the Jacobian matrix which is a function of the initial approximations for the unknown parameters $x_{[0]}$, i.e.,

$$x_{[0]} = [d_{T[0]}, d_{N[0]}, \Lambda_{[0]}, \Omega_{[0]}, \Phi_{[0]}]^T, \quad (7.9)$$

⁵For a successful estimation of x , the two LoS observations 'sets' need to be spatio-temporally coinciding and independent (STCI). As this is hardly ever possible, a region of uniform motion (RUM) needs to be defined and a datum connection (in time and space) needs to be performed. Moreover, the two LoS observation sets need to have a sufficient angular diversity. For in-depth elaboration see Brouwer and Hanssen [17].

which yield initial approximations for the observation vector \underline{y} and $\Delta \underline{y}_{-[0]} = \underline{y} - A(x_{[0]})$. Consequently, when $m \geq 2$, Δx can be estimated using

$$\Delta \hat{x}_{[0]} = \begin{cases} J_{[0]}^{-1} \Delta \underline{y}_{-[0]}, & \text{for } m = 2, \text{ and} \\ Q_{\hat{x}\hat{x}} J_{[0]}^T Q_{yy}^{-1} \Delta \underline{y}_{-[0]} & \text{for } m > 2, \end{cases} \quad (7.10)$$

$$Q_{\hat{x}\hat{x}} = \begin{cases} J_{[0]}^{-1} Q_{yy}^{-1} (J_{[0]}^{-1})^T, & \text{for } m = 2, \text{ and} \\ (J_{[0]}^T Q_{yy}^{-1} J_{[0]})^{-1} & \text{for } m > 2, \end{cases} \quad (7.11)$$

where $Q_{\hat{x}\hat{x}}$ represents the precision of x . The new estimate for \hat{x} is defined as $\hat{x}_{[1]} = x_{[0]} + \Delta \hat{x}_{[0]}$, and can be used to estimate $\Delta x_{[1]}$. Iteration leads to a final estimate for \hat{x} . An estimation of the unknown parameters requires rough initial approximations for which either prior knowledge of the deformation phenomenon can be used, or initial assessments from the original LoS estimates. For $\Lambda_{[0]}$, $\Omega_{[0]}$, and $\Phi_{[0]}$ the best-effort frame orientations are used.

The precision of the five estimated parameters is expressed by the (co)variances in $Q_{\hat{x}\hat{x}}$, sketched for an arbitrary frame orientation in Fig. 7.4. In this example, there is correlation between \hat{d}_T and \hat{d}_N , in the upper 2×2 block. Due to the choice of the pseudo-observations, there is no correlation between the estimated orientation angles $\hat{\Lambda}$, $\hat{\Omega}$, and $\hat{\Phi}$, i.e., $\rho = 0$. Yet, there is correlation between the displacements and the angular estimates. Different frame orientations will result in different levels of correlation.

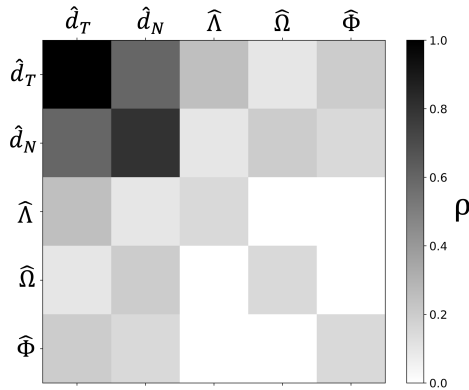


Figure 7.4.: Sketch of (normalized) $Q_{\hat{x}\hat{x}}$ for an arbitrary frame orientation. The diagonal elements represent the precision of the estimated parameters \hat{x} and the off-diagonal terms the correlation between them. There is correlation between the estimated displacements (upper-left 2×2 block) but no correlation between the estimated frame orientation (lower-right 3×3 block). However, there is correlation between the estimated frame orientations and the estimated displacements (e.g., lower left 3×2 block).

7.3.2. THE QUALITY OF THE ESTIMATES

The precision of the estimates (\hat{d}_T, \hat{d}_N) depends on four independent contributions: (i) the actual (true) orientation of the TLN frame, (ii) the actual (true) magnitude of the d_T and d_N displacements, (iii) the alignment precision of the TLN frame, and (iv) the precision of the observations and pseudo-observations. These will be discussed below.

TRUE ORIENTATION OF THE TLN FRAME

The actual (true) orientation of the TLN frame has a dominant impact on the precision of the final estimates. With two LoS observation geometries (ascending and descending), displacement components in the direction of the *null-line* [17] cannot be observed: the more either the transversal or normal direction aligns with the null-line, the less precise that parameter can be estimated. The most favorable option is therefore when the plane spanned by the transversal and normal axis (TN-plane) is orthogonal to the null-line, i.e., when $\Lambda = \phi$ and $\Phi = \zeta$, where ϕ and ζ are the azimuth angle and elevation angle of the null-line, respectively.⁶

Fig. 7.5 shows the Signal-to-Noise Ratio (SNR) for the transversal (lower left) and

⁶In this special case the TLN frame is identical to the null-line aligned (NLA) frame, see Brouwer and Hanssen [17].

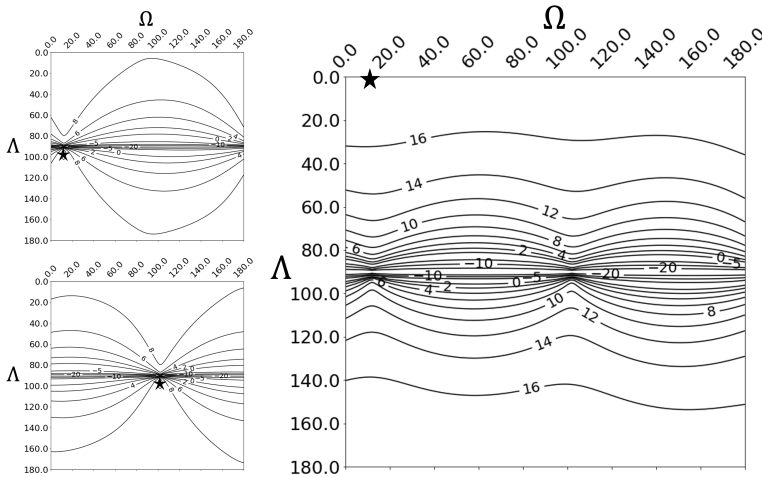


Figure 7.5.: SNR [dB] for the normal (upper left) and transversal (lower left) component for different orientations of the TLN frame. The observation geometry of the simulated ascending and descending acquisition is presented in Tab. 7.1, which result in a null-line orientation, $n(\phi, \zeta) = n(0.14^\circ, 12.14^\circ)$. The right figure shows the sum of the left two figures since one is always interested in estimating both components. It can be seen that the SNR of the two combined directions is greatest when the longitudinal direction is in the direction of the null-line, indicated by the black star. In that specific case, the TN plane is orthogonal to the null-line.

normal (upper left) component as a function of Λ and Ω , with $\Phi = 0^\circ$. We simulate an arbitrary displacement phenomenon with $d_T = d_N$, observed from an ascending and a descending orbit with viewing characteristics as presented in Tab. 7.1. For different frame orientations, we simulate LoS observations and subsequently estimate the unknown parameters x with Eq. (7.10). In Fig. 7.5, we show the SNR for each realization, where $\text{SNR}_T = 10 \log_{10}(d_T / \sigma_{d_T})$, and $\text{SNR}_N = 10 \log_{10}(d_N / \sigma_{d_N})$ represent the transversal and normal direction respectively, shown by the two left figures. The quality of the estimated normal component is best when the transversal direction aligns with the null-line, shown by the black star in Fig. 7.5. Likewise, the quality for d_t is the best when the normal direction aligns with the null-line. Obviously, when one of the two components aligns with the null-line, both satellite geometries have zero sensitivity in that direction, and both observations are entirely attributed to the other component.

In reality, we need to estimate *both* components together. Therefore we show the sum of the SNR ratios in the right figure, i.e., $\text{SNR}_{\text{total}} = \text{SNR}_N + \text{SNR}_T$. The black star shows the most favorable orientation with the highest SNR value, which occurs when the longitudinal direction is aligned with the null-line, e.g., $\Lambda = \phi$ and $\Omega = \zeta$. The quality of the estimates is poor when $\Lambda \approx 90^\circ$, i.e., when the normal or transversal direction is in the direction of the null-line.

TRUE MAGNITUDE OF d_T AND d_N

The quality (both bias and precision) of (\hat{d}_T, \hat{d}_N) is scaled by the actual (but unknown) size of the displacement signal. This follows from the Jacobian in Eqs. (7.8) and (7.9), which requires initial values for $d_{T[0]}$ and $d_{N[0]}$. The quality of the displacement estimates, i.e., $\sigma_{\hat{d}_T}$ and $\sigma_{\hat{d}_N}$, is thus a function of the Jacobian matrix containing the values of d_T and d_N from the second to last iteration step. Therefore, larger estimated displacements lead to a larger uncertainty (or σ values), since $\sigma_{\hat{d}_T}$ and $\sigma_{\hat{d}_N}$ also capture the potential bias due to a misalignment in the frame. In the case of a misalignment, $\sigma_{\hat{d}_T}$ and $\sigma_{\hat{d}_N}$ are biased: larger for larger deformations and smaller for smaller deformations. In the most extreme case, if there is no deformation, there is also no bias.

ALIGNMENT PRECISION OF THE TLN FRAME

Any error in the best-effort orientation approximation of the TLN frame, i.e., a misalignment, results in $d_L \neq 0$, and consequently biased estimates for d_T and d_N .

Table 7.1.: Simulated viewing geometries and consequent null-line orientation.

Geometry	Inc. angle θ	Azim. ZDP α_d
ascending	32°	250°
descending	40°	105°
null-line n :	$\phi = 0.14^\circ$	$\zeta = 12.14^\circ$

Misalignments are taken into account in Eqs. (7.5) and (7.6), via σ_Λ , σ_Ω , and σ_Φ , propagating the alignment uncertainty to the precision for the final estimates, see Eq. (7.11). The alignment precision needs to be chosen conservatively, i.e., not too optimistic. As long as the true 'unknown' frame orientation falls within the estimated uncertainty, then the bias obtained on \hat{d}_T and \hat{d}_N will also fall within the estimated precision defined by $\sigma_{\hat{d}_T}$ and $\sigma_{\hat{d}_N}$. Furthermore, since the frame orientation is both a is both an unknown (as part of x) and a pseudo-observation (as part of y), the final estimated frame orientation is equal to the pseudo-observation, i.e., the initial estimated orientation.

PRECISION OF (PSEUDO) OBSERVATIONS

The fourth contribution to the precision of the estimates (\hat{d}_T, \hat{d}_N) is the quality (or precision) of (i) the LoS observations and (ii) the pseudo-observations, expressed in Q_{yy} in Eq. (7.11). Obviously, a higher quality of the observations, and/or more certainty in the frame orientation, results via $Q_{\hat{x}\hat{x}}$ in higher quality of the final estimates.

7.3.3. INTERPRETATION OF THE RESULTS

For a cartographic visualization of the estimated (d_T, d_N) displacements there are two options. When the orientation of the strapdown coordinate system is uniform over the area of interest, it is possible to create a panchromatic map⁷ for d_T and d_N separately, see, e.g., Figs. 7.11e and f. However, in the more generic case of a spatially variable orientation of the strapdown coordinate system this is not possible anymore, since directionality needs to be considered. A *vector* (quiver) map type is more suitable in this case, see Figs. 7.6 and 7.8. This has the added value that the precision of both magnitude and direction can be expressed using a confidence ellipse. The relative sizes of the vector and the confidence ellipse enable a direct assessment of the significance of the estimate and of the SNR, and hence improve interpretability. In Fig. 7.6, the estimated transversal displacement vector d_T , located at the geometric center of a RUM, is situated at geographic coordinates (x_i, y_i). In this case the normal direction is practically aligned with the up direction.⁸ The error ellipse shows the confidence region, with transversal axis $p\sigma_T$, and longitudinal axis $\sigma_L = d_T \tan(p\sigma_\Lambda)$ where p expresses the desired size of the confidence region, i.e., for $p=2$ we have a 95% confidence region. Both σ_T and σ_Λ follow from Eq. (7.11).

7.4. RESULTS: 2 CASE STUDIES

In this section we apply the strapdown approach in two case studies: subsidence due to solution mining and displacements resulting from ground water pressure in relation to faults.

⁷or similarly a contour map or a dot distribution map.

⁸In other cases, the displacement vector can be situated along the slope.

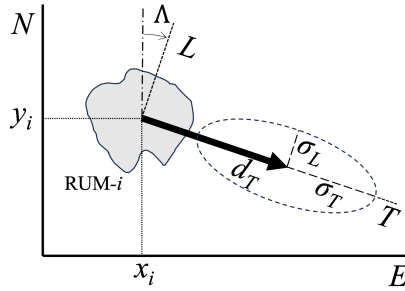


Figure 7.6.: Vector representation of strapdown results of RUM- i at geographic (east,north) coordinates (x_i, y_i) , showing the estimated transversal displacement component, d_T . The error ellipse or confidence region has two axes. The size of transversal axis is σ_T and the size of the longitudinal axis is $\sigma_L = d_T \tan \sigma_\Lambda$.

7.4.1. MAGNESIUM EXTRACTION IN VEENDAM

In Veendam, the Netherlands, solution mining for multicomponent salts occurs at a depth of ~ 1500 m. Around the production caverns, salt starts flowing towards the caverns [13]. Subsequently, the overlaying rock layers move downwards and horizontally towards the center of the cavern, resulting in a subsidence bowl. The observed vertical displacements will be greatest at the center of the bowl, while the horizontal displacements are centripetal, see Sec. 7.2.2. We use the strapdown approach to estimate the unknown 3D displacements. The area is monitored by Sentinel-1 from descending and ascending acquisitions, see Tab. 8.2, using a PSI approach [193]. The LoS results for both geometries are shown in Fig. 7.7. For the descending acquisition, the greatest LoS velocities occur more to the east compared to the ascending acquisition, which is an indicator for significant horizontal displacements. For the strapdown decomposition the ascending and the descending acquisition need to have the same spatial datum, where the velocity is either known or assumed to be equal to zero. In this case the reference points for both geometries are chosen in a presumed stable area outside the mining activities.

Table 7.2.: Acquisition details for Sentinel-1 tracks 15 and 139 at Veendam, the Netherlands.

	S1 track 15	S1 track 139
Heading	ascending	descending
Mean θ	36.3°	44.2°
Mean α_d	261°	98°
Start	Aug 7, 2018	Aug 4, 2018
End	Mar 8, 2020	Feb 16, 2020

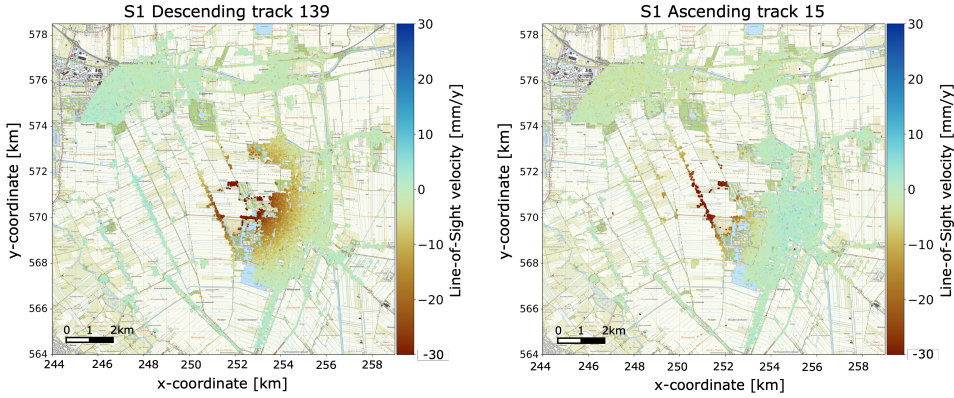


Figure 7.7.: Estimated LoS velocities for S1 descending track 139 and ascending track 15 for Veendam. The location of the maximum LoS velocity differs for both tracks. This is an early indicator for significant horizontal displacements.

RUM DEFINITION

As the orientation of the TLN frame varies within the region, in first iteration we approximate the subsidence bowl assuming radial symmetry and divide it into 12 sectors and five equidistant radial areas, see Fig. 7.8, where each element is assumed to behave as a region of uniform motion (RUM). To account for imperfect circularity we set $\sigma_{\Lambda} = 5^{\circ}$, implying that, with a 95% confidence interval, we conservatively estimate the Λ^0 alignment to be within $\pm 10^{\circ}$. We use $\Omega^0 = 0^{\circ}$ and $\Phi^0 = 0^{\circ}$ due to the absence of significant topography, and we set $\sigma_{\Omega} = 2^{\circ}$ and $\sigma_{\Phi} = 2^{\circ}$, to quantify our confidence in this assumption.

PARAMETER ESTIMATION PER RUM

Independently for each RUM we estimate the mean LoS displacement velocity for each viewing geometry, i.e., $\hat{v}_{\text{LoS}}^{\text{asc}}$ and $\hat{v}_{\text{LoS}}^{\text{dsc}}$, based on all time series of the scatterers within that particular RUM. We approximated $\sigma_{\hat{v}_{\text{LoS}}^{\text{asc}}}$ and $\sigma_{\hat{v}_{\text{LoS}}^{\text{dsc}}}$ by calculating the RMSE of the LoS velocities of the individual scatterers with the mean velocities, these values are used for $Q_{\text{LoS},i}$ in Eq.(7.6). Subsequently, we estimate the average velocities in the transversal and normal direction, \hat{v}_T and \hat{v}_N , with Eqs. (7.5) and (7.6), see Fig. 7.8. The largest mean normal (near-vertical) displacement of ~ 40 mm/y indeed occurs at the center of the subsidence bowl. RUMs A4, A6, A7, and A8 contain only scatterers in one viewing geometry, impeding strapdown estimates.

We estimate the precision for the unknown velocities, $Q_{\hat{x}\hat{x}}$, visualized by 2σ confidence ellipses and error bars for the normal velocities. The minor axes of the ellipses represent the level of confidence due to the uncertainty in the alignment of the frame. The uncertainty of both the transversal and the normal velocity differs per RUM. Since the orientation of the null-line is near-north ($\phi = 0.7^{\circ}$ and $\zeta = 7.1^{\circ}$),

the transversal direction is almost in the direction of the null-line for RUMs 1, 12, 6, and 7, which is properly addressed by the confidence regions for these regions. It can be seen that also the normal component is affected.

For comparison, the conventional biased approach is followed where the north component is neglected and only the east and up components are estimated, leading to a decomposition error [17]. In Fig. 7.9, we show the biased estimated east and up components using that approach. The comparison shows that the strapdown approach captures the entire 3D deformation phenomenon: while we estimate 2D displacements per RUM, we retrieve the full 3D displacement phenomenon by combining all RUMs, hence the ‘2D-local, 3D-global’ characterization.

In Fig. 7.10, we show the difference in estimated velocity between the up component from the east-up approach and the normal component in the strapdown approach. As expected, the greatest errors, up to -5.4 mm/y, occur in RUMs located in the north and south (e.g., 12, 1, 6, and 7), due to the large neglected north component. It also shows that the conventional approach results in biased estimates: for a subsidence bowl it is highly unlikely that—for some reason—there will be zero displacements into the north direction. As a result, in the conventional decomposition the neglected north component is attributed to the estimated up component, and depending on the sign of the north component, the up component is over- or underestimated. Therefore, we expect to see (i) larger differences between the up and normal components for the RUMs in the north and south and (ii) a changing sign for the difference since the true north displacements for these RUMs also have a different sign.

In comparison, the neglect-north approach results in (i) no information on

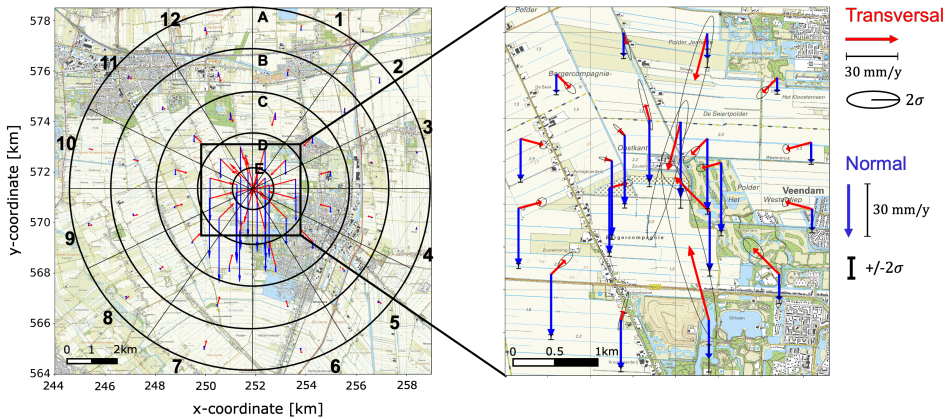


Figure 7.8.: Results for strapdown approach for a subsidence bowl resulting from magnesium solution mining. Red vectors represent the estimated displacement velocity in the Transversal direction (near-horizontal), and their 2σ uncertainty is visualized by a 95% confidence ellipse. Blue vectors represent the displacement velocities in the Normal direction (near-vertical), which have a $\pm 2\sigma$ confidence interval. The vectors start at the center of gravity for each RUM.

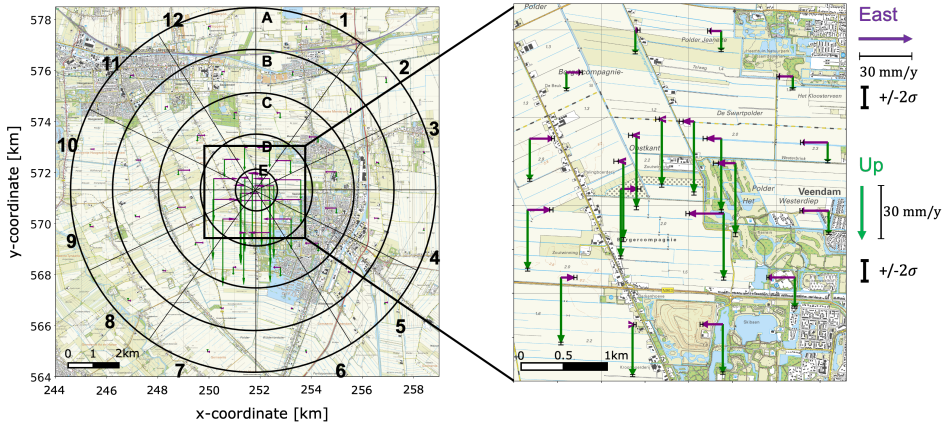


Figure 7.9.: Conventional (biased) results for comparison, showing only east and up displacements, produced by erroneously ignoring the north component. Note that this is a decomposition error [17] with a bias mainly in the up component, see Fig. 7.10.

the north component at all (even if it would be significant enough to be estimated reliably), and (ii) less accurate (i.e., biased) estimates in the east and north components. The strapdown approach leads to three-dimensional unbiased (east-north-up) estimates, accompanied with realistic precision metrics that enable realistic interpretation.

7

7.4.2. HYDROLOGICAL EFFECTS IN RELATION TO FAULTS

From 1900 until 1970, coal was extracted from mines in Limburg, the Netherlands [189]. One of its after-effects is differential ground heave induced by rising mine water [23, 146]. Three major ground heave zones are known, one of which is situated near Brunssum along the NW-SE oriented Feldbiss fault [86, 188]. Here we investigate the displacements near this fault over a relatively short period of four years.

Table 7.3.: Acquisition details Radarsat-2 (Limburg).

	track 109	track 302
Heading	ascending	descending
Mean θ	37.3°	33.4°
Mean α_d	259.2°	100.9°
Start	Dec 14, 2016	Dec 4, 2016
End	Sep 12, 2020	Sep 26, 2020

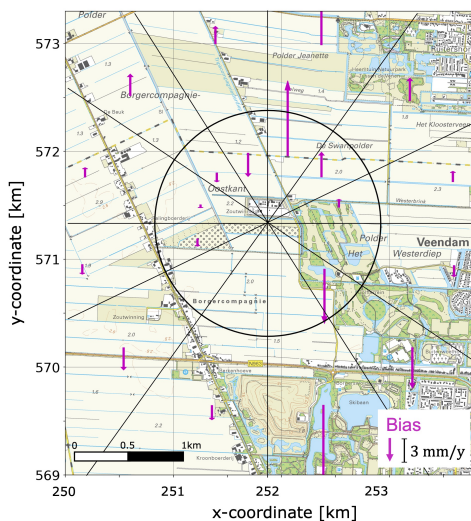


Figure 7.10.: Bias in the estimated Up components introduced by erroneously using the conventional east-up approach. The vectors show the difference with the estimated Normal components per RUM. Upward and downward point vectors show overestimation and underestimation, respectively.

DEFORMATION PHENOMENON AND RUMS

The Brunssum area is monitored by Radarsat-2 from an ascending and a descending geometry, see Tab. 7.3. Differential displacements are estimated using a PSI approach, for both geometries independently [193]. The LoS displacement rate estimates are projected onto the vertical (PoV) with $d_{PoV} = \cos^{-1} \theta d_{LoS}$, see Figs. 7.11a and b. Close to the Feldbiss fault, the two acquisition geometries clearly show different results, which is an indication for significant horizontal displacement components.

For comparison, we estimate the conventional up ('vertical') and east velocities, by neglecting the north-bound displacement components, resulting in biased estimates, see Brouwer and Hanssen [17]. The resulting vertical and east displacement rates are presented in Figs. 7.11c and d, respectively. They suggest that the area is moving upward at the southwest side of the fault, while at the northeast side, the vertical displacements seem minimal. The estimated east displacement rates, Fig. 7.11d, are difficult to interpret, since they underestimate the real horizontal displacement rates.

From the LoS displacement estimates we hypothesize that the surface movement is correlated with the orientation of the Feldbiss fault, and that the horizontal displacements are directed orthogonal to it, as the driving mechanism is most likely related to the redistribution of subsurface water pressure. There is no physical indication to assume a strike-slip component (parallel to the fault) in this case. Therefore, we use the strapdown approach where for each RUM the longitudinal axis is defined parallel to the Feldbiss fault. Since the orientation of the TLN frame is the same for the entire area, we divide the area into grid cells of 150×150 m.

PARAMETER ESTIMATION PER RUM

Per grid cell (RUM), we estimate the mean LoS displacement rate, and the RMSE which serves as a quality estimate for Q_{LoS} in Eq. (7.6) for both the ascending and descending acquisition, assuming a common datum, and we compute the mean incidence angle and azimuth of the ZDP. Subsequently, we estimate the normal and transversal displacement rates using Eqs. (7.5) and (7.6) and estimate the frame orientation parameters to be $\Lambda_{|0|} = -55^\circ$ and $\Omega_{|0|} = \Phi_{|0|} = 0^\circ$, using $\sigma_\Lambda = 20^\circ$ and $\sigma_\Omega = \sigma_\Phi = 5^\circ$ for each grid cell.

The estimated transversal and normal displacement rates per grid cell are shown in Figs. 7.11e and f. For a random subset of grid cells we also added the estimated displacements as vectors including an error bar and 95% confidence ellipse for the normal and transversal component respectively. At the southwest, we find positive displacements in the normal direction, implying that the area moves relatively upward. In this area, on average a maximum velocity in the normal direction of ~ 8 mm/y is found. At the northeast, relative normal displacements are near-zero but significant transversal displacements are estimated. Northeast of the fault, we find positive transversal displacements, while at the southwest of the fault, transversal displacements are negative, meaning that the two sides of the fault move away from each other, i.e., there is extensional strain. The blue band just north-east of the fault shows the largest horizontal displacements, up to ~ 6 mm/y. Since the displacement time-series has a length of almost four years, the total displacement is ~ 2.3 cm. As the area with the largest transversal displacements has a width of ~ 400 m, this results in ~ 23 $\mu\epsilon$ (micro-strain).

Comparing the strapdown with the neglect-north results, we find significant differences. While the results are strongly dependent on the hypothesis that surface movement is correlated with the fault and its orientation—an assumption that can be disputed—we prefer the inclusion of such contextual information over a 'blind' approach with a decomposition in the arbitrary east-up plane. In general, adding extra information to the estimation problem will lead to better interpretable displacement estimates, since (i) we obtain 3D instead of 2D displacement vectors, (ii) we include the horizontal and vertical confidence regions (see Figs. 7.11 e and f), and (iii) we avoid the inherent bias introduced by the neglect-north approach. The approach requires an explicit statement on the contextual information that is used.

7.5. MERITS AND LIMITATIONS

The strapdown method lies halfway in the spectrum between 'geometry-only' methods, which are purely based on the geometry of the observations, agnostic of the expected displacement phenomena, and 'advanced physical' methods, which assume knowledge of the physics of the driving mechanisms and can produce forward or inverse models related to the physical parameters. The strapdown method is based on the assumption that in many cases we can do better than the geometry-only methods, by making pragmatic use of non-disputed contextual knowledge on the problem at hand. It makes sense not to disregard this contextual information, as long as it is explicitly stated and refutable. Likewise, in terms

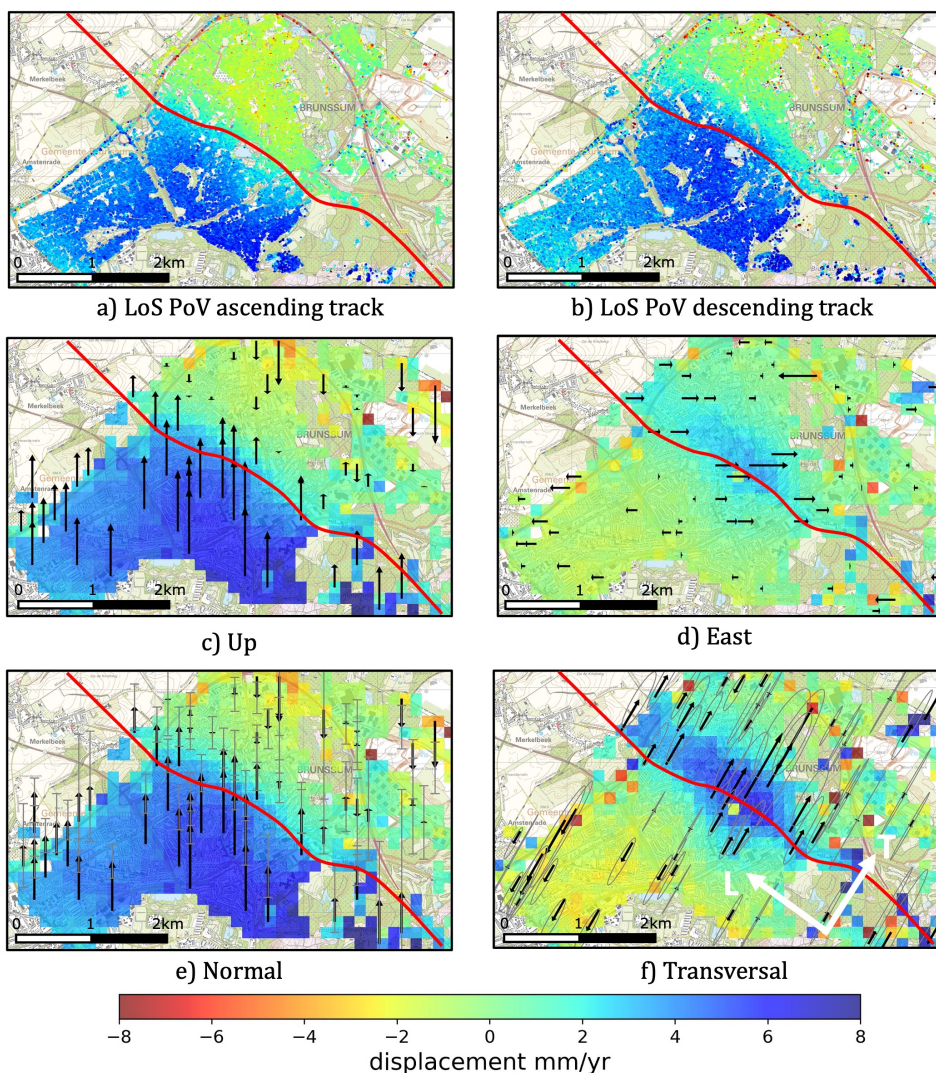


Figure 7.11.: Estimated displacement rates (mm/y) for the area of Brunssum, the Netherlands. The Feldbiss fault runs through the middle of the city in the direction NW-SE, indicated by the red line. (a) and (b): LoS displacement rates projected onto the vertical (PoV) for the ascending and descending track respectively. (c) and (d): vertical and east displacement rates, by neglecting the north component. Note that this is decomposition error that typically results in biased estimates [17]. Blue values in (d) indicates eastbound motion. (e) and (f): normal and transversal displacement rates estimated with the strapdown approach. Blue values in (e) indicate a positive motion in the normal direction, which is upward. Blue and orange values in (f) indicate displacements in the positive and negative transversal direction, respectively. In (c)–(f) we plotted displacement vectors, and for strapdown approach also confidence regions. These vectors are only plotted for a subset of randomly selected RUMs, in order to keep the visualization interpretable.

of limitations, the strapdown method cannot replace a thorough combination of physical information on a particular case study with geometric displacements estimated from InSAR. Inclusion of prior expert knowledge to the estimation problem should always result in a more optimal result. For example, when forward models are available, it may not even be needed to perform a decomposition of the viewing geometries, since it is easy to evaluate the model in the LoS viewing geometry directly. Yet, such a model of the driving mechanisms may not be always available. The conventional east-up decomposition, i.e., a geometry-only method, yields biased results, particularly in the up-direction, and it is in fact a 'neglect-north' approach. There is no physical reason why horizontal displacements in, e.g., the east direction are more common than in the north direction. Applying the unbiased strapdown method requires the orientation of the local TLN reference system at all locations, which comes with uncertainty. Yet, since this uncertainty is expressed and used in the estimation, the resulting displacement vector orientation and magnitude have realistic confidence regions, which mitigates the likelihood of misinterpretation. The strapdown method is dependent on the existence of presumed Regions of Uniform Motion (RUMs), which is essentially an assumption, similar to the geometry-only and advanced-physical methods, and the datasets from different viewing geometries need to find a common reference point.

7.6. CONCLUSIONS

The strapdown method makes it possible to estimate three-dimensional displacements from two satellite imaging geometries for deformation phenomena where the deformation mechanism is known to some extent, using minimal and largely undisputed contextual information. The method uses a location-dependent local reference system, with displacement occurring only in the transversal-normal plane, confined by a RUM. Since the orientation of the local frame is based on the physics of the problem at hand, the strapdown approach gives physically more relevant estimates compared to conventional geometry-only approaches, which are intrinsically biased, while not claiming optimality in the domain of advanced physical models. By quantifying the uncertainty in the knowledge about the orientation of the local frame, proper error propagation enables assessing the quality of the final estimates. In this way, even when the frame orientation is poorly known, it is still possible to estimate transversal and normal displacement components, and subsequently the east and north components, as long as the 'true' frame orientation is within the estimated orientation uncertainty. The method is practical, effective, unbiased, and largely generic, and can be characterized as "2D-local/3D-global".

Cartographic representations of the three-dimensional results include the re-introduction of classic geodetic vector-based visualizations, including confidence ellipses, which enables a more profound interpretation of the results.

8

ISOLATING AND ESTIMATING 3D SURFACE DISPLACEMENTS INDUCED BY GAS EXTRACTION IN THE GRONINGEN GAS FIELD

Since 1964, the Groningen gas field in the Netherlands has experienced significant subsidence due to gas extraction. Although InSAR has been widely used to estimate the field's vertical displacement, capturing its full 3D deformation, including horizontal components, has been challenging. This has only been achieved using spatially sparse GNSS observations. The InSAR strapdown method offers a solution to this problem. However, since InSAR observes total kinematic behavior, we first disentangle the different deformation mechanisms present in the InSAR data using an approach that exploits the spatial smoothness of the deep signal. Then, we apply the strapdown method to estimate vertical and directional horizontal displacement components, using frame orientation parameters estimated directly from the data. We incorporate uncontroversial contextual information and apply a bootstrapping method to improve the quality of the results. With this approach, we obtained reliable three-dimensional displacement estimates for the Groningen gas field, revealing previously unquantified horizontal displacements.

This chapter has been submitted to the *Netherlands Journal of Geosciences*, and is available as preprint: W. S. Brouwer and R. F. Hanssen. "3D surface displacement estimation over the Groningen gas field, the Netherlands". In: *EarthArXiv* (2025). DOI: 10.31223/X5775W <https://doi.org/10.31223/X5775W>

8.1. INTRODUCTION

AFTER production started in 1964, the Groningen gas field in the Netherlands has experienced significant pressure decline, resulting in subsurface compaction and surface displacements (subsidence) [65]. Since 2012, induced seismicity caused over 250,000 damage reports and major societal consequences, including health issues and safety concerns [157, 191, 192]. Monitoring surface displacements is therefore crucial—not only to improve understanding of subsurface processes, but also to support risk mitigation and damage assessment. Moreover, these measurements serve as critical input for inverse modeling efforts to estimate reservoir parameters such as pressure depletion and compaction [108, 185, 187].

Surface displacements have been monitored since the start of gas production: initially with leveling surveys, and since 2003 increasingly with InSAR [103, 105, 108, 135, 186, 187]. However, most studies focused on the vertical component, even though horizontal displacements can be expected—particularly near the field edges [103, 104, 148]. Neglecting this component results in biased estimates of the vertical component and underutilizes InSAR’s full potential, since the observations capture both the vertical and horizontal deformation in the projection of the 3D displacement vector onto the satellite’s line-of-sight (LoS) [17]. Moreover, knowledge on the horizontal displacement gradients is crucial, as it provides information on compression, extension, curvature, and tilt, which can affect infrastructure and buildings even more severely than vertical motion [111].

However, the near-polar orbits and right-looking mode of most SAR satellites limit observations to two effective LoS directions, complicating a full 3D decomposition. Nonetheless, we argue that knowledge on the driving mechanism—gas extraction leading to a subsidence bowl [71, 186]—enables using the strapdown method proposed by Brouwer and Hanssen [14] to decompose the LoS observations into normal (near-vertical) and transversal (inward near-horizontal) components.

A fundamental requirement for the strapdown decomposition is that it utilizes only observations that exclusively represent the deformation signal resulting from gas extraction, here referred to as the *deep* deformation signal. This poses a challenge, as InSAR observations reflect the *total* kinematic behavior, which is the sum of the deep signal, the shallow subsurface signal and *autonomous* behavior of objects and constructions, such as subsiding infrastructure, groundwater effects, or deforming buildings [136]. Therefore, these signal components first need to be disentangled, before we can decompose the deep signal.

Here, we present a systematic approach to disentangle the deep and the shallow or autonomous signal. Subsequently, we apply a local decomposition in transversal and normal components using an orientation based on the iso-displacement lines in the viewing geometries, and convert this to 3D (east, north, up) components, using estimated smoothness parameters obtained from well-estimable parts of the field.

The paper is organized as follows. In Sec. 8.2, we discuss the classification methodology used for the separation of the deep deformation signal from the shallow and autonomous surface motion, and present the results. In Sec. 8.3, we perform the decomposition using only the InSAR observations that reflect the deep signal. We reflect on the method and results in Sec. 8.4.

8.2. SCATTERER CLASSIFICATION: SEPARATING DEEP-ONLY AND MIXED SCATTERERS

To accurately decompose InSAR Line-of-Sight (LoS) observations into their normal and transversal components, it is crucial to include only those scatterers that uniquely represent the deformation mechanism of interest. In this case, the focus is on the subsidence bowl resulting from gas extraction at a reservoir located three kilometers below the surface—referred to as the *deep* deformation signal, d_{deep} . Consequently, all InSAR scatterers are affected by this deep signal. Yet, many scatterers additionally exhibit displacement contributions due to (i) *shallow* processes and/or (ii) *autonomous* movements, leading to a cumulative superposition of three distinct displacement components [80]. Thus, the observed displacement signal¹ is

$$\underline{d}_{\text{obs}} = d_{\text{shlw}} + d_{\text{deep}} + d_{\text{aut}} + \underline{n}, \quad (8.1)$$

where \underline{n} is a noise term and the underline indicates the stochastic nature of the variable. Fig. 8.1 shows an example of InSAR LoS data, that is projected onto the vertical, shown for the province of Groningen (panel A). The colors represent the velocity of scatterers in mm/year, reflecting the total observed deformation behavior. In panel A, the primary deep deformation signal—characterized by its spatial smoothness—is visible. Panels B, C, and D show additional deformation signals, including subsiding levees (B and C) and localized subsidence at the port of Eemshaven (D), see also Fig. 8.2. Including scatterers that are influenced by these “*non-deep*” deformation signals in the subsequent decomposition process (sec. 8.3) would significantly bias the decomposition results. For instance, inadvertently attributing the levee-related deformation in panel C to gas extraction would lead to a significant overestimation of the normal displacement component. Therefore, it is essential to identify and exclude scatterers that display autonomous and/or shallow deformation. To address this, all scatterers will need to be classified into two mutually exclusive classes: the *deep-only* class, and the *mixed* class. The deep-only class consists of a subset of scatterers, $u_{\text{d/o}}$, that solely reflect the deep deformation signal, defined as

$$u_{\text{d/o}} : d_{\text{deep}} \in \mathbb{R} \wedge d_{\text{shlw}} = 0 \wedge d_{\text{aut}} = 0. \quad (8.2)$$

The ‘*mixed*’ class contains the subset of scatterers influenced by a combination of deep, shallow, and autonomous signals, defined as

$$u_{\text{mix}} : d_{\text{deep}} \in \mathbb{R} \wedge d_{\text{shlw}} \in \mathbb{R} \wedge d_{\text{aut}} \in \mathbb{R}. \quad (8.3)$$

Consequently, we assume that all scatterers possess a deep component, though its numerical value may be zero. The proposed classification methodology comprises three subsequent steps and will be discussed below.

¹Note that the displacement vector d , in mm, may also be interpreted as, e.g., an (average or instantaneous) displacement velocity in mm/y, since this is geometry-invariant.

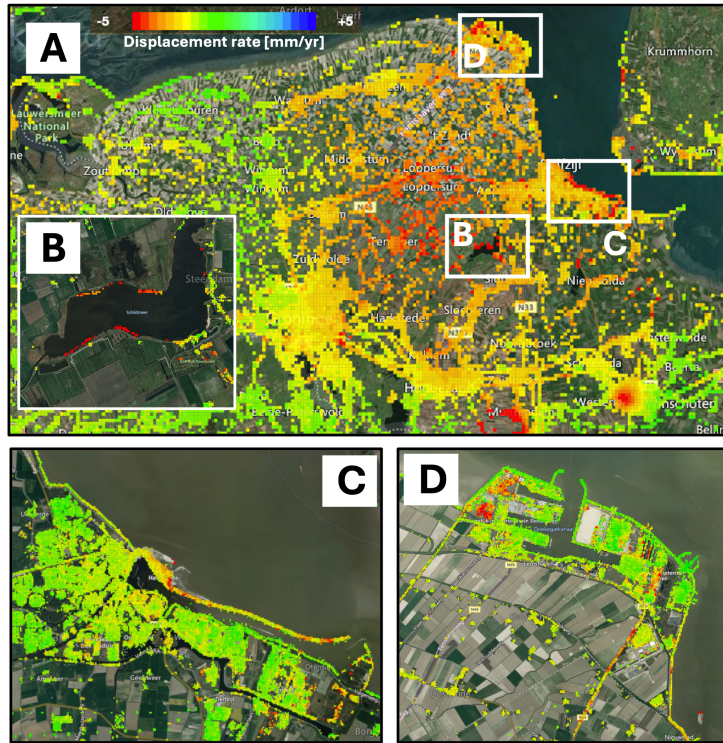


Figure 8.1.: InSAR deformation velocities, derived from Sentinel-1 data, for the province of Groningen. The colors represent the average deformation velocity in the LoS direction projected onto the vertical direction, expressed in mm/year. Panel A shows the dominant, spatially smooth subsidence bowl resulting from gas extraction, with maximum velocities reaching up to 6.5 mm/yr at the center. Due to the deep origin and large extent of the gas reservoir, all scatterers in the area are affected by the deep deformation signal, though its magnitude varies with location. Panels B, C, and D highlight localized autonomous deformation signals, such as subsiding dikes (B and C) and subsidence in the Eemshaven harbor (D). These autonomous signals are spatially less smooth compared to the widespread deep signal.

8.2.1. STEP I: QUADRANT CLASSIFICATION

Given the detection of more than one million coherent point scatterers² in both ascending and descending Sentinel-1 acquisitions (see Tab. 8.2 for acquisition details), all points are initially classified as *mixed* by default, see Fig. 8.4. We then use a quadtree approach to evaluate all scatterers in a quadrant and disentangle them into either the *deep-only* or the *mixed* class. A quadtree is a hierarchical data structure that recursively divides a region into four smaller quadrants, continuing this subdivision process until a predefined criterion or condition is satisfied [64, 154]. For each quadrant, we initially use the Line-of-Sight (LoS) velocities projected onto the vertical (PoV) direction [17]. A plane is then fitted through these velocities, to accommodate gradients in the displacement field, and consequently the residuals between the observations and the fitted plane are computed. If all scatterers within a quadrant reflect only the dominant deep deformation component, these residuals are expected to be relatively small, as the deep signal is assumed to be spatially smooth. However, a quadrant is further subdivided into four sub-quadrants if all of the following three criteria are met: i) the spread of the residues between the LoS PoV observations and the fitted plane exceeds a specified threshold; ii) the quadrant contains more than N scatterers; and iii) the quadrant's size is larger than a predefined minimum. The latter two criteria ensure sufficient data density and statistical reliability within each quadrant.

An example of the resulting quadtree structure is shown in Fig. 8.2. Starting with the large black quadrant (1), a plane is fitted through all PoV velocities. Because of the industrial area at the bottom right—a newly installed solar farm experiencing rapid initial consolidation—the PoV velocities cannot be sufficiently described by a single plane, and the residues between the observations and the plane will thus be large. Therefore, quadrant 1 will be subdivided into the four purple quadrants, after which this process will be repeated. The residues with fitted planes in sub-quadrants 2, 3, and 4 are small—here we use an upper threshold of 1.5 mm/yr for the standard deviation of the residues—and will not be further subdivided. The fifth quadrant is further subdivided into the four orange ones. Thus, the presence of local autonomous or shallow signals requires smaller quadrants to describe the signal.

After this procedure, the quadrants (and thus all scatterers within them) are classified into the two disjunct classes: *deep-only* and *mixed*. Under the assumption that the deep signal is spatially smooth, we classify a quadrant as *deep-only* if (i) it is large (>700 m), (ii) the dispersion (σ) of the residuals of the scatterers with the estimated plane is small (i.e., <1.5 mm/y), and (iii) the gradient of the fitted plane is low (i.e., <0.06 mm/y/m).³ The result for the ascending dataset is shown in Fig. 8.3, where the left panel shows the *deep-only* quadrants and scatterers, and the right panel the *mixed* ones, respectively.

At this point, all scatterers located within a given quadrant inherit a uniform

²We use the Delft taxonomy of scatterer classification proposed by Hu *et al.* [93].

³The rationale for choosing a maximum value of 700 m is that it is ~20% of the reservoir depth, which is three kilometer. The maximum sigma value for the residuals was chosen to be 1.5 mm/yr as we expect to see larger values when autonomous motion takes place. The maximum gradient was chosen an order of magnitude larger (to be conservative) than we estimated at the LoS data near the edges of the field. Note that all values are application dependent.



Figure 8.2.: Example of quadrant classification, starting with the large black quadrant (1). Due to the additional subsidence signal in the bottom right (a newly installed solar farm), this quadrant is further subdivided into four new (purple) quadrants. Quadrants 2, 3, and 4 contain only one deformation phenomenon and will not be further subdivided, whereas quadrant 5 will be split into four new sub-quadrants. This way, areas exhibiting local shallow and autonomous signals are isolated from areas only representing the deep deformation signal.

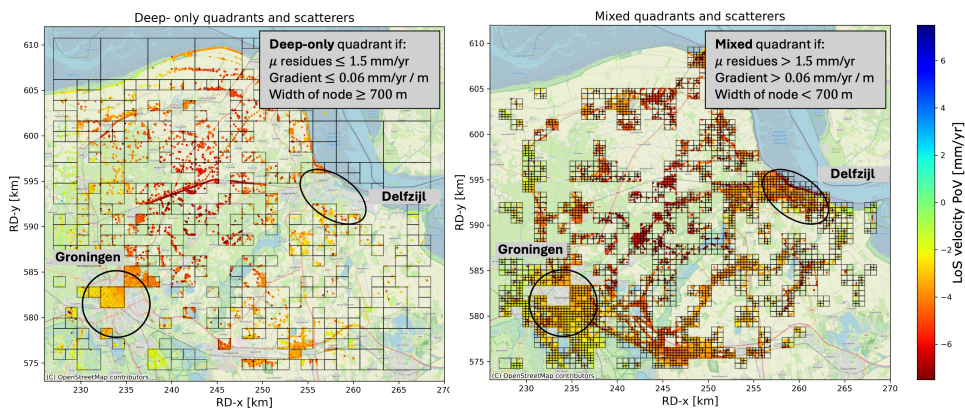


Figure 8.3.: A result of the separation of quadrants into either *deep-only* (left) or *mixed* (right). Large quadrants, where the residues with the fitted plane through the PoV velocities are small are assigned to the deep-only class. Local deformation phenomena, such as subsiding infrastructure, require smaller quadrants to describe the deformation behavior and are assigned to the mixed quadrants. Note that both panels are mutually exclusive.

classification label, depending on the classification of the quadrant. For the Groningen case, the percentage of scatterers per class is presented in the flowchart in Fig. 8.4, where the green and the red values represent the ascending and descending acquisitions, respectively. Indeed, the majority of scatterers is classified as *mixed*. However, some scatterers in *deep-only* quadrants may still exhibit additional autonomous and/or shallow behavior, and some scatterers in *mixed* quadrants may only exhibit a deep signal. This is addressed below in steps II and III.

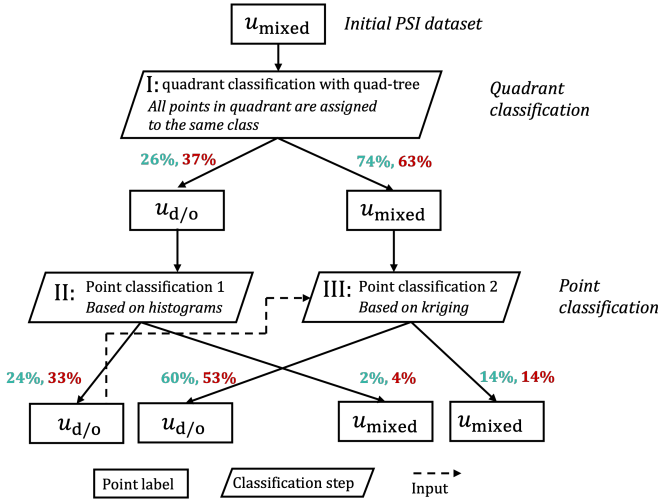


Figure 8.4. Flowchart of the classification procedure: In the first step of the classification process, the quadrants and all scatterers within them are classified into two classes. After quadrant classification, scatterers may erroneously be classified. In the first point classification step, we analyze the histograms of the deep-only labeled scatterers and reclassify the mixed scatterers that were erroneously classified as deep-only. In the second classification, we use information from the deep-only classified scatterers to predict the deep deformation component at the mixed scatterers. We use this information to reclassify the erroneously classified mixed scatterers to deep-only. The percentages in green and red represent the proportion of scatterers belonging to a class for ascending and descending acquisitions, respectively.

8.2.2. STEP II: POINT RECLASSIFICATION DEEP-ONLY TO MIXED

Individual scatterers in *deep-only* quadrants may actually still exhibit additional autonomous and/or shallow behavior. To detect potential scatterers belonging to the mixed class, we analyze the histograms of the PoV velocities in the deep-only quadrants. If all scatterers represent the same deformation signal, the histogram is expected to be symmetrical, only representing random noise. However, if additional deformation components are present, with significant magnitudes, the histogram may become skewed. Since gravity is the main driving force (i.e., points will more often move systematically down than up) we specifically expect a left-skewed

distribution and we assume that the main mode of the histogram corresponds to the deep-only deformation signal.

When fitting a skew-normal distribution to all velocities within a quadrant, we subsequently estimate the main mode of all velocities and their Median Absolute Deviation (MAD)⁴. We reclassify scatterers with velocities outside the range (main mode $\pm 2\text{MAD}$) to *mixed*, following the procedure of Hanssen and van Leijen [79]. An example is shown in Fig. 8.5a, where two deformation mechanisms are present: a gas production facility and the railway in the south, clearly visible in the skewed histogram. Consequently, all scatterers within the selected range are labeled as *deep-only*, while the remaining scatterers in the left tail are classified as *mixed*, see Figs. 8.5c and 8.5d.

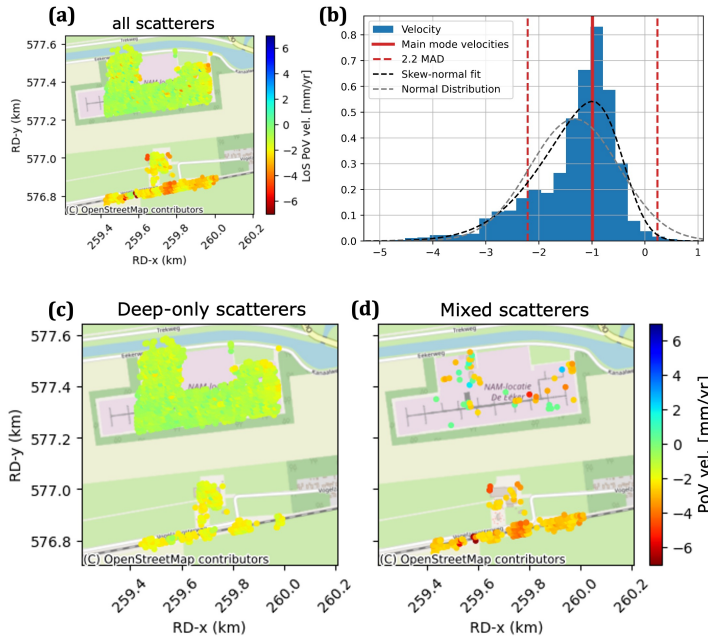


Figure 8.5.: In deep-only quadrants, individual scatterers actually belonging to the mixed class should be detected and reclassified. (a) shows the PoV velocities of all scatterers in such a quadrant, while (b) presents the corresponding histogram. The skewness of the histogram indicates the presence of multiple deformation components. The solid red line marks the main mode velocity, and the dashed red lines indicate the (main mode $\pm 2 \times \text{MAD}$) range. Scatterers outside this range are reassigned to the mixed class (d), while the remaining scatterers are individually classified to the deep-only class (c).

⁴ Similar to the mode being less influenced by outliers than the mean, the MAD is less influenced by the sample size [95].

8.2.3. STEP III: POINT RECLASSIFICATION MIXED TO DEEP-ONLY

After the quadrant classification in step I, some individual scatterers in *mixed* quadrants may actually be representing *deep-only* signals. Identifying those scatterers is important to achieve sufficient spatial point density required for the subsequent geometric decomposition, see Fig. 8.3. For example, Fig. 8.3a shows a lack of deep-only scatterers in the cities of Groningen (southwest) and Delfzijl (east), despite the expectation of finding such scatterers in these areas. Without deep-only scatterers at these locations, a decomposition cannot be performed.

For this 'step III' reclassification, see Fig. 8.4, we include the deep-only scatterers that were the result of step II. The assumption is that for those scatterers the autonomous and shallow deformation components are zero, i.e., $d_{\text{aut}} = d_{\text{shlw}} = 0$, and therefore $d_{\text{obs}}(u_{d/o}) = d_{\text{deep}}(u_{d/o}) + n$, where $u_{d/o}$ identifies a deep-only labeled scatterer. This deep-only signal is expected to exhibit a certain spatial smoothness, which we will use to predict the deep signal at locations of the scatterers that were labeled as mixed, i.e., u_{mix} , after step I. We use ordinary kriging interpolation with

$$\hat{d}_{\text{deep}}(u_{\text{mix}}) = \sum_{i=1}^n \lambda_i d_{\text{obs}}(u_{i,d/o}), \quad (8.4)$$

where $d_{\text{obs}}(u_{i,d/o})$ represents the observed PoV velocities of the *deep-only* classified scatterers, n is the number of deep-only classified scatterers, and λ_i are the kriging weights derived from the variogram corresponding to the deep deformation signal.

The variogram is derived from the observed LoS deformation that is projected onto the vertical of the *deep-only* classified scatterers, which would therefore contain both noise and the deep signal. We fit a Gaussian model through the data, with estimated variogram parameters as presented in Tab. 8.1. The parameters for the ascending and descending dataset are comparable, with slight differences possibly due to the different viewing geometry.

The kriging interpolation provides a prediction of the deep signal at the locations of the mixed scatterers, here denoted as $\hat{d}_{\text{deep}}(u_{\text{mix}})$. Comparing the predicted deep signal with the observed signal, we estimate the concatenated autonomous and shallow behavior of the scatterer with

$$\hat{d}_{\text{aut}}(u_{\text{mix}}) + \hat{d}_{\text{shlw}}(u_{\text{mix}}) = d_{\text{obs}}(u_{\text{mix}}) - \hat{d}_{d/o}(u_{\text{mix}}). \quad (8.5)$$

If the absolute value of $\hat{d}_{\text{aut}}(u_{\text{mix}}) + \hat{d}_{\text{shlw}}(u_{\text{mix}})$ is small, we assume that the observed deformation signal only has a deep component and reclassify those scatterers from

Table 8.1.: Gaussian variogram parameters estimated from the descending and ascending PoV values used for the kriging interpolation in Section 8.2.3. This shows that both viewing geometries result in comparable variogram parameters.

	range [km]	nugget [mm ² /y ²]	sill [mm ² /y ²]
asc	16	0.2	3
desc	17	0.3	4

the *mixed* class to the *deep-only* class. As a practical limit, here we reclassify mixed scatterers into the deep-only class when $|\hat{d}_{\text{aut}}(u_{\text{mix}}) + \hat{d}_{\text{shlw}}(u_{\text{mix}})| < 1.5 \text{ mm/y}$, see footnote 3, to avoid excessive smoothing and to allow for some missed signals. This value was chosen since it is equal to the threshold of the spread of the residues to separate deep-only and mixed quadrants in Sec. 8.2.1 (Step I). When $|\hat{d}_{\text{aut}}(u_{\text{mix}}) + \hat{d}_{\text{s}}(u_{\text{mix}})| \geq 1.5 \text{ mm/y}$, the scatterer remains a mixed scatterer, but with (i) a disentangled deep component and (ii) a concatenated autonomous/shallow component, which can be used for other studies. The result of this three-step approach is a non-overlapping classification of *deep-only* and *mixed* scatterers, whose estimated PoV velocities are shown in Fig. 8.6.

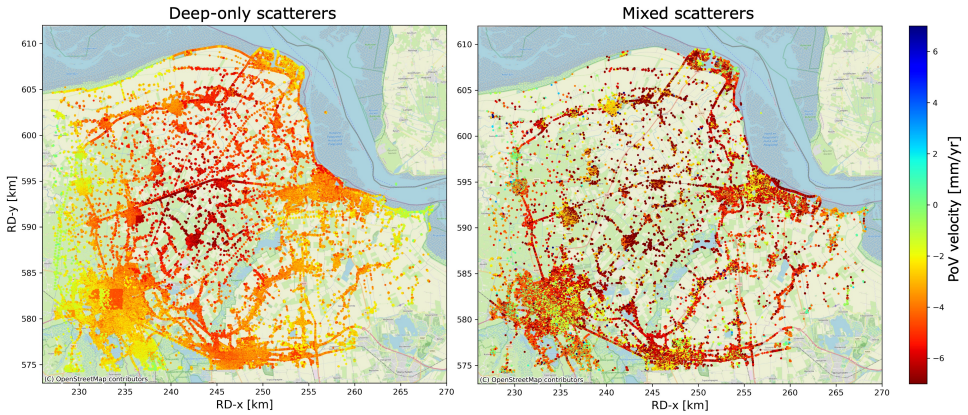


Figure 8.6.: Final result for the classification of scatterers into two disjunct sets of points: *deep-only* (left) and *mixed* (right) for a Sentinel-1 ascending acquisition over Groningen. Both figures share the same color scale shown at the right. Note that the mixed scatterers also represent the deep deformation behavior. It can be seen that the deep-only scatterers show smoother signal in space.

8

A comparison between Figs. 8.6 and 8.3 reveals that the spatial distribution of deep-only classified scatterers has significantly improved.

From the original 74% of point scatterers classified as *mixed* after step I, see Fig. 8.4, about 80%⁵ are ultimately moved to the deep-only class in step III. This shows that the two subsequent point classification steps (II and III) are effective and necessary. The high percentage of reclassified scatterers in step III is likely caused by the large number of scatterers in the cities of Delfzijl and Groningen. Initially, almost all scatterers in those cities were classified as mixed.

8.2.4. DISCUSSION

The proposed classification method separates deep-only and mixed scatterers based on the expected smoothness of the deep signal, and does not require direct physical knowledge on the nature of the scatterers. While these expectations and

⁵60/(60+14)=81% (ascending) and 53/(53+14)=79% (descending)

assumptions may be somewhat heuristic, they are explicitly stated and therefore subject to scrutiny. Importantly, in this study our goal is not to obtain a detailed characterization of autonomous or shallow scatterer behavior. Instead, we aim to remove scatterers exhibiting such motion from the dataset as effectively as possible prior to decomposition. The decomposition process depends on identifying ‘regions of uniform motion’, i.e., RUMs [14]), within which velocities are averaged. As a result, any misclassification—such as incorrectly labeling a mixed scatterer as deep-only—is likely to be attenuated within these regions. As shown in Fig. 4, in the end approximately 85% of scatterers are classified as deep-only, with only 15% identified as mixed. This indicates that the method does not excessively smoothen the data.

8.3. DECOMPOSING DEEP DEFORMATION INTO VERTICAL AND DIRECTIONAL HORIZONTAL COMPONENTS

Working only with the resulting *deep-only* scatterers in both the ascending and descending dataset, we can decompose the LoS observations into normal and transversal components using the strapdown method, as proposed by Brouwer and Hanssen [14]. This uses a local Cartesian coordinate system with transversal, longitudinal, and normal components (TLN), where the displacements occur only in the transversal-normal plane by definition. The frame’s orientation is defined by three angles: Λ , Φ , and Ω , where $\Lambda \in [0^\circ, 360^\circ)$ is the azimuth of the longitudinal direction relative to the geographic north, $\Phi \in (-90^\circ, +90^\circ]$ is the elevation angle of the longitudinal direction relative to the horizontal, and $\Omega \in (0^\circ, +90^\circ]$ is the elevation angle of the transversal direction, see sign conventions in [14].

For subsidence bowls, the normal direction is approximately vertical, while horizontal displacements are expected to be directed toward the center of the bowl, i.e., the longitudinal direction is aligned parallel to the iso-deformation lines, and the transversal direction is near-centripetal.

With the LoS observations from an ascending, $\underline{d}_{\text{LoS}}^{\text{asc}}$, and descending acquisition, $\underline{d}_{\text{LoS}}^{\text{dsc}}$, the transversal and normal displacements, d_T and d_N can be solved from a nonlinear set of observation equations with

$$E\left\{ \begin{array}{c} \underline{d}_{\text{LoS}}^{\text{asc}} \\ \underline{d}_{\text{LoS}}^{\text{dsc}} \\ \underline{\Lambda} \\ \underline{\Omega} \\ \underline{\Phi} \end{array} \right\} = \underbrace{\begin{array}{c} P_T^{\text{asc}}(\Lambda, \Omega, \Phi)d_T + P_N^{\text{asc}}(\Lambda, \Omega, \Phi)d_N \\ P_T^{\text{dsc}}(\Lambda, \Omega, \Phi)d_T + P_N^{\text{dsc}}(\Lambda, \Omega, \Phi)d_N \\ \Lambda \\ \Omega \\ \Phi \end{array}}_{A(x)}, \text{ and} \quad (8.6)$$

$$D\left\{ \begin{array}{c} \underline{d}_{\text{LoS}}^{\text{asc}} \\ \underline{d}_{\text{LoS}}^{\text{dsc}} \\ \underline{\Lambda} \\ \underline{\Omega} \\ \underline{\Phi} \end{array} \right\} = \underbrace{\begin{array}{ccccc} Q_{\text{LoS,asc}} & 0 & 0 & 0 & 0 \\ 0 & Q_{\text{LoS,dsc}} & 0 & 0 & 0 \\ 0 & 0 & \sigma_\Lambda^2 & 0 & 0 \\ 0 & 0 & 0 & \sigma_\Omega^2 & 0 \\ 0 & 0 & 0 & 0 & \sigma_\Phi^2 \end{array}}_{Q_{yy}}, \quad (8.7)$$

where

$$\begin{aligned}
 P_T &= (\sin\theta \sin\alpha_d \cos\Lambda - \sin\theta \cos\alpha_d \sin\Lambda) \cos\Omega - \\
 &\quad (-\sin\theta \sin\alpha_d \sin\Lambda + \sin\theta \cos\alpha_d \cos\Lambda) \sin\Phi + \\
 &\quad \cos\theta \cos\Phi) \sin\Omega \text{ and} \\
 P_N &= (\sin\theta_m \sin\alpha_d \cos\Lambda - \sin\theta \cos\alpha_d \sin\Lambda) \sin\Omega + \\
 &\quad (-\sin\theta_m \sin\alpha_d \sin\Lambda + \sin\theta \cos\alpha_d \cos\Lambda) \sin\Phi + \\
 &\quad \cos\theta \cos\Phi) \cos\Omega.
 \end{aligned}$$

$E\{\cdot\}$ expresses the expectation of the model, and $x = [d_T, d_N, \Lambda, \Omega, \Phi]^T$ is the vector of unknowns. In the model, $\underline{d}_{\text{LoS}}^{\text{asc}}$ and $\underline{d}_{\text{LoS}}^{\text{dsc}}$ are ‘sets’ of LoS observations, i.e., all LoS observations for one viewing geometry over a region of uniform motion (RUM), see Brouwer and Hanssen [14] for further details. The first two rows of $A(x)$ are unique nonlinear equations of x due to the difference in viewing geometry between ascending and descending orbits, defined by the incidence angle towards the radar, θ , and the azimuth of the zero-Doppler plane (ZDP) at the target position towards the satellite, α_d . To resolve the rank deficiency, pseudo-observations for $\underline{\Lambda}$, $\underline{\Omega}$, and $\underline{\Phi}$ are added to the system. These pseudo-observations are also used as initial values in Eq. (8.6) and based on best-effort estimates for the frame orientation, as discussed below. $D\{\cdot\}$ is the dispersion of the observations, where Q_{LoS} is the covariance matrix of the LoS observations for a set. This covariance matrix is a diagonal matrix containing the variances of displacements for each scatterer within the set. The uncertainty in the orientation of the TLN frame is represented in σ_{Λ}^2 , σ_{Ω}^2 , and σ_{Φ}^2 , values that reflect the degree of uncertainty on the orientation of frame. The alignment of the local frame with respect to the local deformation phenomena is a key part of the method, ensuring that displacements occur exclusively in the transversal-normal plane and that the alignment uncertainty is realistically (i.e., conservatively) approximated, to obtain realistic quality metrics for the final displacement estimates.

The nonlinear model of observation equations, i.e. Eqs. (8.6) and (8.7), can be solved using iterative techniques such as the Gauss-Newton method. This process requires linearizing the system of equations and providing initial approximations for the unknown parameters $x_{[0]}$, i.e., Λ , Φ , Ω , d_T , d_N . Below we (i) discuss how the initial values are derived for the Groningen gas field, and (ii) perform the strapdown decomposition, resulting in estimates for the normal and transversal components. As the quality of the estimated transversal components varies with orientation, we (iii) further improve the quality of the estimates based on uncontroversial contextual information.

8.3.1. APPROXIMATING THE ORIENTATION OF THE TLN FRAME

The subsidence signal of the Groningen gas field is notably non-circular, see Fig. 8.6a, which makes accurately estimating the TLN frame orientation important. The LoS observations are projected onto the vertical (PoV) for both viewing geometries to obtain a rough first-order approximation of the gradients of the subsidence

Table 8.2.: Acquisition details for Sentinel-1 tracks 15 and 37 in Groningen, the Netherlands.

	S1 track 15	S1 track 37
Heading	ascending	descending
Mean θ	36.1°	36.9°
Mean α_d	259.3°	100.5°
Start	Feb 2, 2015	Dec 2, 2015
End	June 21, 2023	July 5, 2023

field. Figs. 8.7a and b show the kriging predictions of the PoV velocities for both acquisitions, together with estimated contour lines. It can be seen that, due to the presence of a horizontal component, the contour lines for both datasets differ slightly. We compute the mean value of these two fields, see Fig. 8.7c, to get an initial approximation of the shape of the field with

$$\hat{d}_{\text{PoV}} = \frac{1}{2} \left(\hat{d}_{\text{PoV,asc}} + \hat{d}_{\text{PoV,dsc}} \right), \quad (8.8)$$

where $\hat{d}_{\text{PoV,asc}}$ and $\hat{d}_{\text{PoV,dsc}}$ are the two kriging predictions for a regular grid, and \hat{d}_{PoV} is the mean estimated field. Here, the PoV values are expressed as positive subsidence rates: greater values correspond to greater subsidence and the field attains its maximum at the bowl center. The spatial gradient of this mean field is

$$\nabla \hat{d}_{\text{PoV}} = \left(\frac{\partial \hat{d}_{\text{PoV}}}{\partial x}, \frac{\partial \hat{d}_{\text{PoV}}}{\partial y} \right) = (d_x, d_y), \quad (8.9)$$

where x and y denote the east and north directions respectively, points in the direction of steepest *increase* of the subsidence field. This gradient is directed centripetally and coincides with the transversal direction T of the TLN frame. The azimuth of the transversal axis (measured clockwise from north) is therefore

$$\alpha_T = \text{atan2}(d_x, d_y) \bmod 2\pi, \quad (8.10)$$

where $\text{atan2}(d_x, d_y)$ uses the azimuth convention, with the east component as the first argument and the north component as the second. The longitudinal axis L is by definition perpendicular to T and the azimuth of the longitudinal axis is therefore

$$\Lambda = \left(\alpha_T + \frac{\pi}{2} \right) \bmod 2\pi = \left(\text{atan2}(d_x, d_y) + \frac{\pi}{2} \right) \bmod 2\pi. \quad (8.11)$$

Fig. 8.7c shows the mean contour lines together with the estimated transversal directions as black arrows, which are perpendicular to the contour lines and point toward the bowl center.

The frame alignment also requires estimates for Ω and Φ , because of the absence of significant topography in this region we use $\Omega = 0^\circ$ and $\Phi = 0^\circ$.

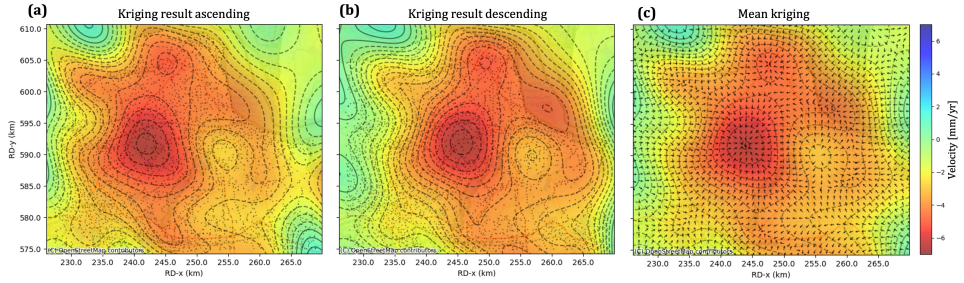


Figure 8.7.: (a) and (b): kriging predictions of ascending and descending *deep-only* PoV velocities on a regular grid with a 200 m resolution. Black dots indicate the locations of the input data, which are (a representative subset of) *deep-only* classified scatterers. A random spatially subset of points is used to reduce the computational load of the kriging estimation. The subset was chosen to ensure good spatial coverage, with points evenly distributed across the area. Due to the presence of a horizontal component the maximum subsidence occurs at a different location for the both acquisitions. (c): mean of the two fields shown in (a) and (b), along with contour lines and the estimated orientation of the transversal axes as vectors, assumed to be perpendicular to the contour lines.

8.3.2. STRAPDOWN DECOMPOSITION

Using the approximated frame orientation we decompose the LoS *deep-only* observations for ‘regions of uniform motion’ (RUMs)—areas where all selected *deep-only* scatterers are assumed to exhibit the same displacement behavior [14]. We divide the province of Groningen into grid cells of 500×500 m, and estimate the mean and the standard deviation of the LoS velocity per grid cell, where the latter serves as an approximation for Q_{LoS} in Eq. (8.7). We conservatively set $\sigma_{\Lambda} = 15^\circ$, to account for imperfections in our initial estimate of the frame orientation, and $\sigma_{\Omega} = \sigma_{\Phi} = 5^\circ$. The nonlinear system of observation equations (8.6) and (8.7) is solved using a Gauss-Newton iteration scheme, which requires initial estimates for the unknown parameters. We set $d_T^{[0]} = d_N^{[0]} = 1$ mm/yr (as we assume that the deep signal is present everywhere), $\Omega^{[0]} = \Phi^{[0]} = 0^\circ$, and use the computed values from Sec. 8.3.1 for $\Lambda^{[0]}$.

Figs. 8.8a and 8.9a show the estimated velocities for the normal and transversal component, respectively, together with corresponding sigma values in Figs. 8.8f and 8.9f. It shows that the magnitude of the estimated normal component is consistent with the estimated contour lines that serve as input for the TLN frame orientation (the contour lines are shown in the figures as a reference). As an additional check on the viability of the approximated TLN frame orientation, we recompute new contour lines based on d_N , see Fig. 8.10. This shows that the orientation of the contour lines match well, with only some minor deviations at the west side of the field. When we derived new estimates for Λ from these new contour lines and look at the difference we find a mean value of 0.1 degrees, and σ value of 8 degrees. Note that these values are small compared to the a priori conservative assumption of $\sigma_{\Lambda} = 15^\circ$. The estimated normal component reaches values of up to

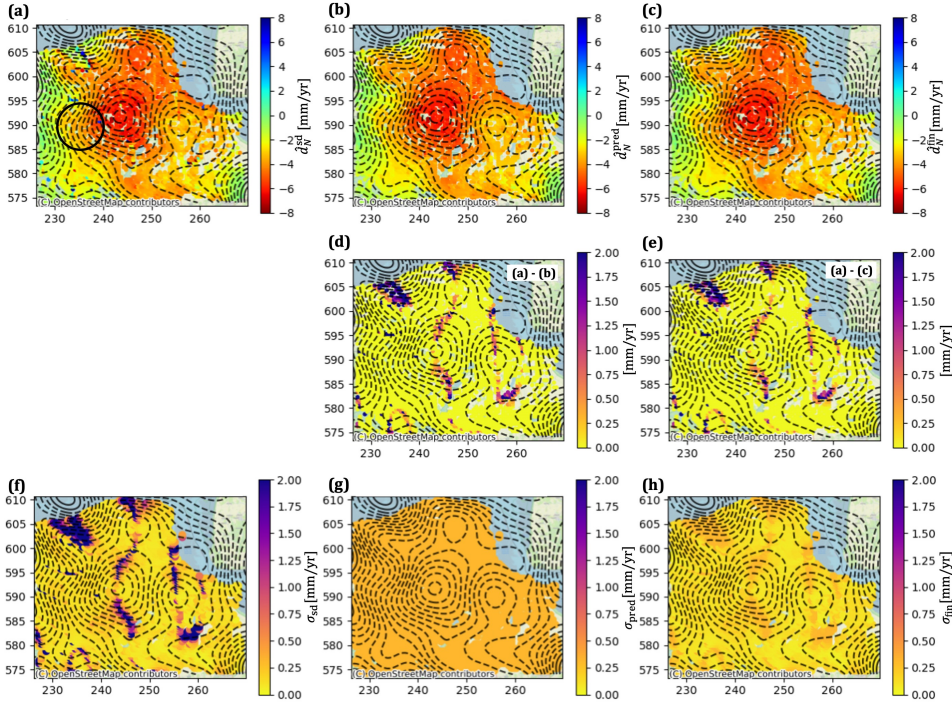


Figure 8.8.: (a) Normal velocities estimated using only the strapdown decomposition, with the corresponding quality values (σ) shown in (f). (b) presents the results obtained via kriging interpolation, \hat{d}_N^{pred} , with corresponding sigmas in (g), and the difference with the strapdown results in (d). In (c), we show the combined estimates for the normal component, \hat{d}_N^{fin} , derived by solving the mathematical model from Eqs. (8.13) and (8.14), with the associated σ values shown in (h), and the difference with the strapdown solution in (e). Notably, the combined approach improves the quality of the estimates—particularly for RUMs where the transversal direction aligns with the north–south direction, see the lower sigma values of (h) compared to (f). The circle in (a) locates the city of Groningen.

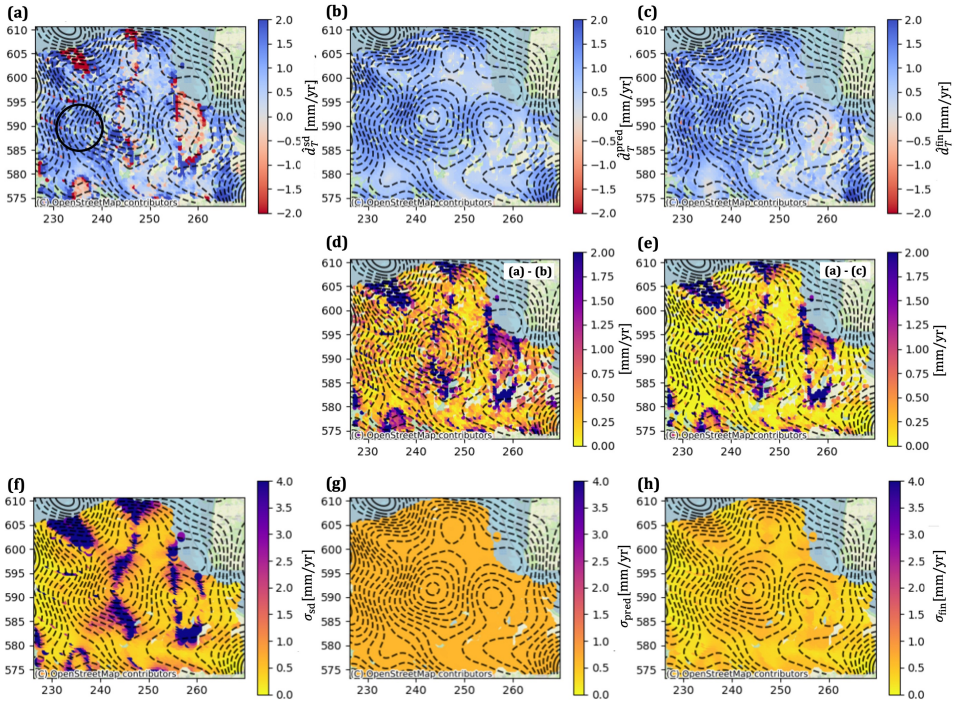


Figure 8.9.: (a) **Transversal** velocities estimated using only the strapdown decomposition, \hat{d}_T^{sd} . Note that the color bar is clipped. Corresponding quality values (σ) shown in (f). (b) presents the results obtained via kriging interpolation, \hat{d}_T^{pred} , with corresponding sigmas in (g), and the difference with the strapdown results in (d). In (c), we show the combined estimates for the transversal component, \hat{d}_T^{fin} , derived by solving the mathematical model from Eqs. (8.13) and (8.14), with the associated σ values shown in (h), and the difference with the strapdown solution in (e). Notably, the combined approach improves the quality of the estimates—particularly for RUMs where the transversal direction aligns with the north–south direction, see the lower sigma values of (h) compared to (f). The circle in (a) locates the city of Groningen.

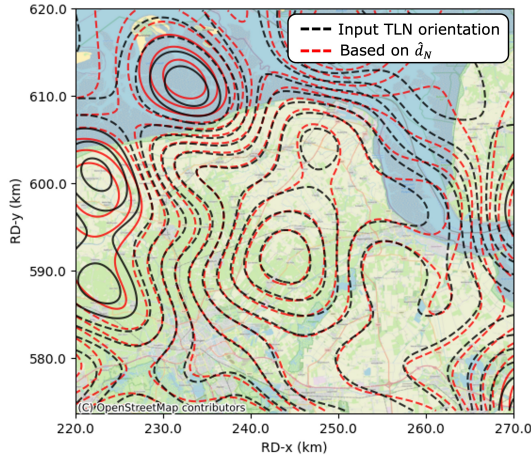


Figure 8.10: Contour lines that served as an input for the strapdown decomposition shown in black, and the contour lines that were estimated from the normal component in red. It can be seen that the input orientation of the TLN frame was rather good since the orientation of the two contour lines is almost identical. We also estimated new values for Λ with the contourlines based on the estimated normal component, and compared them to our initial input for the strapdown decomposition. This resulted in a mean difference of 0.08 degrees and σ of 8 degrees.

–6.5 mm/yr in the middle of the field, at RD coordinates [244000, 592000], north of the city of Ten Post, which is well in line with earlier results [136]. Also, a steeper gradient in the estimated normal velocities at the edges of the field is observed.

The estimated values for the transversal component, see Fig. 8.9a, predominantly show positive (blue) values, which confirms that the estimated frame orientation seemed appropriate. As expected, higher transversal velocities are observed at locations where the contour lines are closer together—particularly around the city of Groningen, indicated with the circle between x -coordinates 230–240 km and y -coordinates 585–595 km. Here, transversal velocities of up to 1.8 mm/yr are estimated, which, given that gas extraction has been ongoing since 1960, would result in approximately 11 cm of cumulative horizontal displacement.

Extreme values for the transversal velocity and large corresponding standard deviations are observed for RUMs where the transversal direction is (almost) aligned with the north direction, see Fig. 8.9e. At these RUMs the transversal direction is close to the orientation of the null line⁶, resulting in an ill-posed problem. Consequently, those unknowns can be estimated with low precision, affecting also the normal component. Below, we address and reduce these adverse effects.

⁶The null line is the direction in three-dimensional space in which no displacements can be observed by both the ascending and descending acquisition. Its orientation can be computed from the viewing geometry of the ascending and descending acquisition and is described by azimuth ϕ and elevation angle ζ , see [17].

8.3.3. IMPROVEMENT USING CONTEXTUAL PREMISES

Since we are analyzing a deformation signal known to be caused by gas extraction from a reservoir at a depth of three kilometers, the estimated extreme transversal velocities shown in Fig. 8.9a are physically unrealistic. Note that the color bar is clipped for visualization purposes, but we observed estimated values beyond ± 10 mm/yr. In fact, (i) the depth of the reservoir is expected to result in a spatial displacement signal with some degree of spatially smoothness in the tangential direction, i.e., roughly parallel to the iso-displacement lines approximated in Fig. 8.7c. While this degree of smoothness may differ slightly depending on the sectorial position, there is (ii) no reason that the transversal displacement gradients are as strong as the observed ones in Fig. 8.9a. Instead, (iii) it is very likely that the extreme values are a consequence of the lower sensitivity in those sectorial positions. Fortunately, (iv), the sensitivity to estimate the transversal displacement gradients in the other sectorial positions is very high.

We consider considerations (i) to (iv) as ‘*contextual premises*’, i.e., statements assumed to be true, but formulated explicitly to allow for scrutiny and potential refutation. Deductively, it follows from the premises that the results from the ‘transversal-sensitive’ RUMs, i.e., with well-solvable displacement estimates, provide insight into the degree of smoothness of the transversal deformation signal, also over the sectorial positions with transversal-less-sensitive RUM’s. We can use this approach to weigh the kinematic estimates from Sec. 8.3.2 and combine them with smoothness conditions derived from other parts of the field. We apply this approach subsequently to the normal and to the transversal component of the velocity.

NORMAL COMPONENT

In order to quantify the smoothness, we compute the variogram of the normal velocity using the strapdown estimates of only well-solvable RUMs, i.e., RUMs where the direction of the transversal component is at least 15 degrees away from the orientation of the null line,⁷ which has an elevation and azimuth angle of $\zeta = 7.8^\circ$ and $\phi = 0.0^\circ$, respectively. The resulting variogram, shown in Fig. 8.11a, is an approximation of the signal’s smoothness. Since the variogram is based on velocities from the strapdown decomposition, it has a non-zero nugget to account for imperfections in the decomposed results. We fitted a Gaussian variogram model with a range of 18.5 km, a nugget of $0.1 \text{ mm}^2/\text{yr}^2$, and a sill of $2.3 \text{ mm}^2/\text{yr}^2$. The variogram values are the kriging weights, to predict a new normal velocity based on the expected smoothness of the signal, for each RUM, using

$$\hat{d}_N^{\text{pred}} = \sum_{i=1}^n \lambda_i \hat{d}_N^{\text{sd}}, \quad (8.12)$$

where i is the identifier of a RUM that is at least 15 degrees away from the orientation of the null line, \hat{d}_N^{sd} is the normal displacement velocity from the strapdown decomposition, and λ are the kriging weights derived from the variogram model. In this way, we predict a new normal velocity for all RUMs, based solely

⁷See footnote 6.

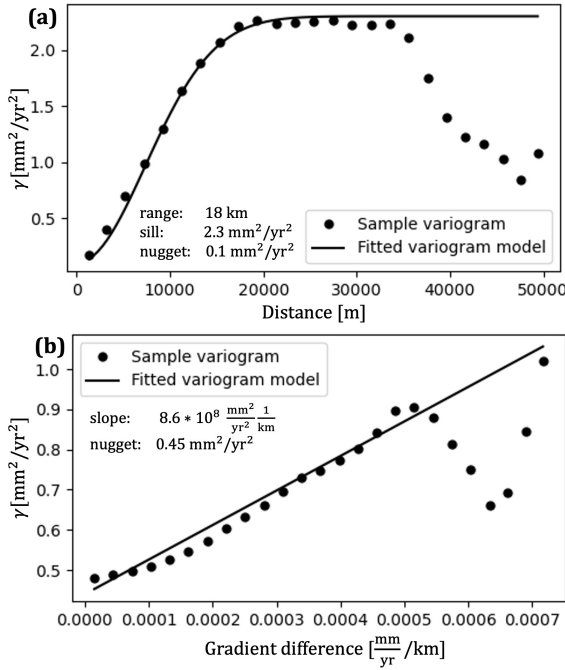


Figure 8.11: (a) shows the variogram of the **normal** deformation signal. The x-axis shows the range in meters. A Gaussian model was fitted to the variogram. Due to the bowl-shaped subsidence signal, the semivariance initially increases with distance. However, since the radius of the subsidence bowl is approximately 30 km, the semivariance decreases beyond 35 km. (b) shows the variogram of the **transversal** deformation signal, where we fitted a linear model. In this case, the range values represent differences in the gradient of the subsidence bowl rather than geometric distances. This reflects the expectation that RUMs on the same contour show a similar transversal deformation.

on the RUMs for which the strapdown estimates were reliable. This results in two normal displacement velocity estimates per RUM, \hat{d}_N^{sd} and \hat{d}_N^{pred} , each with an associated variance. The final estimate for the normal component is then obtained by combining these values through the following mathematical model

$$E\left\{\underbrace{\begin{bmatrix} \hat{d}_N^{\text{sd}} \\ \hat{d}_N^{\text{pred}} \end{bmatrix}}_y\right\} = \underbrace{\begin{bmatrix} 1 \\ 1 \end{bmatrix}}_A d_N^{\text{fin}}, \text{ and} \quad (8.13)$$

$$D\left\{\underbrace{\begin{bmatrix} \hat{d}_N^{\text{sd}} \\ \hat{d}_N^{\text{pred}} \end{bmatrix}}_y\right\} = \underbrace{\begin{bmatrix} \sigma^2_{\hat{d}_N^{\text{sd}}} & 0 \\ 0 & \sigma^2_{\hat{d}_N^{\text{pred}}} \end{bmatrix}}_{Q_y}, \quad (8.14)$$

where d_N^{fin} is the final normal displacement velocity. The results for \hat{d}_N^{pred} and d_N^{fin} and their corresponding variances are shown in Figs. 8.8b, c, g, and h, respectively.

Figs. 8.8d and e present the differences for \hat{d}_N^{pred} and d_N^{fin} with the estimated velocities from the (kinematic) strapdown decomposition, see Sec 8.3.2. It shows that \hat{d}_N^{pred} is spatially smooth, with uniform standard deviation (σ) values for all RUMs. The differences between the predicted and the strapdown velocities, show that significant differences occur primarily for the RUMs where the sigma value for the normal velocity was large.

Comparing the final estimates and their associated variances, see Figs. 8.8c and h, it is clear that for the RUMs that had an unfavorable TLN frame orientation, the final velocities strongly converges towards the velocities obtained from the kriging interpolation. Conversely, for RUMs that had a trustworthy normal velocity we see a minimal change, with final values relying more on the estimated values from the strapdown decomposition.

8

TRANSVERSAL COMPONENT

An analogous approach is followed for the transversal velocities. Similarly to normal velocities, the transversal component also exhibits spatial smoothness. However, its magnitude is more strongly correlated with the gradient of the subsidence bowl [111]. Therefore, rather than weighting RUMs by spatial distance in the kriging interpolation, weights are assigned based on *gradient differences*. To derive the corresponding kriging weights, we again computed a variogram, shown in Fig. 8.11b, where the x -axis of the variogram represents the gradient difference between RUMs. We fitted a linear model with a nugget value of $0.45 \text{ mm}^2/\text{yr}^2$ and a slope of $8.6 \cdot 10^8 \text{ mm}^2/\text{yr}^2/\text{km}$. The variogram model is used to determine the weights for the kriging interpolation, see Eq. (8.12), and subsequently to calculate the kriging velocities, as shown in Fig. 8.9b.

As with the normal component, we estimate the final values for the transversal component using both the strapdown and kriging velocities, i.e., \hat{d}_T^{sd} and \hat{d}_T^{pred} , respectively, using Eqs. (8.13) and 8.14, see Fig. 8.9c. For the 'poorly estimable RUMs', i.e., RUMs where the transversal direction is nearly aligned with the null line,

we observe significant differences between the strapdown velocities and the final result. In these cases, the final estimate aligns closely with the kriging interpolation.

Considering both the transversal and normal components, we see a clear benefit from incorporating the smoothness of the signal, particularly for the poorly estimable RUMs. The extreme estimates (which are physically highly unlikely) and the high sigma values have significantly decreased. The RUMs that already had precise estimates remain largely unchanged.

8.3.4. FROM 2D LOCAL TO 3D GLOBAL

With the estimated transversal and normal displacement velocities and the frame orientation defined by angles Λ , Φ , and Ω we can transform the estimates in the TLN frame to east, north, and up components with

$$d_{\text{ENU}} = R_1 R_2 R_3 d_{\text{TLN}}, \quad (8.15)$$

where R_1 , R_2 , and R_3 , are the rotation matrices with the angles of the TLN frame, see Brouwer and Hanssen [14, Eqs. 3–5] and d_{TLN} is defined as $[d_T^{\text{fin}}, 0, d_N^{\text{fin}}]^T$. Consequently, the variance-covariance matrix of d_{ENU} is

$$Q_{d_{\text{ENU}}} = R_1 R_2 R_3 Q_{d_{\text{TLN}}} R_3^T R_2^T R_1^T, \quad (8.16)$$

where

$$Q_{d_{\text{TLN}}} = \begin{bmatrix} \sigma_{d_T^{\text{fin}}}^2 & 0 & 0 \\ 0 & \sigma_{d_L^{\text{fin}}}^2 & 0 \\ 0 & 0 & \sigma_{d_N^{\text{fin}}}^2 \end{bmatrix} = \begin{bmatrix} \sigma_{d_T^{\text{fin}}}^2 & 0 & 0 \\ 0 & (d_T^{\text{fin}})^2 \sigma_{\Lambda}^2 & 0 \\ 0 & 0 & \sigma_{d_N^{\text{fin}}}^2 \end{bmatrix}. \quad (8.17)$$

For the value for $\sigma_{d_L^{\text{fin}}}^2$ we refer to Brouwer and Hanssen [14, Fig. 6]. Obviously, while $Q_{d_{\text{TLN}}}$ is considered a diagonal matrix, the datum transformation results in $Q_{d_{\text{ENU}}}$ being a full matrix, where the non-zero covariance terms describe the orientation and shape of the 3D confidence ellipsoid. As the frame orientation differs per RUM, the transformation must be applied per RUM.

8.3.5. COMPARISON WITH GNSS

To validate the results, the estimated InSAR displacements are compared with estimated GNSS displacements of more than 30 continuous GPS stations installed to continuously monitor ground displacements. For each GNSS station, the ENU GNSS velocity is compared to the InSAR ENU velocity that correspond to the RUM where the GNSS station is situated in. The differences between the two estimates are computed as

$$\Delta d_i^{I \rightarrow E} = \hat{d}_i^{GIE} - \hat{d}_i^I, \quad (8.18)$$

where \hat{d}_i^{GIE} denotes the displacement velocity of a GNSS station situated in RUM i , expressed in the ETRF89 reference frame, and \hat{d}_i^I represents the estimated InSAR velocity for the same RUM [116]. Note that the InSAR velocities are inherently estimated relative to an InSAR reference point, which is located outside the gas

production area. The InSAR-derived velocities can be expressed with respect to the ETRF89 reference frame as well, by applying a correction to the estimated InSAR velocities. If $\Delta d_i^{I \rightarrow E} \neq 0$, the estimated offset $\Delta d_i^{I \rightarrow E}$ can be added to the InSAR velocities to align them with ETRF89. This procedure needs to be performed independently for each displacement component. After computing the differences between the GNSS velocities and the InSAR velocities in these RUM grid cells we found $\Delta d_i^{I \rightarrow E}$ for each component. The obtained offsets are $\Delta d_{i, \text{east}}^{I \rightarrow E} = -0.16$ mm/yr, $\Delta d_{i, \text{north}}^{I \rightarrow E} = -0.05$ mm/yr, and $\Delta d_{i, \text{up}}^{I \rightarrow E} = 0.78$ mm/yr for the east, north, and up components respectively.

In Fig. 8.12 we show the differences between the estimated InSAR and GNSS velocities for the east, north, and up components after correction for the offsets. Additionally, we show the histograms of the residuals. This shows that the residuals are approximately normally distributed, with relatively small standard deviations, i.e., $\sigma_E = 0.35$ mm/yr, $\sigma_N = 0.46$ mm/yr, and $\sigma_U = 0.78$ mm/yr. As the values are small, this yields confidence in the reliability of the InSAR-derived velocities.

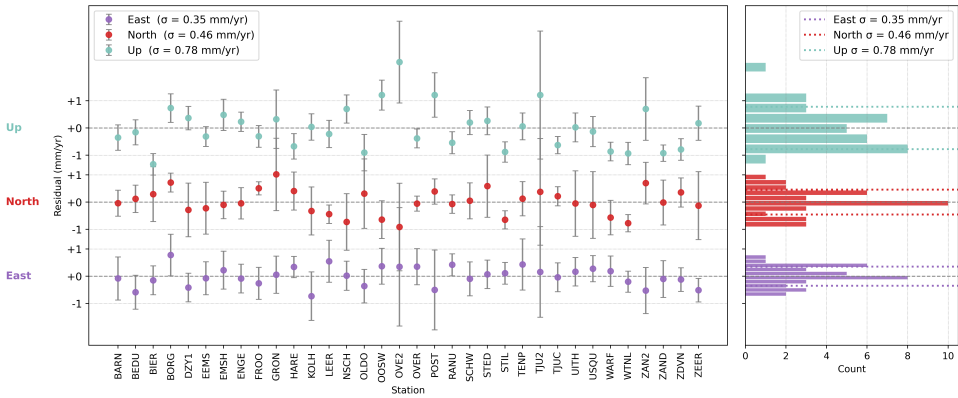


Figure 8.12.: Residuals between InSAR and GNSS velocity estimates for each GNSS station, after applying the correction to obtain both estimates in the ETRF89 reference frame. The residuals are shown for the east, north, and up component shown in purple, red, and green respectively. In the right panel, the corresponding histograms are shown, where the residuals are approximately normally distributed, with standard deviations of $\sigma_E = 0.35$ mm/yr, $\sigma_N = 0.46$ mm/yr, and $\sigma_U = 0.78$ mm/yr, for the east, north and up components respectively. As the values are small, this yields confidence in the reliability of the InSAR-derived velocities.

8.3.6. RESULTS

Combining the results of both the transversal and normal components into a single final product, see Fig. 8.13, provides a 3D representation of the displacement field over Groningen, expressed in the ETRF89 reference frame. The background colors and contour lines represent the estimated up velocities, with maximum values occurring near the center of the field, reaching up to 6.5 mm/yr at [53.30705°N,

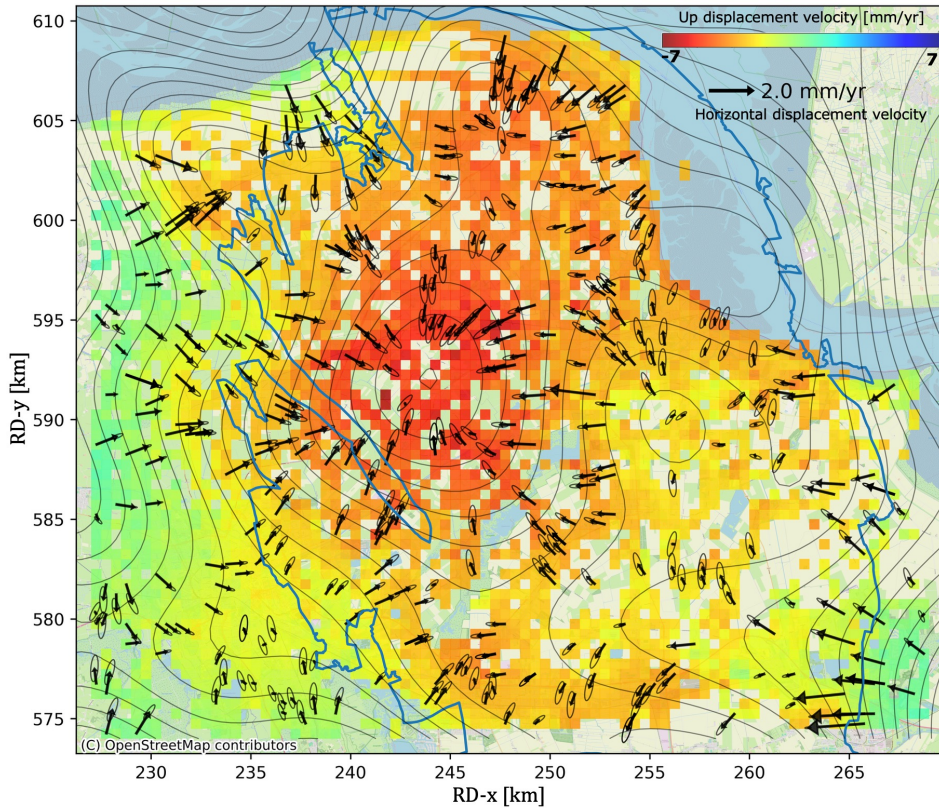


Figure 8.13.: Estimated 3D displacements velocities over Groningen using the two InSAR viewing geometries and the strapdown approach. The outline of the reservoir is shown by the blue line. The colors in the background and the contour lines correspond to the vertical direction. Where the maximum vertical (up) velocities occur in the center of the field and reach values up to 6.5 mm/yr. The black vectors represent the horizontal direction, and the ellipses the corresponding 2σ confidence regions. At the edges of the field, where contour lines are closer together, the estimated horizontal velocities are largest.

6.72238°E] (ETRF89), near the village of Ten Post. A local maximum of 6.1 mm/yr is found at coordinates [53.28713°N, 6.88673°E], ~6 km SSW of Delfzijl. Note that the precision of the up component $\sigma_{d_n}^2$ is computed for every grid cell, but not visualized in Fig. 8.13.

The black vectors show the estimated horizontal motion, and surrounding ellipses indicate corresponding 2σ confidence regions of the estimates. While directional horizontal motion is estimated for every colored 500×500 m grid cell in the image, only a random subset of 10% of the actual vectors is displayed to avoid clogging the image. At the edges of the field, where the contour lines are denser, the estimated horizontal velocities are larger, as would be expected from theory [111]. Unlike the initial output from the strapdown decomposition, the estimated directional and magnitude precision is now more uniform across the entire field, with realistic estimates varying over the sectorial position. We observe maximum horizontal displacements around the village of Bedum, ~9 km NNE of Groningen city.

Expressing the estimated displacements with their east, north, and up components, the quality of these estimates is described with a full 3×3 variance-covariance matrix. The dataset corresponding to this result has been made publicly available, see [18]. For the centroid of each RUM, the estimated displacement velocities in the east, north, and up directions are provided, along with their associated uncertainties, in terms of variances and covariances. This results in a total of nine parameters per RUM: three velocities: d_e, d_n, d_u , three variances: $\sigma_{d_e}^2, \sigma_{d_n}^2, \sigma_{d_u}^2$, and three covariances: $\sigma_{d_e, d_n}, \sigma_{d_e, d_u}, \sigma_{d_n, d_u}$. With these results it is possible to run inverse models or predict future positions.

8.4. CONCLUSIONS

This study provides the first estimation of the full three-dimensional displacement field in Groningen resulting from gas extraction, derived from InSAR observations using the strapdown method, and accompanied by a detailed quality assessment. The approach is data-driven, but incorporates falsifiable prior knowledge on the expected smoothness of the deformation signal caused by the gas extraction at multiple stages of the analysis. The assumed smoothness of the deep deformation component allows us to classify scatterers into two distinct classes. The *deep-only* classified scatterers are isolated and used in the strapdown decomposition. We have shown that the local frame orientation can be estimated directly from satellite LoS data, to a sufficient degree of precision. The strapdown approach propagates the associated orientation uncertainties, to take them into account in the estimation and quality assessment of the final displacement parameters.

Using the RUMs where the precision for the estimated transversal and normal velocities is good, it is possible to provide smoothness constraints that can, in turn, be used to improve displacement estimates for RUMs where the initial strapdown estimates were poor.

As a result, we obtain reliable estimates for the displacements across the entire province of Groningen during the period 2015–2023, with a maximum subsidence velocity of 6.5 mm/yr, and directional horizontal displacements induced by gas

extraction, which are significant, up to 1.8 mm/yr. For 50% of the analyzed area, the estimated horizontal displacements are greater than twice the standard deviation of the estimator. In other words, for half of the area we can derive a statistically significant estimate of the horizontal component.

9

CONCLUSIONS AND RECOMMENDATIONS

THIS study aimed to define an optimal, application-specific mathematical model for InSAR parameter estimation by addressing the following main research question:

Can the PS-InSAR parameter estimation problem be reformulated and improved to provide more precise, reliable, and physically meaningful parameter estimates, aiming for better interpretable and actionable information?

Yes. We have demonstrated that incorporating contextual knowledge about the problem and intended use of the data is the only way to produce an InSAR product that is optimally suited to its application. This application-aware and -aligned (triple-A or AAA) approach yields more precise and physically meaningful parameter estimates. We have also developed a method to quantify and present uncertainties with the estimates, resulting in more reliable and actionable InSAR results.

InSAR results are highly sensitive to various choices made throughout the parameter estimation process—ranging from the selection of models and data to the assumptions and parameter settings. A model or processing strategy that performs well in one context may yield suboptimal or even misleading results in another. As a result, a single, generic InSAR information product does not exist, despite the abundance of generic, nationwide or region-wide displacement products that might suggest otherwise. The quality and suitability of such products cannot be assessed without knowledge of the intended application or the context in which they are used. In fact, the mere concept of optimality can only be defined in the context of a particular application. Thus, to obtain optimal results, parameter estimation (i.e., ‘processing’) must be tailored to the specific application. Such tailoring should be informed by knowledge on the application, the desired output, and the required precision, and is essential at multiple stages in the InSAR parameter estimation process.

This begins with estimating relative parameters, such as the displacement time series of individual points with respect to a common reference point, derived from the double-differenced (DD) phases along arcs. This process requires a tailored functional and stochastic model for each arc, as well as a tailored Confidence-Optimized Robust Geodetic (CORG) network configuration. The selection of the functional model and the design of the CORG network should be guided by knowledge of the application and relevant quality criteria, as different choices yield different parameter estimates. Application-awareness and contextual information should also be used to obtain physically interpretable three-dimensional (3D) deformation estimates from the InSAR line-of-sight (LoS) results. Incorporating knowledge of the underlying deformation mechanism enables the estimation of full 3D deformation fields, including quality control.

Thus, to achieve reliable and physically meaningful InSAR results, we must first understand what signal we are interested in, why we are analyzing it, and how precise the estimated parameters need to be. Only with such application-specific knowledge, i.e., in a triple-A situation, can we make informed decisions about the model selection, assumptions, and processing strategy, resulting in more precise, more reliable, and physically more meaningful results.

THE STOCHASTIC MODEL

To make informed decisions about which scatterers and arcs to include in the InSAR parameter estimation process, and to enhance the interpretability and reliability of the resulting estimates, it is crucial to have an a priori stochastic model that describes the quality of the observed phases independently of the (displacement) estimates. Until now, no such model existed. We introduced a novel approach that derives an epoch-specific quality estimate (proxy) for individual scatterers based on their amplitude time series (Chapter 2) and defined an empirical relation between the Normalized Median Absolute Deviation (NMAD) of the amplitude and the standard deviation (σ) of the observed phases. The NMAD of the amplitude is more robust to outliers than the more common Normalized Amplitude Dispersion (NAD).

The impact of this scatterer- and epoch-specific stochastic model is threefold. First, by applying proper error propagation, both in the arc parameter estimation (Sec. 3.5) and subsequently in the network adjustment (Sec. 5.2.1), we can now **assign a time-varying quality metric (standard deviation)** to the estimated relative displacement time series. This was previously only possible in hindsight, using residuals from fitted models, which created an undesirable entanglement with the (validity of the) functional model. Second, the stochastic model **facilitates statistical testing** of both the arc-based estimates and the final network-adjusted parameters. Third, it provides a quality metric for each scatterer and each arc (both in time and in space) allowing for **more informed decisions about which scatterers and arcs to include** in the analysis (Sec. 5.3). This last aspect, in particular, has a significant impact on the precision of the estimated InSAR parameters.

THE APPLICATION-AWARE AND -ALIGNED NETWORK

The use of a reliable stochastic model at arc level forms the foundation for an application-aligned network, see Sec. 5.2.2. While many network topologies exist, the chosen network directly affects the estimated relative parameter values and their associated quality for points relative to a common reference. Since each InSAR application comes with its own objectives and quality requirements, each application demands an application-aware and -aligned (i.e., triple-A) network.

Since the stochastic model of Chapter 2 provides a priori information on arc quality it facilitates the identification of arcs most likely to yield reliable and precise estimates, allowing to prioritize high-quality arcs (Sec. 5.3). Unlike conventional networks that are based on a topology related to the spatial location (i.e., maximizing the minimum angle of triangles of vertices) we define a Confidence-Optimized Robust Geodetic (CORG) network, that explicitly maximizes estimation quality. This approach supports iterative evaluation and refinement of the CORG network based on application-specific quality criteria.

Once the CORG network is designed, it should be adjusted to transform arc parameters into datum-connected parameters for points. Rather than adjusting the CORG network on explicitly unwrapped phases, it should be adjusted in the parameter space, (i.e., the estimated arc parameters) where the absolute ('unwrapped') phase is also an estimated parameter as it follows implicitly during the estimation of the unknown parameters and consequently, cannot be assumed

deterministic (Chapter 4). In a triple-A context, each arc may have its own stochastic and functional model, chosen according to the application and the available contextual information, and therefore resulting in a varying parameter space across arcs. Therefore, the CORG network should be adjusted on the shared parameters and the reduced phase (see Sec. 3.5). Although we did not focus specifically on optimizing the functional model, we developed a method that allows each arc to be assigned its own functional model and defined which relative arc parameters should be estimated. Where we propose to use the relative cross-range distance as a better alternative to the commonly used relative height, see Sec. 3.3.

The impact of this triple-A network approach is that: (i) it results in a **higher precision of datum-connected point parameters** by incorporating the physical, kinematic, and stochastic characteristics of arcs into the CORG network design, thereby optimizing it for the intended application; (ii) it has an **improved reliability** through a mathematical formulation that enables statistical testing; and (iii) it provides **stochastic estimates**, where each point time series is accompanied by a time-varying standard deviation, enabling the results to be interpreted as stochastic signals and making them more actionable for application-specific analyses.

INSAR GEOMETRY

The estimated displacement time series are orthogonal projections of the actual 3D displacement vector onto the line-of-sight (LoS) direction of the satellite, which are usually not directly physically interpretable. Therefore, decomposing them into (some of) the 3D displacement components is often required. This decomposition relies on the availability of **spatio-temporally coinciding independent** (STCI) observations. Yet, in practice, this condition is rarely fulfilled. Therefore, we introduce **Regions of Uniform Motion** (RUMs): areas in which all observation points move uniformly. Additionally, at least three independent viewing geometries with sufficient angular diversity are required, see Sec. 6.3.

In reality, however, the orbital geometry of SAR satellites limits the number of effective viewing geometries to two at most. These two viewing geometries result in a **null line**, where its direction determines the direction where no displacements can be observed (Sec. 6.4). To improve the interpretability of results, the orientation of the null line should be stated with the InSAR product. We defined a novel null-line aligned (NLA) reference frame, that produces unbiased estimates of the displacements in a plane orthogonal to the null-line. The NLA-frame has optimal characteristics for geophysical and geotechnical modeling.

An evaluation of current practices reveals three recurring type of errors: **attribution, projection, and decomposition errors**, see Sec. 6.5. These errors underline the need for improved standards in the generation and interpretation of InSAR products. It is recommended to use descriptive subscripts, d_{LoS} , d_{PoV} , d_{PoV^\perp} , or d_{PoEU} to unambiguously define projected InSAR products, both textual as well as in maps and graphs. For vector decompositions, we advise against using the commonly applied east-up plane decomposition due to its ingrained bias. Instead, we recommend using either the coordinate system aligned with the null line or the strapdown approach, as these are the only two decomposition methods that result in unbiased estimates.

THE STRAPDOWN METHOD

The strapdown method, as described in Chapter 7, enables the estimation of 3D displacement vectors from two satellite viewing geometries for deformation phenomena where the underlying mechanism is (at least partially) known. The method uses **a local reference frame** with transversal, longitudinal, and normal (TLN) axes, defined such that displacements occur exclusively in the transversal and normal directions. Since this frame orientation is based on physical deformation phenomena and incorporates minimal yet largely undisputed contextual information, the strapdown method yields more relevant physical estimates.

By explicitly quantifying the uncertainty in the orientation of the local frame and propagating these errors, the method provides reliable estimates of transversal and normal displacements, which can subsequently be transformed into east, north, and up components. Hence, it is **“2D local/3D global”**.

This approach is practical, effective, unbiased, and largely generic. Successful application of the strapdown method requires that all data (i.e., scatterers) within a RUM represent the **same deformation phenomenon**. However, InSAR results often capture a combination of multiple deformation signals. Through a case study on gas extraction in Groningen, the Netherlands, we demonstrate that realistic prior assumptions on the smoothness of the deformation signal can help to effectively disentangle multiple deformation mechanisms (Sec. 8.2).

The strapdown method relies on knowledge of the orientation of the TLN frame, which may not always be directly available. We show that this orientation can be approximated directly from the LoS observations (Sec. 8.3). Consequently, areas where the transversal or normal direction aligns with the null line result in displacement estimates with a low confidence. For wide-area deformation signals exhibiting some degree of spatial smoothness, it is possible to infer this smoothness from regions with high-confidence estimates. These inferred smoothness constraints can then be used to update and improve estimates for RUMs with a lower estimation confidence. This framework allows optimal integration of contextual information about the deformation phenomenon to achieve **consistent estimation quality** across the entire area. Applying this method to the Groningen gas extraction case study, we provide **InSAR-based 3D displacement estimates** accompanied by confidence ellipses, with **vector-based visualizations** facilitating a more profound interpretation of the results.

9.1. CONTRIBUTIONS

This research has provided the following contributions.

- Development of a methodology and metric for an independent a priori stochastic model for each individual point (and arc), describing the time variable quality of the phase observations.
- Development of the Confidence-Optimized Robust Geodetic Network design methodology, enabling more precise and reliable (displacement) parameter estimates. By incorporating proper error propagation throughout the

estimation process, the resulting displacement time series are accompanied by point-specific and epoch-specific quality metrics.

- Definition of the null line, as an important metric for InSAR interpretation, and the NLA (null-line-aligned) coordinate system.
- Introduction of error terminology related to 3D displacement estimation from InSAR LoS observations: attribution error, projection error, and decomposition error.
- Development of the strapdown method to estimate "2D-local/3D-global" deformations from InSAR LoS observations.
- InSAR based 3D displacement estimates of Groningen, the Netherlands, induced by the Gas extraction.

9.2. RECOMMENDATIONS

Based on the outcomes of this study, several recommendations for future research are outlined below.

Account for atmospheric phase delays in wide-area processing The mathematical model for arc parameter estimation (discussed in Chapters 2 and 3) and network adjustment (Chapter 5) are specifically formulated for short-arcs, where atmospheric phase delays can be safely assumed negligible. While atmospheric noise is included in the stochastic model (Sec. 2.4.1), systematic atmospheric phase delays are not explicitly estimated. As suggested in Sec. 5.5, merging multiple local networks (each small enough to disregard atmospheric phase delays) offers a methodology to process wider areas. However, to link a large number of such networks reliably, explicit estimation of atmospheric phase delays becomes essential and should be integrated into the methodology.

Implementing a dynamic functional model per arc In a generic sense, we argue that each arc requires a tailored functional model to reflect the unique kinematic behavior of each scatterer. Chapter 3 introduces a method that defines a geometric arc-specific functional model without using contextual information on the expected kinematic or physical behavior. However, this can be improved by adopting dynamic kinematic models based on smoothness constraints, such as the recursive least-squares approach proposed by Wang *et al.* [202]. Unlike static parameterizations, this method captures the independent temporal behavior of each scatterer without enforcing a predefined model. Combined with the stochastic model from Chapter 2, this approach is expected to result in an optimal application-driven mathematical model for the arc parameter estimation.

Enable recursive monitoring with the quality-driven application-specific network By adopting recursive estimation for arc parameters, the proposed CORG network (Chapter 5) can be extended into a real-time monitoring network, as the network adjustment as proposed in Chapter 5 is based on the estimated *parameters*. Each new satellite acquisition yields new phase observations for the points from which the instantaneous LoS position, instantaneous LoS velocity, thermal expansion factor,

and cross-range distance per arc can be estimated using the method of Wang *et al.* [202]. These parameter estimates can then be recursively integrated into the network, yielding updated displacement estimates for the network points after every new satellite acquisition. This would facilitate an efficient method to monitor the behavior of selected points.

Simultaneous estimation of arc parameters and network adjustment As the network needs to be adjusted on the parameter space, this requires that the parameters for each arc first need to be estimated from the double-differenced phase observations. Although the covariance between arcs is known for the DD phase observations, it remains challenging to determine the covariance of the estimated parameters, when different functional and stochastic models are used across arcs. A possible solution is therefore to perform the arc parameter estimation simultaneously with the network adjustment.

Estimating time-varying 3D displacements over the Groningen gas field In Chapter 8, we estimated the first InSAR-based 3D displacement velocities induced by the gas extraction in Groningen. However, as of October 1, 2024, gas production has been definitively halted, and surface deformations are expected to decrease [50, 136]. Consequently, it would be valuable to apply the strapdown decomposition to displacement time series rather than velocities. When working with velocities, we already selected scatterers expected to reflect only the deep deformation signal, based on their velocity behavior (see Sec. 8.3). However, some scatterers may exhibit additional seasonal signals that do not average out in displacement time series as they do in velocities. Therefore, alternative selection criteria are required to identify scatterers that reliably represent the deep deformation signal.

A

STATISTICS OF THE SLC, SD, AND DD PHASORS

IN Sec. 2.3 three possible methods for calculating the temporal phase differences were discussed, leading to the conclusion that the '*embracing mother*' approach is appropriate. Here, we confirm this through simulations in the complex domain. Additionally, we present how the variance-covariance matrices (VCM) of the SLC phasor, the time-differenced (SD) phasors, and the double-differences (DD) phasors are computed.

A.1. THE SINGLE TEMPORAL PHASE DIFFERENCES IN THE COMPLEX DOMAIN

We analyze the stochastic behavior of the single-difference phasors by simulating 350 complex SLC phasors, represented by the gray dots in Fig. A.1c. Phasor \underline{P}_i is defined as

$$\underline{P}_i = A_i \exp i\underline{\psi}_i, \quad (\text{A.1})$$

with amplitude A_i and SLC phase $\underline{\psi}_i$. The noise follows a circular Gaussian distribution [7] represented as the noise of the real and imaginary components, that are defined as σ_{Re_i} and σ_{Im_i} respectively. We simulate SLC phasors with an amplitude of 2, and Signal-to-Clutter Ratio (SCR) of 20 dB. From this, we compute the real and imaginary components, along with their standard deviations, which are presented in the histograms in Figs. A.1 (a) and (b), yielding $\sigma_{\text{Re}_i} = 0.19$ and $\sigma_{\text{Im}_i} = 0.20$. The amplitude A_i is computed with

$$\underline{A}_i = \sqrt{(\text{Re}\{\underline{P}_i\})^2 + (\text{Im}\{\underline{P}_i\})^2}, \quad (\text{A.2})$$

and is shown in Fig. A.1 (e). Note that the dispersion of the amplitude, σ_A , equals the clutter, i.e., $\sigma_{A_i} = \sigma_{\text{Re}_i} = \sigma_{\text{Im}_i}$, which is confirmed by Fig. A.1(g). Additionally, we compute the corresponding SLC phase values using

$$\underline{\psi}_i = \arctan\left(\frac{\text{Im}\{\underline{P}_i\}}{\text{Re}\{\underline{P}_i\}}\right), \quad (\text{A.3})$$

visualized by the gray dots in (d) and their distribution is depicted in (f). The estimated standard deviation for the SLC phase is $\sigma_{\psi_i} = 0.09$ rad.

After defining epoch 50 as the mother acquisition, we compute the temporally differenced (SD) phasors \underline{P}_i^{md} , through complex multiplication, indicated by the gray crosses in (c). The corresponding phase time series and histogram are shown in black in (d) and (f). We compute the phasor statistics, obtaining $\sigma_{\text{Re}_i^{md}} = 0.41$ and $\sigma_{\text{Im}_i^{md}} = 0.37$. Notably, these values are higher than the SLC clutter values, suggesting noisier temporal phase differences. However, since the amplitude of the SD phasor also increased, as shown in (g), the SCR of the SD phasor, \underline{P}_i^{md} , remained equal to that of the SLC phasor, \underline{P}_i . This is further supported by the phase dispersion derived from the SD phasor, where $\sigma_{\phi_i} = 0.09$ rad, a value identical to σ_{ψ_i} , as demonstrated by the two histograms in (f).

These simulations confirm that the ‘embracing-mother’ approach (see Sec. 2.3.1) is the only valid method for computing the temporal phase differences. Of the three methods discussed in Sec. 2.3.1, it is the only one that yields $Q_{\phi_i} = Q_{\psi_i}$. The other two methods lead to an increase in σ_{ϕ_i} relative to σ_{ψ_i} .

Using complex notation, the single phase differences in the ‘embracing-mother’ approach are computed with

$$\underline{P}_i^{md} = \underline{P}_i^d \cdot P_i^{m*} = \underline{A}_i^d A_i^m \exp(i(\underline{\psi}_i^d - \psi_i^m)), \quad (\text{A.4})$$

where \underline{P}_i^d is a vector of phasors (hence the stochastic nature) and P_i^{m*} is the complex conjugate of the realization of the phasor value at mother epoch m . Consequently, the noise of the SD phasor is derived with

$$\sigma_{P_i^{md}} = |A_i^m| \cdot \sigma_{P_i}, \quad (\text{A.5})$$

where $\sigma_{P_i^{md}}$ represents the clutter, i.e., $\sigma_{P_i^{md}} = \sigma_{\text{Re}_i^{md}} = \sigma_{\text{Im}_i^{md}}$. Hence, the clutter scales with the amplitude of the phasor of the mother epoch. However, since the signal of the SD phasor is amplified with the same factor, both the SCR and the phase dispersion of the single differences remain equal to those of the SLC phases.

A.2. THE SPATIO-TEMPORAL DOUBLE DIFFERENCES IN THE COMPLEX DOMAIN

When the temporally differenced phasors are computed for two points i and j , the double differenced phasors are computed with

$$\underline{P}_{ij} = \underline{P}_j \cdot \underline{P}_i^* \quad (\text{A.6})$$

$$= \underline{A}_j \underline{A}_i \exp(i(\underline{\phi}_j - \underline{\phi}_i)), \quad (\text{A.7})$$

which is the multiplication of two stochastic quantities. For conciseness, we have omitted the superscript that denotes the temporal phase differences. From error propagation laws, when we have a quantity D that is defined as $D = B \cdot C$, then the

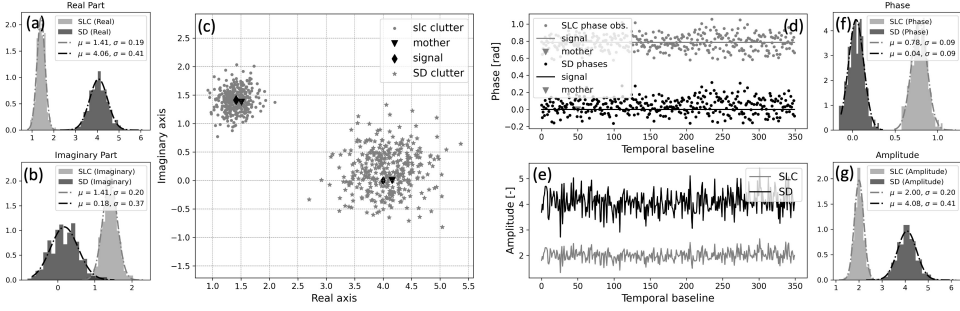


Figure A.1: c) We simulate 350 SLC phasors with an amplitude of 2 and a SCR of 20 dB, represented by the gray dots. After defining an arbitrary mother acquisition, shown by the triangle, we computed the SD phasors using Eq. (A.4), shown by crosses in (c). (a), (b), (f), and (g) show the histograms of the clutter, phase, and amplitude respectively. The gray distributions correspond to the SLC phasors where the black distributions correspond to the SD phasors. It can be seen that, while the clutter of the SD phasors became larger (see a and b), the dispersion of the SD phases is the same as the dispersion of the SLC phase (see f). This is declared by the fact that amplitude of the SD phasors also became larger, and therefore the SCR remained equal.

standard deviation of D is computed with

$$\sigma_D = |D| \sqrt{\left(\frac{\sigma_B}{B}\right)^2 + \left(\frac{\sigma_C}{C}\right)^2 + 2\frac{\sigma_{BC}}{BC}}. \quad (\text{A.8})$$

Using this relation, the dispersion of the DD phasors is computed with

$$\sigma_{P_{ij}} = |\mu_{A_i} \mu_{A_j}| \sqrt{\left(\frac{\sigma_{P_i}}{\mu_{A_i}}\right)^2 + \left(\frac{\sigma_{P_j}}{\mu_{A_j}}\right)^2}, \quad (\text{A.9})$$

where $\sigma_{P_{ij}}$ represents the clutter of the DD phasors and $\sigma_{P_{ij}} = \sigma_{\text{Re}_{ij}} = \sigma_{\text{Im}_{ij}} = \sigma_{A_{ij}}$.

In Fig. A.2, we illustrate the stochastic behavior of the DD phasor for point j relative to point i . The lightest (silver) dots in (c) represent the SD values for point i , the gray dots correspond to the SD values for point j , and the black dots represent the DD values. It is evident that the phase dispersion of the DD phases depends on the phase dispersion of both points i and j . In Fig. A.2f it can be seen that $\sigma_{\phi_i} = 0.09$ rad and $\sigma_{\phi_j} = 0.18$ rad. When we consequently compute the expected phase dispersion using Eq. (2.15), we expect $\sigma_{\phi_{ij}^{m,d}} = \sqrt{0.09^2 + 0.18^2} = 0.2$ rad, which is indeed in accordance to the values that we find in the simulation, which is 0.21 rad, see the histogram in Fig. A.2f.

In Eq. (A.9) we demonstrated how the VCM for the DD phasors in the complex domain can be derived, requiring the mean and standard deviation of the amplitude of the SD phasors for points i and j . However, in Sec. 2.4.3 we argued that for assessing phase quality, the Normalized Median Absolute Deviation (NMAD) is preferred over the Normalized Amplitude Dispersion (NAD), as the latter provides an

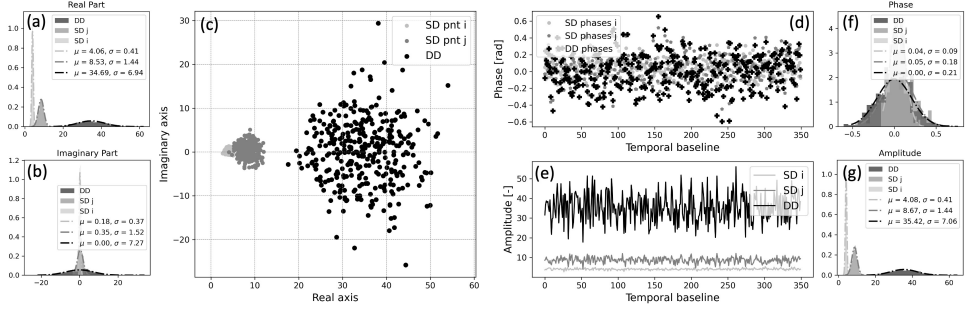


Figure A.2.: (c) shows the SD phasors of point i and point j in silver and gray respectively. Using Eq. (A.9) the DD phasors of point j relative to i are computed shown by the black dots. In (d) the corresponding phase values are shown, with the histograms in (f). It can be seen that stochastic behavior of the DD phase values is a function of both point i and point j since both are stochastic quantities.

overly conservative estimate in the presence of outliers. Therefore, we propose using the median amplitude and the median absolute deviation of the amplitude, rather than the mean and standard deviation in Eq. (A.9). This results in,

$$\sigma_{P_{ij}} = |\tilde{A}_i \tilde{A}_j| \sqrt{\left(\frac{k \text{MAD}(A_i)}{\tilde{A}_i}\right)^2 + \left(\frac{k \text{MAD}(A_j)}{\tilde{A}_j}\right)^2}, \quad (\text{A.10})$$

where \tilde{A} and $\text{MAD}(A)$ are the median and median absolute deviation of the amplitude values of all the single temporal phasors with a particular partition respectively.

A.3. NMAD AND SCR RELATION

We can also show that the SCR and the phase dispersion are related quantities. The NAD and SCR are related with

$$\text{SCR [dB]} = 20 \log_{10} \frac{\text{signal}}{\text{clutter}} = 20 \log_{10} \frac{\mu_A}{\sigma_A} = 20 \log_{10} \frac{1}{\text{NAD}}. \quad (\text{A.11})$$

Since the MAD and σ_A are related according to Eq. (2.17), and for normally distributed data $\mu_A = \tilde{A}$, Eq. (A.11) can be rewritten as

$$\text{SCR [dB]} = 20 \log_{10} \frac{1}{k \text{NMAD}}. \quad (\text{A.12})$$

Combining Eqs. (A.12) and (2.21), we can derive an equation that relates the phase dispersion to the SCR for a PS:

$$\sigma_{\psi, \text{TVc}} = 1.3 k^{-1} 10^{-\frac{\text{SCR}}{20}} + 1.9 \left(k^{-1} 10^{-\frac{\text{SCR}}{20}} \right)^2 + 11.6 \left(k^{-1} 10^{-\frac{\text{SCR}}{20}} \right)^3. \quad (\text{A.13})$$

BIBLIOGRAPHY

- [1] Adam, N., F. Rodriguez Gonzalez, A. Parizzi, and W. Liebhart. “Wide area persistent scatterer interferometry”. In: *2011 IEEE International Geoscience and Remote Sensing Symposium*. 2011, pp. 1481–1484. DOI: [10.1109/IGARSS.2011.6049347](https://doi.org/10.1109/IGARSS.2011.6049347) (cit. on p. 2).
- [2] Alatza, S., I. Papoutsis, D. Paradissis, C. Kontoes, and G. A. Papadopoulos. “Multi-temporal InSAR analysis for monitoring ground deformation in Amorgos island, Greece”. In: *Sensors* 20.2 (2020), p. 338 (cit. on p. 115).
- [3] Alatza, S., I. Papoutsis, D. Paradissis, C. Kontoes, G. A. Papadopoulos, and C. Raptakis. “InSAR time-series analysis for monitoring ground displacement trends in the western Hellenic Arc: The Kythira Island, Greece”. In: *Geosciences* 10.8 (2020), p. 293 (cit. on pp. 113, 116).
- [4] Amelung, F., S. Jónsson, H. Zebker, and P. Segall. “Widespread uplift and ‘trapdoor’ faulting on Galapagos volcanoes observed with radar interferometry”. In: *Nature* 407.6807 (2000), pp. 993–996 (cit. on p. 2).
- [5] Ansari, H., F. De Zan, and A. Parizzi. “Study of systematic bias in measuring surface deformation with SAR Interferometry”. In: *IEEE Transactions on Geoscience and Remote Sensing* 59.2 (2021), pp. 1285–1301. DOI: [10.1109/TGRS.2020.3003421](https://doi.org/10.1109/TGRS.2020.3003421) (cit. on p. 55).
- [6] Baarda, W. *A testing procedure for use in geodetic networks, volume 5 of Publications on Geodesy*. 2nd ed. Delft: Netherlands Geodetic Commission, 1968 (cit. on pp. 7, 66).
- [7] Bamler, R. and P. Hartl. “Synthetic aperture radar interferometry”. In: *Inverse Problems* 14 (1998), pp. 1–54 (cit. on p. 177).
- [8] Barra, A., L. Solari, M. Béjar-Pizarro, O. Monserrat, S. Bianchini, G. Herrera, M. Crosetto, R. Sarro, E. González-Alonso, R. M. Mateos, *et al.* “A methodology to detect and update active deformation areas based on Sentinel-1 SAR images”. In: *Remote Sensing* 9.10 (2017), p. 1002 (cit. on p. 3).
- [9] Bechor, N. B. and H. A. Zebker. “Measuring two-dimensional movements using a single InSAR pair”. In: *Geophysical Research Letters* 33.16 (2006) (cit. on p. 122).
- [10] Berardino, P., G. Fornaro, R. Lanari, and E. Sansosti. “A new algorithm for surface deformation monitoring based on small baseline differential SAR Interferograms”. In: *IEEE Transactions on Geoscience and Remote Sensing* 40.11 (2002), pp. 2375–2383 (cit. on p. 5).

- [11] Bodemdalingskaart. *The Dutch ground motion service*. 2020. URL: <https://bodemdalingskaart.nl/en-us/> (visited on 07/18/2025) (cit. on p. 2).
- [12] Boni, R., F. Cigna, S. Bricker, C. Meisina, and H. McCormack. “Characterisation of hydraulic head changes and aquifer properties in the London Basin using Persistent Scatterer Interferometry ground motion data”. In: *Journal of Hydrology* 540 (2016), pp. 835–849 (cit. on p. 115).
- [13] Brinkman, J. *Invloed van bodemdaling door zoutwinning Nedmag op bebouwing*. Deltares report, 2016 (cit. on p. 134).
- [14] Brouwer, W. S. and R. F. Hanssen. “Estimating three-dimensional displacements with InSAR: the strapdown approach”. In: *Journal of Geodesy* 98.110 (2024), pp. 1–15. DOI: [10.1007/s00190-024-01918-2](https://doi.org/10.1007/s00190-024-01918-2) (cit. on pp. 117, 121, 144, 153, 154, 156, 163).
- [15] Brouwer, W. S. and R. F. Hanssen. “An analysis of InSAR displacement vector decomposition fallacies and the strap-down solution”. In: *2021 IEEE International Geoscience and Remote Sensing Symposium IGARSS*. 2021, pp. 2927–2930. DOI: [10.1109/IGARSS47720.2021.9554216](https://doi.org/10.1109/IGARSS47720.2021.9554216) (cit. on p. 8).
- [16] Brouwer, W. S. and R. F. Hanssen. *No-DRaMA software*. 2022. URL: <https://gitlab.tudelft.nl/drama/drama> (visited on 07/14/2022) (cit. on pp. 112, 120).
- [17] Brouwer, W. S. and R. F. Hanssen. “A treatise on InSAR geometry and 3-D displacement estimation”. In: *IEEE Transactions on Geoscience and Remote Sensing* 61 (2023), pp. 1–11. DOI: [10.1109/TGRS.2023.3322595](https://doi.org/10.1109/TGRS.2023.3322595) (cit. on pp. 101, 122, 128, 129, 131, 136–138, 140, 144, 147, 159).
- [18] Brouwer, W. S. and R. F. Hanssen. *3D displacement estimates due to deep-seated hydrocarbon production in Groningen from satellite radar interferometry, 2015-2023 [Data set]*. 2025. DOI: [10.4121/34394aab-6139-4397-9235-f9f041ac9299](https://doi.org/10.4121/34394aab-6139-4397-9235-f9f041ac9299) (cit. on p. 166).
- [19] Brouwer, W. S. and R. F. Hanssen. “3D surface displacement estimation over the Groningen gas field, the Netherlands”. In: *EarthArXiv* (2025). DOI: [10.31223/X5775W](https://doi.org/10.31223/X5775W) (cit. on p. 143).
- [20] Brouwer, W. S. and R. F. Hanssen. “On the definition of an independent stochastic model for InSAR time series”. In: *IEEE Transactions on Geoscience and Remote Sensing* 63 (2025), pp. 1–11. DOI: [10.1109/TGRS.2025.3600893](https://doi.org/10.1109/TGRS.2025.3600893) (cit. on pp. 11, 41, 67).
- [21] Brouwer, W. S., Y. Wang, F. J. van Leijen, and R. F. Hanssen. “On the stochastic model for InSAR single arc point scatterer time series”. In: *IGARSS 2023 - 2023 IEEE International Geoscience and Remote Sensing Symposium*. 2023, pp. 7902–7905. DOI: [10.1109/IGARSS52108.2023.10282629](https://doi.org/10.1109/IGARSS52108.2023.10282629) (cit. on p. 14).
- [22] Bürgmann, R., P. A. Rosen, and E. J. Fielding. “Synthetic aperture radar interferometry to measure Earth’s surface topography and its deformation”. In: *Annual review of earth and planetary sciences* 28.1 (2000), pp. 169–209 (cit. on p. 2).

- [23] Caro Cuenca, M., A. J. Hooper, and R. F. Hanssen. "Surface deformation induced by water influx in the abandoned coal mines in Limburg, The Netherlands observed by satellite radar interferometry". In: *Journal of Applied Geophysics* 88 (2013), pp. 1–11 (cit. on pp. 127, 137).
- [24] Cascini, L., G. Fornaro, and D. Peduto. "Advanced low-and full-resolution DInSAR map generation for slow-moving landslide analysis at different scales". In: *Engineering Geology* 112.1-4 (2010), pp. 29–42 (cit. on pp. 117, 123).
- [25] Caspary, W. and J. Rüeger. *Concepts of network and deformation analysis*. Vol. 11. University of New South Wales Kensington, Australia, 1987 (cit. on pp. 66, 72).
- [26] Cavalié, O. and S. Jónsson. "Block-like plate movements in eastern Anatolia observed by InSAR". In: *Geophysical Research Letters* 41.1 (2014), pp. 26–31 (cit. on p. 125).
- [27] Chang, L., R. P. B. J. Dollevoet, and R. F. Hanssen. "Railway infrastructure monitoring using satellite radar data". In: *International Journal of Railway Technology* 3 (2014), pp. 79–91 (cit. on pp. 126, 127).
- [28] Chang, L. and R. F. Hanssen. "A probabilistic approach for InSAR time-series postprocessing". In: *IEEE Transactions on Geoscience and Remote Sensing* 54.1 (2016), pp. 421–430. DOI: [10.1109/TGRS.2015.2459037](https://doi.org/10.1109/TGRS.2015.2459037) (cit. on pp. 4, 12, 34, 39, 40, 45).
- [29] Chang, L. "Monitoring civil infrastructure using satellite radar interferometry". PhD thesis. Delft: Delft University of Technology, July 1, 2015 (cit. on p. 39).
- [30] Chang, L., R. P. Dollevoet, and R. F. Hanssen. "Monitoring line-infrastructure with multisensor SAR interferometry: products and performance assessment metrics". In: *IEEE Journal of Selected Topics in Applied Earth Observations and Remote Sensing* 11.5 (2018), pp. 1593–1605 (cit. on pp. 8, 117, 123, 124, 126, 127).
- [31] Chen, F., H. Lin, Z. Li, Q. Chen, and J. Zhou. "Interaction between permafrost and infrastructure along the Qinghai-Tibet Railway detected via jointly analysis of C-and L-band small baseline SAR interferometry". In: *Remote sensing of environment* 123 (2012), pp. 532–540 (cit. on p. 3).
- [32] Colesanti, C. and J. Wasowski. "Investigating landslides with space-borne Synthetic Aperture Radar (SAR) interferometry". In: *Engineering geology* 88.3-4 (2006), pp. 173–199 (cit. on p. 123).
- [33] Conroy, P. "Monitoring highly dynamic Land Surface motion with satellite radar interferometry". PhD thesis. TU Delft, 2025 (cit. on pp. 38, 40).
- [34] Conroy, P., S. A. N. van Diepen, and R. F. Hanssen. "SPAMS: A new empirical model for soft soil surface displacement based on meteorological input data". In: *Geoderma* (2023). DOI: [10.1016/j.geoderma.2023.116699](https://doi.org/10.1016/j.geoderma.2023.116699) (cit. on p. 39).

- [35] Conroy, P., S. A. N. van Diepen, S. van Asselen, G. Erkens, F. J. van Leijen, and R. F. Hanssen. “Probabilistic estimation of InSAR displacement phase guided by contextual information and artificial intelligence”. In: *IEEE Transactions on Geoscience and Remote Sensing* 60 (2022), pp. 1–11. DOI: [10.1109/TGRS.2022.3203872](https://doi.org/10.1109/TGRS.2022.3203872) (cit. on pp. 4, 34, 108).
- [36] Costantini, M. “A novel phase unwrapping method based on network programming”. In: *IEEE Transactions on Geoscience and Remote Sensing* 36.3 (1998), pp. 813–821. DOI: [10.1109/36.673674](https://doi.org/10.1109/36.673674) (cit. on pp. 6, 66).
- [37] Costantini, M., F. Malvarosa, F. Minati, L. Pietranera, and G. Milillo. “A three-dimensional phase unwrapping algorithm for processing of multitemporal SAR interferometric measurements”. In: *IEEE International Geoscience and Remote Sensing Symposium*. Vol. 3. 2002, 1741–1743 vol.3. DOI: [10.1109/IGARSS.2002.1026239](https://doi.org/10.1109/IGARSS.2002.1026239) (cit. on pp. 7, 66, 72).
- [38] Costantini, M., A. Ferretti, F. Minati, S. Falco, F. Trillo, D. Colombo, F. Novali, F. Malvarosa, C. Mammone, F. Vecchioli, *et al.* “Analysis of surface deformations over the whole Italian territory by interferometric processing of ERS, Envisat and COSMO-SkyMed radar data”. In: *Remote Sensing of Environment* 202 (2017), pp. 250–275 (cit. on p. 2).
- [39] Costantini, M., F. Minati, F. Trillo, A. Ferretti, F. Novali, E. Passera, J. Dehls, Y. Larsen, P. Marinkovic, M. Eineder, *et al.* “European ground motion service (EGMS)”. In: *2021 IEEE International Geoscience and Remote Sensing Symposium IGARSS*. IEEE. 2021, pp. 3293–3296 (cit. on p. 2).
- [40] Costantini, M., F. Minati, F. Trillo, A. Ferretti, E. Passera, A. Rucci, J. Dehls, Y. Larsen, P. Marinkovic, M. Eineder, R. Brcic, R. Siegmund, P. Kotzerke, A. Kenyeres, V. Costantini, S. Proietti, L. Solari, and H. S. Andersen. “EGMS: Europe-wide ground motion monitoring based on full resolution Insar processing of all Sentinel-1 acquisitions”. In: *IGARSS 2022 - 2022 IEEE IGARSS*. 2022, pp. 5093–5096. DOI: [10.1109/IGARSS46834.2022.9884966](https://doi.org/10.1109/IGARSS46834.2022.9884966) (cit. on pp. 2, 34, 115).
- [41] Crosetto, M., B. Crippa, M. Mróz, M. Cuevas-González, and S. Shahbazi. “Applications based on EGMS products: A review”. In: *Remote Sensing Applications: Society and Environment* (2025), p. 101452 (cit. on pp. 2, 4).
- [42] Crosetto, M., L. Solari, M. Mróz, J. Balasis-Levinsen, N. Casagli, M. Frei, A. Oyen, D. A. Moldestad, L. Bateson, L. Guerrieri, *et al.* “The evolution of wide-area DInSAR: From regional and national services to the European Ground Motion Service”. In: *Remote Sensing* 12.12 (2020), p. 2043 (cit. on p. 122).
- [43] De Boor, C. *A practical guide to splines*. Vol. 27. springer New York, 1978 (cit. on p. 41).
- [44] De Zan, F., M. Zonno, and P. Lopez-Dekker. “Phase inconsistencies and multiple scattering in SAR interferometry”. In: *IEEE Transactions on Geoscience and Remote Sensing* 53.12 (2015), pp. 6608–6616 (cit. on p. 55).

- [45] Dehls, J. F., A. Kenyeres, S. Tóth, Y. Larsen, and P. Marinkovic. “Towards geodetically robust datum connection of large-scale EGMS results - EGMS perspective”. In: *IGARSS 2022 IEEE International Geoscience and Remote Sensing Symposium*. 2022, pp. 5097–5100. DOI: [10.1109/IGARSS46834.2022.9884349](https://doi.org/10.1109/IGARSS46834.2022.9884349) (cit. on p. 2).
- [46] Dehls, J. F., Y. Larsen, P. Marinkovic, T. R. Lauknes, D. Stødle, and D. A. Moldestad. “INSAR. No: A national InSAR deformation mapping/monitoring service in Norway—From concept to operations”. In: *IGARSS 2019 IEEE International Geoscience and Remote Sensing Symposium*. IEEE. 2019, pp. 5461–5464 (cit. on p. 2).
- [47] Dheenathayalan, P., D. Small, A. Schubert, and R. F. Hanssen. “High-precision positioning of radar scatterers”. In: *Journal of Geodesy* 90.5 (2016), pp. 403–422. DOI: [10.1007/s00190-015-0883-4](https://doi.org/10.1007/s00190-015-0883-4) (cit. on p. 108).
- [48] Diestel, R. *Graph Theory*. 5th ed. Vol. 173. Graduate Texts in Mathematics. Springer, 2017 (cit. on p. 66).
- [49] Dzurisin, D. and M. Lisowski. “Analytical volcano deformation source models”. In: *Volcano deformation: Geodetic monitoring techniques* (2007), pp. 279–304 (cit. on p. 126).
- [50] Eerste Kamer der Staten-Generaal. *Wetsvoorstel beëindiging gaswinning Groningen*. https://www.eerstekamer.nl/wetsvoorstel/36441_beeindiging_gaswinning. [Online; accessed 16-July-2025]. 2024 (cit. on p. 175).
- [51] Eineder, M., C. Minet, P. Steigenberger, X. Cong, and T. Fritz. “Imaging geodesy, toward centimeter-level ranging accuracy with TerraSAR-X”. In: *IEEE Transactions on Geoscience and Remote Sensing* 49.2 (2011), pp. 661–671. DOI: [10.1109/TGRS.2010.2060264](https://doi.org/10.1109/TGRS.2010.2060264) (cit. on p. 21).
- [52] Esfahany, S. S. “Exploitation of distributed scatterers in synthetic aperture radar interferometry”. PhD thesis. TU Delft, 2017. DOI: [10.4233/uuid:22d46f1e-9061-46b0-9726-760c41404b6f](https://doi.org/10.4233/uuid:22d46f1e-9061-46b0-9726-760c41404b6f) (cit. on p. 23).
- [53] European Space Agency. *Sentinel 1 SAR Acquisition Modes*. 2021. URL: <https://sentinels.copernicus.eu/web/sentinel/user-guides/sentinel-1-sar/acquisition-modes/interferometric-wide-swath> (visited on 02/19/2021) (cit. on p. 104).
- [54] Even, M., M. Westerhaus, and H. Kutterer. “German and European ground motion service: A comparison”. In: *PFJ—Journal of Photogrammetry, Remote Sensing and Geoinformation Science* 92.3 (2024), pp. 253–270 (cit. on p. 4).
- [55] Evers, M., A. Thiele, H. Hammer, and S. Hinz. “PSDefoPAT—persistent scatterer deformation pattern analysis tool”. In: *Remote Sensing* 15.19 (2023), p. 4646 (cit. on p. 3).
- [56] Fatholahi, N., M. Akhoondzadeh, and A. Bahroudi. “An investigation of surface deformation over oilfield in Southwest Iran (2003–2010) using InSAR and physical modelling”. In: *International Journal of Remote Sensing* 41.14 (2020), pp. 5355–5370 (cit. on p. 119).

- [57] Feigl, K. L., F. Sarti, H. Vadon, S. McClusky, S. Ergintav, P. Durand, R. Bürgmann, A. Rigo, D. Massonnet, and R. Reilinger. “Estimating slip distribution for the Izmit mainshock from coseismic GPS, ERS-1, RADARSAT, and SPOT measurements”. In: *Bulletin of the Seismological Society of America* 92.1 (2002), pp. 138–160 (cit. on p. 2).
- [58] Ferretti, A., A. Fumagalli, E. Passera, and A. Rucci. “InSAR data calibration in wide area processing”. In: *IGARSS 2022-2022 IEEE International Geoscience and Remote Sensing Symposium*. IEEE, 2022, pp. 5101–5104 (cit. on p. 2).
- [59] Ferretti, A., D. Perissin, C. Prati, and F. Rocca. “On the physical nature of SAR Permanent Scatterers”. In: *URSI Commission F Symposium on Microwave Remote Sensing of the Earth, Oceans, Ice and Atmosphere, Ispra, Italy, 20–21 April, 2005*. 2005, 6 pp. (Cit. on p. 39).
- [60] Ferretti, A., C. Prati, and F. Rocca. “Nonlinear subsidence rate estimation using permanent scatterers in differential SAR interferometry”. In: *IEEE Transactions on Geoscience and Remote Sensing* 38.5 (2000), pp. 2202–2212 (cit. on pp. 16, 66, 68).
- [61] Ferretti, A., C. Prati, and F. Rocca. “Permanent scatterers in SAR interferometry”. In: *IEEE Transactions on Geoscience and Remote Sensing* 39.1 (2001), pp. 8–20 (cit. on pp. 2, 5, 6, 12, 13, 16, 23, 24, 66).
- [62] Fialko, Y., D. Sandwell, D. Agnew, M. Simons, P. Shearer, and B. Minster. “Deformation on nearby faults induced by the 1999 Hector Mine earthquake”. In: *Science* 297.5588 (2002), pp. 1858–1862 (cit. on p. 122).
- [63] Fialko, Y., M. Simons, and Y. Khazan. “Finite source modelling of magmatic unrest in Socorro, New Mexico, and Long Valley, California”. In: *Geophysical Journal International* 146.1 (2001), pp. 191–200 (cit. on pp. 2, 102, 110).
- [64] Finkel, R. A. and J. L. Bentley. “Quad trees a data structure for retrieval on composite keys”. In: *Acta informatica* 4 (1974), pp. 1–9 (cit. on p. 147).
- [65] Fokker, P. A., F. J. Van Leijen, B. Orlic, H. Van Der Marel, and R. F. Hanssen. “Subsidence in the dutch wadden sea”. In: *Netherlands Journal of Geosciences* 97.3 (2018), pp. 129–181 (cit. on p. 144).
- [66] Ford, A. L., R. R. Forster, and R. L. Bruhn. “Ice surface velocity patterns on Seward Glacier, Alaska/Yukon, and their implications for regional tectonics in the Saint Elias Mountains”. In: *Annals of Glaciology* 36 (2003), pp. 21–28 (cit. on p. 123).
- [67] Fornaro, G., D. Reale, and S. Verde. “Bridge thermal dilation monitoring with millimeter sensitivity via multidimensional SAR imaging”. In: *IEEE Geoscience and Remote Sensing Letters* 10.4 (2012), pp. 677–681 (cit. on p. 39).
- [68] Fowler, C. M. R. *The solid earth: an introduction to global geophysics*. Cambridge University Press, 1990 (cit. on p. 127).
- [69] Fuhrmann, T. and M. C. Garthwaite. “Resolving three-dimensional surface motion with InSAR: Constraints from multi-geometry data fusion”. In: *Remote Sensing* 11.3 (2019), p. 241 (cit. on pp. 102, 103).

- [70] Geertsma, J. "A basic theory of subsidence due to reservoir compaction: the homogeneous case". In: *Verhandelingen van het Koninklijk Nederlands geologisch mijnbouwkundig Genootschap* 28 (1973), pp. 43–62 (cit. on p. 126).
- [71] Geertsma, J. "Land subsidence above compacting oil and gas reservoirs". In: *Journal of Petroleum Technology* (1973), pp. 734–744 (cit. on p. 144).
- [72] Ghiglia, D. C. and L. A. Romero. "Robust two-dimensional weighted and unweighted phase unwrapping that uses fast transforms and iterative methods". In: *Journal of the Optical Society of America A* 11.1 (Jan. 1994), pp. 107–117 (cit. on p. 53).
- [73] Goldstein, R. M., H. A. Zebker, and C. L. Werner. "Satellite radar interferometry: Two-dimensional phase unwrapping". In: *Radio Science* 23.4 (July 1988), pp. 713–720 (cit. on p. 53).
- [74] Grafarend, E. W. and F. Sansò. *Optimization and design of geodetic networks*. Springer Science & Business Media, 2012 (cit. on pp. 66, 72).
- [75] Gray, A. L., K. E. Mattar, and P. W. Vachon. "InSAR results from the RADARSAT Antarctic mapping mission data: estimation of data using a simple registration procedure". In: *International Geoscience and Remote Sensing Symposium, Seattle, Washington, USA, 6–10 July 1998*. 1998, pp. 1638–1640 (cit. on p. 122).
- [76] Greif, V. and J. Vlcko. "Monitoring of post-failure landslide deformation by the PS-InSAR technique at Lubietova in Central Slovakia". In: *Environmental Earth Sciences* 66.6 (2012), pp. 1585–1595 (cit. on pp. 117, 123).
- [77] Guo, R., L. Sumin, Y. Chen, X. Li, and L. Yuan. "Identification and monitoring landslides in longitudinal range-gorge region with InSAR fusion integrated visibility analysis". In: *Landslides* (2020), pp. 1–18 (cit. on p. 119).
- [78] Haghshenas Haghghi, M. and M. Motagh. "Sentinel-1 InSAR over Germany: Large-scale interferometry, atmospheric effects, and ground deformation mapping". In: *ZfV: Zeitschrift für Geodäsie, Geoinformation und Landmanagement* 2017.4 (2017), pp. 245–256 (cit. on p. 115).
- [79] Hanssen, R. F. and F. J. van Leijen. *Bodemdalingskaart Nederland, Geodetische Analyse*. Accessed: 2024-09-25. 2017 (cit. on p. 150).
- [80] Hanssen, R. F. *Radar Interferometry: Data Interpretation and Error Analysis*. Dordrecht: Kluwer Academic Publishers, 2001. DOI: 10.1007/0-306-47633-9 (cit. on pp. 3, 5, 9, 12–14, 21, 34, 37, 38, 66, 102, 103, 107, 122, 145).
- [81] Hanssen, R. F. "A radar retroreflector device and a method of preparing a radar retroreflector device (Patent filed 2017)". English. NL2019103B1. 2019 (cit. on p. 108).
- [82] Hanssen, R. F. "Stochastic modeling of time series radar interferometry". In: *International Geoscience and Remote Sensing Symposium, Anchorage, Alaska, 20–24 September 2004*. 2004, cdrom, 4 pages (cit. on pp. 4, 6, 12, 52).

- [83] Hanssen, R. F., T. M. Weckwerth, H. A. Zebker, and R. Klees. “High-resolution water vapor mapping from interferometric radar measurements”. In: *Science* 283 (1999), pp. 1295–1297. DOI: [10.1126/science.283.5406.1297](https://doi.org/10.1126/science.283.5406.1297) (cit. on p. 35).
- [84] Hanssen, R. F., I. Weinreich, S. Lehner, and A. Stoffelen. “Tropospheric wind and humidity derived from spaceborne radar intensity and phase observations”. In: *Geophysical Research Letters* 27.12 (2000), pp. 1699–1702 (cit. on p. 35).
- [85] Harary, F. *Graph Theory*. Reading, Massachusetts: Addison-Wesley, 1969 (cit. on p. 68).
- [86] Heitfeld, M. and J. e. a. Klunker. *Na-ijlende gevolgen steenkolenwinning Zuid-Limburg - Summary report with integrated Bow-Tie-Analysis*. Vol. 1. Projectgroep GS-SL, 2016 (cit. on p. 137).
- [87] Hooper, A. “A multi-temporal InSAR method incorporating both persistent scatterer and small baseline approaches”. In: *Geophysical Research Letters* 35 (2008), p. L16302. DOI: [10.1029/2008GL03465](https://doi.org/10.1029/2008GL03465) (cit. on p. 5).
- [88] Hooper, A., J. Biggs, P. Prats-Iraola, F. Albino, F. De Zan, A. Parizzi, M. Rodriguez-Cassola, P. Lopez-Dekker, and B. Rommen. “Harmony: science objectives and mission overview”. In: *ESA LPS 2022*. 2022 (cit. on p. 110).
- [89] Hooper, A., P. Segall, and H. Zebker. “Persistent scatterer interferometric synthetic aperture radar for crustal deformation analysis, with application to Volcán Alcedo, Galápagos”. In: *Journal of Geophysical Research: Solid Earth* 112.B7 (2007) (cit. on p. 2).
- [90] Hooper, A., H. Zebker, P. Segall, and B. Kampes. “A new method for measuring deformation on volcanoes and other non-urban areas using InSAR persistent scatterers”. In: *Geophysical Research Letters* 31 (Dec. 2004), L23611, doi:10.1029/2004GL021737 (cit. on pp. 2, 4, 6, 12).
- [91] Hu, E., F. J. van Leijen, L. Chang, J. Wu, and R. F. Hanssen. “Monitoring deformation along railway systems combining multi-temporal InSAR and LiDAR data”. In: *Remote Sensing* 11.19 (2019), p. 2298 (cit. on p. 2).
- [92] Hu, E. and J. Wu. “Detecting spatio-temporal urban surface changes using identified temporary coherent scatterers”. In: *Journal of Systems Engineering and Electronics* 32.6 (2021), pp. 1304–1317 (cit. on pp. 4, 6, 12).
- [93] Hu, E., J. Wu, L. Chang, and R. F. Hanssen. “Incorporating temporary coherent scatterers in multi-temporal InSAR using adaptive temporal subsets”. In: *IEEE Transactions on Geoscience and Remote Sensing* 57.10 (2019), pp. 7658–7670. DOI: [10.1109/TGRS.2019.2915658](https://doi.org/10.1109/TGRS.2019.2915658) (cit. on pp. 4, 6, 12, 25, 147).
- [94] Hu, J., Z. Li, X. Ding, J. Zhu, L. Zhang, and Q. Sun. “Resolving three-dimensional surface displacements from InSAR measurements: A review”. In: *Earth Science Reviews* 133 (2014), pp. 1–17 (cit. on pp. 102, 103).
- [95] Huber, P. J. “Robust statistics”. In: *International encyclopedia of statistical science*. Springer, 2011, pp. 1248–1251 (cit. on p. 150).

- [96] Imamoglu, M., F. Kahraman, Z. Cakir, and F. B. Sanli. "Ground deformation analysis of Bolvadin (W. Turkey) by means of multi-temporal InSAR techniques and Sentinel-1 data". In: *Remote Sensing* 11.9 (2019), p. 1069 (cit. on pp. 113, 116).
- [97] Janna, C., N. Castelletto, M. Ferronato, G. Gambolati, and P. Teatini. "A geomechanical transversely isotropic model of the Po River basin using PSInSAR derived horizontal displacement". In: *International Journal of Rock Mechanics and Mining Sciences* 51 (2012), pp. 105–118 (cit. on pp. 113, 115, 116).
- [98] Joughin, I. R., R. Kwok, and M. A. Fahnestock. "Interferometric estimation of three-dimensional ice-flow using ascending and descending passes". In: *IEEE Transactions on Geoscience and Remote Sensing* 36.1 (1998), pp. 25–37 (cit. on pp. 8, 123).
- [99] Kalia, A., M. Frei, and T. Lege. "A Copernicus downstream-service for the nationwide monitoring of surface displacements in Germany". In: *Remote Sensing of Environment* 202 (2017), pp. 234–249 (cit. on p. 2).
- [100] Kampes, B. M. and R. F. Hanssen. "Ambiguity resolution for permanent scatterer interferometry". In: *IEEE Transactions on Geoscience and Remote Sensing* 42 (11 2004), pp. 2446–2453. DOI: [10.1109/TGRS.2004.835222](https://doi.org/10.1109/TGRS.2004.835222) (cit. on pp. 2, 53).
- [101] Kampes, B. M. "Displacement parameter estimation using permanent scatterer interferometry". PhD thesis. Delft, the Netherlands: Delft University of Technology, Sept. 2005 (cit. on pp. 7, 24, 34, 35).
- [102] Kampes, B. M. *Radar Interferometry: Persistent Scatterer Technique*. Dordrecht, The Netherlands: Springer, 2006. DOI: [10.1007/978-1-4020-4723-7](https://doi.org/10.1007/978-1-4020-4723-7) (cit. on pp. 7, 66, 67, 72).
- [103] Ketelaar, G. *Satellite radar interferometry: Subsidence monitoring techniques*. Vol. 14. Springer Science & Business Media, 2009 (cit. on pp. 2, 8, 144).
- [104] Ketelaar, G., H. Bähr, S. Liu, H. Piening, W. van der Veen, R. F. Hanssen, F. J. van Leijen, H. van der Marel, and S. Samiei-Esfahany. "Integrated monitoring of subsidence due to hydrocarbon production: consolidating the foundation". In: *Proceedings of the International Association of Hydrological Sciences* 382 (2020), pp. 117–123 (cit. on pp. 8, 144).
- [105] Ketelaar, G., F. van Leijen, P. Marinkovic, and R. Hanssen. "On the use of point target characteristics in the estimation of low subsidence rates due to gas extraction in Groningen, the Netherlands". In: *Fourth International Workshop on ERS/Envisat SAR Interferometry, 'FRINGE05', Frascati, Italy, 28 Nov-2 Dec 2005*. 2006, 6 pp. (Cit. on p. 144).
- [106] Ketelaar, G., F. J. van Leijen, P. Marinkovic, and R. F. Hanssen. "Multi-track PS-InSAR datum connection". In: *2007 IEEE International Geoscience and Remote Sensing Symposium*. 2007, pp. 2481–2484. DOI: [10.1109/IGARSS.2007.4423346](https://doi.org/10.1109/IGARSS.2007.4423346) (cit. on p. 2).

- [107] Ketelaar, V. B. H. *Monitoring surface deformation induced by hydrocarbon production using satellite radar interferometry*. Springer, 2008 (cit. on p. 108).
- [108] Kim, S. “Data assimilation for subsidence analysis of the Groningen region: A multi-scale study with importance sampling”. PhD thesis. Delft, the Netherlands: Delft University of Technology, 2025 (cit. on p. 144).
- [109] Klemm, H., I. Quseimi, F. Novali, A. Ferretti, and A. Tamburini. “Monitoring horizontal and vertical surface deformation over a hydrocarbon reservoir by PSInSAR”. In: *First break* 28.5 (2010) (cit. on pp. 113, 115, 116).
- [110] Koch, K.-R. *Parameter estimation and hypothesis testing in linear models*. Berlin: Springer-Verlag, 1999 (cit. on pp. 4, 12).
- [111] Kratzsch, H. *Mining subsidence engineering*. Springer Science & Business Media, 1983. DOI: [10.1007/978-3-642-81923-0](https://doi.org/10.1007/978-3-642-81923-0) (cit. on pp. 126, 144, 162, 166).
- [112] Kuang, S. “Geodetic network analysis and optimal design: concepts and applications”. In: (1996) (cit. on pp. 66, 72).
- [113] Kulshrestha, A., L. Chang, and A. Stein. “Use of LSTM for sinkhole-related anomaly detection and classification of InSAR deformation time series”. In: *IEEE Journal of Selected Topics in Applied Earth Observations and Remote Sensing* 15 (2022), pp. 4559–4570 (cit. on p. 34).
- [114] Kuzu, R. S., L. Bagaglini, Y. Wang, C. O. Dumitru, N. A. A. Braham, G. Pasquali, F. Santarelli, F. Trillo, S. Saha, and X. X. Zhu. “Automatic detection of building displacements through unsupervised learning from InSAR data”. In: *IEEE Journal of Selected Topics in Applied Earth Observations and Remote Sensing* 16 (2023), pp. 6931–6947 (cit. on p. 3).
- [115] Lanari, R., M. Bonano, F. Casu, C. D. Luca, M. Manunta, M. Manzo, G. Onorato, and I. Zinno. “Automatic generation of Sentinel-1 continental scale DInSAR deformation time series through an extended P-SBAS processing pipeline in a cloud computing environment”. In: *Remote Sensing* 12.18 (2020), p. 2961 (cit. on p. 2).
- [116] Lapadat, A. M., H. Andreas, W. S. Brouwer, S. A. N. van Diepen, D. Pradipta, and R. F. Hanssen. “Land subsidence in Jakarta in three dimensions (2014-2025) using InSAR-GNSS datum connection and the strapdown decomposition”. In: (2025). DOI: <https://doi.org/10.31223/X5R45H> (cit. on p. 163).
- [117] Leys, C., C. Ley, O. Klein, P. Bernard, and L. Licata. “Detecting outliers: Do not use standard deviation around the mean, use absolute deviation around the median”. In: *Journal of experimental social psychology* 49.4 (2013), pp. 764–766 (cit. on p. 24).
- [118] Lopez-Dekker, P. and A. Theodosiou. *DRaMA software*. 2022. URL: <https://gitlab.tudelft.nl/drama/drama> (visited on 07/14/2022) (cit. on p. 106).

- [119] Ma, Z., J. Liu, Y. Aoki, S. Wei, X. Liu, Y. Cui, J. Hu, C. Zhou, S. Qin, T. Huang, *et al.* “Towards big SAR data era: An efficient Sentinel-1 near-real-time InSAR processing workflow with an emphasis on co-registration and phase unwrapping”. In: *ISPRS Journal of Photogrammetry and Remote Sensing* 188 (2022), pp. 286–300 (cit. on p. 2).
- [120] Mahapatra, P. “Geodetic network design for InSAR: Application to ground deformation monitoring”. PhD thesis. TU Delft, 2015 (cit. on pp. 66, 67, 72).
- [121] Mardia, K. V. and P. E. Jupp. *Directional Statistics*. Chichester: John Wiley & Sons, 2000 (cit. on p. 70).
- [122] Massonnet, D. and F. Adragna. “A full-scale validation of radar interferometry with ERS-1: the landers earthquake”. In: *Earth Observation Quarterly* 41 (1993), pp. 1–5 (cit. on pp. 2, 102).
- [123] Massonnet, D., P. Briole, and A. Arnaud. “Deflation of Mount Etna monitored by spaceborne radar interferometry”. In: *Nature* 375.6532 (1995), pp. 567–570 (cit. on pp. 2, 102).
- [124] Massonnet, D. and K. L. Feigl. “Radar interferometry and its application to changes in the Earth’s surface”. In: *Reviews of geophysics* 36.4 (1998), pp. 441–500 (cit. on p. 122).
- [125] Mateus, P., G. Nico, and J. Catalão. “Maps of PWV temporal changes by SAR interferometry: A study on the properties of atmosphere’s temperature profiles”. In: *IEEE Geoscience and Remote Sensing Letters* 11.12 (2014), pp. 2065–2069 (cit. on p. 35).
- [126] Mattar, K. E., P. W. Vachon, D. Geudtner, A. L. Gray, I. G. Cumming, and M. Brugman. “Validation of Alpine glacier velocity measurements using ERS tandem-mission SAR data”. In: *IEEE Transactions on Geoscience and Remote Sensing* 36.3 (May 1998), pp. 974–984 (cit. on pp. 8, 123).
- [127] Mele, A., M. Crosetto, A. Miano, and A. Prota. “Adafinder tool applied to EGMS data for the structural health monitoring of urban settlements”. In: *Remote Sensing* 15.2 (2023), p. 324 (cit. on p. 3).
- [128] Minh, D. H. T., N. Yen-Nhi, T. T. Lê, T. C. Le, H. S. Bui, Q. V. Vuong, and T. Le Toan. “Quantifying horizontal and vertical movements in Ho Chi Minh city by Sentinel-1 radar interferometry”. In: *Preprints.org* not peer-reviewed (2021) (cit. on pp. 113, 115, 116).
- [129] Mohr, J. J., N. Reeh, and S. N. Madsen. “Three-dimensional glacial flow and surface elevation measured with radar interferometry”. In: *Nature* 291 (1998), pp. 273–276 (cit. on p. 123).
- [130] Mohr, J. J. “Repeat track SAR interferometry. An investigation of its utility for studies of glacier dynamics”. PhD thesis. Copenhagen: Technical University of Denmark, May 1997 (cit. on pp. 8, 117, 123).
- [131] Monserrat, O., M. Crosetto, M. Cuevas, and B. Crippa. “The thermal expansion component of persistent scatterer interferometry observations”. In: *IEEE Geoscience and Remote Sensing Letters* 8.5 (2011), pp. 864–868 (cit. on p. 39).

- [132] Mulder, G., F. J. van Leijen, J. Barkmeijer, S. de Haan, and R. F. Hanssen. “Estimating single-epoch integrated atmospheric refractivity from InSAR for assimilation in numerical weather models”. In: *IEEE Transactions on Geoscience and Remote Sensing* 60 (2022), pp. 1–12. DOI: [10.1109/TGRS.2022.3177041](https://doi.org/10.1109/TGRS.2022.3177041) (cit. on p. 35).
- [133] Mulder, G., F. J. van Leijen, and R. F. Hanssen. “A generic approach to parameterize the turbulent energy of single-epoch atmospheric delays from InSAR time series”. In: *IEEE Transactions on Geoscience and Remote Sensing* 61 (2023), pp. 1–13. DOI: [10.1109/TGRS.2023.3295898](https://doi.org/10.1109/TGRS.2023.3295898) (cit. on pp. 77, 86).
- [134] Müller, D. and A. Preusse. “Use of the area of main influence to fix a relevant boundary for mining damages in Germany”. In: *International Journal of Mining Science and Technology* 28.1 (2018), pp. 79–83 (cit. on p. 126).
- [135] NAM. *Bodemdeling door Aardgaswinning: NAM gasvelen in Groningen, Friesland, en het noorden van Drenthe. Status Rapport 2015 en Prognose tot het jaar 2080*. NAM rapport nr. 201511213444. in Dutch. Assen: Nederlandse Aardolie Maatschappij B.V, 2015 (cit. on p. 144).
- [136] NAM. *Bodemdeling door aardgaswinning - Statusrapport 2020 en Prognose tot het jaar 2080 (december 2020)*. Assen: NAM, 2020 (cit. on pp. 144, 159, 175).
- [137] Navarro, J. A., R. Tomás, A. Barra, J. I. Pagán, C. Reyes-Carmona, L. Solari, J. Vinielles, S. Falco, and M. Crosetto. “ADAtools: Automatic detection and classification of active deformation areas from PSI displacement maps”. In: *ISPRS International Journal of Geo-Information* 9.10 (2020), p. 584 (cit. on p. 3).
- [138] Ng, A. H.-M., H. Wang, Y. Dai, C. Pagli, W. Chen, L. Ge, Z. Du, and K. Zhang. “InSAR reveals land deformation at Guangzhou and Foshan, China between 2011 and 2017 with COSMO-SkyMed data”. In: *Remote Sensing* 10.6 (2018), p. 813 (cit. on p. 115).
- [139] Nof, R. N., G. Baer, A. Ziv, E. Raz, S. Atzori, and S. Salvi. “Sinkhole precursors along the Dead Sea, Israel, revealed by SAR interferometry”. In: *Geology* 41.9 (2013), pp. 1019–1022 (cit. on p. 115).
- [140] Notti, D., G. Herrera, S. Bianchini, C. Meisina, J. C. García-Davalillo, and F. Zucca. “A methodology for improving landslide PSI data analysis”. In: *International Journal of Remote Sensing* 35.6 (2014), pp. 2186–2214 (cit. on p. 123).
- [141] Özer, I. E., F. J. van Leijen, S. N. Jonkman, and R. F. Hanssen. “Applicability of satellite radar imaging to monitor the conditions of levees”. In: *Journal of Flood Risk Management* 12.S2 (2019), e12509 (cit. on pp. 8, 117, 123, 126).
- [142] Palamà, R., A. Barra, M. Cuevas-González, O. Monserrat, and M. Crosetto. “Ground motion classification from European ground motion service data using extreme gradient boosting”. In: *IGARSS 2024-2024 IEEE International Geoscience and Remote Sensing Symposium*. IEEE. 2024, pp. 10736–10739 (cit. on p. 3).

- [143] Pawluszek-Filipiak, K. and A. Borkowski. "Integration of DInSAR and SBAS techniques to determine mining-related deformations using Sentinel-1 data: The case study of Rydułtowy mine in Poland". In: *Remote Sensing* 12.2 (2020), p. 242 (cit. on pp. 113, 116).
- [144] Pepe, A. and R. Lanari. "On the extension of the minimum cost flow algorithm for phase unwrapping of multitemporal differential SAR interferograms". In: *IEEE Transactions on Geoscience and Remote Sensing* 44.9 (2006), pp. 2374–2383. DOI: [10.1109/TGRS.2006.873207](https://doi.org/10.1109/TGRS.2006.873207) (cit. on pp. 7, 66, 72).
- [145] Pepe, A. and F. Calò. "A review of interferometric synthetic aperture RADAR (InSAR) multi-track approaches for the retrieval of Earth's surface displacements". In: *Applied Sciences* 7.12 (2017), p. 1264 (cit. on p. 116).
- [146] Pöttgens, J. "Uplift as a result of rising mine waters". In: *The Development Science and Art of Mineral Surveying, Proceedings of the 6th International Congress. International Society for Mine Surveying, Harrogate UK*. Vol. 2. 1985 (cit. on p. 137).
- [147] Qin, X., L. Zhang, X. Ding, M. Liao, and M. Yang. "Mapping and characterizing thermal dilation of civil infrastructures with multi-temporal X-band synthetic aperture radar interferometry". In: *Remote Sensing* 10.6 (2018), p. 941 (cit. on p. 39).
- [148] Qin, Y., J. Salzer, H. Maljaars, and P. B. Leezenberg. *High resolution InSAR in the Groningen area 2018-2019 Advanced Services*. Tech. rep. NAM, SkyGeo, 2019 (cit. on pp. 8, 144).
- [149] Raucoules, D., C. Maisons, C. Carnec, S. Le Mouelic, C. King, and S. Hosford. "Monitoring of slow ground deformation by ERS radar interferometry on the Vauvert salt mine (France): Comparison with ground-based measurement". In: *Remote Sensing of Environment* 88.4 (2003), pp. 468–478 (cit. on p. 115).
- [150] Rocca, F. "3D motion recovery with multi-angle and/or left right interferometry". In: *Proceedings of the third International Workshop on ERS SAR*. 2003 (cit. on pp. 102, 109, 110, 122).
- [151] Rousseeuw, P. J. and C. Croux. "Alternatives to the median absolute deviation". In: *Journal of the American Statistical Association* 88.424 (1993), pp. 1273–1283 (cit. on p. 24).
- [152] Rucci, A., D. Vasco, and F. Novali. "Monitoring the geologic storage of carbon dioxide using multicomponent SAR interferometry". In: *Geophysical Journal International* 193.1 (2013), pp. 197–208 (cit. on pp. 113, 116).
- [153] Sadeghi, Z., T. J. Wright, A. J. Hooper, C. Jordan, A. Novellino, L. Bateson, and J. Biggs. "Benchmarking and inter-comparison of Sentinel-1 InSAR velocities and time series". In: *Remote Sensing of Environment* 256 (2021), p. 112306 (cit. on p. 4).
- [154] Samet, H. "The quadtree and related hierarchical data structures". In: *ACM Computing Surveys (CSUR)* 16.2 (1984), pp. 187–260 (cit. on p. 147).

- [155] Scheiber, R. and A. Moreira. “Coregistration of interferometric SAR images using spectral diversity”. In: *IEEE Transactions on Geoscience and Remote Sensing* 38.5 (2000), pp. 2179–2191 (cit. on p. 122).
- [156] Schreiber, O. “Die Anordnung der Winkelbeobachtungen im Göttinger Basisnetz”. In: *Zeitschrift für Vermessungswesen* 11 (1882), pp. 129–161 (cit. on pp. 7, 66, 72).
- [157] Schreuder, W., N. Busscher, T. Postmes, A. Zijlstra, and E. Vojvodic. “Insight into impact: The societal consequences of gas extraction in Groningen and ways of thinking for the future”. In: (2023) (cit. on p. 144).
- [158] Shanker, P. and H. Zebker. “Persistent scatterer selection using maximum likelihood estimation”. In: *Geophysical Research Letters* 34.22 (2007) (cit. on p. 23).
- [159] Short, N., A.-M. LeBlanc, W. Sladen, G. Oldenborger, V. Mathon-Dufour, and B. Brisco. “RADARSAT-2 D-InSAR for ground displacement in permafrost terrain, validation from Iqaluit Airport, Baffin Island, Canada”. In: *Remote Sensing of Environment* 141 (2014), pp. 40–51 (cit. on p. 115).
- [160] Simons, M., D. Bekaert, A. Borsa, A. Donnellan, E. Fielding, C. Jones, R. Lohman, Z. Lu, F. Meyer, S. Owen, *et al.* “NISAR requirements and validation approach for solid earth science”. In: *2021 IEEE IGARSS*. IEEE. 2021, pp. 543–546 (cit. on p. 110).
- [161] Solari, L., A. Ciampalini, F. Raspini, S. Bianchini, and S. Moretti. “PSInSAR analysis in the Pisa Urban Area (Italy): a case study of subsidence related to stratigraphical factors and urbanization”. In: *Remote Sensing* 8.2 (2016), p. 120 (cit. on p. 115).
- [162] Sousa, J. J. “Potential of integrating PSI methodologies in the detection of surface deformation”. PhD thesis. University of Porto, Portugal, 2009 (cit. on p. 2).
- [163] Sousa, J. J., A. J. Hooper, R. F. Hanssen, L. C. Bastos, and A. M. Ruiz. “Persistent Scatterer InSAR: A comparison of methodologies based on a model of temporal deformation vs. spatial correlation selection criteria”. In: *Remote Sensing of Environment* 115.10 (2011), pp. 2652–2663 (cit. on pp. 3, 4).
- [164] Strang, G. *Linear algebra and its applications*. 3rd ed. Fort Worth: Harcourt Brace Jovanovich College Publishers, 1988 (cit. on pp. 8, 102).
- [165] Staudinger, M. “A cost orientated approach to geodetic network optimisation”. PhD thesis. Vienna University of Technology, 1999 (cit. on pp. 66, 72).
- [166] Stramondo, S., F. Bozzano, F. Marra, U. Wegmuller, F. Cinti, M. Moro, and M. Saroli. “Subsidence induced by urbanisation in the city of Rome detected by advanced InSAR technique and geotechnical investigations”. In: *Remote Sensing of Environment* 112.6 (2008), pp. 3160–3172 (cit. on p. 115).

- [167] Strozzi, T., A. Luckman, T. Murray, U. Wegmuller, and C. Werner. "Glacier motion estimation using SAR offset-tracking procedures". In: *IEEE Transactions on Geoscience and Remote Sensing* 40.11 (2002), pp. 2384–2391. DOI: [10.1109/TGRS.2002.805079](https://doi.org/10.1109/TGRS.2002.805079) (cit. on p. 122).
- [168] Sun, H., Q. Zhang, C. Zhao, C. Yang, Q. Sun, and W. Chen. "Monitoring land subsidence in the southern part of the lower Liaohe plain, China with a multi-track PS-InSAR technique". In: *Remote Sensing of Environment* 188 (2017), pp. 73–84 (cit. on p. 115).
- [169] Svingkas, N., C. Loupasakis, P. Tsangaratos, I. Papoutsis, A. Kiratzi, and C. H. Kontoes. "A deformation study of Anthemountas graben (northern Greece) based on in situ data and new InSAR results". In: *Arabian Journal of Geosciences* 13.13 (2020), pp. 1–13 (cit. on p. 115).
- [170] Tamburini, A., M. Bianchi, C. Giannico, and F. Novali. "Retrieving surface deformation by PSInSAR™ technology: A powerful tool in reservoir monitoring". In: *International Journal of Greenhouse Gas Control* 4.6 (2010), pp. 928–937 (cit. on pp. 113, 116).
- [171] Tang, W., P. Yuan, M. Liao, and T. Balz. "Investigation of ground deformation in Taiyuan Basin, China from 2003 to 2010, with atmosphere-corrected time series InSAR". In: *Remote Sensing* 10.9 (2018), p. 1499 (cit. on p. 115).
- [172] Tarantola, A. *Inverse Problems Theory*. New York: Elsevier, 1987 (cit. on pp. 106, 109).
- [173] Teatini, P., N. Castelletto, M. Ferronato, G. Gambolati, C. Janna, E. Cairo, D. Marzorati, D. Colombo, A. Ferretti, A. Bagliani, *et al.* "Geomechanical response to seasonal gas storage in depleted reservoirs: A case study in the Po River basin, Italy". In: *Journal of Geophysical Research: Earth Surface* 116.F2 (2011) (cit. on pp. 113, 116).
- [174] Teatini, P., L. Tosi, T. Strozzi, L. Carbognin, U. Wegmüller, and F. Rizzetto. "Mapping regional land displacements in the Venice coastland by an integrated monitoring system". In: *Remote Sensing of Environment* 98.4 (2005), pp. 403–413 (cit. on p. 115).
- [175] Teunissen, P. J. G. "Least-squares estimation of the integer GPS ambiguities". In: *Invited Lecture, Section IV Theory and Methodology, IAG General Meeting, Beijing, China, august 1993*. Also in: Delft Geodetic Computing Centre, LGR Series, No. 6, 1994. 1993 (cit. on p. 53).
- [176] Teunissen, P. J. G. "Least-squares estimation of the integer GPS ambiguities". In: *Publications and annual report 1993*. LGR-Series 6. Delft geodetic computing centre, 1994, pp. 59–74 (cit. on p. 53).
- [177] Teunissen, P. J. G. "The least-squares ambiguity decorrelation adjustment: a method for fast GPS integer ambiguity estimation". In: *Journal of Geodesy* 70.1-2 (1995), pp. 65–82 (cit. on p. 53).

- [178] Teunissen, P. J. G. “On InSAR ambiguity resolution for deformation monitoring”. In: *Artificial Satellites* 41 (1 2006), pp. 17–22. DOI: [10.2478/v10018-007-0002-8](https://doi.org/10.2478/v10018-007-0002-8) (cit. on p. 53).
- [179] Teunissen, P. J. G. and A. R. Amiri-Simkooei. “Least-squares variance component estimation”. In: *Journal of Geodesy* 82.2 (2008), pp. 65–82 (cit. on p. 12).
- [180] Teunissen, P. J. G. *Adjustment Theory: An Introduction*. 2nd ed. TU Delft OPEN Publishing, 2024. DOI: [10.59490/tb.95](https://doi.org/10.59490/tb.95) (cit. on pp. 66, 70, 107).
- [181] Teunissen, P. J. G. *Testing Theory: An Introduction*. 3rd ed. TU Delft OPEN Publishing, 2024. DOI: [10.59490/tb.96](https://doi.org/10.59490/tb.96) (cit. on p. 70).
- [182] Titterton, D., J. L. Weston, and J. Weston. *Strapdown inertial navigation technology*. Vol. 17. IET, 2004 (cit. on p. 123).
- [183] Torres, R., I. Navas-Traver, D. Bibby, S. Lokas, P. Snoeij, B. Rommen, S. Osborne, F. Ceba-Vega, P. Potin, and D. Geudtner. “Sentinel-1 SAR system and mission”. In: *2017 IEEE Radar Conference (RadarConf)*. IEEE, 2017, pp. 1582–1585 (cit. on p. 21).
- [184] Truong, C., L. Oudre, and N. Vayatis. “Selective review of offline change point detection methods”. In: *Signal Processing* 167 (2020), p. 107299 (cit. on pp. 27, 46, 47).
- [185] Van Eijs, R. M. and O. van der Wal. “Field-wide reservoir compressibility estimation through inversion of subsidence data above the Groningen gas field”. In: *Netherlands Journal of Geosciences* 96.5 (2017), s117–s129 (cit. on p. 144).
- [186] Van Thienen-Visser, K., J. Pruiksma, and J. Breunese. “Compaction and subsidence of the Groningen gas field in the Netherlands”. In: *Proceedings of the International Association of Hydrological Sciences* 372.372 (2015), pp. 367–373 (cit. on p. 144).
- [187] Van Thienen-Visser, K. and P. A. Fokker. “The future of subsidence modelling: compaction and subsidence due to gas depletion of the Groningen gas field in the Netherlands”. In: *Netherlands Journal of Geosciences* 96.5 (2017), s105–s116 (cit. on pp. 8, 144).
- [188] Van Balen, R., C. Kasse, J. Wallinga, and H. Woolderink. “Middle to Late Pleistocene faulting history of the Heerlerheide fault, Roer Valley Rift System, influenced by glacio-isostasy and mining-induced displacement”. In: *Quaternary Science Reviews* 268 (2021), p. 107111 (cit. on p. 137).
- [189] Van Bergen, E., H. Pagnier, and P. Van Tongeren. “Peat, coal and coalbed methane”. In: *Geology of the Netherlands. Royal Netherlands Academy of Arts and Sciences* (2007), pp. 265–282 (cit. on p. 137).
- [190] Van De Kerkhof, B., V. Pankratius, L. Chang, R. Van Swol, and R. F. Hanssen. “Individual scatterer model learning for satellite interferometry”. In: *IEEE Transactions on Geoscience and Remote Sensing* 58.2 (2019), pp. 1273–1280 (cit. on p. 12).

- [191] van der Voort, N. and F. Vanclay. "Social impacts of earthquakes caused by gas extraction in the Province of Groningen, The Netherlands". In: *Environmental Impact Assessment Review* 50 (2015), pp. 1–15. DOI: <https://doi.org/10.1016/j.eiar.2014.08.008> (cit. on p. 144).
- [192] Van der Lee, T. *Groningers boven gas: Eindrapport van de parlementaire enquêtecommissie aardgaswinning Groningen*. Tech. rep. Den Haag, 2023 (cit. on p. 144).
- [193] van Leijen, F. J. "Persistent scatterer interferometry based on geodetic estimation theory". PhD thesis. TU Delft, 2014 (cit. on pp. 2, 4–6, 12, 16, 24, 34, 35, 66–68, 72, 134, 138).
- [194] van Leijen, F. J., Z. Perski, and R. F. Hanssen. "Error propagation and data quality assessment for ASAR persistent scatterer interferometry". In: *European Conference on Synthetic Aperture Radar*. 2006, p. 6 (cit. on p. 66).
- [195] Van Loan, C. F. and G. Golub. "Matrix computations (Johns Hopkins studies in mathematical sciences)". In: *Matrix Computations* 5 (1996), p. 32 (cit. on p. 70).
- [196] Van Natijne, A., T. Bogaard, F. van Leijen, R. Hanssen, and R. Lindenbergh. "World-wide InSAR sensitivity index for landslide deformation tracking". In: *International Journal of Applied Earth Observation and Geoinformation* 111 (2022), p. 102829 (cit. on pp. 8, 108, 117, 123).
- [197] Vecchioli, F., M. Costantini, F. Minati, and M. Zavagli. "A novel algorithm for point coherence estimation in SAR Interferometry". In: *IGARSS 2023-2023 IEEE International Geoscience and Remote Sensing Symposium*. IEEE. 2023, pp. 7868–7871 (cit. on pp. 4, 6, 12).
- [198] Von Mises, R. *Mathematische Theorie der Wahrscheinlichkeit und Statistik*. Leipzig und Wien: F. Deuticke, 1918 (cit. on p. 70).
- [199] Wang, L., K. Deng, and M. Zheng. "Research on ground deformation monitoring method in mining areas using the probability integral model fusion D-InSAR, sub-band InSAR and offset-tracking". In: *International journal of applied earth observation and geoinformation* 85 (2020), p. 101981 (cit. on p. 119).
- [200] Wang, Y., W. Brouwer, F. van Leijen, and R. F. Hanssen. "Constrained recursive parameter estimation for InSAR arcs". In: *2024 IEEE International Geoscience and Remote Sensing Symposium IGARSS*. Athens, Greece, 2024 (cit. on p. 68).
- [201] Wang, Y., W. S. Brouwer, F. J. Van Leijen, and R. F. Hanssen. "Non-parametric InSAR time series analysis of arcs using complex B-Splines". In: *IGARSS 2023-2023 IEEE International Geoscience and Remote Sensing Symposium*. IEEE. 2023, pp. 8238–8241 (cit. on pp. 35, 40).
- [202] Wang, Y., W. S. Brouwer, F. J. van Leijen, and R. F. Hanssen. "Instantaneous state InSAR: Estimation and prediction for near real-time displacement monitoring". 2026. DOI: [10.1109/TGRS.2026.3681072](https://doi.org/10.1109/TGRS.2026.3681072) (cit. on pp. 34, 40, 48, 174, 175).

- [203] Wright, T., E. Fielding, and B. Parsons. “Triggered slip: observations of the 17 August 1999 Izmit (Turkey) earthquake using radar interferometry”. In: *Geophysical Research Letters* 28.6 (2001), pp. 1079–1082 (cit. on p. 2).
- [204] Wright, T. J., B. E. Parsons, and Z. Lu. “Toward mapping surface deformation in three dimensions using InSAR”. In: *Geophysical Research Letters* 31.1 (2004) (cit. on pp. 102, 103, 109, 110, 118, 122).
- [205] Xie, C., Z. Li, J. Xu, and X. Li. “Analysis of deformation over permafrost regions of Qinghai-Tibet plateau based on permanent scatterers”. In: *International Journal of Remote Sensing* 31.8 (2010), pp. 1995–2008 (cit. on p. 3).
- [206] Yang, M., P. Lopez-Dekker, P. Dheenathayalan, F. Biljecki, M. Liao, and R. F. Hanssen. “Linking persistent scatterers to the built environment using ray tracing on urban models”. In: *IEEE Transactions on Geoscience and Remote Sensing* 57.8 (2019), pp. 5764–5776. DOI: [10.1016/j.isprsjprs.2019.10.006](https://doi.org/10.1016/j.isprsjprs.2019.10.006) (cit. on pp. 37, 108).
- [207] Yazici, B. V. and E. Tunc Gormus. “Investigating persistent scatterer InSAR (PSInSAR) technique efficiency for landslides mapping: a case study in Artvin dam area, in Turkey”. In: *Geocarto International* (2020), pp. 1–19 (cit. on pp. 113, 116, 119).
- [208] Yu, B., G. Liu, R. Zhang, H. Jia, T. Li, X. Wang, K. Dai, and D. Ma. “Monitoring subsidence rates along road network by persistent scatterer SAR interferometry with high-resolution TerraSAR-X imagery”. In: *Journal of Modern Transportation* 21 (2013), pp. 236–246 (cit. on p. 125).
- [209] Yun, S., P. Segall, and H. Zebker. “Constraints on magma chamber geometry at Sierra Negra Volcano, Galápagos Islands, based on InSAR observations”. In: *Journal of Volcanology and geothermal research* 150.1-3 (2006), pp. 232–243 (cit. on pp. 113, 115, 116).
- [210] Yunjun, Z., H. Fattahi, and F. Amelung. “Small baseline InSAR time series analysis: Unwrapping error correction and noise reduction”. In: *Computers & Geosciences* 133 (2019), p. 104331 (cit. on pp. 4, 6, 12).
- [211] Zebker, H. A., P. A. Rosen, R. M. Goldstein, A. Gabriel, and C. L. Werner. “On the derivation of coseismic displacement fields using differential radar interferometry: The Landers earthquake”. In: *Journal of Geophysical Research* 99.B10 (1994), pp. 19617–19634 (cit. on p. 102).
- [212] Zebker, H. A. and R. M. Goldstein. “Topographic mapping from interferometric synthetic aperture radar observations”. In: *Journal of Geophysical Research: Solid Earth* 91.B5 (1986), pp. 4993–4999. DOI: [10.1029/JB091iB05p04993](https://doi.org/10.1029/JB091iB05p04993) (cit. on p. 37).
- [213] Zheng, M., K. Deng, H. Fan, and S. Du. “Monitoring and analysis of surface deformation in mining area based on InSAR and GRACE”. In: *Remote Sensing* 10.9 (2018), p. 1392 (cit. on p. 115).

- [214] Zhou, L., J. Guo, J. Hu, J. Li, Y. Xu, Y. Pan, and M. Shi. “Wuhan surface subsidence analysis in 2015–2016 based on sentinel-1a data by SBAS-InSAR”. In: *Remote Sensing* 9.10 (2017), p. 982 (cit. on p. 115).
- [215] Zhu, X. X., S. Montazeri, C. Gisinger, R. F. Hanssen, and R. Bamler. “Geodetic SAR tomography”. In: *IEEE Transactions on Geoscience and Remote Sensing* 54.1 (2015), pp. 18–35 (cit. on p. 108).

ACKNOWLEDGEMENTS

It is easier to go down a hill than up it, but the view is much better at the top

Henry Ward Beecher

Exactly five years ago, I wrote in my Master's thesis that doing research is like mountain climbing. Now, after completing a PhD, this comparison has never felt more fitting. Climbing can be tough, and at times the summit feels impossibly far away. The weather turns, the path ahead becomes unclear, and there are moments when you wonder how long the journey will take. What helps is not to focus only on the top, but to set smaller goals along the way, celebrating each step forward. And when you finally reach the summit, the view makes it all worthwhile. It is precisely the challenging climb that makes you appreciate the top and feel proud of how far you have come. But perhaps the most important thing is that you never climb alone. Over the past years, I have always climbed together with others, tied together by a rope, trusting that someone will catch me if I fell. We searched for the right path together, often without knowing exactly where to go or how far we still had to go. And along the way, we shared many beautiful views, whether at the summit or halfway up, after overcoming a challenging section.

There are many people I would like to thank. First and foremost, **Ramon**. You were the one who actually suggested climbing this mountain. At the time, I found it intimidating, not knowing the exact route we had to take. But soon, I realized that you did not know the way either. However, you taught me that exactly this uncertainty is part of the process. I especially cherish our many brainstorming sessions, where we often had no clear way forward, yet somehow always managed to take small steps ahead. You showed me that curiosity and enthusiasm are enough to move forward, even without a clear path. I will always remember your question: "Are we happy now?" It taught me to look at my work with a more critical view. You also encouraged me to explore beyond the most common path. Because of that, I spent a month in China, attended many conferences, took part in a TV program, and even had the opportunity to have dinner with the minister. What sometimes felt like detours turned out to be valuable experiences that contributed more to this research than I could have thought.

I would also like to thank **Freek** for all your explanations of the Delft way of InSAR parameter estimation and DePSI, which formed the starting point of this thesis, as well as for your critical feedback and careful reading of many chapters. My thanks also go to the committee, **Roland, Rob, Ling, Sami, and Gini**, for their thoughtful comments and valuable feedback, which helped improve this work. I am grateful to

SkyGeo for providing the InSAR data used in Chapters 7 and 8. I would also like to thank **Esther, Chayenne, Marius, and Samantha** from DeepNL. I have very warm memories of our Thursdays working together in Utrecht and Delft. A special thanks to **Femke**, who showed me that even as a professor, things can still feel exciting and uncertain, and that it is okay to be open about that. That lesson in vulnerability gave me confidence. Many thanks also to **Mengshi** for making it possible for me to spend a month working on my PhD at Kunming University in China. This not only helped my research progress, but also led to many new and unforgettable experiences. To all my wonderful **colleagues at GRS**: thank you. Starting with the Caroline InSAR group: **Phil, Simon, Yuqing, Dita, Alex, Lina, and Isabel** and the Bsc and Msc students that joined our group. Thank you for all the enjoyable huddles, where insightful discussions often raised more questions than they answered, yet always pushed the research in the right direction. And of course, thank you for all the adventures we shared during conferences, or when we once again had to go out for leveling field measurements. Of course, I would also like to thank all other **GRS PhDs**, many of whom have already graduated. Thank you for the coffee breaks, lunch breaks, and casual conversations that always made the working day that much more enjoyable. A special thank you also goes to the **ladies of the secretariat**, where I could always drop by for a chat and where it was always so welcoming that I inevitably stayed longer than intended. **Sandra**, thank you for our amazing adventures in Iceland. I still smile when I think of our first river crossing in the Land Cruiser and swimming in a crater lake. **Paco**, you cannot go unmentioned. Thank you for the Iceland adventures, because of you I can never walk with my hands behind my back anymore (even though I still think it does not make us look older, just wiser), and for always making time to talk, no matter how busy you were. To my office mates in the “**cool new room**”: without you, the final months would have been far too dull. I just hope I did not distract you too much. **Maaïke** and **Sophie**, thank you for all the fun: our writing afternoons at the Coffee Company, cocktail evenings to unwind, and many other great moments. Only after you both left did I realize how empty it suddenly felt. **Paulina, Romy, and Daan**, I hope we will continue our Thursday morning coffee traditions for a long time. Have we tried all the cakes at Labs yet? I would also like to thank my paranympths, Sophie and **Paco**. My PhD neighbors for much of this journey, always there for a coffee break, a chat, or just a good conversation when work could wait. Finally, a special thank you to **Gilles** for the beautiful design of this thesis cover. It was fun to step away from equations for a moment and think about my research in a more creative way. You managed to create something that truly feels like me.

And outside the university, I was also never alone. Of course, the “**bolletjes**”—without you, studying would never have been this much fun, and I might never have started a PhD at all. I also want to thank my **climbing friends** and especially the “**levensgenieters**”. You helped me clear my mind and focus on completely different things. Climbing and camping remain my greatest passions. Coming back from our adventures always gave me new energy and ideas. A special thank you to my sisters **Nienke** and **Femke**. There are few people who know me as well as you do, and with whom I can be so completely myself. Thank you also for

all the adventures we have shared throughout our lives, climbing, cycling, skiing, camping, and, fortunately, also simply relaxing together on the couch. **Aris**, thank you for being so close. You made the final months of working on this thesis much more enjoyable. Thank you for the confidence you had in me, which helped me regain confidence in myself as well. I hope we will share many more adventures together. Finally, my **parents**: I owe you more than I can put into words. You taught me to dare to climb in the first place. How often did I come home not knowing how to continue or where to go? Yet you were always there, calmly supporting me from the ground, helping me find the courage to keep going and to keep exploring.

LIST OF PUBLICATIONS

PUBLICATIONS

- **W.S. Brouwer** and R.F. Hanssen, "A treatise on InSAR geometry and 3-D displacement estimation", *IEEE Transactions on Geoscience and Remote Sensing*, Vol. 61, 2023. <https://doi.org/10.1109/TGRS.2023.3322595>
- **W.S. Brouwer** and R.F. Hanssen, "Estimating three-dimensional displacements with InSAR: the strapdown approach", *Journal of Geodesy*, Vol. 98, 2024. <https://doi.org/10.1007/s00190-024-01918-2>
- **W.S. Brouwer** and R.F. Hanssen, "On the definition of an independent stochastic model for InSAR time series", *IEEE Transactions on Geoscience and Remote Sensing*, Vol. 63, 2025. <https://doi.org/10.1109/TGRS.2025.3600893>
- **W.S. Brouwer** and R.F. Hanssen, "3D surface displacement estimation over the Groningen gas field, the Netherlands", *Submitted to Netherlands Journal of Geosciences*, August 2025. <https://doi.org/10.31223/X5775W>,
- Y. Wang, **W.S. Brouwer**, F.J. van Leijen, and R.F. Hanssen. "Instantaneous State InSAR: Estimation and Prediction for Near Real-Time Displacement Monitoring". *IEEE Transactions on Geoscience and Remote Sensing*, Vol. 64, 2026. <https://doi.org/10.1109/TGRS.2026.3681072>,
- A.M. Lapadat, H. Andreas, **W.S. Brouwer**, S.A.N. van Diepen, D. Pradipta, and R.F. Hanssen, "Land subsidence in Jakarta in Three Dimensions (2014-2025) using InSAR-GNSS Datum Connection and the Strapdown Decomposition.", *submitted to Remote Sensing of Environment*, January 2026. <https://doi.org/10.31223/x5r45h>,

IN PREPARATION

- **W.S. Brouwer** and R.F. Hanssen, "Classification of Geodetic Deformation Monitoring in Eulerian and Lagrangian frameworks and its consequences for derived products", 2026.

CONFERENCE PAPERS (PEER REVIEWED)

- **W.S. Brouwer** and R.F. Hanssen, "An analysis of InSAR displacement vector decomposition fallacies and the strapdown solution", *Proceedings of the 2021 IEEE International Geoscience and Remote Sensing Symposium*, Brussels, Belgium, 2021. <https://doi.org/10.1109/IGARSS47720.2021.9554216>
- **W.S. Brouwer**, Y. Wang, F.J. van Leijen, and R.F. Hanssen, "On the stochastic model for InSAR single arc point scatterer time series", *Proceedings of the 2023 IEEE International Geoscience and Remote Sensing Symposium*, Pasadena, United States, 2023. <https://doi.org/10.1109/IGARSS52108.2023.10282629>

-
- **W.S. Brouwer** and R.F. Hanssen, "On the treatment of the reference image for InSAR parameter estimation for point scatterers", *Proceedings of the 2024 IEEE International Geoscience and Remote Sensing Symposium*, Athens, Greece, 2024. <https://doi.org/10.1109/IGARSS53475.2024.10641373>
 - Y. Wang, **W.S. Brouwer**, F.J. Van Leijen, and R.F. Hanssen. "Non-Parametric InSAR Time Series Analysis of Arcs Using Complex B-Splines", *Proceedings of the 2023 IEEE International Geoscience and Remote Sensing Symposium*, Pasadena, United States, 2023. pp. 8238–8241 <https://doi.org/10.1109/IGARSS52108.2023.10282940>
 - Y. Wang, **W. Brouwer**, F. van Leijen, and R.F. Hanssen. "Constrained recursive parameter estimation for InSAR arcs", *Proceedings of the 2024 IEEE International Geoscience and Remote Sensing Symposium*, Athens, Greece, 2024. pp. 10689–10693 <https://doi.org/10.1109/IGARSS53475.2024.10642786>

OTHER

- **W.S. Brouwer**, and R.F. Hanssen, "3D displacement estimates due to deep-seated hydrocarbon production in Groningen from satellite radar interferometry, 2015-2023", 2025, 4TU.ResearchData. dataset. <https://doi.org/10.4121/34394aab-6139-4397-9235-f9f041ac9299>
- **W.S. Brouwer**, A. Theodosiou, P. Lopez-Dekker, and R.F. Hanssen, "No-DRaMA Software", 2022, [Online]. Available: <https://gitlab.tudelft.nl/drama/drama>
- Television broadcast: Willebrord Snellius, 12 June 2024, Jekels Jacht, NTR. https://ntr.nl/Jekels-jacht/496/detail/Willebrord-Snellius/VPWON_1344301
- Deelname als tafelwetenschapper bij de Avond van wetenschap en maatschappij: De onstuimige dynamiek van de Nederlandse bodem gezien vanuit de ruimte, 9 oktober 2023

CURRICULUM VITAE

Wietske Sara BROUWER



Outside of research, I enjoy: alpinism in the mountains, wild camping and making campfires, trail running and cycling, rock climbing, reading a book by a mountain stream in the Alps, ski mountaineering, thyme tea, and red wine.

- 2021–2025 **Ph.D. in Geoscience & Remote Sensing**
Delft University of Technology, The Netherlands
- 2024 **Research visit in China**
Yunnan University, Kunming, China
- 2018–2021 **M.Sc. in Geoscience & Remote Sensing**
Delft University of Technology, The Netherlands
- 2019 **Research project in Kathmandu**
Smartphones4water, Kathmandu, Nepal
- 2014–2018 **B.Sc. in Civil Engineering**
Delft University of Technology, The Netherlands
- 2008–2014 **High School**
UniC Utrecht, The Netherlands
- 27-08-1996 **Born in Utrecht, the Netherlands**

InSAR products are the outcome of processing choices, model assumptions, and the intended use of the data. Thus, different choices inevitably lead to different results. This study revisits the fundamental decisions underlying InSAR parameter estimation, starting from the radar observations and following the complete chain from points, via arcs and networks, to displacement products and their three-dimensional interpretation. It discusses how stochastic and functional models should be defined, how application-aware and application-aligned (triple-A) networks can be constructed, and how displacement estimates can be interpreted in three dimensions. By rethinking these foundations, this work moves beyond generic wide-area products towards interpretable, trustworthy, and actionable InSAR information products.